Scuola Normale Superiore di Pisa
Corso di Perfezionamento in Fisica

Tesi di Perfezionamento

Analysis of sensitivity and noise sources for the Virgo gravitational wave interferometer

Author
Gabriele Vajente

Supervisors
Prof. Francesco Fidecaro
Prof. Lorenzo Foá

Acknowledges

Working at the commissioning of the Virgo detector has been a challenging and exciting job. I had the opportunity to work together with many extraordinary people and researchers, and from everyone I could learn many things. There are many people I would like to thank here. I will try to remember some of them, even if this might make a quite long list...

To Francesco, for the warm welcome when I first decided to enter in the Virgo world, and for all the help I received during my Ph.D. work.

To all the INFN Pisa group, for their support and sympathy.

To Stefano and Matteo, from whom I learnt many things.

To Adalberto, for his great passion and for all the daily questions on the experiment status.

To Marina, Maddalena and Simona, for all the time spent together sharing the same office and for their friendship, which sometimes made the work lighter.

To Paolo, for the hours spent discussing about this strange interferometer and how to improve it.

To my fellow lockers, Enrico and Bas, for all the long night shifts spent together, eating a quick pizza before going back to work.

To Matt and Lisa, who taught me most of what I know about locking an interferometer

To Edwige, Julien, Eric, Dominique, Heinrich, Ettore, Giovanni, Irene, Enrico, Francois, Nicolais, Fabien, all the commissioning team, the operators, EGO and the entire collaboration, for their work and their support.

To Diego, for all the time he spent teaching me control theory and physics, but most of all for his friendship.

To my friends Luca, Francesca, Ilaria, Angela, Paola, Tiziana, Sandro, ... for listening to me when I needed somebody to complain to. *Ai miei amici, per avermi ascoltato quando avevo bisogno di qualcuno con cui lamentarmi.*

To my parents and my family, without them nothing of this all would have been possible. *Ai miei genitori e alla mia famiglia, senza di loro niente di tutto questo sarebbe stato possibile.*

To Claudia, and no words are enough. *A Claudia, e le parole non bastano.*

Introduction

The existence of gravitational radiation, known as *gravitational waves*, is one of the most important predictions of the General Theory of Relativity [1, 2]: every accelerating massive body loses energy by emitting a traveling distortion of the space-time metric. Despite this great generality, the gravitational interaction weakness imposes stringent requirements on the bodies that can emit non negligible amounts of energy by gravitational waves: actually only very massive astrophysical objects are candidates for being detectable sources of this form of radiation.

The detection of gravitational waves coming from the universe is a challenging task and even though experimental efforts have been going on since several decades, so far no direct detection has been achieved. There are only strong indirect evidence of the existence of gravitational radiation coming from binary pulsar systems [3, 4, 5].

Nowadays the most sensitive instruments developed with the aim of detecting gravitational waves are large scale interferometers [6]: the two LIGO detectors in the United States [7], the German-British GEO600 in Germany [8], the Japanese TAMA300 [9] and the French-Italian Virgo [10]. There are also plans for an Australian interferometer [11].

On May 18^{th} 2007 the Virgo detector started a joint data taking run with the LIGO Scientific Collaboration until October 1^{st} 2007, opening the perspective of measuring the sky position of the gravitational wave source. This is also the first Virgo long science run (VSR1: Virgo Science Run 1).

The *commissioning* of a gravitational wave interferometric detector is a complex work, consisting in a large number of different tasks. This thesis is mainly concerned with the development of strategies for the control of the optical system and with all the efforts directed toward improving the sensitivity of the detector. The main topics are: characterization of the longitudinal sensing and control system; study of the origin of the noise limiting the current detector sensitivity; development of techniques for the characterization of non-stationary noises.

The outline of this thesis is the following:

- The first two chapters are of an introductory nature. *Chapter one* describes very briefly the basic theory of gravitational waves, the possible astrophysical sources and the principles behind their interferometric detection. *Chapter two* describes in detail the Virgo detector, focusing on all those aspects that are needed for the discussions of the remaining chapters.

- The following two chapters introduces the principles of the interferometer sensing and control systems. *Chapter 3* describes the longitudinal sensing and control system, while *Chapter 4* discuss the basic principles of the angular one.

- The main part of this thesis, which directly describes the author's work, starts with *Chapter 5*. It describes several studies aimed at the characterization of the longitudinal sensing and control system. These activities have been carried out mainly by the author in collaboration with the *locking team*, with the main goal of gaining a better understanding of the system and to improve its performance in terms of stability, robustness and noise.

- The second main section of this work contains several chapters dedicated to the study and characterization of the detector noise and sensitivity. *Chapter 6* introduces the techniques used for the measurement of the sensitivity and some basics tools for noise studies, like the coherence analysis. *Chapter 7* describes the application of these techniques to the Virgo interferometer configuration running during VSR1, being this one of the main commissioning tasks carried out by the author. *Chapter 7* also summarize all the main sources of noises that couple linearly with the main output gravitational channel, describing the typical performances obtained during the science run.

- *Chapter 8* describes some tools and techniques developed by the author to study the long-term variation of the detector output noise. It is based on the on-line computation of band-limited RMS of the main detector output signal.

- Finally *Chapter 9* describes a fast algorithm, developed within the GEO600 collaboration and implemented in Virgo by the author, to detect fast transient noises in the output signals and its application to the Virgo data.

Several appendices describes some ancillary topics that are relevant for all of the work of this thesis. *Appendix A* contains an analytic derivation of the behavior of fields and signal inside some simple optical systems. *Appendix B* details the lock acquisition procedure used in Virgo to reach science configuration during VSR1. *Appendix C* briefly describes basic notions about linear

systems and transforms. *Appendix D* describes the topic of signal analysis, focusing mainly on spectral techniques. *Appendix E* describes in some details the topic of feed-back control systems, widely used in gravitational wave detectors like Virgo. Finally *Appendix F* describes a software implementation of the demodulation technique.

Contents

Chapter 1

Gravitational waves

The goal of this chapter is to briefly introduce the theory of gravitational radiation, the possible astrophysical sources, the effect on test masses and the basic principles of interferometric detection.

1.1 Linearized Einstein's equation

Despite that the Einstein's equation for space-time metric is non linear, it is possible to specialize it to the case of small perturbations of a flat Minkowski metric $\eta_{\mu\nu}$:

$$g_{\mu\nu} = \eta_{\mu\nu} + h_{\mu\nu}$$

where $||h_{\mu\nu}|| \ll 1$. It can be shown (see [1, 2] for a detailed discussion) that there exists a particular choice of coordinates, corresponding to the *Lorentz gauge* for the metric, where the Einstein's equation reduces to

$$\left(\partial_t^2 - \nabla^2\right)\, h_{\mu\nu} = 0$$

with the additional constraint:

$$\partial_\beta h^\beta_\alpha = \frac{1}{2}\partial_\alpha h^\beta_\beta$$

These two equations are very similar to the ones that describe the propagation of electro-magnetic radiation, and therefore they can be solved by plane waves with wave-vector k_μ:

$$h_{\mu\nu}(x) = A_{\mu\nu}\, e^{ik\cdot x}$$

where the field amplitude $A_{\mu\nu}$ is transverse:

$$A_\mu k^\mu = 0$$

The Lorentz gauge is not uniquely fixed, and the remaining arbitrariness is enough to impose four further conditions on the $A_{\mu\nu}$. In particular, given the

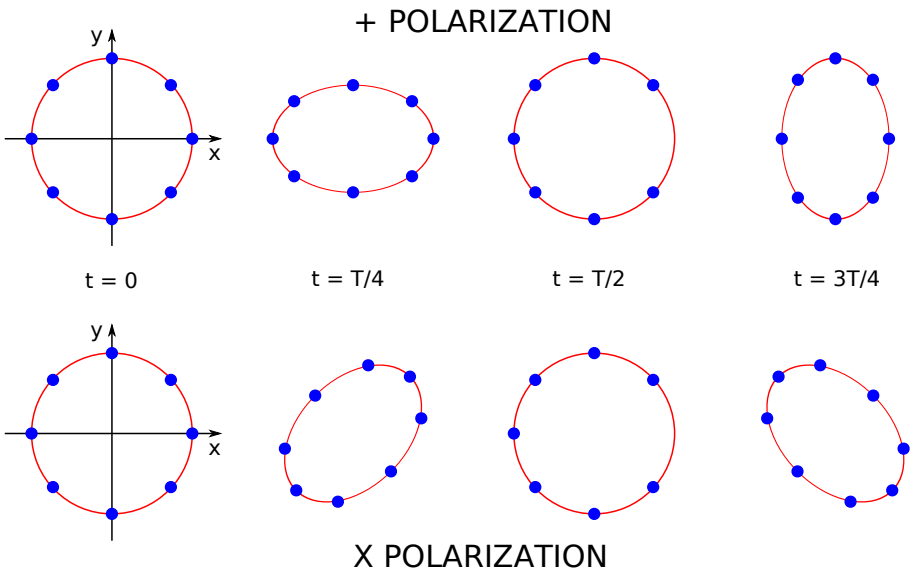

Figure 1.1: Effect of plus and cross polarized gravitational waves propagating along the z axis on a ring of free falling masses. The strain is shown every quarter of period.

observer 4-velocity u_μ it is possible to perform a further coordinate change such that:

$$\begin{aligned} A_{\mu\nu}u^\mu &= 0 \\ A^\mu_\mu &= 0 \end{aligned}$$

In total there are eight constraints for the ten components of the symmetric amplitude tensor. The two remaining degrees of freedom are indeed the two physical polarizations of the gravitational wave in the *transverse-traceless gauge*. For a gravitational wave propagating along the z axis, the metric can be expressed as

$$h_{\mu\nu} = \begin{pmatrix} 0 & 0 & 0 & 0 \\ 0 & A_+ & A_\times & 0 \\ 0 & A_\times & -A_+ & 0 \\ 0 & 0 & 0 & 0 \end{pmatrix} e^{ik\cdot x}$$

The two polarizations are usually known as *cross* and *plus*. The important result that follows from this solution is that the effect of a gravitational wave on the space-time metric has an intrinsic differential nature. This means that the distance between two nearby test masses in the metric generated by a gravitation wave is modulated at the wave frequency with opposite sign in the x and y direction (see fig. 1.1). The relative change in the distance is given by the amplitude of the gravitational wave h, usually called *strain amplitude*.

For example, assuming a plus-polarized gravitational wave travelling along the z direction, the effect on the metric is given by

$$ds^2 = c^2\,dt^2 + (1 + h_+)\,dx^2 + (1 - h_+)\,dy^2$$

It can be shown that the effect on a light ray propagating between two free-falling masses is a change in the optical path and a deviation of the direction of propagation. This second effect is however negligible as long as the gravitational wave is weak [1, 2]. Therefore, for a path lying along the x axis, at first order in the strain amplitude h:

$$dx = \pm c\,dt\,\left[1 - \frac{1}{2}\,h_+(t)\right]$$

The effect has the opposite sign for the y direction.

The propagation of a light ray over a finite distance in the field of a monochromatic gravitational wave of frequency $\nu_g = \omega_g/2\pi$ can be described in terms of *retarded time*. Suppose a light pulse is emitted from a free-falling mass at a given time, reflected by another mass at a distance L, and detected back at the first mass at a certain time t_0. It can be shown [12] that the emission time of the pulse depends on the gravitational wave amplitude and frequency and is given by

$$t_r = t_0 - \frac{2L}{c} + \varepsilon\,h\,\frac{L}{c}\,\mathrm{sinc}\left(\frac{\omega_g L}{c}\right)\cos\left(\omega_g(t - L/c)\right)$$

where $\varepsilon = 1$ for the x direction and -1 for the y. Consider two light pulses emitted on a free falling mass in the origin of the coordinate system toward two other distant masses at a distance L along the x and y axes, reflected back to the origin and detected there. The two pulses arrive at the origin with a time lag given by the difference in the optical paths due to the effect of the gravitational wave:

$$\delta t_{GW} = h\,\frac{2L}{c}\,\mathrm{sinc}\left(\frac{\omega_g L}{c}\right)\cos\left(\omega_g(t - L/c)\right) \tag{1.1}$$

1.2 Astrophysical sources

In the far field and slow motion approximation, the gravitational wave field generated by a source can be expressed as [1, 2]

$$h^{\mu\nu}(\mathbf{r}, t) = \frac{2G}{c^4}\,\frac{1}{r}\left[\frac{d^2}{dt^2}I^{\mu\nu}\right]_{t-r/c}$$

where $\mathbf{r}$ is the distance from the source to the observer and $I^{\mu\nu}$ is the trace-reduced quadrupole momentum associated with the energy density $\rho(\mathbf{x}, t)$ of the source:

$$I^{\mu\nu}(t) = \int d^3x\,\rho(\mathbf{x}, t)\,\left(x^\mu x^\nu - \frac{1}{3}x^2\eta^{\mu\nu}\right)$$

The conservation of the stress-energy tensor (which, to first order, is equivalent to the conservation of mass, linear and angular momentum) implies that the first contribution to the emission of gravitational waves comes from the quadrupole term.

To estimate the order of magnitude of the intensity of such radiation the quadrupole momentum of a body of mass M and size R can be approximated with $Q = \varepsilon R^2 M$, where ε is a factor measuring the asymmetry of the mass distribution. Expressing the second derivative of R as the typical speed v of internal motion of the body one obtains

$$h \sim \varepsilon^2 \frac{GM}{c^2} \frac{1}{r} \left(\frac{v}{c}\right)^2$$

The multiplicative factor in front of the previous equation is a very small quantity

$$\frac{G}{c^2} = 7.4 \cdot 10^{-28} \text{ m/Kg}$$

and since the design sensitivity of interferometric detector like Virgo is around $h \sim 10^{-22}$ at 100 Hz it is clear that only astrophysical sources can generate strong enough gravitational radiation to be detectable on earth.

These sources are usually classified depending on the time evolution of the signal they generate: *periodic sources* like pulsars and in general spinning neutron stars or other massive bodies; *quasi-periodic sources* such as coalescing binary systems of neutron stars or black holes; *impulsive sources* (bursts) like supernovae or coalescing systems at the merging point; *stochastic background* of cosmological or astrophysical origin.

1.2.1 Neutron stars

Spinning neutron stars can emit gravitational radiation at once and twice the rotation frequency f if a mass asymmetry is present:

$$h \approx 3 \cdot 10^{-27} \left(\frac{10\ kpc}{r}\right) \left(\frac{f}{200\ Hz}\right)^2 \left(\frac{\varepsilon}{10^{-6}}\right)$$

where ε is the asymmetry in the momenta of inertia of the star. Despite the weakness of these signals, their almost periodic nature makes it possible to integrate over a long period of time to improve the signal-to-noise ratio.

Upper limits on the value of the asymmetry ε can be obtained assuming that the entire spin-down rate of the star is due to energy loss through gravitational radiation. For the Crab pulsar, spinning at 30 Hz, this gives $\varepsilon \approx 7 \cdot 10^{-4}$, corresponding to an amplitude $h \approx 10^{-24}$ at 60 Hz. This signal is possibly detectable with one year of integration with the Virgo design sensitivity [13]. Theoretical prediction of ε are affected by large uncertainties and can range from 10^{-7} up to 10^{-4} [14].

Objects	Range	Expected rate
NS-NS	30 Mpc	0.0003-0.3/yr
NS-BH	60 Mpc	0.0004-0.5/yr
BH-BH	145 Mpc	0.001-3/yr

Table 1.1: Expected rates for the detection of coalescing binary systems. The quoted range corresponds to the expected one from first generation ground based interferometric detectors.

In our galaxy the number of spinning neutron star is of the order of 10^8 [13] but most of them rotate at a frequency lower than 10 Hz, making them undetectable with present ground interferometers.

1.2.2 Coalescing binaries

Binary system composed of two neutron stars (NS), two black holes (BH) or a neutron star and a black hole lose energy by means of gravitational radiation. The frequency of the emitted wave is the double of the orbital one, and it increases the closer the two bodies become, until they merge together. The lifetime of these objects can be of millions of years, but the gravitational radiation can be detected only in the last minutes of their life, when the orbital frequency is above several hertz. When the distance is still large enough (during the *inspiral phase*) the orbit can be computed using the post-Newtonian formalism [5] and the emitted wave-form is known, allowing the use of matched-filtering technique for an efficient detection. The expected frequencies can go up to a maximum of about 1 kHz for NS-NS systems, with a permanence time at a given frequency scaling like $f^{8/3}$.

With the foreseen sensitivity of first generation gravitational wave detectors like Virgo, the expected rates of detectable inspiralling events are affected by large uncertainties [15, 16] and are listed in table 1.1.

When the two objects become close enough, they merge together. During this period the gravitational signal is expected to be burst-like, with frequencies around 1 kHz.

1.2.3 Supernovae

Since the modelling of this kind of events is very difficult and almost unknown, the expected signal is taken to be burst-like, with a duration of few milliseconds. The intensity of the gravitational radiation depends strongly on the amount of energy ΔE emitted in this form. An estimate can be given by [17]

$$h \approx 2.7 \cdot 10^{-20} \left(\frac{\Delta E}{M_\odot c^2} \right)^{1/2} \left(\frac{1\ kHz}{f} \right)^{1/2} \left(\frac{10\ Mpc}{r} \right)$$

A low value of the emitted energy, expected of the order of $\Delta E/M_{SUN}c^2 = 10^{-6}$, would make the amplitude too small for detecting events in the Virgo cluster, where a rate of several supernovae per month is expected [18]. In any case an event in our galaxy (with rates of few per century) will be detectable with reasonable signal-to-noise ratio by first and intermediate gravitational wave detectors.

1.2.4 Stochastic background

A stochastic background can be originated by the incoherent sum of random gravitational wave signals coming for example from astrophysical galactic sources [19] or it can have a cosmological origin. The expected noise floor from astrophysical sources is however well below the present detector sensitivities [20] and even below the one of advanced ground detectors.

The estimates for the gravitational background of cosmological origin are affected by large uncertainties. Their are usually expressed in terms of the ratio Ω_{gw} between the energy density in the gravitational background and the one needed to close the universe [21]:

$$\Omega_{gw}(f) = \frac{1}{\rho_{critical}} \frac{d\rho_{gw}}{d\log f}$$

The best sensitivity to this kind of signal is obtained with coincident analysis between different detectors. The network of first generation ground-based interferometers is expected to be sensitive to Ω_{gw} of the order of 10^{-5}. The standard inflationary model foresees a much smaller value of the order of 10^{-14}, while super-string theories suggest scenarios with a stochastic background of the order of 10^{-9}, strong enough to be detected by advanced ground interferometers [22].

1.3 Interferometric detection

The intrinsic differential nature of the effect of a gravitational wave on a set of test masses makes optical interferometers very efficient detection instruments, since they are extremely sensitive to changes in the relative length of the two orthogonal arms [6].

1.3.1 DC detection with a Michelson interferometer

The simplest optical configuration for detecting a differential motion is a Michelson interferometer (see fig. 1.2). A laser beam impinges on a half reflecting beam splitter, the two emerging beams are sent toward orthogonal directions, reflected back by two mirrors and they recombine at the beam splitter. The *static tuning* $\alpha = 2k(l_a - l_b)$ of the interferometer is the phase difference at the beam splitter

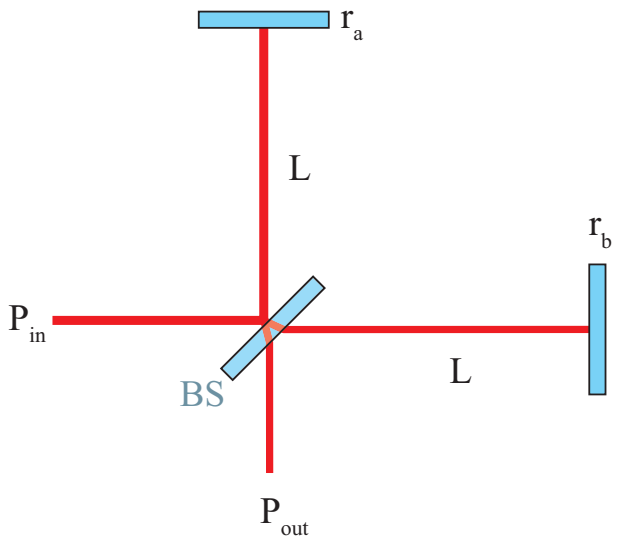

Figure 1.2: Scheme of a simple Michelson interferometer.

between the two reflected beams. The power detected at the output port is:

$$P_{out} = \frac{P_{in}}{2} \frac{r_a^2 + r_b^2}{2} \left[1 + C \cos\left(\alpha + \Phi_{GW}\right)\right] \tag{1.2}$$

where C is the *contrast* which depends on the amplitude reflectivity of the two arm mirrors r_a and r_b:

$$C = \frac{2 r_a r_b}{r_a^2 + r_b^2} \tag{1.3}$$

and which for perfectly reflecting mirrors is equal to 1. For mirrors like those used in Virgo, where $r \approx 1$, C is very close to unity as well as the quantity $(r_a^2 + r_b^2)/2$.

When a gravitational wave passes through the Michelson interferometer, the light beams coming back from the two arms and recombining at the output port undergo an additional different dephasing given by eq. 1.1:

$$\delta\Phi_{GW}(t) = \frac{2\pi c}{\lambda} h \frac{2L}{c} \operatorname{sinc}\left(\frac{\omega_g L}{c}\right) \cos\left[\omega_g (t - L/c)\right] \tag{1.4}$$

The effect is a variation of the power detected at the output port which can be expressed at first order in the gravitational wave amplitude:

$$\delta P_{out}(t) = \frac{P_{in}}{2} C \sin\alpha \cdot \delta\Phi_{GW}(t) \tag{1.5}$$

The term $\operatorname{sinc}(\omega_g L/c)$ is close to 1 for gravitational waves of frequency below few thousands of Hz.

If there were no sources of noise limiting the ability to detect power fluctuations, the best choice for the tuning of the interferometer would be the one that maximizes the sine in eq. 1.5, that corresponds to having half of the maximum power in the output port. This condition is usually called *gray fringe*, while the tuning that give minimum and maximum powers are called respectively *dark fringe* and *bright fringe*.

In reality there is a fundamental limitation to the accuracy of power measurements, given by the *shot noise*, which is connected to the quantum nature of light. This can be intuitively explained as the Poisson distribution related with the process of counting the photons hitting the detector [23, 24]. The amplitude spectral density (see app. D) of the shot noise is given by

$$\mathcal{S}_P(f) = \sqrt{2\, h_P\, \nu\, P} \qquad f \geq 0 \tag{1.6}$$

where h_P is the Planck constant, ν is the frequency of the light and P is the power impinging on the photo-detector. This power spectral density is flat, i.e. it does not depend on the frequency.

Therefore the best tuning for a Michelson interferometer is found maximizing the *signal-to-noise ratio*:

$$SNR(f) = \frac{\mathcal{S}_{\delta P}}{\mathcal{S}_P} = \frac{1}{2}\sqrt{\frac{P_{in}}{h_p \nu}}\, \frac{C \sin\alpha}{\sqrt{1+\cos\alpha}}\, \frac{2\pi L}{\lambda} \mathcal{S}_h(f) \tag{1.7}$$

where $\mathcal{S}_h(f)$ is the spectral density of the gravitational wave signal, L is the average length of the two arms, and P_{in} is the input power of the interferometer.

The maximum of the SNR with respect to the static tuning α is

$$\cos\alpha = \frac{-1+\sqrt{1-C^2}}{C} \tag{1.8}$$

Since the contrast is close to 1, the best tuning of a Michelson interferometer is very close to the dark fringe condition, being $\cos\alpha \approx -1 + \sqrt{2(1-C)}$. This technique is usually called *DC detection*.

The minimum detectable signal is defined as the one having a SNR equal to 1. It is given by the equivalent spectral density in h of the shot noise. Considering that $C \approx 1$ the result is

$$\mathcal{S}_h(f) = \frac{\lambda}{4\pi L}\sqrt{\frac{2 h_P \nu}{P_{in}}} \tag{1.9}$$

For a input laser beam of $10W$ as in Virgo, with a wavelength $\lambda = 1.064\ \mu$m the shot-noise limited sensitivity for a simple Michelson interferometer with 3 km long arms is

$$\mathcal{S}_h(f) \approx 5.4 \cdot 10^{-21}\ \mathrm{Hz}^{-1/2} \tag{1.10}$$

1.3.2 Frontal modulation technique

The present gravitational wave interferometer uses *heterodyne or AC detection technique*. In the *frontal modulation scheme* the input beam is modulated in phase using an *electro-optical modulator* driven with a sinusoidal signal at a frequency Ω. In this way the input electromagnetic field $\psi(t) = A\,e^{i\omega t}$ is changed to

$$\psi_m(t) = A\,e^{i[\omega t + m\sin(2\pi\Omega t)]} = A\sum_{n=-\infty}^{+\infty} J_n(m)\,e^{i(\omega + n\cdot 2\pi\Omega)t} \tag{1.11}$$

where $J_n(m)$ are the Bessel functions and m is the *modulation depth*. The effect can be described as the creation of *radio-frequency sidebands* around the main *carrier* frequency, spaced by multiples of the modulation frequency Ω. More details are discussed in appendix A.

The Michelson interferometer is slightly modified introducing a macroscopic asymmetry ΔL between the two arms, called *Schnupp asymmetry*. In this way the resonance condition for the carrier and the sidebands can be different. Therefore it is possible to have the carrier tuned at destructive interference, while the sidebands are still present in the output port. Using the same conventions of the previous section, in this condition the output field is

$$E_{out} \propto \frac{E_{in}}{2} e^{i\omega t}\ \left[J_0(m)(r_a - r_b) - 2e^{2i\pi\Omega t}\,e^{4\pi i\Omega L/c}\,J_1(m)\sin\left(\frac{2\pi\Omega\Delta L}{c}\right)\right]$$

The output signal is extracted by mixing the photo-diode output current with a reference sine or cosine oscillating at Ω and then by applying a low-pass filter with a corner frequency much lower than the modulation one. In this way the *demodulated* signal contains contributions coming from the beating of the carrier with the two first order sidebands (see app. A):

$$P_{out}^{(dem)} = -\frac{1}{4}e^{-ik_\Omega(\Delta L - 2L)}\left(-1 + e^{2i\Delta L k_\Omega}\right) m\frac{m^2-4}{2} r_2 r_3 t_1^2 \sin(2Dk) \tag{1.12}$$

where D is a small deviation from the dark fringe tuning of the interferometer. In particular this signal is zero in the dark fringe condition.

The effect of a gravitation wave is to introduce an additional dephasing to the two beams recombining at the dark port. This is for all purposes equivalent to a differential deviation from the dark fringe. The response of the demodulated signal to a gravitational wave is therefore linear.

Using eq. 1.12 to compute the response to a gravitational signal and considering the shot noise level corresponding to the sidebands power at the dark port, it is possible to show that the shot-noise limited sensitivity that can be obtained with the AC detection scheme is the same as in the DC scheme. The advantages of this different method are those already anticipated: the detection is shifted at the modulation frequency Ω where the laser intensity and frequency noise are much lower; moreover the control of the interferometer is simpler if

the static tuning is chosen in order to have destructive resonance at the dark port.

1.3.3 Fabry-Perot cavities

The limit on the sensitivity of a Michelson interferometer comes from two main elements: the arms length and the input laser power. Since it is not technically easy to have arms longer than $3-4$ km and input power higher than some tens of W, it is important to find other ways to improve the sensitivity.

One way to increase the effective length of the arms is to substitute them with resonant cavities. In this way the light is stored for a longer time inside the arms, being reflected multiple times back and forth, and therefore enhancing the dephasing due to gravitational waves. For detailed computations of the fields inside a Fabry-Perot resonant cavity see app. A.

The cavity is on resonance when its length is tuned in order to have constructive interference between the field transmitted by the input mirror and the one which has done a round trip inside the cavity. In this condition the power stored inside the cavity can be enhanced by a large factor, which depends on the *finesse* of the cavity

$$\mathcal{F} = \frac{\pi\sqrt{r_I r_E}}{1 - r_I r_E}$$

where r_I and r_E are the input and end mirror reflectivity respectively. With totally reflecting end mirrors, the reflection coefficient of the cavity around resonance is always almost equal to -1. The phase varies from 0 when the cavity is not resonant, to π at resonance. The response of the cavity to a small variation of its length around the resonant one is given by

$$\delta\phi \approx \frac{2\mathcal{F}}{\pi}\frac{2\pi}{\lambda}\,\delta L$$

For a single mirror at the same distance of the end one, the change in phase would have been

$$\delta\phi \approx \frac{2\pi}{\lambda}\,\delta L$$

The effect of the resonant cavity is therefore to amplify the optical response to a length change by a factor

$$g = \frac{2\mathcal{F}}{\pi}$$

If the two arms of a Michelson interferometer are substituted by two resonant cavities with the same length, the effect of a gravitational wave is enhanced by this factor. For the Virgo interferometer, the two arm resonant cavities have a finesse of about 50, resulting in a gain of a factor 30.

A more precise computation of the dephasing of the reflected field must take into account a dependence on the frequency of the cavity length perturbation. In fact one can expect an effect to be visible when the period of the motion

is comparable with the *storage time* of the cavity, which is of the order of $\tau = \mathcal{F}L/c \approx 0.5$ ms. Indeed the response of the cavity exhibits a pole:

$$\delta\phi = \frac{2\pi}{\lambda}\frac{2\mathcal{F}}{\pi}\frac{1}{\sqrt{1+\left(\frac{f}{f_c}\right)^2}} \tag{1.13}$$

at a frequency given by

$$f_c = \frac{c}{4\mathcal{F}L} \tag{1.14}$$

which for the Virgo arm cavities is about 500 Hz.

In conclusion if the two arms of a Michelson interferometer are replaced by two resonant Fabry-Perot cavities, the sensitivity that can be obtained is frequency dependent:

$$\mathcal{S}_h(f) = \frac{1}{8\mathcal{F}L}\sqrt{\frac{2ch_P\lambda}{P_{in}}}\sqrt{1+\left(\frac{f}{f_c}\right)^2} \tag{1.15}$$

For Virgo this would give the limit shown in fig. 1.3, corresponding to a sensitivity of $2 \cdot 10^{-22}\mathrm{Hz}^{-1/2}$ at 100 Hz. Virgo has been commissioned in this configuration (*recombined interferometer*), but with reduced power, starting from the end of 2003, and it has been operated during the commissioning runs C3 (April 2004), C4 (June 2004) and C5 (December 2005).

1.3.4 Power recycling

One way to increase the power circulating inside the interferometer, thus reducing the limitation in sensitivity due to shot noise, is the *power recycling technique*. The idea is that when the interferometer is tuned at dark fringe, since the losses in the arms are very low, all the incoming power is reflected back to the laser. Therefore introducing a mirror (*power recycling mirror*, see fig. 1.4) between the laser and the beam splitter reflecting back this light can strongly enhance the power circulating inside the interferometer.

The effect of such a mirror can be computed describing the Michelson Fabry-Perot interferometer with an equivalent mirror of reflectivity r_{MICH} (close to one in absolute value if the interferometer is tuned at dark fringe). Therefore the full *power recycled interferometer* is equivalent to a Fabry-Perot cavity composed by this mirror and the power recycling mirror [12]. The *recycling gain* is defined as the ratio between the input power and the power circulating inside the central part of the interferometer:

$$G_{PR} = \left(\frac{t_{PR}}{1 - r_{PR}r_{MICH}}\right)^2 \tag{1.16}$$

This increase in the power at the beam splitter mirror translates directly in an improvement of the shot noise limit to the sensitivity. For the final Virgo

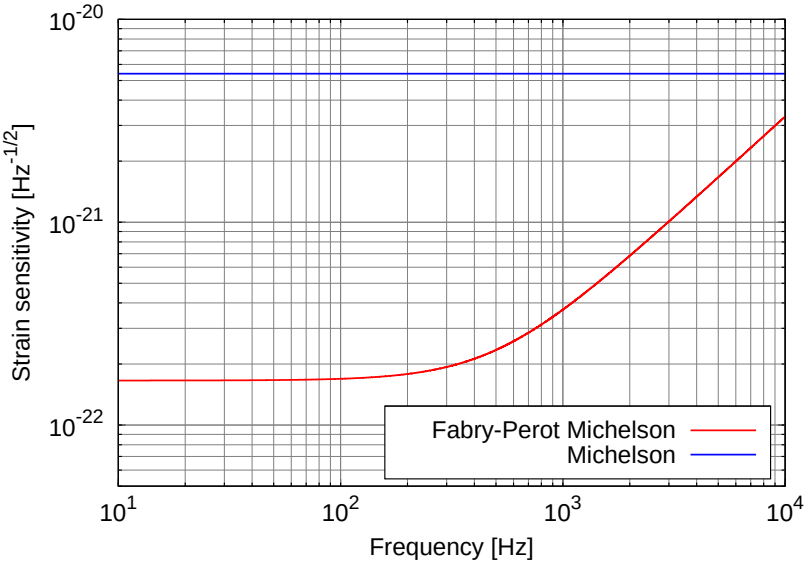

Figure 1.3: Spectral density equivalent to shot noise for a Michelson interferometer with 10 W input power, 3 km long arms with Fabry-Perot cavities with finesse equal to 50, compared to that of a simple Michelson without resonant arms.

configuration the recycling gain is about 50 and therefore the shot-noise-limited sensitivity is given by

$$\mathcal{S}_h(f) = 3 \cdot 10^{-23} \sqrt{1 + \left(\frac{f}{f_c}\right)^2} \ \mathrm{Hz}^{-1/2} \tag{1.17}$$

1.4 Data analysis techniques

Discarding all the complexity of a gravitational wave interferometer, from the data analysis point of view, the detector output is a single time series which reconstruct as well as possible the gravitational signal:

$$s(t) = h(t) + n(t)$$

where $n(t)$ is the detector noise and $h(t)$ contains all the gravitational information. This is given by the convolution of the directional response of the detector, the *antenna pattern* $F(\tilde{\Omega})$, and the gravitational signal [25]:

$$h(t) = \sum_{A=+,\times} \int_{-\infty}^{+\infty} df \int_{S^2} d\tilde{\Omega}\ h_A(f,\tilde{\Omega})\ e^{2\pi i f(t-\tilde{\Omega}\cdot\mathbf{x}/c)}\ F_A(\tilde{\Omega})$$

The antenna pattern is clearly different for the two polarizations and depends on the spatial orientation of the detector [6].

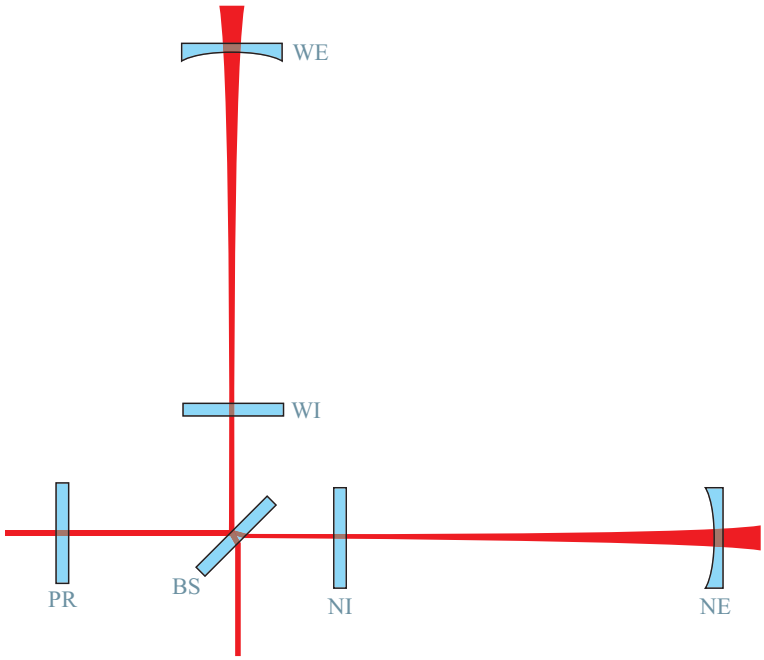

Figure 1.4: Simplified scheme of a power-recycled, Fabry-Perot interferometer.

The goal of any data analysis technique is to detect the presence of a gravitational wave signal in the detector output, discriminating it from the detector noise. The expected wave-forms depend strongly on the source, and so do the techniques used for the detection.

1.4.1 Coalescing binaries

The expected wave-form (*chirp*) can be predicted with good accuracy from Post-Newtonian computations:

$$h(t) = A\,\nu(t)^{2/3}\,\cos(\phi(t) + \phi_0)$$

where A is an amplitude depending on the source distance and orientation with respect to the detector. The time evolution of the frequency can be written, in the Newtonian approximation, as

$$\nu(t) = \nu_0\,(1 - t/\tau)^{8/3}$$

where ν_0 is the frequency at the time when the observation starts ($t = 0$) and τ is the remaining time until coalescence. The phase $\phi(t)$ must instead be computed in the Post-Newtonian approximation. The typical wave-form is shown in fig. 1.5.

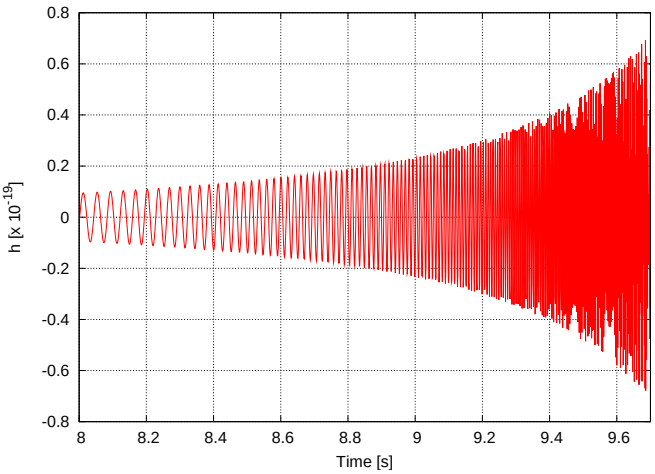

Figure 1.5: Example of expected wave-form from a coalescing binary system (chirp).

Being the expected signal known a priori, and assuming the detector noise to be Gaussian, it is possible to use a *matched filter* technique to obtain an optimal detection algorithm. If the Fourier transform of the expected signal (the *template*) and of the detector output are denoted respectively by $\tilde{g}(f)$ and $\tilde{s}(f)$, an inner product can be defined as

$$\langle s|g\rangle = \int_{-\infty}^{+\infty} df\, \frac{\tilde{s}(-f)\tilde{g}(f)}{S_n(f)}$$

where S_n is the detector noise power spectrum. If the expected signal is not present, this gives a zero-mean random variable with variance depending on the template normalization. Therefore, the following definition of signal-to-noise ratio is directly proportional to the signal amplitude

$$SNR = \frac{\langle g|s\rangle}{\sqrt{\langle g|g\rangle}}$$

For a given choice of the two body masses the expected wave-form is known and its amplitude depends linearly on the inverse of the source distance. Therefore the previous equation can be inverted to yield the maximum distance of a detectable coalescing event given the detector sensitivity. This gives a useful figure of merit of the detector sensitivity: the maximum distance at which a 1.4 solar masses NS-NS coalescence is detectable with SNR equal to 8 is usually quoted as the *range* or *horizon* of the detector. The *optimal-oriented* horizon refers to the situation of a source with a sky position and orientation such to maximize the detector efficiency. When an average over all sky position and orientation is performed the *averaged* horizon is obtained.

During Virgo normal operation the averaged horizon D_{NS-NS} is computed on-line using a wave-form model based on the stationary phase approximation [26]. This yields the following equation:

$$\frac{D_{NS-NS}}{\text{Mpc}} = 10^{-20}\sqrt{\int_{40\text{ Hz}}^{2300\text{ Hz}} \frac{f^{-7/3}}{S_h(f)}\,df}$$

where $S_h(f)$ is the one-sided power spectral density of the detector noise expressed in units of gravitational strain.

The efficiency of the matched filter detection algorithm depends on the matching between the template and the real signal parameters. Since there is no way to know a priori which are the parameters of the incoming signal, the search algorithm must be able to detect with good efficiency any possible source. This is obtained computing and using a suitable template bank: the entire parameters space is covered in tiles and a template is produced for each of these. The number of tiles is a compromise between computational time and detection efficiency: increasing the number of templates will increase both.

1.4.2 Stochastic background

Being the contribution of a stochastic background indistinguishable from the detector noise, the only way to detect it is to look for correlations between at least two different detectors. Indeed the output of each detector can be viewed as the sum of its own instrumental noise plus a stochastic signal from the background:

$$s_i(t) = n_i(t) + h_i(t)$$

The different $n_i(t)$ are uncorrelated, while the $h_i(t)$ are. They depend on the detectors position and orientation through the antenna patterns:

$$h_i(t) = \sum_A \int d\tilde{\Omega}\, F_i^A(\tilde{\Omega}) \int_{-\infty}^{+\infty} df\, e^{2\pi i f\left(t - \frac{\mathbf{x_i}\cdot\tilde{\Omega}}{c}\right)}\, \tilde{h}_A(f,\tilde{\Omega})$$

where $\tilde{h}_A(f,\tilde{\Omega})$ describes the stochastic background distribution in frequency and angle.

The detection technique is based on the computation of the correlation between the output of two (or more) different detectors:

$$C_{ij}(t,t') = E\left[s_i(t)s_j(t')\right] = E\left[h_i(t)h_j(t')\right]$$

and the second equality follows from the fact that the detector noises are uncorrelated. If the spectrum of the stochastic background is assumed to be broadband, or in other words without narrow spectral features, the correlation can be written as [21]:

$$C_{ij}(t-t') = \int_{-\infty}^{+\infty} df\, e^{2\pi i f(t-t')}\, \gamma(\mathbf{r}_{ij},f)\, H(f)$$

where γ represent the *overlap function* of the two detector, which depends on their relative orientations and distance

$$\gamma(\mathbf{r}_{ij}), f) = \frac{5}{8\pi} \sum_A \int d\tilde{\Omega}\, e^{2\pi i f \frac{\tilde{\Omega}\cdot\mathbf{r}_{ij}}{c}}\, F_i^A(\tilde{\Omega})\, F_j^A(\tilde{\Omega})$$

and $H(f)$ contains the information on the spectral properties of the stochastic background, here for simplicity assumed isotropic:

$$H(f) = \frac{3H_0^2}{16\pi^2}\, |f|^{-3}\, \Omega_{gw}(|f|)$$

1.4.3 Continuous signals

In the case of continuous periodical signals, the expected wave-form is well known. For example the gravitational wave emitted by a spinning neutron star is given by [27]:

$$\begin{aligned} h_+(t) &= h_0 \sin\alpha \left[\frac{1}{2}\cos\alpha \sin i \cos i \cos\omega\tau(t) - \sin\alpha \frac{1+\cos^2 i}{2} cos 2\omega\tau(t)\right] \\ h_\times(t) &= h_0 \sin\alpha \left[\frac{1}{2}\cos\alpha \sin i \sin\omega\tau(t) - 7\sin\alpha\cos i \sin 2\omega\tau(t)\right] \end{aligned}$$

neglecting the neutron star spin down and Doppler effect related to possible orbital motion. However it is necessary to take into account the detector and source relative motion, dominated mainly by the earth rotation and revolution:

$$\tau(t) = t + \frac{\hat{n}\cdot\mathbf{x}(t)}{c}$$

where $\mathbf{x}$ is the receiver position with respect to a fixed origin.

If the detector and source were relatively fixed, the signal would be monochromatic and the detection would reduce to the analysis of a sine wave in presence of Gaussian noise. This can be easily carried out by computing the power spectrum of the detector output, integrating for a very long period. The obtained signal-to-noise ratio would be

$$SNR = \frac{\sqrt{T}A}{2\sqrt{S_{noise}(f)}}$$

where S_{noise} is the detector noise power spectrum and A the signal amplitude.

However in the real case the Doppler effect due to the earth motion modulates the signal. The most important contribution comes from the change in phase of the received signal

$$\frac{d\phi(t)}{dt} = \omega\left(1 + \frac{\hat{n}\cdot\mathbf{v}(t)}{c}\right)$$

which, even if small, produces a large effect over long integration periods.

This makes necessary to compensate the Doppler effect to have an efficient detection. Like in the case of coalescing binaries, if the position in the sky of the source is known, the expected wave-form can be computed and a matched filter can be used. This is equivalent to computing the power spectrum using non-equispaced samples, considering equal time interval for $\tau(t)$ but not for t. The general method consist in computing the *Lomb periodogram* [28]. Another proposed approach is to directly resample the detector output signal to compensate the Doppler effect and to proceed afterward with a monochromatic signal search [29]. In both cases the detection algorithm depends on the source position and orientation with respect to the detector. A template search similar to that used for coalescing binaries must be set up, covering the entire parameter space with a suitable set of tiles.

1.4.4 Bursts

The characteristics of burst signals are almost completely unknown, and therefore it is not possible to implement matched filtering techniques. A detection algorithm for bursts must be able to detect short transient signals over a background of stationary Gaussian noise. It usually consist in selecting a suitable list of candidate events based of thresholds on suitable signal statistics. A simple method, implemented in the HACR algorithm described in chapter 9, compute a time-frequency map of the detector output and select triggers based on the excess of power in each bin with respect to the mean power spectrum statistics. More sophisticated algorithms used banks of band-pass filters to reconstruct the power in selected frequency bins (*power filters*), or the correlation with a set of templates of sine-Gaussian signals. More recent algorithm uses a decomposition of the detector output by means of *wavelet transforms* [30].

In all cases, the expected signal from a gravitational wave burst can be very similar to transient noises coming from the detector, triggered for example by environmental events. For this reason a large part of the burst analysis is devoted to the identification of the time intervals and frequency bands with good data quality (*data conditioning*). Even after this the number of candidate events can be very large, due to the non-stationary nature of the detector noise. A large part of these candidates must be discarded by using suitable *vetoes*: for example it is possible to discard a candidate which is coincident in time with a noise transient in some channel which cannot contain any gravitational wave information. Such channels can come for example from environmental sensors, like seismometers, microphones or magnetometers. Since the number of expected gravitational events is very small, such vetoes must have a very low false alarm rate.

Finally, the best way to exclude candidates coming from noise events is to perform a coincidence analysis between different detectors. Indeed, assuming

the noises of the two detectors to be uncorrelated, any coincident candidate is likely to come from a real burst event.

Chapter 2

The Virgo detector

This chapter describes the Virgo interferometer for gravitational wave detection, in all the main aspects needed for the rest of this thesis.

2.1 Optical lay-out

The Virgo gravitational wave detector is a power recycled interferometer with arms replaced by 3 km long resonant Fabry-Perot cavities. Its schematic optical lay-out is shown in fig. 2.1. The two arm cavities are called *north* and *west*. The two mirrors that compose each cavity are called (north or west) *input* and *end* mirror, while the first mirror encountered by the input beam is the *power recycling mirror*. It is customary to abbreviate the name of the mirrors: NI and NE for north cavity input and end mirrors, WI and WE for the west cavity, BS for the beam splitter and PR for the power recycling. The distance between the beam splitter and the power recycling mirror is approximately 6 m, while the distance between the beam splitter and the two input mirrors is on average 6 m, with a Schnupp asymmetry of $l_N - l_W = 0.88$ m.

The main beams coming out from the interferometer are named as follows:

B1 is the dark fringe beam, the one reflected eastward from the beam splitter, resulting from the recombination of the two beams coming from the arm cavities.

B2 is the beam reflected back by the power recycled mirror.

B5 is the beam coming from the secondary anti-reflection-coated surface of the beam splitter mirror. This beam therefore sees a small fraction of the beam reflected back from the north cavity, and is used as an indicator of the field inside the recycling cavity.

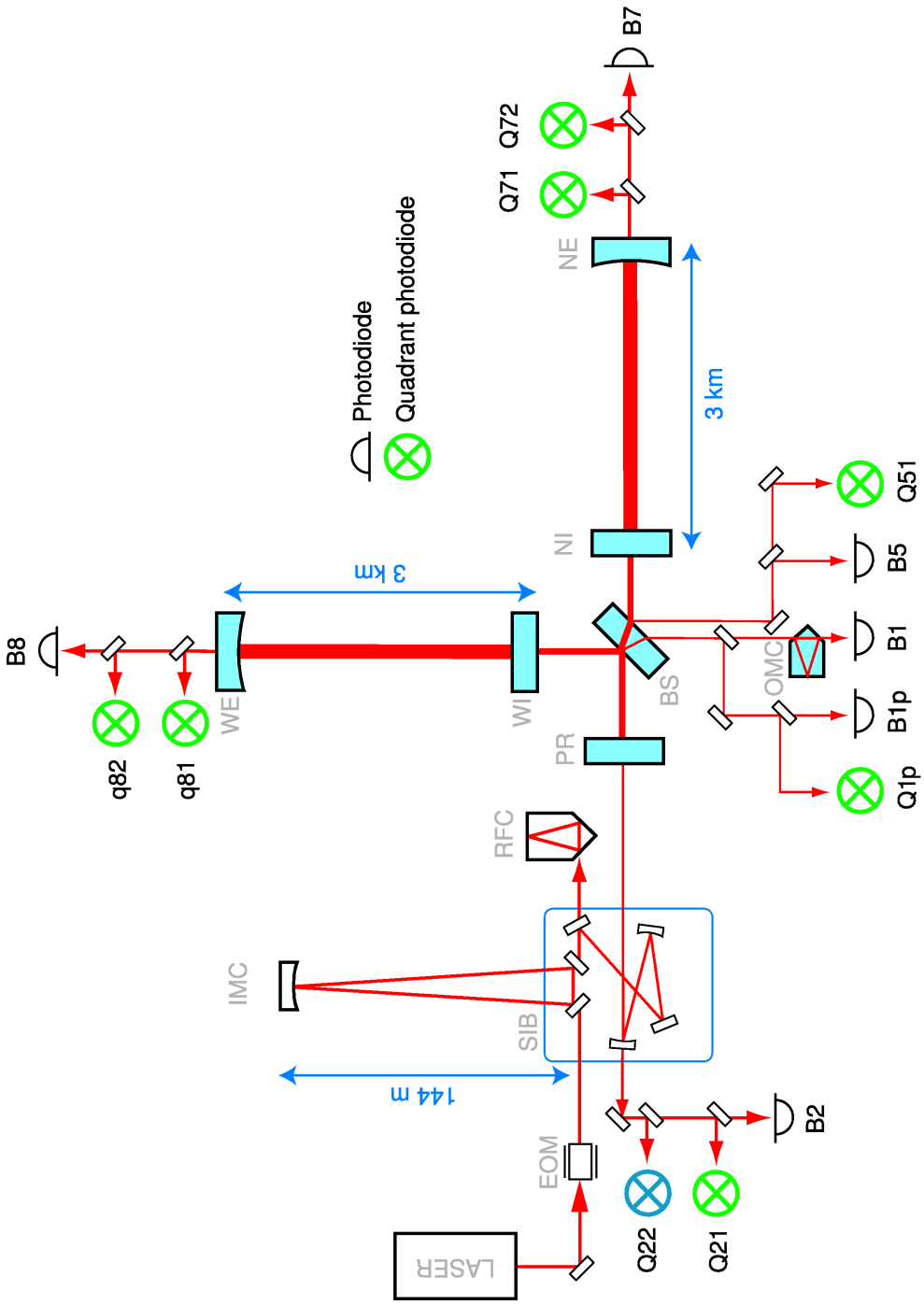

Figure 2.1: Schematic optical lay-out of the Virgo detector. Please refer to the text for more details.

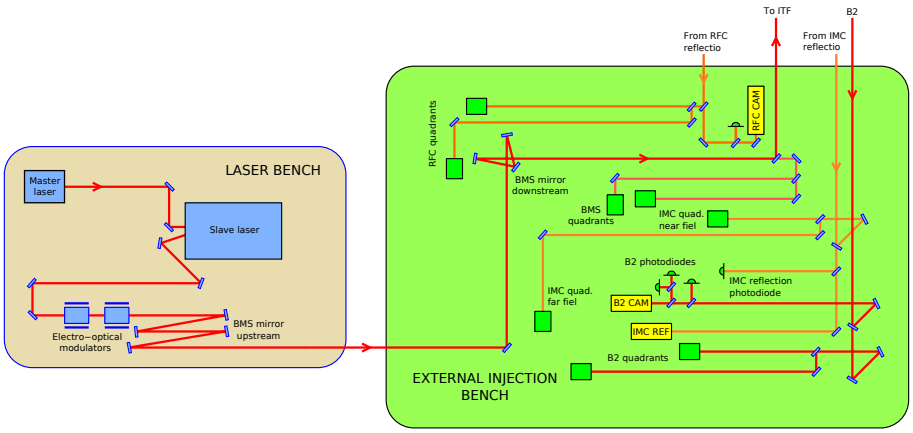

Figure 2.2: Simplified scheme of the two external optical benches in the laser laboratory.

B7 is the beam transmitted through the north arm cavity, thus seen past the north end mirror.

B8 like the previous one but for the west arm cavity.

2.2 Injection system

The input of the Virgo detector is a 20 W laser beam with a wave-length of 1064 nm, generated by a Nd:YVO_4 high power slave laser, injection-locked to a high stability solid state Nd:YAG master laser. In this way the higher power and frequency stability of the master laser is transferred to the slave. The two lasers are hosted in the *laser bench*, one of two optical benches located inside the *laser laboratory* (see fig. 2.2). The power produced by the slave laser can be controlled acting on the current of two pumping diodes. The beam generated by the slave laser passes through two electro-optical modulators, used to generate three different modulation frequencies at about 6 MHz, 8 MHz and 22 MHz.

The pointing of the beam is controlled at the level of the two laser laboratory benches by the *beam monitoring system* (BMS). The beam can be translated and steered by two mirrors mounted on piezo-electric actuators. The first mirror (upstream) is placed on the laser bench, while the second mirror (downstream) is mounted on the *external injection bench*. The error signals for the beam pointing control are obtained from two quadrant-split photo-diodes placed on the external bench. These are photo-detector with sensitive area divided in four sectors, similar to those used for the angular sensing and control (see chap. 4). The difference between opposite sectors are used to reconstruct signals sensitive to the spot position. After the BMS system the beam is sent into the vacuum

to the suspended injection bench.

The external injection bench is also used to collect several beams coming back from the suspended bench: the reflection of the input mode cleaner and of the reference cavity, as well as the beam reflected by the interferometer (B2). These beams are sensed by normal and quadrant photo-detectors and by digital cameras. The first kind of detectors are used mainly for the longitudinal sensing and control system and for the longitudinal control of the injection system. The quadrants are instead used to control the interferometer angular degrees of freedom (see chap. 4). The cameras finally are used mainly for diagnostic purposes. The laser and external injection benches are contained inside acoustic isolation enclosures.

Before entering the main interferometer, the beam passes through the *input mode cleaner* (IMC), a triangular cavity 144 m long with a finesse of about 1000. The role of this cavity is to filter the laser beam suppressing all transverse mode different from the fundamental Gaussian one (see also chap. 4). The IMC cavity is maintained on resonance for the carrier frequency using a Pound-Drever-Hall technique based on a 22 MHz demodulation of the IMC reflection. The 22 MHz sidebands are indeed not resonant inside the input mode cleaner, while the carrier, the 6 MHz and the 8 MHz are. The length control of the IMC is strongly linked to the frequency stabilization of the laser. The topology of the first stage of frequency stabilization is explained in deeper details in chap. 3.

The input mode cleaner cavity is made of a highly reflecting terminal mirror and of the two input mirrors that composes the *dihedron*, mounted on the *suspended injection bench* (see fig. 2.3). The beam reflected by the cavity is sent back to the external bench. The transmitted beam passes instead through a *Faraday isolator*: the beam is completely transmitted from the bench to the interferometer, while in the other direction it is attenuated by a factor of about 1000. This avoids the light reflected by the power recycling mirror to enter the IMC and interfere with the main one. The reflection of the Faraday isolator is used to reconstruct the B2 beam.

The beam transmitted by the Faraday isolator is sent afterward to a telescope composed of two parabolic mirrors, used to match the beam to the resonant mode of the interferometer and to control its position and pointing. Moreover, a small part of the IMC transmission is sent through a periscope to the lower part of the bench to the *reference cavity* RFC, a rigid cavity 30 cm long. This is used as part of the laser frequency pre-stabilization system and of the full interferometer longitudinal control (see chap. 3).

Part of the beam transmitted by the IMC is sent to an in-vacuum photodetector on the suspended bench, used as error signal for the laser power stabilization. This control system is split in two parts. The high frequency path uses only the signal above some Hz as error signal for a loop that acts on the

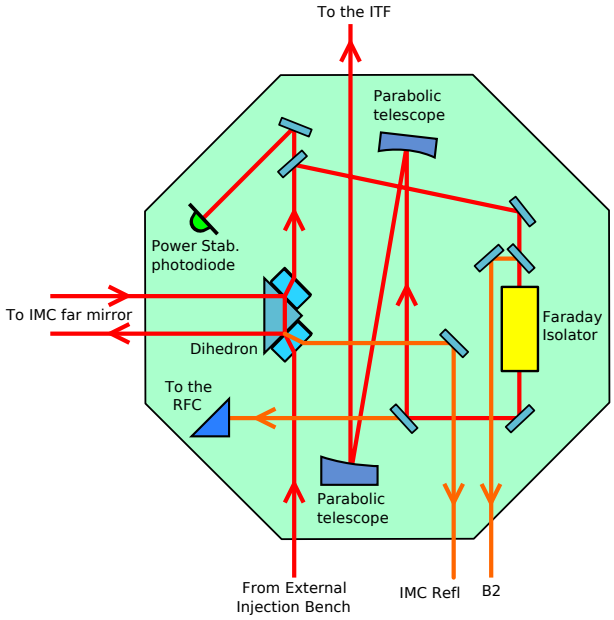

Figure 2.3: Simplified scheme of the suspended injection bench.

slave laser pumping current to stabilize the power transmitted by the IMC with a bandwidth of about 60 kHz. This leaves the mean value of the IMC transmission free to vary. Another slow servo loop allows its stabilization with a bandwidth of about 10 mHz and an adjustable setting point.

2.3 Mirrors

The mirrors used in Virgo are made of high quality fused silica, with a diameter of 35 cm and a mass of about 21 kg for power recycling and cavities mirrors. The beam splitter is slightly smaller, with a diameter of 23 cm and a mass of 5 kg. All mirrors are flat, except the two end ones which are concave. The main parameters for the six main Virgo mirrors are listed in tab. 2.1, 2.2 and 2.3: the radius of curvature ROC of the reflecting face, the reflectivity R and transmissivity T of the two faces, the losses on the high-reflectivity HR and anti-reflection coated AR surfaces. In this configuration the finesse of the two arm Fabry-Perot resonant cavities is about 50 and the recycling gain for carrier and sidebands respectively 40 and 30.

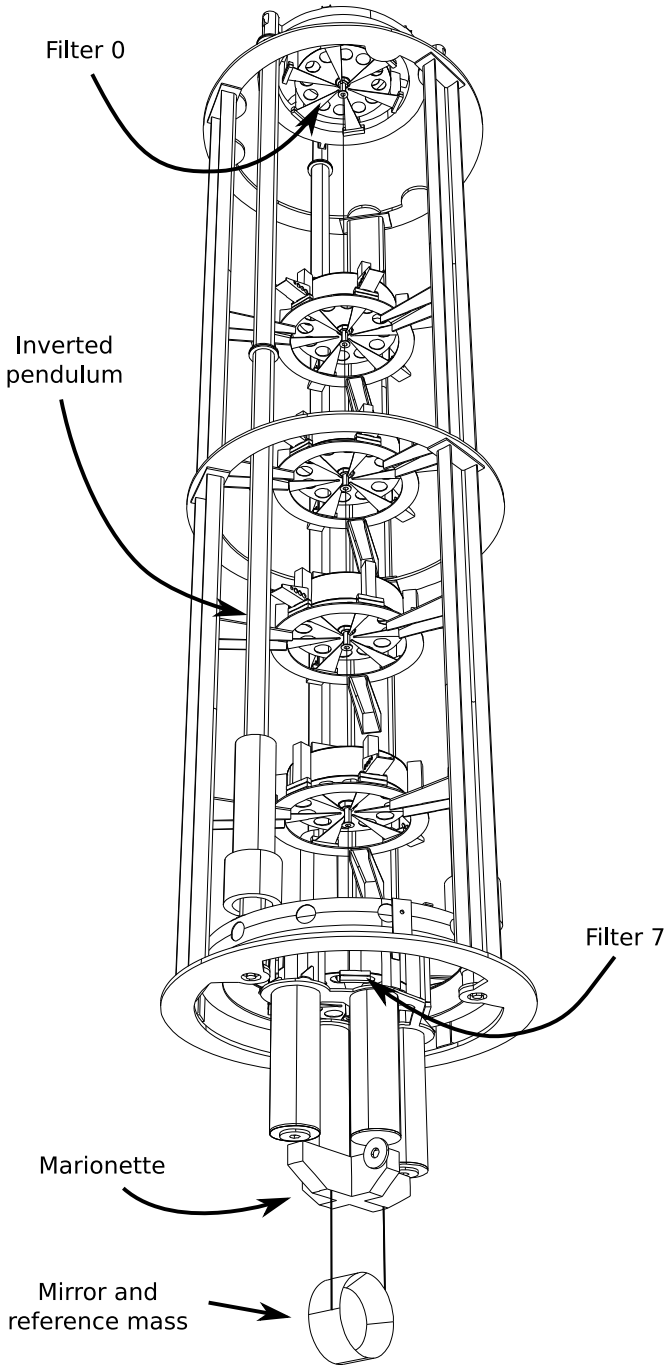

Figure 2.4: Mechanical scheme of the super-attenuator.

Mirror	R 1^{st} face	T 2^{nd} face	Losses HR	Losses AR
NI	132 ± 2 ppm	$11.8 \pm 0.03\%$	9.25 ppm	0.9 ppm
WI	171 ± 0.6 ppm	$11.66 \pm 0.02\%$	15.38 ppm	1.7 ppm

Table 2.1: List of input mirrors parameters.

Mirror	ROC	T 2^{nd} face	Losses HR
NE	3580 ± 17 m	42.9 ± 0.02 ppm	4.67 ppm
WE	3601 ± 15 m	38.3 ± 0.7 ppm	9.19 ppm

Table 2.2: List of end mirrors parameters.

2.4 Suspension and mirror control

One key feature of the Virgo interferometer is the use of high-performance passive seismic isolation systems, called *super-attenuators* (see fig. 2.4), which exploit the attenuation properties of simple pendulum. Indeed, assuming viscous damping, any horizontal motion of the suspension point is transmitted to the suspended mass with an attenuation given by

$$\frac{z_{MASS}}{z_{TOP}} = \frac{f_0^2}{\sqrt{\left[f_0^2 - f^2\right]^2 + \frac{f_0^2 f^2}{Q^2}}} \tag{2.1}$$

where f_0 is the resonant frequency of the pendulum and Q its quality factor. In particular for frequencies above the resonant one, any motion of the top suspension point is suppressed by a factor $(f/f_0)^2$.

The mirrors are suspended to a chain of seven pendulums, with all longitudinal resonant frequencies below 2.5 Hz [31]. Therefore the seismic isolation obtained at 10 Hz is of the order of 10^{14} with respect to the ground motion [32]. Vertical attenuation is obtained replacing the upper five pendulum terminal masses with seismic filters (see fig. 2.5). Two consecutive pendulum wires are connected by a system of elastic metallic blades. The resonant frequency of this system would however be too high, given the necessary stiffness of the metal to support the weight of the entire suspension. They are therefore combined with two sets of magnets in repelling configuration. They form a magnetic anti-spring [33] that combined with the blades gives a low resonant frequency, comparable to that of the horizontal modes. The overall seismic attenuation of the super-attenuator chain is shown in fig. 2.7 for both the horizontal and vertical degrees of freedom. The vertical transfer function is rescaled by a factor 100 to take into account that vertical motions couples much less than horizontal one with the interferometric signals.

The top stage of the entire suspension chain is another vertical filter (*Filter*

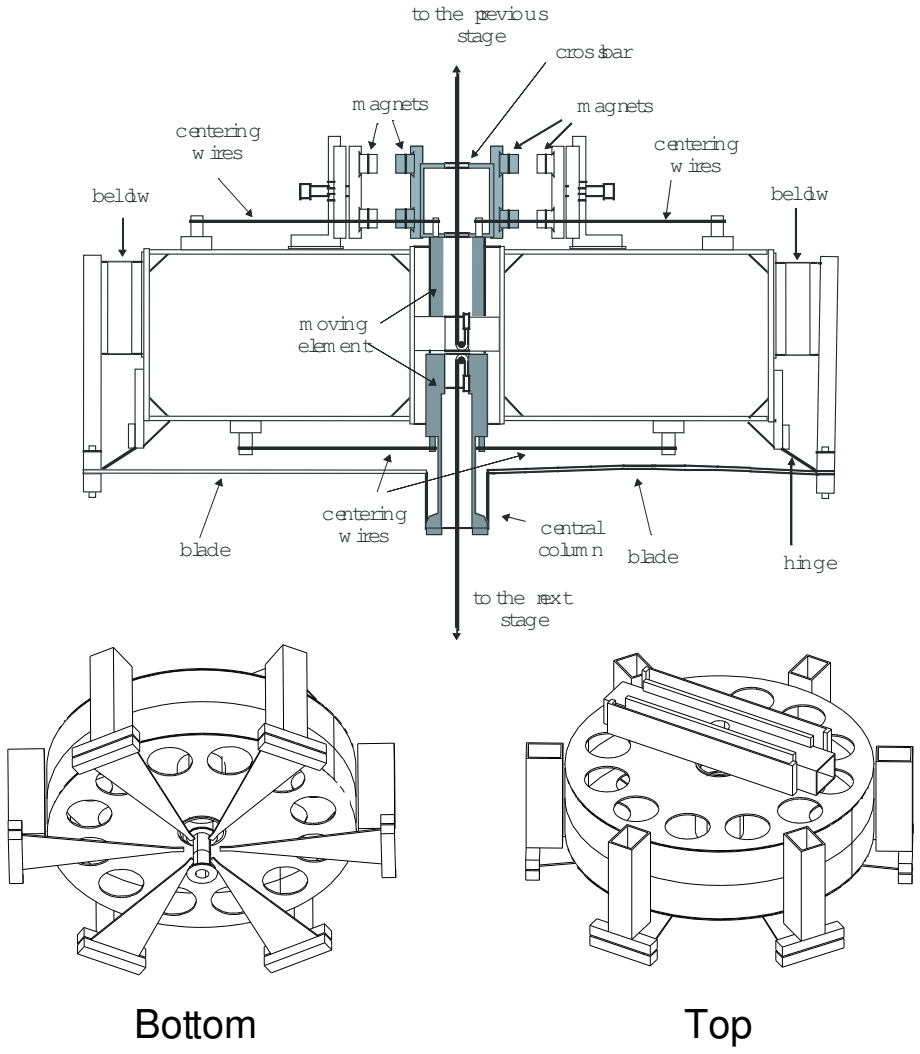

Figure 2.5: Schemes of a vertical isolation filter. The top panel is a schematic drawing, the bottom ones show the full filter viewed from the bottom and from the top.

Mirror	R 1^{st} face	R 2^{nd} face	T 2^{nd} face	Losses
BS	50.25 ± 0.18 %	519 ± 10 ppm		6.85 ppm (HR)
PR	1.8 ± 0.2 ppm		5.13 ± 0.02 %	25.54 ppm (HR)
				2.5 ppm (AR)

Table 2.3: List of PR and BS mirrors parameters.

0), sustained by three legs that form the *inverted pendulum* [34]. The elasticity of the leg joints, combined with the opposite effect of the gravitational force, gives a system with a resonance at about 40 mHz. This is used as pre-isolation stage to reduce the seismic motion of the top suspension point.

The two lower stages of the suspension are quite different from the standard filters. Indeed, the mirror is surrounded by a metallic *reference mass* (see fig. 2.6) which is used as a reaction mass to apply forces to the mirror using four coil-magnets pairs on the back side of the mirror. Both the mirror and the reference mass are separately suspended to the marionette by four wires each. In this way it is possible to act on the mirror also steering the marionette. To this purpose there are four magnets attached to the marionette itself and four coils attached to pillars coming down from the last vertical isolation filter (*Filter 7*).

2.4.1 Suspension control

The active control of each super-attenuator is split in four parts. The inverted pendulum is controlled at the level of the top stage of the suspension, the filter 0, by the *inertial damping system* [35]. The top platform, connected to the inverted pendulum, hosts three accelerometers and a *linear voltage differential transformer* (LVDT) used as absolute position sensor (see fig. 2.8). All signals are acquired by analog-to-digital converters (ADC) and processed by custom digital-signal-processors (DSP). These signals are combined together, using the LVDT at frequencies below 50-100 mHz and the accelerometers at higher frequencies, and used to control the top suspension point horizontal motion and the filter 0 rotation around the vertical axis. The cross-over frequency can be changed maintaining the control system active, to cope with different microseismic conditions. The correction signals for each suspension are computed separately by one DSP system, completely devoted to the inertial damping of the corresponding tower. The computed correction is then applied to the top stage by coil-magnet actuators.

The length of each suspension stage is also measured by individual LVDT sensors, summed together and used to control the vertical position of the payload.

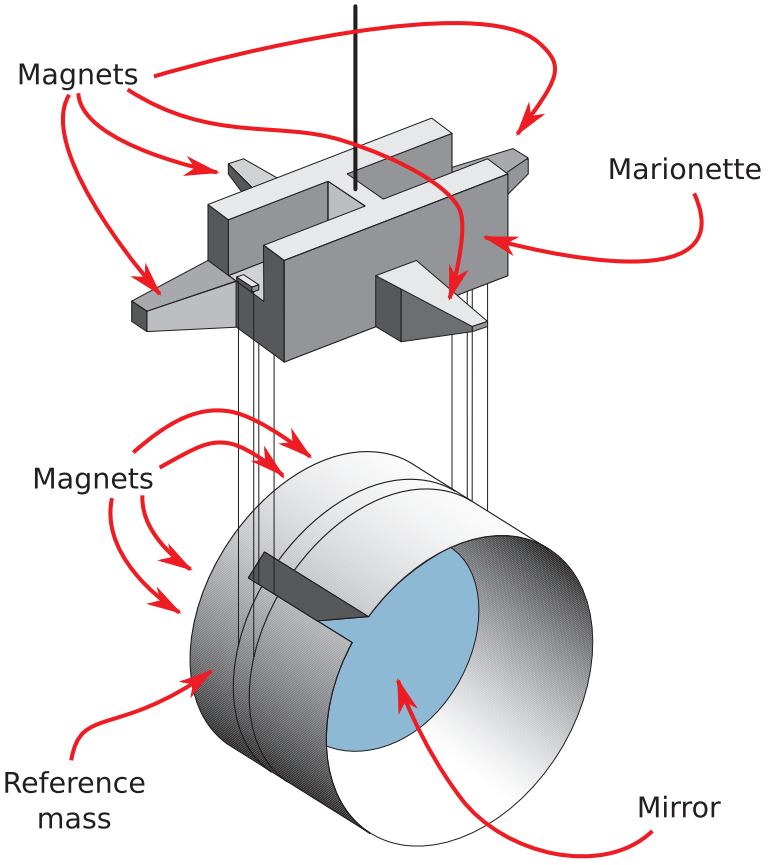

Figure 2.6: Scheme of the bottom part of the super-attenuator, including the marionette and the payload, composed of a mirror and its reference mass.

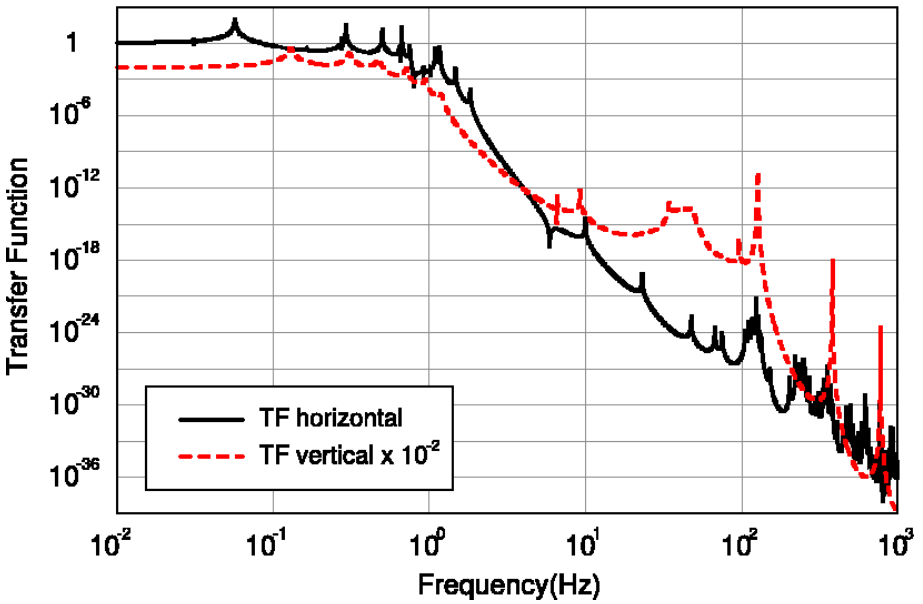

Figure 2.7: Computed transfer function from seismic motion of the ground to mirror displacement, for both the vertical and horizontal degrees of freedom. The vertical transfer function is rescaled by a factor 10^{-2}, assuming a estimated coupling of vertical to horizontal motion of one hundredth. A lower limit measurement of this transfer function is described in [32].

The mirror angular and longitudinal (orthogonal to the mirror surface) motions can be controlled both acting at the mirror or at the marionette level (*local control system [36]*). As already anticipated four magnets are glued to the back face of each mirror, in correspondence to four coils attached to the reference mass. By controlling the current flowing through these coils it is possible to apply longitudinal and torsional forces to the mirror, using another suspended point as reference. In this way the control is free from any contamination with the ground micro-seismic motion. Other four magnets are attached to the marionette, in correspondence to coils that are suspended through pillars coming down from the filter 7. Any current applied to these coils results in a force on the marionette, which is then transmitted by the last pendulum stage to the mirror and the reference mass.

The error signals for the local control systems are obtained using *position sensing devices* (PSD): these are optical levers obtained using low power red laser diodes and quadrant-split photo-detectors (see fig. 2.9). These optical levers are used to measure the angular and longitudinal position of the mirror and also the angular one of the marionette, using a small mirror attached to it. When the motion is too large for the dynamical range of the PSD sensors, the

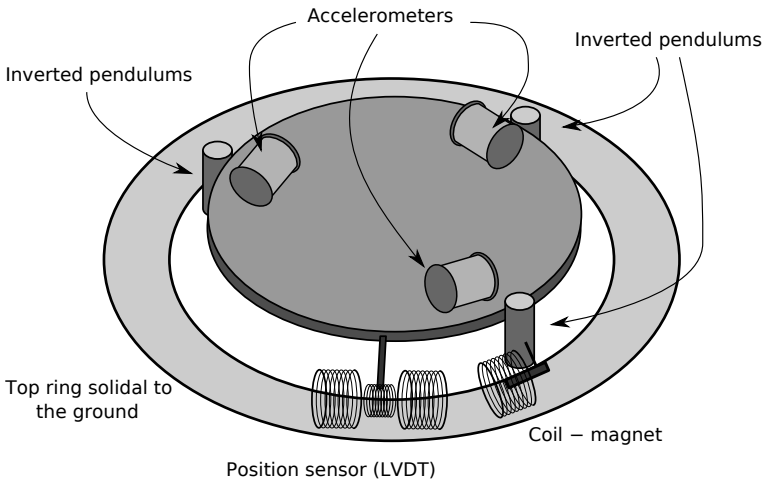

Figure 2.8: Scheme of the top stage of the super-attenuator, hosting the sensors and actuators used for the inertial damping system.

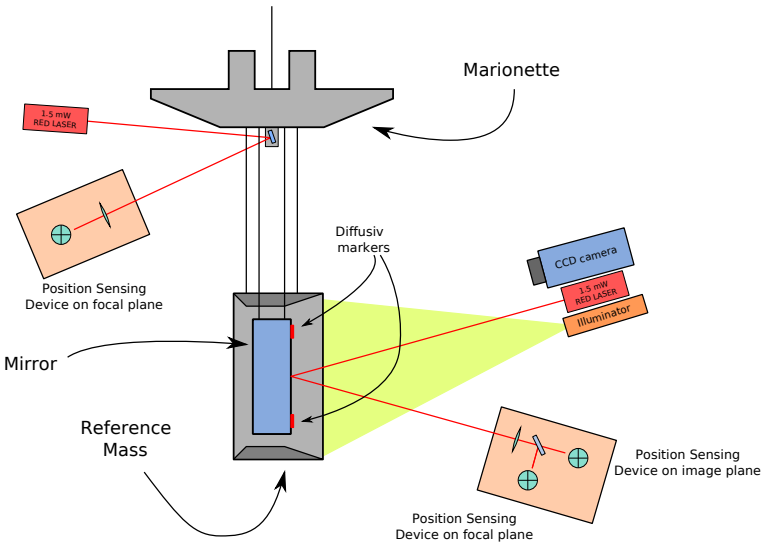

Figure 2.9: Scheme of the local control sensing system, including the marionette and mirror optical levers.

rough position is reconstructed using a camera which looks at diffusive markers attached to the mirror itself.

All local control signals for each single mirror are acquired by ADC boards and processed by a dedicated DSP. This system also receives global interferometric signals for the longitudinal and angular sensing and control, transmitted to the central and terminal buildings by *digital optical links*.

The current flowing into each coil is controlled by custom *coil drivers*. Indeed, the digital correction computed by the DSPs are converted by *digital-to-analog converters* (DAC) to a voltage signal which is suitably amplified and translated into a current flowing in the coil. These coil drivers have two different control sections: the *high power* is capable of applying stronger forces to the mirror, at the price of a higher noise level, while the low-noise one has a lower peak-to-peak range and better noise performances. The first section is used during the lock acquisition procedure (see sec. B) when the free swinging mirror must be stopped and strong forces are needed. The second one is engaged only close to the final detector state. In order to reduce as much as possible the required dynamics of the actuators, part of the control force is re-allocated from the mirror-reference mass actuators to higher stages: the very low frequency component is sent to the inertial damping control system through serial links between the different DSPs; the intermediate frequency component is actuated on the marionette and only the high frequency one is sent to the reference mass coils.

Short suspensions

The two detection and injection suspended optical benches, as well as the mode cleaner terminal mirror, are suspended to a short version of the super-attenuators. This consists in a shorter inverted pendulum and a suspension with only two intermediate vertical filters. The isolation performances of this system are matched to the IMC and suspended benches requirements and clearly lower than those of the full super-attenuators.

2.5 Detection system

All the relevant beams coming out of the interferometer are sensed using *photo-detectors* that convert the laser power impinging on them in a electric signal. The typical power hitting a photo-detector can range from some μW to 100 mW. The output signal is first pre-amplified in order to enhance the carrier and the first modulation harmonic with respect to the higher ones. This signals is then split in three parts. One is low-passed and used to give a signal measuring the total power that hits the detector. The other two are sent to a demodulation electronic. Here the two signals are mixed with two reference sinusoidal waves

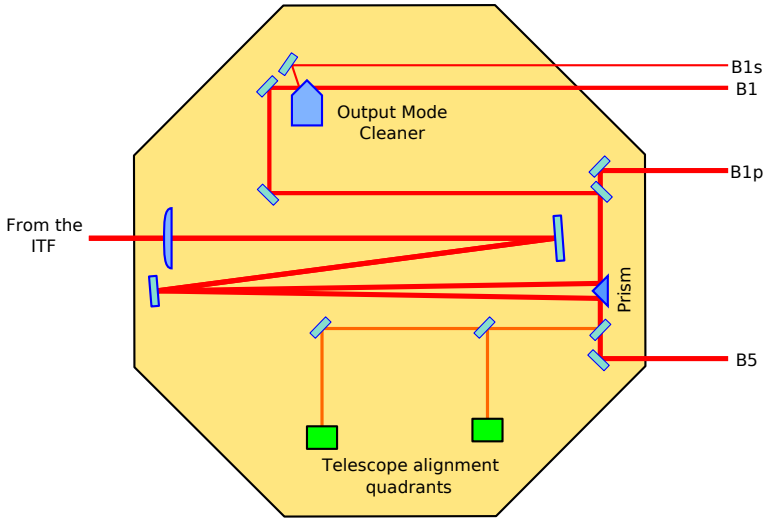

Figure 2.10: Simplified scheme of the suspended detection bench.

at the modulation frequency, dephased by 90 degrees. The results of the two mixing are then low-passed to obtain the demodulated *in-phase* and *quadrature* signals. A similar electronics works also for the quadrant-split photo-detectors used to generate angular error signals. They generate one power output for each single sector and demodulated signals for the difference between opposite ones. There are only two exceptions to this scheme: on the B2 beam there is a photo-detector which is demodulated at three times the main modulation frequency and a quadrant detector demodulated at 8 MHz.

The secondary face of the beam splitter has a small wedge with respect to the main one. In this way the beam splitter secondary face pick-off beam B5 and the main dark fringe beam B1 are collimated together toward the *suspended detection bench* (see fig. 2.10). Here the two beams are focused using a single telescope. Its mirrors are mounted on translation stages and can be moved remotely to optimize the telescope alignment. After the telescope the two beams are separated by a prism. A small fraction of the B5 beam is sent to in-vacuum quadrant-split detectors to obtain error signals for the telescope alignment. The main part of the B5 beam is sent out of the vacuum to the *external detection bench*, while the B1 beam is split in two parts: a small fraction of the total power (about 1%) is sent again to the external bench to the B1p detectors. The main part of the dark fringe beam is instead sent to a rigid triangular cavity, the *output mode cleaner*. This cavity can be maintained on resonance by controlling its temperature. In this way only the fundamental Gaussian mode is transmitted to the B1 beam and to the external bench, while all other higher order modes are reflected to the B1s beam. The detector contrast is therefore

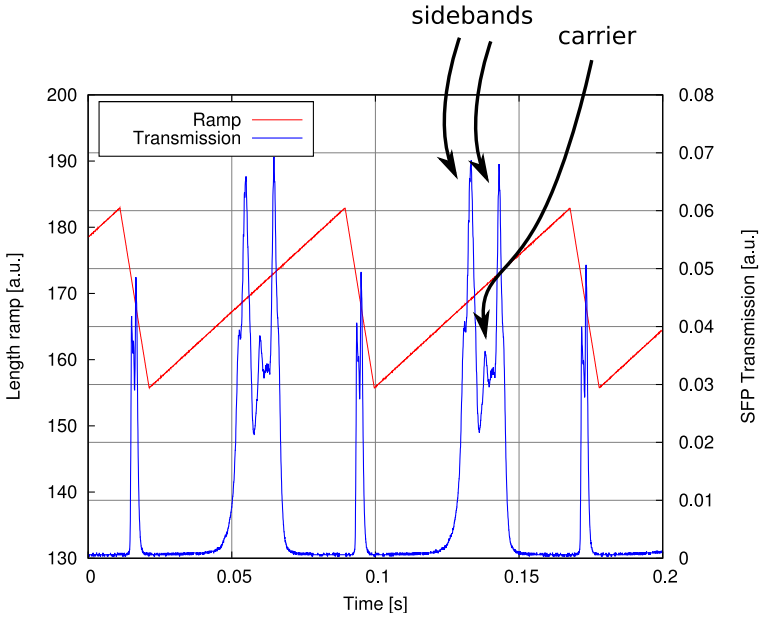

Figure 2.11: Example of the scanning Fabry-Perot signals. The red curve is the ramp applied to the cavity length, while the blue one is the power detected by a photo-diode placed in transmission of the cavity.

enhanced, since all spurious modes generated by mis-matching or mis-alignment are rejected.

The external detection bench is placed inside an acoustic isolation in the *detection laboratory* and hosts all the photo-detectors and quadrant detectors used to sense the B1p, B1 and B5 beam, as well as several digital cameras used to monitor the beams shape and position. Part of the B1p beam is sent to a *scanning Fabry-Perot cavity* (SFP) [37]. This is a 25 cm long Fabry-Perot resonant cavity with one of two mirror mounted on a piezo-actuator. If the length of the cavity is scanned over some free spectral ranges, the frequency of the laser light that resonate changes accordingly. This cavity can therefore be used as an optical spectrum analyzer to separate the power in the carrier and in the two sidebands. A typical example of the output signal is shown in fig. 2.11. The length of the cavity is scanned at about 10 Hz and the output signal is analyzed on-line to reconstruct the power in the carrier and sidebands fields. These values are computed every second and added to the main data stream.

As already explained the B2 beam is sensed by photo-detectors placed on the external injection bench. The beams transmitted by the two arm cavities are also used. They are quite large (of the order of 5 cm in diameter) and their size is reduced using suitable telescopes, the first lens being a large doublet. As well as in the detection bench, the beam is split between cameras, photo-

detectors and quadrant-split photo-detectors. The two *end optical benches* are also surrounded by acoustic enclosures.

All the photo-detectors output are converted to digital signals by ADC boards and post-processed by the *photo-diode read-out* processes. These take care of digitally filtering the signals (for example to compensate for anti-aliasing), of calibrating them in suitable units and to distribute all the results to the data acquisition system.

2.6 Data distribution and storage

All the digital signals that come from photo-detectors read-out, DSP, environmental probes and so on are collected by the *data acquisition system* (DAQ) and redistributed to all the processes that need them. Some of the most critical signals are sent independently via optical or serial links.

All the digital signals are distributed on-line with a small latency of a couple of seconds in *frame format* [38]. Additional programs that run on local machines can access through the network any data and process it to produce new signals and channels that are also available in the main data stream. Example are the noise monitoring tools like *NonStatMoni* and *VirgoHACR* described in chapters 8 and 9 respectively.

The frames are also saved to disk storage farms for off-line analysis and reading. The actual buffer allows a simultaneous storage of all the detector signals for several months.

2.7 Global control system

The longitudinal and angular control of an interferometer needs to use optical signals coming from photo-detectors to compute the force to be applied to the mirrors to maintain the correct resonance conditions. The system that take care of collecting suitable error signals, performing all the needed computation and output the correction signal is called the *global control*. It is a piece of software running on a dedicated real-time Unix machine, directly interfaced with the photo-diode read-out system and with digital optical links used to send the computed correction to the suspensions DSP control systems.

2.8 Environmental monitoring

The environmental conditions inside the laboratories, the buildings and outside are monitored by several temperature and humidity probes. In particular there are temperature probes inside each optical bench and inside the external isola-

tion oven that surround the suspension towers. Also the external temperature and wind speed are monitored by a small weather station.

Moreover, acoustic and seismic noise is monitored by microphones, accelerometers and episensors placed in different positions: there are sensors attached to each optical bench, inside the acoustic isolation enclosures, as well as seismometers attached to the ground in each building. Microphones are also mounted inside the laboratories and buildings to monitor the environmental acoustic noise.

Finally several magnetic probes are mounted inside the experimental buildings, to monitor the level of electro-magnetic noise.

All these probes, together with a set of portable ones, have been widely used to characterize the contamination by environmental noise of the detector sensitivity (see also sec. 7.11).

2.9 The Virgo design sensitivity

The best possible sensitivity that can be attained by the Virgo detector in the present configuration is called the *design sensitivity*. There are several fundamental sources of noise that limit it, depending on the frequency of interest [39] (see fig. 2.12).

Seismic noise

The micro-seismic motion of the ground can be approximated by a simple model given by

$$\mathcal{S}_x(f) \approx \frac{A_0}{f^2} \tag{2.2}$$

where the coefficient A_0 can be estimated to be of the order of 10^{-7} m Hz$^{-1/2}$. Using this estimate and the super-attenuator transfer function, the residual seismic noise at the level of the mirror can be computed. This is relevant only at frequencies below roughly 3 Hz and negligible at higher frequencies, since the suspension attenuation goes like f^{14}.

Newtonian noise

This noise is given by the fluctuation of the static gravitational field, modulated mainly by ground-air interface motion due to seismic activity. The contribution to the strain sensitivity can be estimated by [40]:

$$\mathcal{S}_h^{NN}(f) = \frac{3 \cdot 10^{-11}}{f^2} \tilde{x}_{seism}(f) \tag{2.3}$$

This formula is however strongly model dependent [41]. Therefore the contribution of Newtonian noise is shown in fig. 2.12, but it is not taken into account

in the total design noise. The contribution as computed by this model is in any case negligible inside the observational bandwidth (10-10000 Hz).

Thermal noise

The thermal noise that contributes to the design sensitivity comes from energy loss processes in the suspension wires and in the mirrors [42, 43]. The main contributions come from the pendulum thermal noise at frequencies between 3 and 30 Hz. The intermediate region between 30 and 300 Hz is instead limited by the sum of the contributions coming from the thermal excitation of the suspension wire violin modes and of the mirror resonant mode.

Shot noise

The shot noise is coming from the intrinsic fluctuation of the power detected by the dark fringe photo-detector [44]. Its contribution to the strain sensitivity, including the effect of the light modulation [45] is given by

$$h_{shot}(f) = \sqrt{\frac{3}{2}}\frac{1}{8LF}\sqrt{2h_P\frac{\lambda c}{\eta C P_{in}}}\sqrt{1+\left(\frac{f}{f_{FP}}\right)^2} \tag{2.4}$$

where $C = 50$ is the recycling factor, $P_{in} = 10$ W is the input power, $F = 50$ is the cavity finesse and f_{FP} their pole:

$$f_{FP} = \frac{c}{4LF} \sim 500 \text{ Hz} \tag{2.5}$$

The shot noise starts to be relevant for frequencies above roughly 300 Hz and it is the limiting source of noise above 1 kHz.

Total

In conclusion the expected design sensitivity, assuming an input laser power of 10 W, is

$$\begin{aligned} h &\approx 3 \cdot 10^{-21} \text{ Hz}^{-1/2} \text{ at } 10 \text{ Hz} \\ h &\approx 7 \cdot 10^{-23} \text{ Hz}^{-1/2} \text{ at } 100 \text{ Hz} \end{aligned}$$

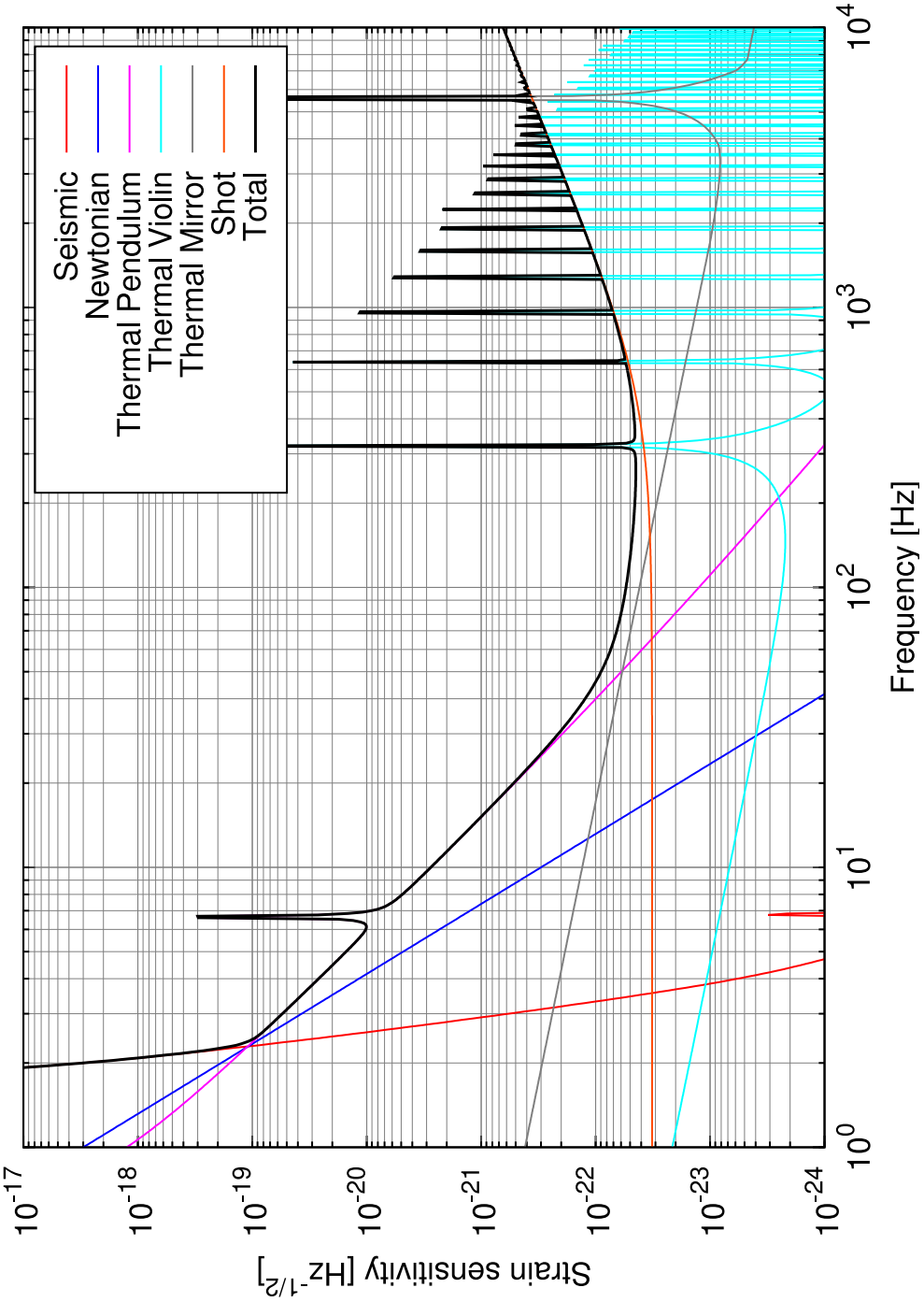

Figure 2.12: Design sensitivity for the Virgo detector, with all the main fundamental sources of noise.

Part I

Control systems

Chapter 3

Longitudinal sensing and control

This chapter describes in general the degrees of freedom involved and the control scheme adopted for the length sensing and control system. The lock acquisition technique used in Virgo during the science run is described in details in Appendix B.

3.1 General control scheme

In a power-recycled Fabry-Perot interferometer, the length sensing and control system (called in Virgo *locking system*) has the role of reconstructing and controlling the position of six mirrors, in order to maintain the correct resonance conditions of light fields inside the system:

- the carrier field must be resonant inside the long arm Fabry-Perot cavities, to enhance as much as possible the optical response to a gravitational signal;
- the carrier field must also be resonant in the central part of the interferometer, namely in the compound cavity composed of the power recycling and the two input mirrors, to profit from the increase of internally circulating power;
- the carrier field must finally undergo destructive interference at the dark port, to have the most sensitive configuration (*dark fringe*);
- the two sideband fields must be completely reflected (anti-resonance condition) from the long arm cavities, to be used as reference for the carrier dephasing;

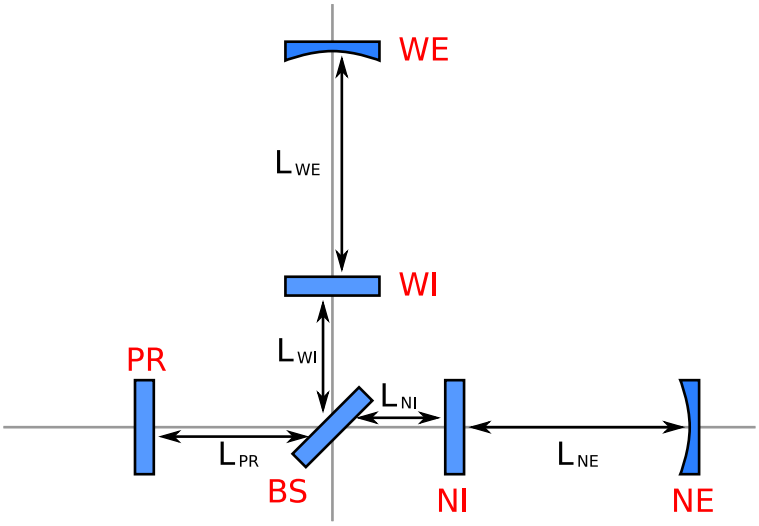

Figure 3.1: Definition of lengths in a power-recycled Fabry-Perot interferometer.

- the two sideband fields must also be resonant in the central cavity, to profit again from the increase of circulating power. In general they are not interfering destructively at the dark port.

The motion of the main six mirrors (see fig. 3.1) in the direction parallel to the beam (*longitudinal direction*) are relevant to the above stated resonance conditions. Only four of these degrees of freedom are in reality important. One combination of the mirror motions indeed corresponds to a global translation of the entire interferometer and it is clearly irrelevant, since only the relative distance between mirrors is important. The resonance conditions of the two long arm cavities are independent from the rest of the interferometer and therefore their lengths can be considered as two of the degrees of freedom to be controlled. Usually these two lengths are combined together in the *common* and *differential modes*:

$$L_{CARM} = \frac{L_{NE} + L_{WE}}{2} \tag{3.1}$$

$$L_{DARM} = \frac{L_{NE} - L_{WE}}{2} \tag{3.2}$$

The lengths of the central part of the interferometer can be combined to form the following two degrees of freedom:

$$L_{PRCL} = L_{PR} + \frac{L_{NI} + L_{WI}}{2} \tag{3.3}$$

$$L_{MICH} = L_{NI} - L_{WI} \tag{3.4}$$

The first gives the length of the power recycling compound cavity, composed of the PR mirror and the NI and WI ones. The second is instead the differential

degree of freedom of the central Michelson interferometer. The remaining degree of freedom can be expressed as

$$L_5 = L_{PR} - \frac{L_{NI} + L_{WI}}{2} \tag{3.5}$$

and it has no effect on the dephasing of the light fields inside the central part.

In conclusion four degrees of freedom need to be controlled by the lengths sensing and control system:

- common mode motion of the long cavities (CARM)
- differential mode motion of the long cavities (DARM)
- differential motion of the central Michelson interferometer (MICH)
- length change of the power recycling cavity (PRCL)

There is still another degree of freedom which must be taken into account: a change in the laser frequency is equivalent to a global change of scale. Indeed the dephasing of the light field when travelling over a distance L is given by $\phi = kL = 2\pi\nu L/c$ and therefore the following equivalence equation holds:

$$\frac{\delta\nu}{\nu} = \frac{\delta L}{L} \tag{3.6}$$

If the propagation happens inside a Fabry-Perot cavity, the dephasing amplification due to the finesse must be considered and the effective length L is larger than the physical one by the cavity finesse (more details in app. A.4).

Eq. 3.6 implies that also the laser frequency must be controlled, otherwise it will be seen by the interferometer as a change in lengths. The most sensitive elements are of course the long Fabry-Perot cavities: to be able to acquire the lock it is necessary that the residual fluctuations of the laser frequency are small, otherwise the dynamical range of the actuators might not be enough [46] to acquire and maintain the resonance condition. The spectral density of frequency fluctuations of a free running laser like the one employed in Virgo can be approximated by [47]:

$$\delta\nu \approx \frac{10^4}{f}\frac{Hz}{\sqrt{Hz}} \tag{3.7}$$

which for a frequency in the infra-red region

$$\nu = \frac{c}{\lambda} = \frac{c}{1.064 \cdot 10^{-6}\ \mathrm{m}} = 2.82 \cdot 10^{14} Hz \tag{3.8}$$

corresponds to an equivalent length noise for a Fabry-Perot cavity 3000 m long:

$$\delta L_{RMS} \approx 4 \cdot 10^{-9} m \tag{3.9}$$

which is of the same order of magnitude of the resonance width of the cavity itself (see appendix A):

$$\delta L_{WIDTH} = \frac{\lambda}{4\mathcal{F}} \approx 5 \cdot 10^{-9} m \tag{3.10}$$

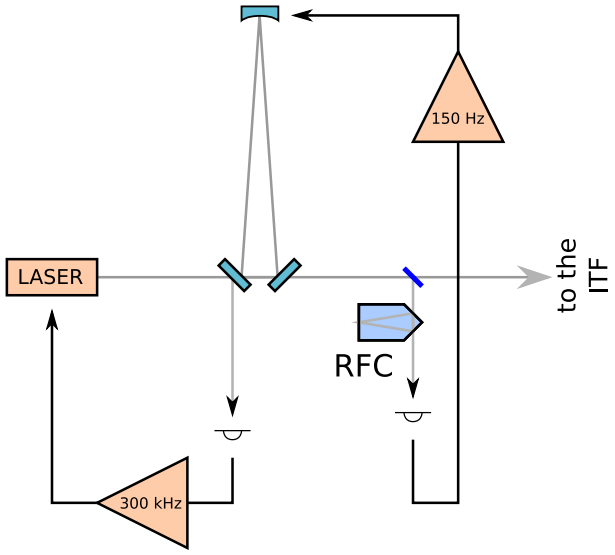

Figure 3.2: Scheme of the injection system and the laser frequency pre-stabilization control architecture.

From these consideration it appears clear that in order to be able to acquire the lock of a Fabry-Perot cavity, a pre-stabilization of the laser frequency is needed.

3.2 Laser frequency pre-stabilization

The pre-stabilization is obtained with a Pound-Drever-Hall like technique. The input beam is phase-modulated at 22 MHz. This frequency is not resonant inside the input mode cleaner (IMC) cavity and therefore it can be used for extracting a Pound-Drever-Hall signal in reflection. Since at high frequency the cavity is a very good length reference, the PDH signal can be used for locking the laser frequency to the cavity length. The bandwidth of the corresponding control loop is about 300 kHz. In this way the laser frequency follows exactly the lengths variations of the IMC, even at low frequency where the motion of the suspended injection bench and of the mode cleaner end mirror can be quite large. To correct this unwanted behavior, the reference cavity (RFC) is used: being a rigid cavity its length variations at low frequencies are small. Therefore the PDH signal in reflection of this cavity is used to lock the length of the IMC, with a bandwidth of about 100 Hz.

In this configuration (usually called *stand-alone injection system*) the frequency of the laser is locked to the reference cavity at low frequencies (below 100 Hz) and to the length of the input mode cleaner at higher frequencies (up to 300 kHz). This is enough to reduce its total RMS fluctuation to few Hertz,

which makes it no more an issue to lock a single Fabry-Perot cavity.

This frequency stabilization is however not enough to reach the design sensitivity for the full interferometer [48] and therefore a second stage of frequency stabilization (SSFS) is needed. The only possible better length reference are the 3 km long arm cavities.

3.3 Requirements

All lengths must be kept close enough to the correct operating point that realizes the already explained resonance conditions. It is important to understand the requirements on the accuracy of the control loops, or in other words the maximum allowed residual RMS motions. In order to keep the optical system close to the resonance, all length fluctuations should be much smaller than the resonance width. Taking into account the width of the power recycling cavity resonance and the enhancing effect of the Fabry-Perot cavities, the following requirements are found [46]:

$$\begin{aligned} \delta L_{PRCL} &< 2 \cdot 10^{-10} \text{ m (RMS)} \\ \delta L_{MICH} &< 5 \cdot 10^{-10} \text{ m (RMS)} \\ \delta L_{CARM} &< 6 \cdot 10^{-12} \text{ m (RMS)} \\ \delta L_{DARM} &< 3 \cdot 10^{-11} \text{ m (RMS)} \end{aligned}$$

Since the dark fringe signal is the one carrying information about differential displacement of the end test masses and in conclusion about gravitational waves, an additional requirement is that the noise in this channel must be as small as possible.

3.4 Signal extraction

The *lock acquisition* procedure is the sequence of operations which are needed to bring the interferometer from a completely uncontrolled state to the operating point with the best possible sensitivity, which is the *steady locked* condition. The techniques used for the lock acquisition differs strongly from detector to detector: the LIGO one is described for example in [49], the TAMA technique in [50] and the GEO600 one in [51].

The error signals for the reconstruction and control of the lengths are obtained with the usual frontal modulation technique. The input beam is phase-modulated at a frequency Ω of about 6.2 MHz. This modulation frequency is transmitted through the input mode cleaner and enters the interferometer. The output beams are demodulated at Ω to obtain several signals. The combinations

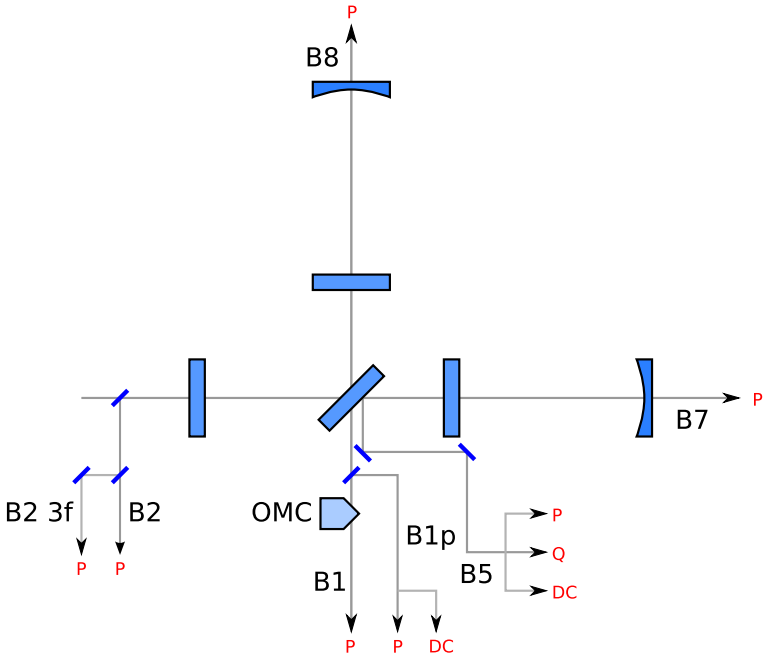

Figure 3.3: Simplified scheme of all beams and signals used in the length sensing and control system.

used for the reconstruction of the error signals change during the lock acquisition procedure [46], since their response to the different lengths varies with the evolution of the interferometer state.

The following signals are used, at different steps and in different combinations (see fig. 3.3):

- the demodulated in-phase signals obtained from the beams transmitted by the north and west cavities (their standard names are `Pr_B7_ACp` and `Pr_B8_ACp`);
- both in-phase and quadrature demodulated signals from the reflection of the anti-reflection-coated face of the beam splitter (`Pr_B5_ACp` and `Pr_B5_ACq`);
- the in-phase signal at the dark port, both before and after the output mode cleaner (`Pr_B1p_ACp` and `Pr_B1_ACp`);
- the in-phase demodulated signal obtained from the reflected beam (`Pr_B2_ACp`);
- the in-phase signal obtained from the reflected beam, demodulated at 3Ω (`Pr_B2_3f_ACp`);

The correct demodulation phase for each photo-detector is usually chosen in order to maximize the contribution from one of the lengths and minimize all others, and it is experimentally tuned for each step of the lock acquisition sequence.

Moreover, several power signals are used for normalization or for setting up thresholds:

- the powers transmitted by the two arms: `Pr_B7_DC` and `Pr_B8_DC`;
- the power in the beam reflected by the anti-reflection coated surface of the beam splitter `Pr_B5_DC`. This is a pick-up of the power reflected by the north arm and if the power recycling mirror is aligned it can be used as a good estimator of the power circulating inside the recycling cavity;
- from the same beam also an estimation of the power in the sidebands can be obtained, by demodulating at 2Ω. This signal is dominated by the beating of the two sidebands and if their spatial overlap is good it is roughly equivalent to their mean power. This signal depends of course on its demodulation phase, which is chosen in order to maximize the quadrature component `Pr_B5_2f_ACq`;

A full discussion of the optical response of each of these signals to the four different longitudinal degrees of freedom can be found in [46] and [52]. In summary the response of each signal depends on which are the fields that beat to generate it.

The Ω demodulated signal in the B2 beam can be viewed as generated by the reflection of the compound power recycling cavity. It comes from the beating of the carrier field with the first order sidebands. All these three fields are resonant inside the compound cavity, but with different recycling gains. Moreover the carrier is also resonant inside the long arm cavities and therefore it is mainly sensitive to the CARM degree of freedom. If this d.o.f. is controlled with very high gain with the frequency stabilization servo, its contribution can be neglected and the demodulated signals from B2 will be sensitive mainly to the central cavity degrees of freedom MICH and PRCL, in the two different quadratures. The signal obtained still from B2 but demodulated at 3Ω is generated instead mainly by the beating of the first order with the second order sidebands. The latter are not resonant inside the recycling cavity: this makes the situation similar to the standard PDH configuration and therefore this signal will be sensitive mainly to change in the PRCL degree of freedom. In reality the 3Ω signal has also a small contribution from the beating of the carrier with the third order sidebands, which again makes a small contamination of CARM in this signal.

The signals transmitted by the two arm cavities are instead clearly dominated by the variation of the two cavity lengths. If the mean length is controlled

with high gain by the frequency stabilization servo, both demodulated transmitted signals are sensitive to the DARM degree of freedom. The same is also true for the reflection of the cavities. In particular the recombination of the two reflected fields, that takes place at the dark port, gives the most sensitive demodulated signal to DARM motion. This is therefore the main gravitational wave channel.

Finally, the demodulated signals extracted from beam-splitter pick-off beam B5 are sensitive to dephasing of the carrier and sidebands fields inside the central cavity. Again the carrier dephasing is dominated mainly by the CARM degree of freedom. This makes one of the two B5 quadratures a very sensitive CARM error signal. The sideband dephasing depends instead only on the state of the central area and in particular of the MICH degree of freedom.

The detailed response of each demodulated signal to every lengths can be computed analytically or obtained by means of simulation, as it is done in sec. 5.1.

Taking into account the full optical path from the interferometer to the photo-diodes it is possible to convert the power actually impinging on the detector with the one inside the interferometer. For B7 and B8 beams the transmission of the end mirror must be taken into account (42.9 ± 0.2 ppm for NE mirror, 38.3 ± 0.7 ppm for WE, see [53]) together with the properties of all mirrors and lenses on the external benches. The conversion factors from the power impinging on the photo-diode and the one inside the two cavities are $5.2 \cdot 10^4$ for north cavity and $5.8 \cdot 10^4$ for west cavity. In a similar way the transmission to the B5 beam must take into account the reflectivity of the secondary face of the beam splitter mirror (519 ± 10 ppm [53]) and the conversion factor is $2.5 \cdot 10^3$.

3.5 Actuation

The outcome of the longitudinal sensing and control system is a vector of corrections to be applied to the mirrors. The signals expressed in terms of the physical degrees of freedom (DARM, CARM, MICH, PRCL) must be converted to the actual corrections to be sent to every single mirror. This is a simple geometrical computation. DARM and CARM are summed and subtracted to give the NE and WE corrections:

$$\begin{aligned} C_{NE} &= C_{CARM} + C_{DARM} \\ C_{WE} &= C_{CARM} - C_{DARM} \end{aligned}$$

The corrections for MICH and PRCL are mixed together since a motion of the BS mirror changes also the power recycling cavity length. A displacement of BS, perpendicular to its surface in the PR and WI mirrors direction has the effect of making the PR-BS distance shorter, the BS-NI one longer and of leaving

unchanged the distance BS-WI. A displacement of the PR mirror instead only affects the distance between PR and BS. In summary:

$$\begin{aligned} \Delta L_{PR} &= \Delta PR - \sqrt{2}\Delta BS \\ \Delta L_{NI} &= \sqrt{2}\Delta BS \\ \Delta L_{WI} &= 0 \end{aligned}$$

By inverting these equations it is possible to find the correct combination of MICH and PRCL corrections to be applied to each mirror:

$$\begin{aligned} C_{BS} &= \frac{1}{\sqrt{2}} C_{MICH} \\ C_{PR} &= C_{PRCL} + \frac{1}{2} C_{MICH} \end{aligned}$$

and therefore the PRCL correction is applied only on the PR mirror while the MICH one is split between the two.

The actual coefficients in the driving matrix are different from those reported here since they must take into account also the different gain of coils-magnets actuators for different mirrors.

3.6 The Variable-Finesse technique

The lock acquisition procedure used in Virgo is based on the *variable-finesse technique* [46]: the final state of the interferometer is reached passing through several intermediate stable states.

If the power recycling mirror is removed (or misaligned in order to avoid its reflections interfering with other beams inside the interferometer) the two arm cavities are completely independent and they can be controlled using the PDH signals extracted from the transmitted beams. If the two cavities are locked in this way, their reflection is stable and the entire interferometer can be considered as a simple Michelson with the two locked cavities in place of two simple mirrors. Therefore the beam splitter can be controlled independently from the arms.

The second observation is that the full interferometer can be viewed as a resonant cavity composed by the power recycling mirror and an equivalent one which models the total reflectivity and transmissivity of the optical system composed by the beam splitter and the two arm cavities. If these are maintained at resonance, the reflectivity of this compound mirror is determined by the interference condition at the dark port: the more is the power which exit the interferometer through the dark port, the lower is the reflectivity of the equivalent mirror. In conclusion it is possible to vary the finesse of the equivalent cavity by tuning the operating point of the beam splitter mirror. In a low finesse configuration, the mixing of different degrees of freedom in the optical signals is

small. This makes the control of the interferometer easier. For a more detailed discussion of the variable finesse technique refer to [46].

3.7 Lock acquisition strategy

The lock acquisition strategy used during the Science Run is explained in details in Appendix B. The state of longitudinal sensing and control in the final configuration, at the end of the lock acquisition procedure, can be summarized as follows:

- the DARM degree of freedom is controlled using the dark fringe itself as error signal (`Pr_B1_ACp`) with unity gain frequency at 100 Hz;
- the PRCL degree of freedom uses the `Pr_B2_3f_ACp` signal below 5 Hz and `Pr_B2_ACp` above. The unity gain frequency of this loop is at 40 Hz.
- the MICH degree of freedom is controlled using `Pr_B5_ACq`. Its control loop has a unity gain frequency at 15 Hz and a strong roll-off above 50 Hz;
- the gains of these three longitudinal loops are stabilized by slow servo using as error signal the demodulation of calibration lines;
- the laser frequency is stabilized on the mean length of the arm cavities, using `Pr_B5_ACp` as error signal and with unity gain frequency at about 25 kHz; at the same time the common mode of the arm cavities is locked on the demodulated reflection of the reference cavity, with a bandwidth of about 1 Hz;
- all longitudinal actuators are in low-noise configuration: the very low frequency part of the correction is applied also at the top stage of the suspension, while for the two cavity end mirrors the correction is re-allocated at intermediate frequencies to the marionette;
- the re-injection of MICH and PRCL noise in the dark fringe signal is reduced by using noise subtraction techniques.

Chapter 4

Angular sensing and control

The discussion of resonant conditions inside optical systems, as carried out so far, implicitly considered good alignment conditions of the mirrors with respect to the optical axes. If left free in their angular degrees of freedom, the mirrors will be subjected to motions due to the residual seismic noise at low frequency. When the interferometer is not locked, every suspension works in stand-alone condition and the angular position of the payload is controlled by local sensors which measure the mirror pointing with respect to the ground. This control system is however not sufficient to obtain good performances of the detector in science mode state, for two main reasons. First of all the typical residual fluctuation of the angular degrees of freedom of a mirror is of the order of 1 μrad, usually too large to obtain the required sensitivity. Second the local control reconstruction of the mirror angular position is subjected to slow drifts (with time scale of the order of hours), driven mainly by temperature effects, and therefore it is not possible to maintain for long times a correct alignment of the optics. Moreover, the local system clearly can not guarantee a correct global alignment of all the mirrors with respect to the input beam, since it has access only to local data.

For all these reasons a *global automatic alignment system* is needed. This system must be able to measure the angular position of the mirrors with respect to the beam and to act in order to correct possible mis-alignments. This chapter describes the basic principles of functioning of the *angular sensing and control* system, usually called *alignment system*. For a more detailed description see [54].

The following convention is adopted to refer to the three angular degrees of freedom of a mirror (see fig. 4.1):

ϑ_x is the rotation around the horizontal axis in the mirror plane (pitch)

ϑ_y is the rotation around the vertical axis in the mirror plane (yaw)

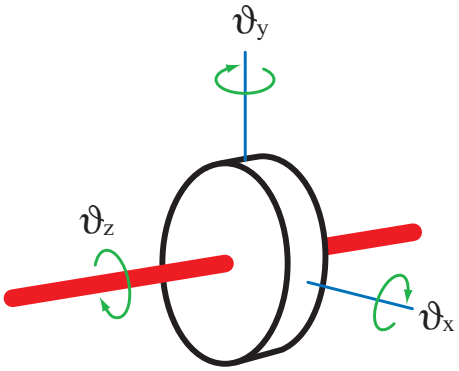

Figure 4.1: Definition of the mirror three angular degrees of freedom.

ϑ_z is the rotation around the axis perpendicular to the mirror (roll) which corresponds usually with the beam axis

4.1 Gaussian beam optics

4.1.1 The par-axial diffraction equation

In the general case the propagation of light inside an optical system is described by the Maxwell equations and by the corresponding wave equation

$$\left(\Delta + k^2\right) \mathcal{E}_k(x, y, z) = 0 \tag{4.1}$$

In the simpler case of a laser beam inside an interferometer, the propagation is well described in the *par-axial approximation* [12, 55]. The light field is supposed to propagate mainly along one direction called z and all its transverse variations to be small. If the field is written as

$$\mathcal{E}(x, y, z) = e^{ikz} E(x, y, z) \tag{4.2}$$

and the variation along z of the envelope is small $\left|\frac{\partial E}{\partial z}\right| \ll kE$, the wave equation simplifies to the *par-axial diffraction equation*:

$$\left(2ik\partial_z + \Delta_{trans}\right) E = 0 \tag{4.3}$$

which can be used to describe the propagation of an almost monochromatic beam concentrated along the z direction. Under the assumption of cylindrical symmetry the *fundamental Gaussian solution* of the par-axial diffraction equation can be found

$$\Psi(r, z) = \frac{1}{\sqrt{1 + \frac{z^2}{b^2}}} e^{-\frac{r^2}{w^2(z)}} e^{ik\frac{r^2}{2R(z)}} e^{-i \arctan \frac{z}{b}} e^{ikz} \tag{4.4}$$

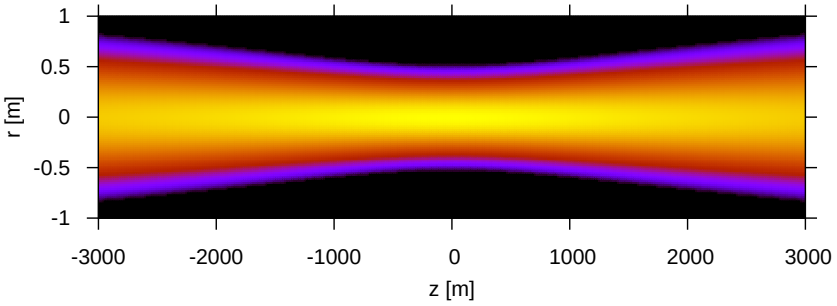

Figure 4.2: Intensity map of the fundamental solution of the par-axial diffraction equation. The color scale is logarithmic.

where

$$\begin{aligned} w(z) &= w_0\sqrt{1+\frac{z^2}{b^2}} \\ R(z) &= z\left(1+\frac{b^2}{z^2}\right) \\ b &= \frac{kw_0^2}{2} \end{aligned}$$

The transverse intensity shape is a Gaussian function for every z. Its width is minimum when $z = 0$, at the *waist* of the beam, and increases for larger z according to the function $w(z)$ (see fig. 4.2). The constant phase surfaces of this beam are parabolic, with a decreasing curvature given at $r = 0$ by $R(z)$. When propagating along z the field undergoes an addition dephasing with respect to the one predicted in the plane-wave approximation. This is the *Gouy phase*

$$\phi_G = -\arctan\frac{z}{b} \tag{4.5}$$

4.1.2 Transverse electro-magnetic modes

Starting from the fundamental solution of eq. 4.4 it is possible to relax the requirement of cylindrical symmetry and search for solutions with different transverse shape. The most useful set of solution is given by the *Hermite-Gauss* functions, also called *electro-magnetic transverse modes* (TEM). They depends on two integer indexes n and m:

$$\begin{aligned} TEM_{mn}(x,y,z) &= N_{mn}e^{ikz}H_m\left(\frac{\sqrt{2}x}{w(z)}\right)H_n\left(\frac{\sqrt{2}y}{w(z)}\right) \\ &\quad e^{-i(n+m+1)\arctan(z/b)}e^{ik\frac{r^2}{2R(z)}}e^{-\frac{r^2}{w^2(z)}} \end{aligned} \tag{4.6}$$

Order	Polynomial
0	1
1	$2x$
2	$4^2 - 2$
3	$8x^3 - 12x$

Table 4.1: Hermite polynomials of lowest order.

where the normalization coefficient N_{mn} is chosen in order to make this set orthonormal

$$N_{mn} = \sqrt{\frac{2}{\pi w_0^2 \, 2^{n+m} m! n!}} \tag{4.7}$$

and the $H_n(t)$ are the *Hermite polynomials* that can be defined for example as [56]:

$$H_n(t) = e^{t^2} \left(-\frac{d}{dt} \right)^n e^{-t^2} \tag{4.8}$$

Given a value of the beam size at the waist w_0, these solutions form a complete, orthonormal set, meaning that every beam can be expressed as a linear combination of these functions.

The first Hermite polynomials are listed in table 4.1 and the transverse intensity pattern of the first TEM modes are shown in fig. 4.3.

4.2 Fabry-Perot resonant cavities

The effect of the reflection of a beam on a mirror can be described with the usual plane-wave contribution plus a variable dephasing which takes into account the shape of the mirror:

$$R(x, y) = ire^{2ikf(x,y)} \tag{4.9}$$

where $f(x, y)$ describes the position of the reflecting surface as a displacement from a plane with constant z taken as reference. In general if a TEM mode with given waist size and position is reflected by an arbitrary mirror, its shape will change and in general it will not be possible to describe it as a single TEM mode with the same waist size and position. Therefore only a fraction of the reflected beam power will be in the same mode of the incident beam, thus reducing the effective reflectivity of the mirror for the mode.

However, if the shape of the mirror follows exactly one constant phase surface of the incident beam, the reflected one will have exactly the same mode. This means that the optimal shape for the mirrors in a resonant cavity is curved. If the cavity is long enough, the parabolic constant phase surfaces are almost indistinguishable from spherical one.

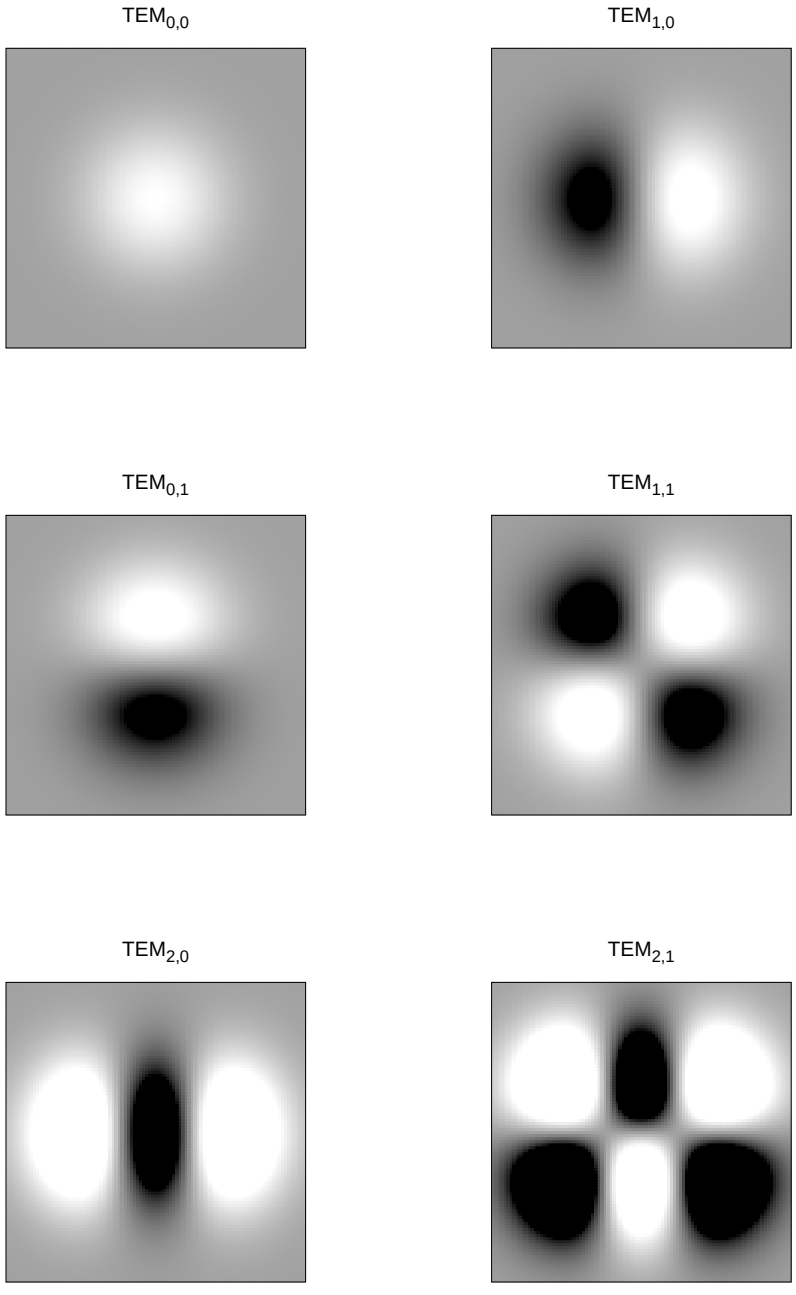

Figure 4.3: Transverse intensity maps of the first TEM modes.

The typical example of a resonant cavity is given by a flat input mirror and a curved terminal one. The input mirror must be placed at the waist of the incoming beam, which is the only position where the constant phase surface is plane. The curvature of the constant phase surface at the position of the end mirror is given by

$$R(L) = L\left(1 + \frac{b^2}{L^2}\right) \tag{4.10}$$

To have an *optimally matched* cavity this must be equal to the radius of curvature of the end mirror. This can be viewed in a different way, saying that the length L of the cavity and the radius of curvature R_C of the end mirror unambiguously determines the waist size of the modes resonant in the cavity:

$$w_0^2 = \frac{2}{k}\sqrt{L(R_C - L)} \tag{4.11}$$

In particular a resonant mode exists only if the radius of curvature of the end mirror is larger than the length of the cavity.

The resonance condition for the different TEM modes can be obtained as usual imposing the total phase lag over a round trip inside the cavity to be a multiple of 2π. From eq. 4.6:

$$\Delta\phi = 2kL + \pi - 2(m + n + 1)\arctan\frac{L}{b} = 2\pi N \tag{4.12}$$

In particular this equation shows that if the $TEM_{0,0}$ mode is resonant, all the other modes are not, except in the case of degeneracy. The difference of the resonant frequency of a $TEM_{m,n}$ mode with respect to the fundamental one is given by

$$\Delta\nu_{m,n} = \frac{c}{2L}\left(P + \frac{m+n}{\pi}\arctan\frac{L}{b}\right) \tag{4.13}$$

being P a suitable integer number.

4.3 Cavity response to mis-alignments

The optical axis of a resonant cavity can be easily defined in a flat-curved or curved-curved cavity, to be the only line perpendicular to both the mirror surfaces at the points where it intersects them. The resonant modes described in the previous section are always referred to this optical axis. A tilt of one of two mirrors has the effect of changing the cavity axis, see fig. 4.4.

Simple geometrical considerations show that a tilt of the input mirror of an angle α has the effect of rotating the cavity axis by the same amount and of translating it by

$$a_{IN} = (R_C - L)\sin\alpha\cos\alpha \tag{4.14}$$

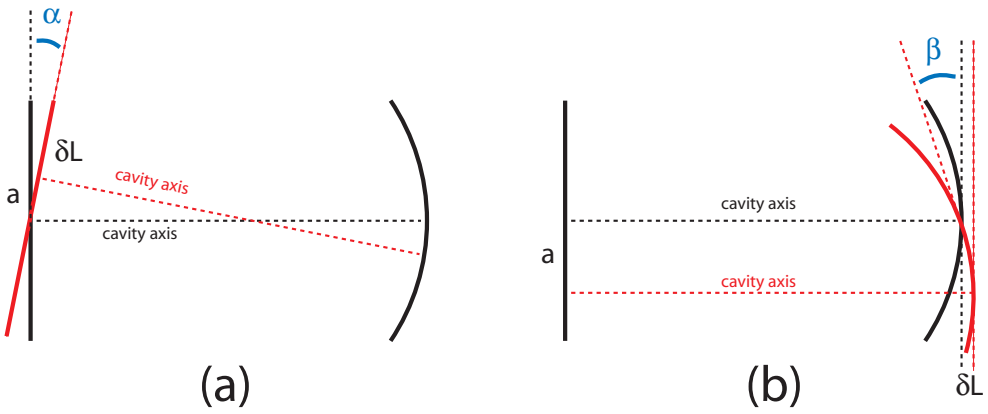

Figure 4.4: Scheme of mis-alignments of input and end mirrors in a resonant cavity.

where L is the cavity length when aligned and R_C the radius of curvature of the end mirror. Moreover, the length of the cavity changes by

$$\delta L_{IN} = (R - L)(1 - \cos\alpha) \tag{4.15}$$

Since only small deviation of the mirrors from their aligned position are relevant here, the previous equations can be approximated at the first order in the angle. The effect of an input mirror misalignment is to tilt and translate the cavity axis, since the length changes only at second order:

$$a_{IN} \sim (R - L)\alpha \tag{4.16}$$

$$\theta_{IN} = \alpha \tag{4.17}$$

In a similar way, the effect of a tilt of the end mirror by an angle β produces only a translation of the axis and a change in the cavity length:

$$a_{END} = R\sin\beta \tag{4.18}$$

$$\delta L_{END} = R(1 - \cos\beta) \tag{4.19}$$

and as before the change in the cavity length is second order in the angle, while the axis translation can be approximated

$$a_{END} \sim R\beta \tag{4.20}$$

The input beam is assumed to be matched to the aligned cavity resonant mode: this means that the waist of the beam is in the input mirror plane and its size correspond to the one of the cavity resonant mode.

The effect of the mis-alignments is derived exploiting the property that the set of cavity TEM modes is complete: therefore it is always possible to describe

the mode of the input beam in terms of the cavity eigen-modes. This is most simply done by considering two coordinate systems: the first one S corresponding to the beam axis and the second one S' to the cavity axis. The resonant modes of the cavity are easily expressed in the S' system. Considering first only a translation of the cavity axis, assumed to be along x, the link between the two coordinate systems is given by

$$\begin{aligned} x' &= x - a \\ y' &= y \\ z' &= z \end{aligned}$$

The expansion of the input beam in cavity modes can be performed at any longitudinal coordinate z. The simplest choice is of course the waist $z = 0$. The input beam is described by eq. 4.6 in the S coordinate system. By simple substitution and considering only terms of first order in a the result, in the cavity coordinate system S', is found to be:

$$\begin{aligned} TEM_{0,0}^{IN}(0,x,y) &= TEM_{0,0}^{CAV}(0,x',y')\left(1+2\frac{ax'}{w_0^2}\right) \\ &= TEM_{0,0}^{CAV}(0,x',y') + \frac{a}{w_0}TEM_{1,0}^{CAV}(0,x',y') \end{aligned}$$

In the case of a rotation, the link between the two coordinate systems is given by

$$\begin{aligned} x &= x'\cos\theta - z'\sin\theta \\ y &= y' \\ z &= x'\sin\theta + z'\cos\theta \end{aligned}$$

The magnitude of the mode can be expressed as

$$\left|TEM_{0,0}^{IN}\right| = \left|TEM_{0,0}^{CAV}\right| e^{-\frac{x'^2}{w_0^2}\sin^2\theta} \tag{4.21}$$

and the difference is irrelevant being second order in the angle. However, the beam is also subjected to a x-dependent phase difference since the waist plane is different in the two coordinate systems. This phase is given by

$$\phi(x') = kx'\sin\theta \sim kx'\theta \tag{4.22}$$

and therefore

$$\begin{aligned} TEM_{0,0}^{IN}(0,x,y) &= TEM_{0,0}^{CAV}(0,x',y')\left(1+2ik\theta x'\right) \\ &= TEM_{0,0}^{CAV}(0,x',y') + i\frac{k}{2w_0}TEM_{1,0}^{CAV}(0,x',y') \end{aligned}$$

In conclusion, the effect of input or end mirror misalignment can be described, in the cavity optical axis reference system, as the creation of additional

transverse modes proportional to the tilts:

$$\begin{aligned} TEM_{0,0}^{IN} &= TEM_{0,0}^{CAV} + \alpha \left[\frac{R-L}{w_0} + i\frac{k}{2w_0} \right] TEM_{1,0}^{CAV} \\ &+ \beta \frac{R}{w_0} TEM_{1,0}^{CAV} \end{aligned} \tag{4.23}$$

In the general case only the $TEM_{0,0}$ mode is resonant inside the cavity and therefore all other components are reflected.

4.4 Wave-front sensors

To build a system capable of controlling the alignment of a resonant cavity it is necessary to extract error signals that measure the position of the mirrors with respect to the beam axis. The most common technique is called *wave-front sensing* [57, 58]. It uses quadrant-split photo-detectors (*quadrants* in brief): the sensitive area of these photo-diodes being divided into four sectors. The light power impinging on each of them can be measured separately. These sensors can be used in "+" or "×" configuration. In the first case the difference between the two opposite halves of the sensors can be obtained and used to extract both a power or a demodulated signal. In the second case the difference is taken between opposite quadrants.

These sensors are able to detect the superposition of different TEM modes. Suppose that the beam hitting a "+" sensor can be described as

$$E(x,y) = \alpha\, TEM_{0,0} + \beta\, TEM_{1,0} \tag{4.24}$$

Assuming that the size of the beam is much smaller than the sensor radius, the right and left halves of the sensor will detect a power given by

$$\begin{aligned} P_L &= \int_{x<0} |E(x,y)|^2\, dxdy = |\alpha|^2 \int_{x<0} |TEM_{0,0}|^2\, dxdy \\ &+ |\beta|^2 \int_{x<0} |TEM_{1,0}|^2\, dxdy + 2\mathrm{Re}\ \alpha^*\beta \int_{x<0} TEM_{0,0}^* TEM_{1,0} dxdy \\ P_R &= \int_{x>0} |E(x,y)|^2\, dxdy = |\alpha|^2 \int_{x>0} |TEM_{0,0}|^2\, dxdy \\ &+ |\beta|^2 \int_{x>0} |TEM_{1,0}|^2\, dxdy - 2\mathrm{Re}\ \alpha^*\beta \int_{x>0} TEM_{0,0}^* TEM_{1,0} dxdy \end{aligned}$$

Since the magnitude of all TEM modes is even with respect to both x and y, in the difference between the two signals only the interference term survives:

$$D = 4\mathrm{Re}\ \alpha^*\beta \int_{x>0} TEM_{0,0}^* TEM_{1,0} dxdy \tag{4.25}$$

In conclusion the difference signals from *quadrant-split photo-detectors* are sensitive only to the interference between even and odd TEM modes, and therefore makes a perfect candidate to obtain an error signal for an alignment control system.

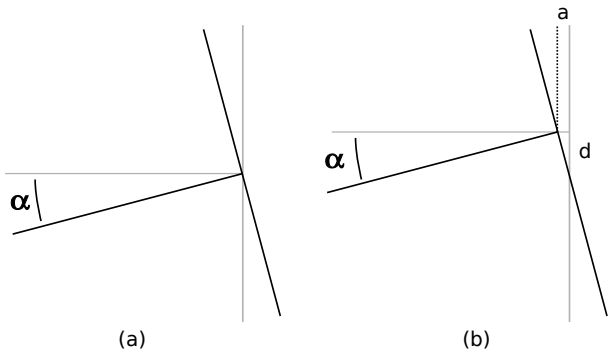

Figure 4.5: Effect of beam mis-centering with respect to the rotation axis of the mirror.

4.5 Coupling of angular noise

From the discussion of the previous two sections it follows that angular motions of the mirrors are seen by normal photo-detector only at the second order in the tilt angle, since they detects only the total power impinging on them. This is however true only if the beam axis passes through the mirror rotation center, which is essentially defined by the way the angular actuation is performed.

Referring to fig. 4.5, if the beam axis is translated of d from the mirror center, a rotation of an angle α will produce also an effective longitudinal displacement given by

$$a = d \tan \alpha \sim d\alpha \tag{4.26}$$

This displacement is at any effect indistinguishable from a real longitudinal motion of the mirror and it acts as an external source of noise for the longitudinal control system.

It is therefore important to ensure that the rotation center of the mirror coincides as well as possible with the beam axis, in order to reduce the linear term in the coupling of angular noise into the detector main output signals.

4.6 The Anderson technique

The technique used in Virgo to extract complete information on the mis-alignment of the cavity mirror has been firstly developed by Anderson [59] and differs from the one used in other interferometric detectors like LIGO [60] since it implies an additional constraint on the main modulation frequency.

When a cavity is locked, the $TEM_{0,0}$ mode is resonant for the carrier and anti-resonant for the two sidebands. In this condition the $TEM_{1,0}$ and $TEM_{0,1}$ modes of the carrier are not resonant in the cavity. Any mis-alignment of the

cavity mirror will generate one of these modes but they will not be present in a significant fraction in transmission of the cavity since they are not resonant. On the contrary, the two sidebands $TEM_{0,0}$ modes will be anti-resonant and almost completely reflected by the cavity. Since the resonant frequency of the $TEM_{1,0}$ mode is different from that of the fundamental mode, it is however possible to choose the modulation frequency to be an integer multiple of this frequency difference. In this way the $TEM_{1,0}$ and $TEM_{0,1}$ modes of one of the two sidebands, the upper for example, will be resonant inside the cavity. Any misalignment will generate one of these mode that, being resonant, will be present in the transmission port. Here a wave-front sensor will detect the beating of any $TEM_{0,0}$ and $TEM_{1,0}$ modes: the only possible combination is the carrier for the first and the upper sideband for the second. This component can be extracted using a demodulation technique on the difference signals of the quadrant sensor and this can be used as an error signal for the alignment system.

From eq. 4.23 it follows that tilts of the input or end mirrors will result in a superimposition of the two modes with different phase. This implies that using both the in-phase and quadrature signal from the wave-front sensor allows a full reconstruction of the two mirrors position.

Moreover, as already pointed out when discussing eq. 4.6, different transverse modes acquire different dephasing when propagating, due to the Gouy phase term. It is therefore possible to place a pair of wave-front sensors on the same beam, at different distances to profit of the different Gouy phase that the fundamental and first transverse modes will acquire in the propagation. However, since the distance needed for a significant change in the phase is of the order of hundreds of meters, normally telescopes are used for this goal.

4.7 Virgo angular sensing and control scheme

The automatic alignment system in a complex interferometer like Virgo deals with the control of two degrees of freedom for each of the six main mirrors. Moreover a control of the input beam pointing must be implemented to avoid slow drifts that might move the beams out of the mirror centers, leading to worse performances of the detector.

The error signals are obtained from a set of quadrant sensors placed on all the main beams. Referring to fig. 4.6, there are two couples of sensors in the beams transmitted by the two cavities (named Q71, Q72 and Q81, Q82 respectively); two other quadrants are placed on the beam reflected by the interferometer (named Q21 and Q22); one quadrant is placed on the dark fringe beam, before the output mode cleaner (Q1p) and finally one on the beam splitter pick-off beam (Q51). Each quadrant produces several output signals: the power im-

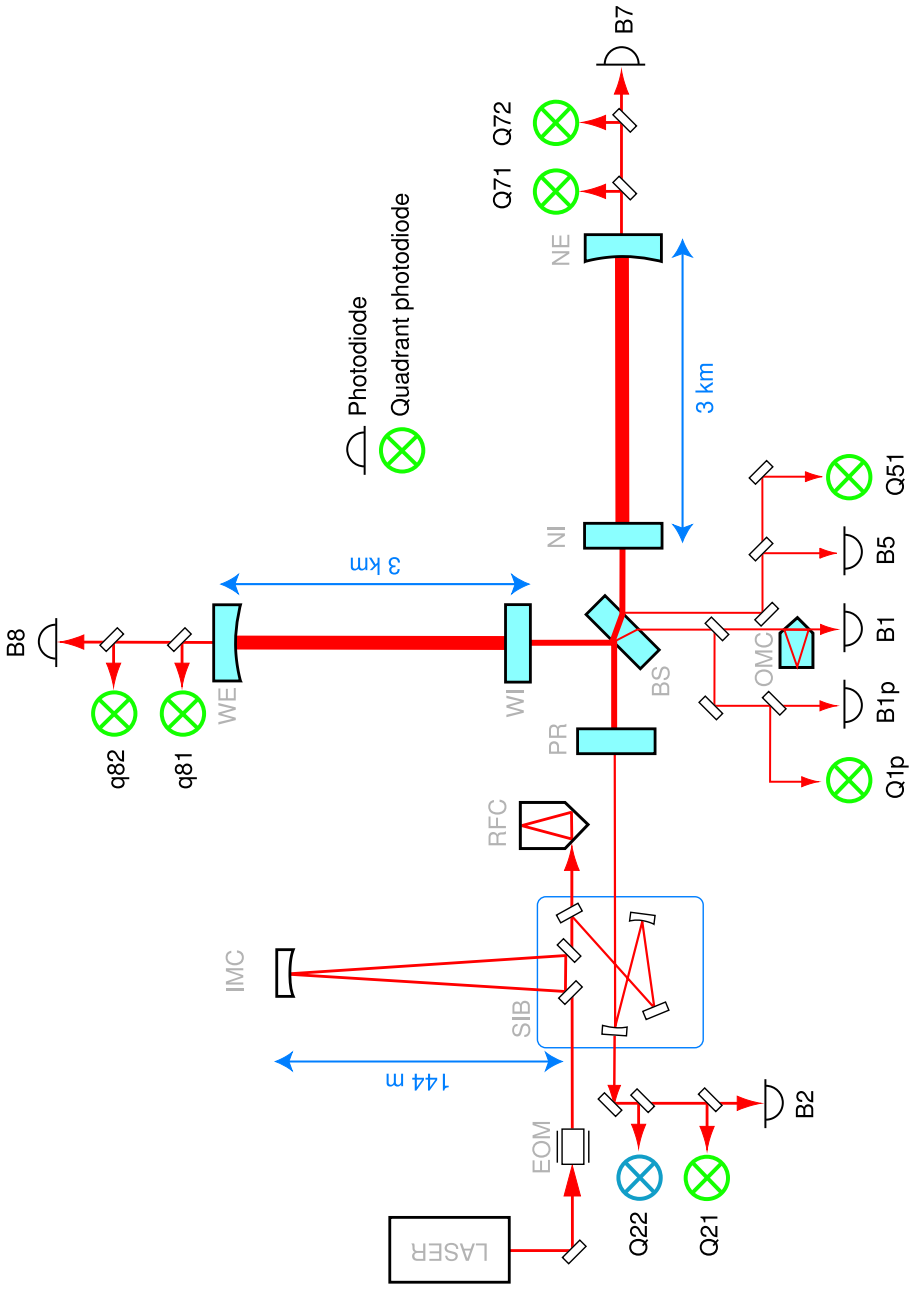

Figure 4.6: Position of the various quadrant sensors used for the automatic alignment system of the Virgo interferometer.

pinging on each one of the four sectors and the demodulated difference between opposite sectors. The normalized difference of the powers detected by opposite sectors can be computed to obtain signals sensitive to the beam position on the quadrant.

In total there are 8 quadrants giving a total of 16 demodulated and 16 power asymmetry signals: therefore a total of 32 to control 14 degrees of freedom. These are organized and controlled in the following way:

- The tilts of the two end mirrors, both in ϑ_x and ϑ_y are controlled in common and differential combinations. These degrees of freedom are called *differential* and *common end modes*. The differential mode is controlled using the signal coming from the dark fringe quadrant (Q1p) while the common mode error signal is obtained from the quadrants in reflection of the interferometer (Q21 and Q22), both demodulated and asymmetry signals.

- The power recycling mirror is controlled using error signals obtained from the quadrant on the beam splitter pick-off beam (Q51).

- The two input mirrors are controlled using as error signals the spot position in transmission of the two cavities, measured using cameras on these beams (B7 and B8).

- The beam splitter mirror control uses two signals coming from one of the quadrants placed on the beam transmitted by the west arm cavity (Q81).

- The input beam is finally steered using error signals coming from one of the quadrants placed in reflection of the interferometer (Q21).

There are two different configurations for the control of the various angular degrees of freedom. In the *automatic alignment* configuration the angular degrees of freedom are controlled using only the global error signals obtained from the quadrant sensors. The bandwidth of the control in this configuration is of the order of a couple of Hz. The angular correction is normally applied at the level of the marionette. In this configuration the local control system is completely switched off. A typical example of the open loop transfer function for these controls is shown in fig. 4.7.

On the other hand, in the *drift control* configuration the local control of the mirror is still active, and the global signals are used, after passing through a low pass filter, only to adjust the set point. In this way the high frequency motion of the mirror is still controlled by the robust local system, with a bandwidth of some Hz, while slow drifts are compensated using the global signals. This control path has a bandwidth of the order of tens of mHz.

During the science run the automatic alignment configuration was used for the end mirrors common and differential modes, for the power recycling mirror

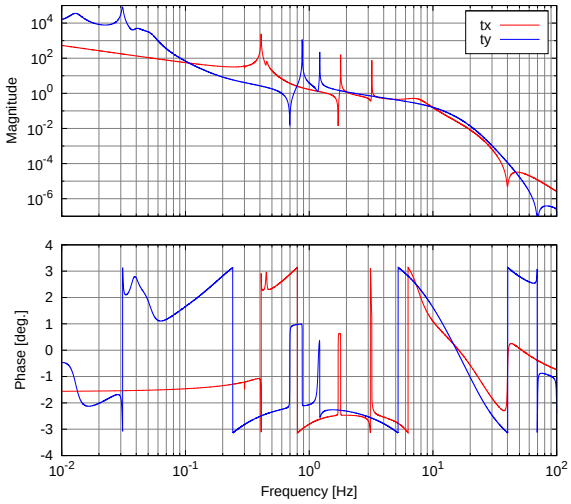

Figure 4.7: Theoretical open loop transfer functions for the angular control of the end mirror differential mode in ϑ_x and ϑ_y.

and for the ϑ_x d.o.f. of the beam splitter. All other degrees of freedom were working in drift control configuration.

The noise performances are described in sec. 7.5. Several actions has been performed to reduce as much as possible the contribution of angular control noise to the sensitivity: mainly the implementation of better control filters to reduce the re-introduction of noise above the unitary gain frequency and a systematic campaign of beam centering on the mirrors to reduce as much as possible the coupling of angular noise to longitudinal signals.

4.8 Conclusions

The angular sensing and control system has proved to have very good performances, both from the point of view of long term reliability and stability and of noise performances (see sec. 7.5 for the noise performances and [54] for more details on the alignment system). The study of the relation between the angular and longitudinal degrees of freedom has been started. In particular a reduction of angular to longitudinal coupling has been obtained checking and maintaining the centering of the beam on mirrors. An important topic is the relation between angular and longitudinal working points, which will be studied in the near future.

Chapter 5

Longitudinal controls characterization

The task of characterizing the longitudinal sensing and control system deals with several aspects, which are described in the following sections:

- study of the loop properties, stability and performances;
- measurement of the system transfer functions and reconstruction of the properties of the optical part.
- identification of the operating point and its dependence on parameters;

The performances of the locking system in terms of control noise are discussed in more details in Sec. 7.3.

5.1 Expected optical response of the system

One of the most important topic is the characterization of the interferometer optical transfer functions. These describe the response of each photo-diode demodulated signal to motions of the mirrors or better to the physical degrees of freedom.

The theoretical transfer functions for an ideal interferometer can be obtained by analytical computations [46, 52] or by means of simulations. Using this second approach, it is easier to use frequency domain simulations, since they can directly give results in terms of transfer function. Here the *Finesse* [61] program has been used, with a configuration which uses nominal parameters for the Virgo interferometer, listed in table 5.1. In this simulation all demodulation phases have been tuned using a procedure as close as possible to the one used experimentally, mainly by maximizing the in-phase component with respect to

Parameter	Value
Input power	10 W
Length of cavities	2999.9 m
Distance PR-BS	6.08 m
Distance BS-NI	6.20 m
Distance BS-WI	5.41 m
Modulation freq.	6.264150 MHz
PR refl. and trans.	0.95, 0.05
NI refl. and trans.	0.8819, 0.118
WI refl. and trans.	0.8833, 0.1166
NE refl. and trans.	0.99985, $42.9 \cdot 10^{-6}$
WE refl. and trans.	0.99985, $38.3 \cdot 10^{-6}$
BS sec. face refl.	$520 \cdot 10^{-6}$

Table 5.1: List of main parameters used in the Finesse simulation.

the quadrature one in correspondence of suitable calibration lines. However, these results should be intended mainly as a rough estimation of the general features that characterize the optical transfer function.

The results are shown in fig. 5.1 and 5.2 for all four demodulated signals used to control the longitudinal degrees of freedom and frequency noise. It is clear that most of the signals are dominated by the contribution of the CARM loop, which corresponds to the laser frequency noise. This is another point in favour of having a very high gain frequency stabilization servo. The response of the SSFS error signal (`Pr_B5_ACp`) shows a single pole at low frequency, which is typical of a system composed of two coupled cavities [46, 52], in this case the power recycling and the two arm cavities. The transfer functions related to the dark fringe signal (`Pr_B1_ACp`) are characterized by the presence of the arm cavity pole at about 500 Hz (fig. 5.1).

Since the frequency stabilization is so peculiar, being engaged since the beginning of the lock acquisition procedure, and having such a high gain at the frequency of interest of the other loops, it is customary to decouple it from the other controls. In other words, from the point of view of locking characterization, the SSFS servo can be considered almost as a part of the optical system. It has however two main effects: it reduces almost to zero the contribution of frequency noise and it changes the frequency response of the various photo-diodes to longitudinal motions.

Referring to fig. 5.3, the SSFS loop can be modeled by its optical transfer function F_{f2} from frequency noise f to the error signal s_2 and its corrector filter G_2. A generic longitudinal loop is instead composed of its own optical transfer function F_{z1} and the corresponding corrector filter G_1. The off-diagonal matrix

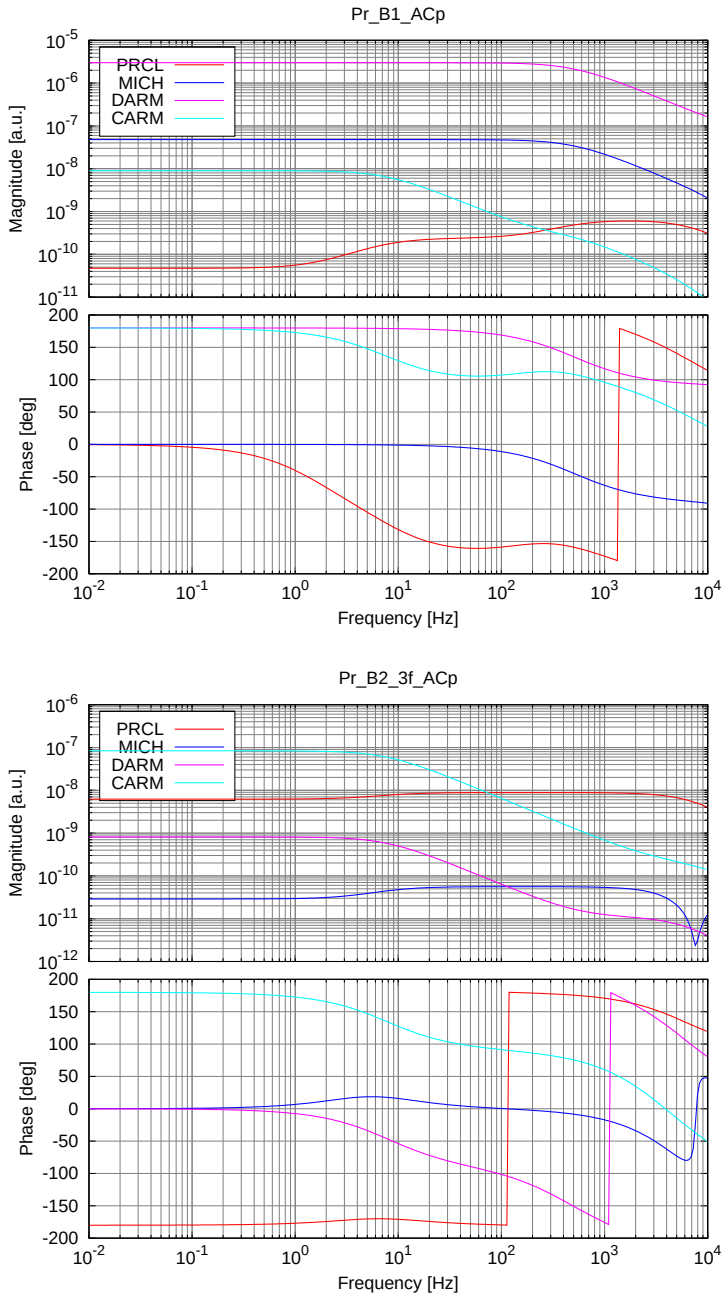

Figure 5.1: Optical transfer function from longitudinal motions to the photodiodes used for longitudinal sensing and control. These results are computed using frequency domain simulations. **Top:** dark fringe in-phase demodulated signal `Pr_B1_ACp`. **Bottom:** in-phase demodulated signal (at 3Ω) from the interferometer reflected beam `Pr_B2_3f_ACp`.

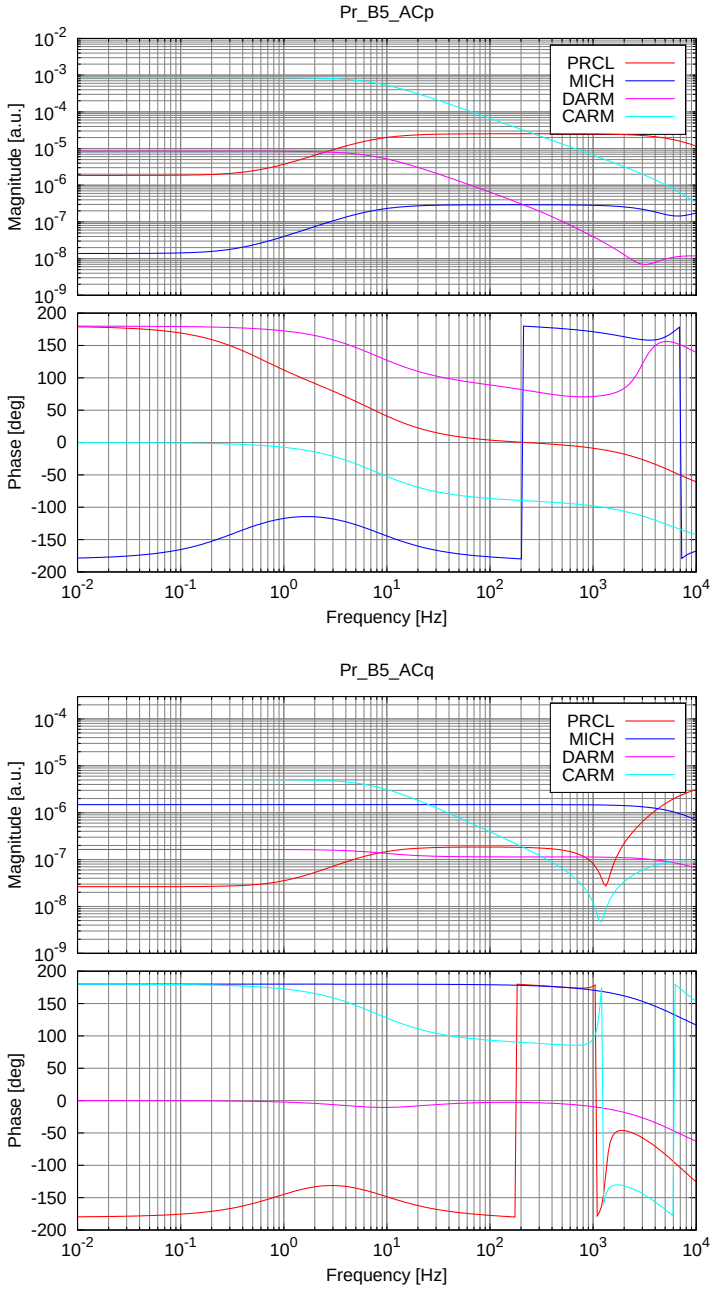

Figure 5.2: Optical transfer function from longitudinal motions to the photodiodes used for longitudinal sensing and control. These results are computed using frequency domain simulations. **Top:** in-phase demodulated signal from the beam splitter pick-off `Pr_B5_ACp`. **Bottom:** quadrature demodulated signal from the beam splitter pick-off `Pr_B5_ACp`.

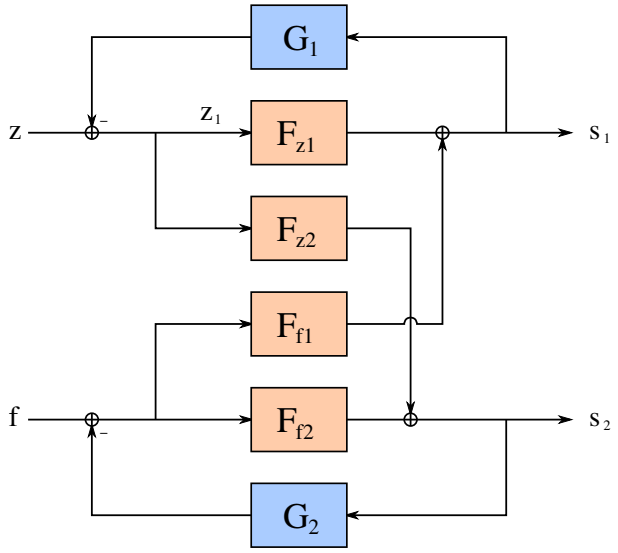

Figure 5.3: Scheme of a double control loop, used in the text to compute the effect of the high gain SSFS loop on the optical transfer functions. Here z denotes a generic longitudinal degree of freedom, while f is the laser frequency. Optical transfer functions are denoted with the capital letter F. The corrector filter are denoted with the capital letter G.

elements which links the two loops are denoted by F_{z2} and F_{f1}. The two error signals are linked together by the following linear system of equations:

$$\begin{cases} s_1 = F_{z1}\left(z - G_1 s_1\right) + F_{f1}\left(f - G_2 s_2\right) \\ s_2 = F_{f2}\left(f - G_2 s_2\right) + F_{z2}\left(z - G_1 s_1\right) \end{cases} \tag{5.1}$$

The part one is interested in is the effect of the loop 2 on the response of the first error signal to z. Therefore terms containing f can be ignored and it is possible to solve for s_1

$$s_1 = \frac{F_{z1} - \frac{F_{f1}F_{z2}G_2}{1+F_{f2}G_2}}{1 + G_1\left(F_{z1} - \frac{F_{f1}F_{z2}G_2}{1+F_{f2}G_2}\right)}\, z \tag{5.2}$$

Similarly the expression giving the residual longitudinal motion z_1 can be obtained:

$$z_1 = \frac{1}{1 + G_1\left(F_{z1} - \frac{F_{f1}F_{z2}G_2}{1+F_{f2}G_2}\right)}\, z \tag{5.3}$$

and finally the optical transfer function, defined as the response in function of frequency of the error signal to a longitudinal motion, is given by the ratio of eq.5.2 and 5.3:

$$F'_{z1} = F_{z1} - \frac{F_{f1}F_{z2}G_2}{1 + F_{f2}G_2} \tag{5.4}$$

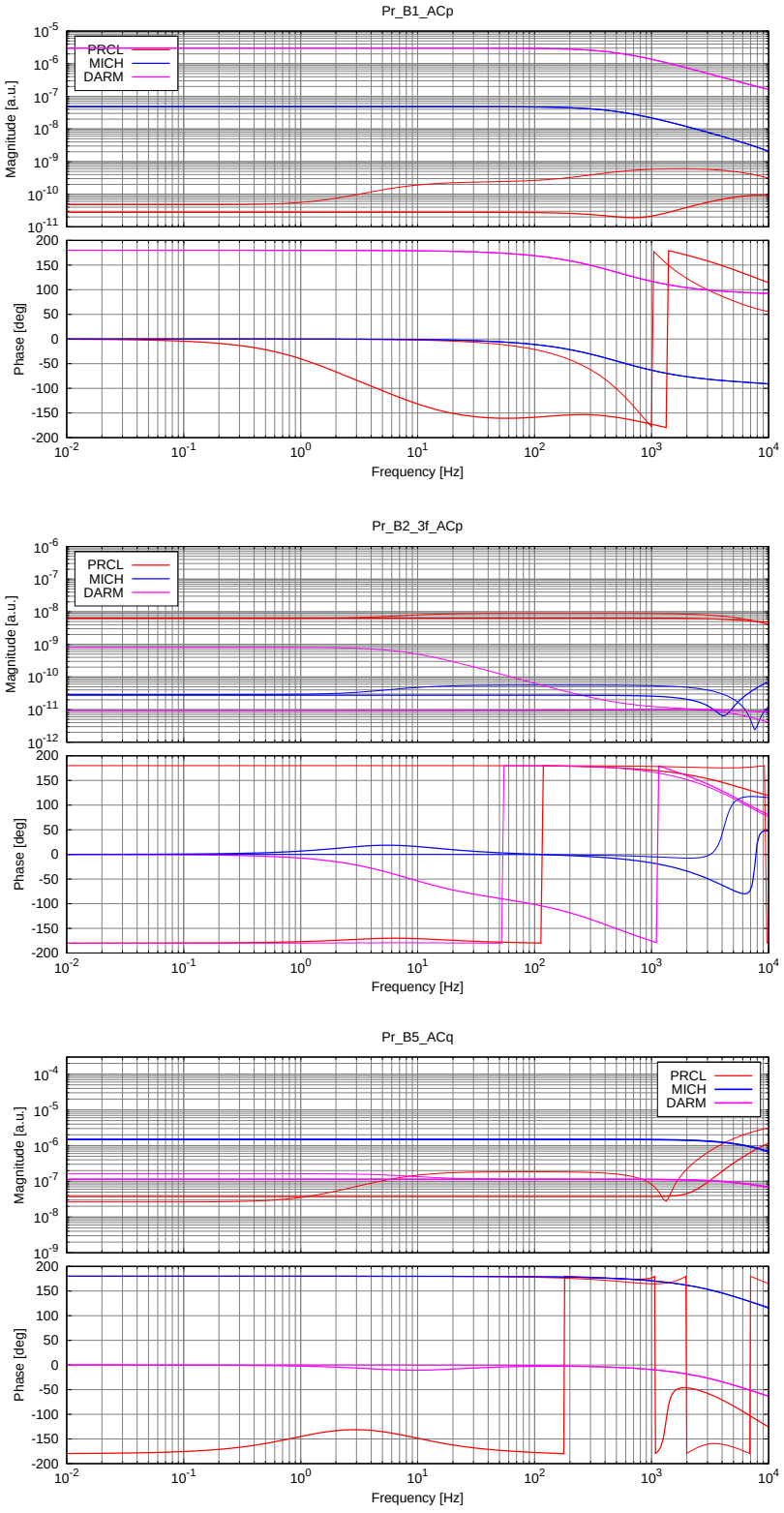

Figure 5.4: Optical transfer function from longitudinal motions to photo-diodes, corrected by the action of the SSFS high gain loop (thick lines) compared with the "free" one (thin lines). The flattening effect is clearly visible.

If the open loop gain of the SSFS loop, given by $F_{f2}G_2$ is much larger than one at the frequencies of interest, this expression can be very well approximated by

$$F'_{z1} \approx F_{f1}\left(\frac{F_{z1}}{F_{f1}} - \frac{F_{z2}}{F_{f2}}\right) \tag{5.5}$$

which is independent from the shape of the frequency servo open loop transfer function. Therefore eq. 5.4 can be used assuming a corrector filter for the SSFS which gives a simple integrator with unity gain frequency at 25 kHz as open loop transfer function. The equivalent optical transfer functions are shown in fig. 5.4. The main effect of the SSFS loop is to flatten all transfer functions up to the cavity pole at 500 Hz for the dark fringe signal and up to several thousands of Hz for the other ones.

In conclusion, the *optical matrix*, composed of all these optical transfer functions, is expected to be constant in all the frequency range of interest for the longitudinal sensing and control system.

5.2 Properties of the control loops

As explained in appendix E, adding a suitable amount of noise inside a control loop, for example to the error signal, it is possible to measure its open loop transfer function. This measurement is indeed very useful to understand the stability margins of the control systems.

The result is shown in fig. 5.5 for the DARM degree of freedom. The gain margins are $\times 1.5$ and $\times 1/2.7$, meaning that the overall gain of the loop can be decreased of a factor 2.7 or increased of a factor 1.5 before reaching an instability. The typical instability frequencies are 40 Hz for too low gain and 150 Hz for too high gain. The phase margin of the loop is 15 degrees. The unity gain frequency is at 100 Hz.

Fig. 5.6 shows the results for the PRCL degree of freedom. The gain margins are $\times 3.7$ and $\times 1/4.8$ and the typical instability frequencies are around 6 Hz for too low gain and 100 Hz for too high gain. The phase margin of the loop is 60 degrees.

Finally fig. 5.7 shows the results for MICH. The gain margins are $\times 1.7$ and $\times 1/2.1$ with instability points at about 6 Hz and 30 Hz. The phase margin is 30 degrees.

In conclusions all loops behave as expected and with reasonable stability margins.

5.3 Properties of the SSFS loop

Because of its analog nature and its high unity gain frequency, the properties of the SSFS loop can not be measured using the standard data acquisition system,

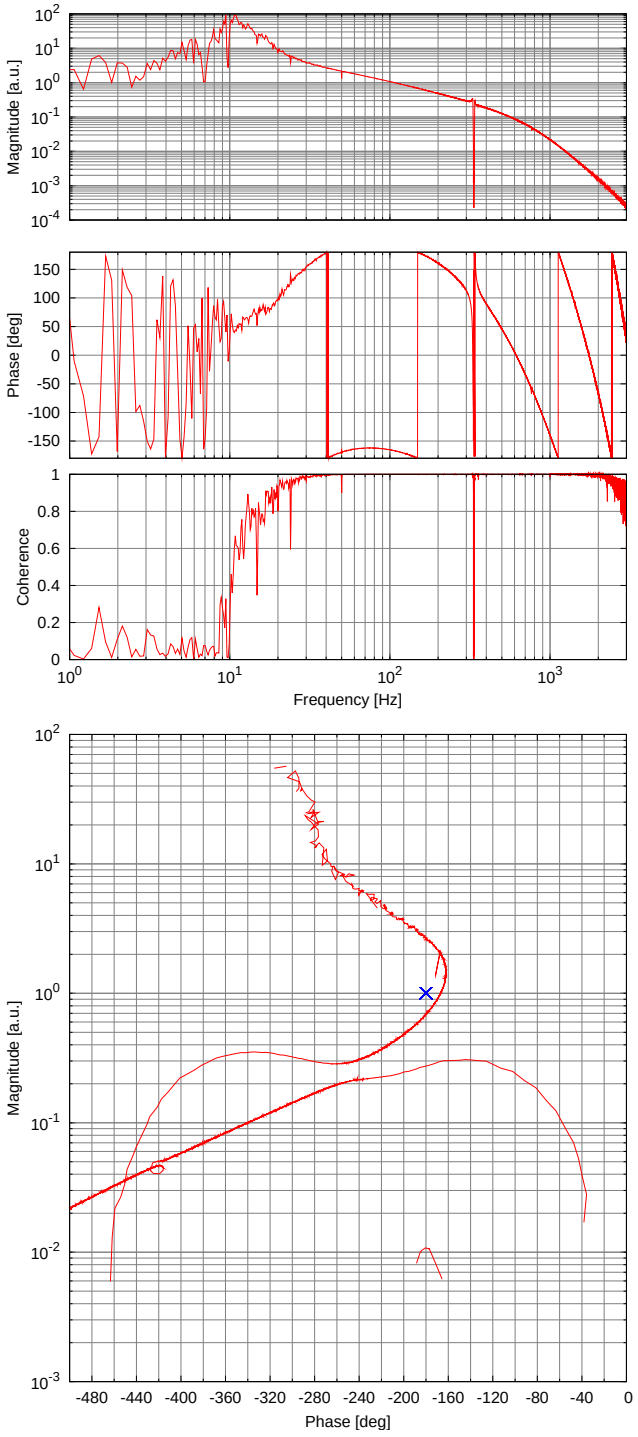

Figure 5.5: Measurement of the DARM open loop transfer function.

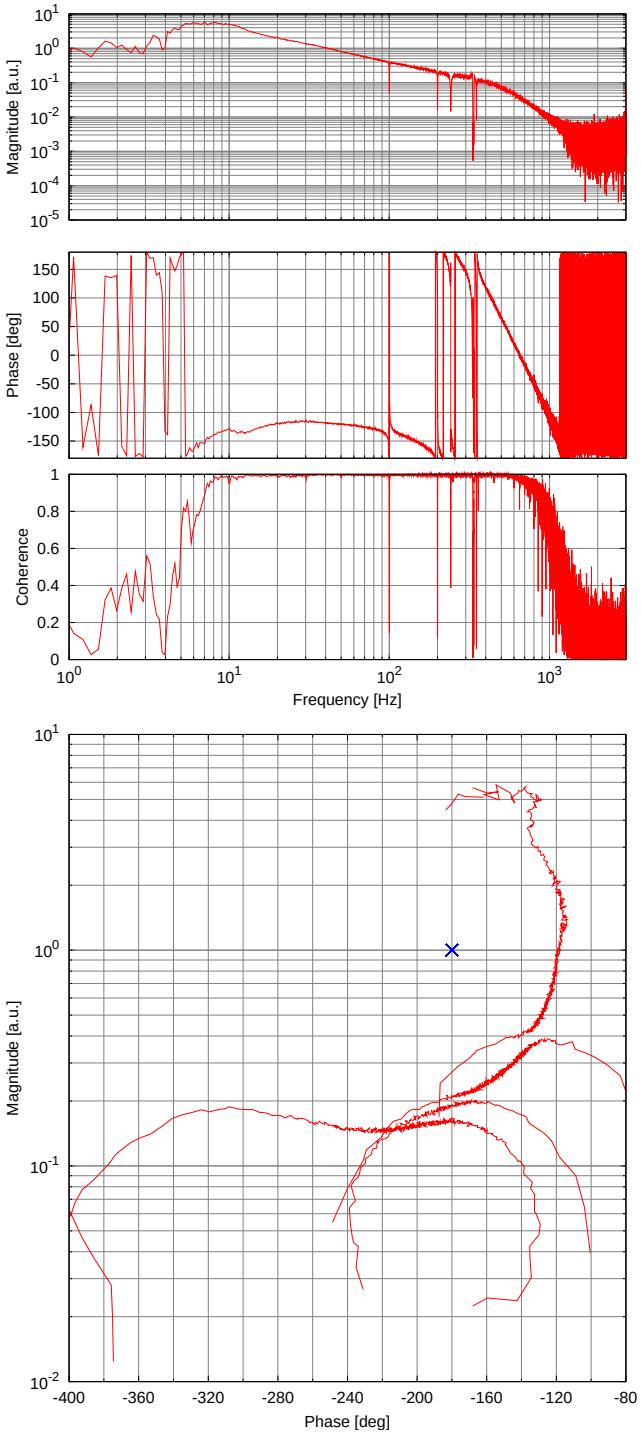

Figure 5.6: Measurement of the PRCL open loop transfer function.

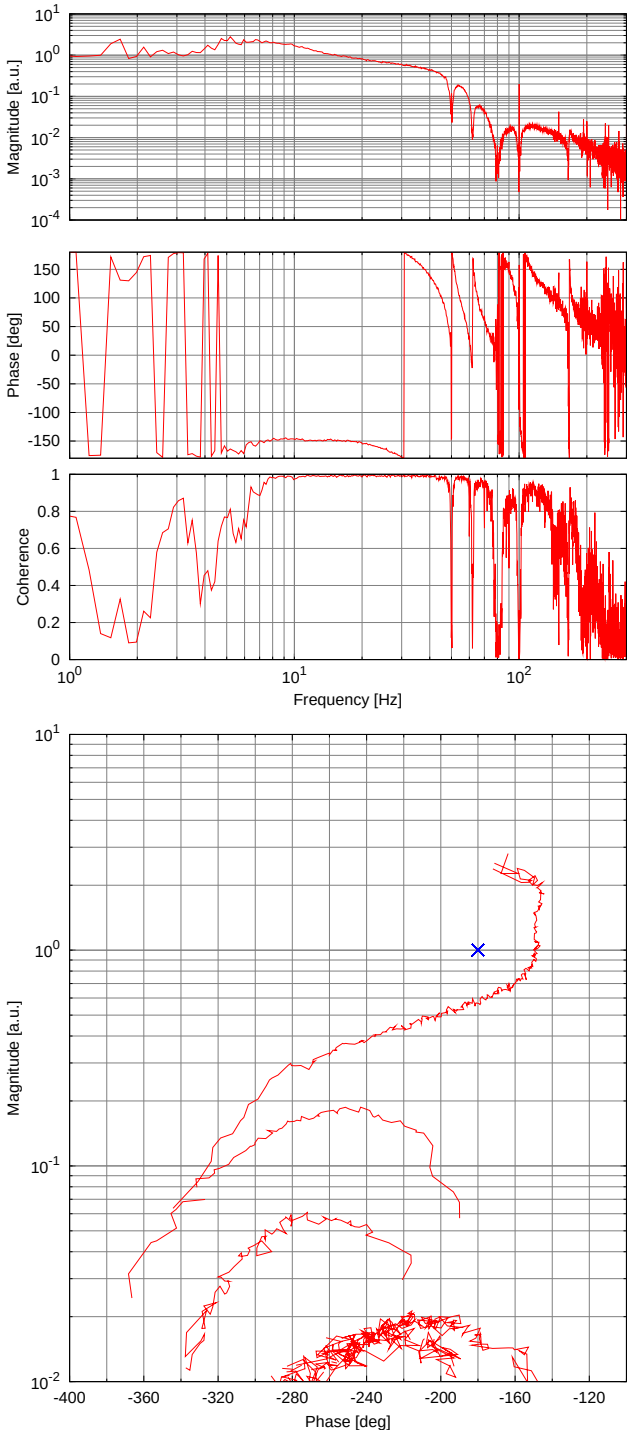

Figure 5.7: Measurement of the MICH open loop transfer function.

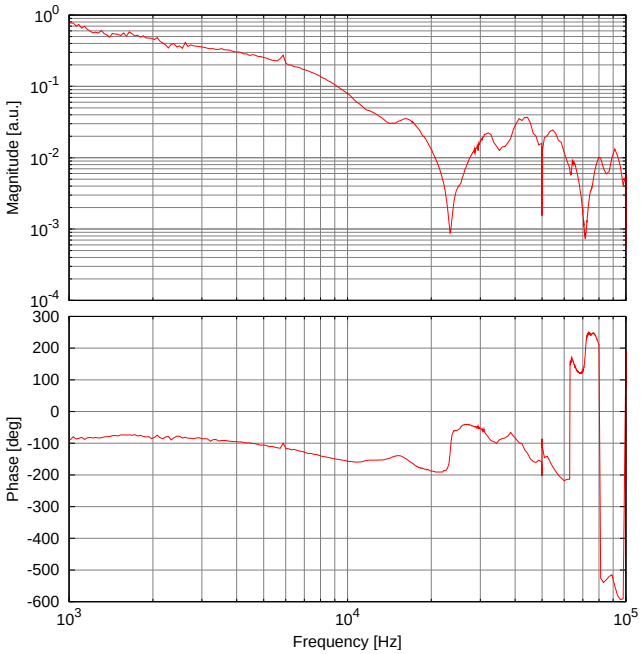

Figure 5.8: Optical transfer function for the SSFS loop: it is measured between the correction and the error signals of the SSFS loop, while adding noise to the error point.

which is limited to a sampling frequency of 20 kHz. All the following measurement have therefore been performed using a spectrum analyzer, by adding sweep sine excitations to the error signal and measuring both the open loop transfer function and the optical transfer function of the interferometer.

The optical transfer function (fig. 5.8) is measured form the correction to the error signal of the SSFS loop. It clearly shows a deep notch at exactly half line-width of the Fabry-Perot cavities (about 25 kHz) and at its multiples. The corrector filter (fig. 5.9) has been developed in order to compensate as well as possible the feature at 25 kHz, otherwise the phase rotation at this frequency would made impossible to have high UGF.

The open loop transfer function of the SSFS, when the interferometer is in its final state, is shown in fig. 5.10. The unity gain frequency is at about 23 kHz, the gain margin is 2 in both directions and the phase margin is of about 25 degrees. The gain at 1 kHz is about 500 and it is increasing approximately like $1/f$ for lower frequencies, since the optical transfer function is flat below the cavity pole at 500 Hz and the corrector filter behave like a simple integrator in this region.

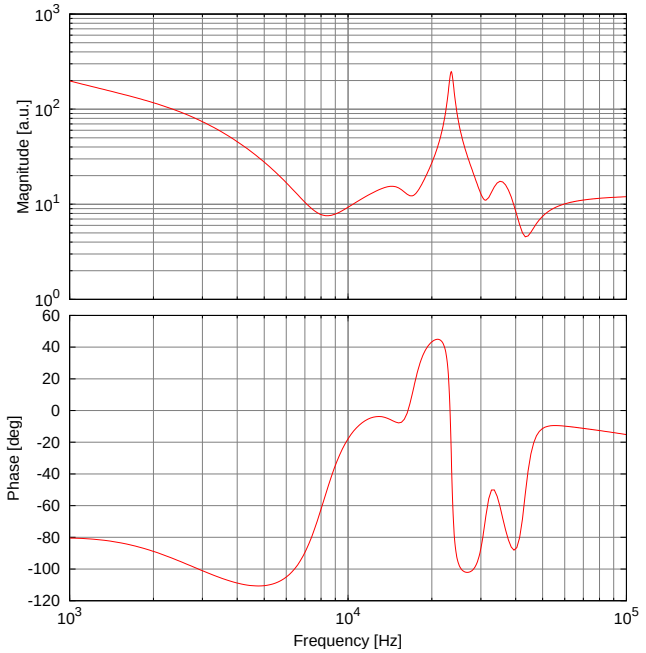

Figure 5.9: Transfer function of the analog corrector filter for the SSFS loop, from the error to the correction signals.

5.4 Noise subtraction techniques

In order to reduce the contribution of MICH and PRCL control noises to the dark fringe signal, a *noise subtraction technique* is used [62]. The idea is to cancel the contribution of the control noise a longitudinal loop introduce in the dark fringe signal by adding a suitable correction to the end mirror differential mode. The sum of the two paths, one passing through the longitudinal noise coupling and the other through the added correction, can be made to vanish.

Referring to fig. 5.11, the DARM loop is labeled by the number 1 and its error signal, denoted as b, is the dark fringe. The other control loop, which is here assumed to be MICH, is denoted by M and its error signal by e. The coupling from MICH motion to the dark fringe signal is modeled by the (unknown) transfer function F_{M1}.

The coupling of MICH noise can be seen as a bad diagonalization of the DARM error signal. To improve it the dark fringe can be mixed with the signal used for MICH. However, this approach is not the one used, since it is preferred to use the dark fringe signal as it is to reconstruct the gravitational information.

The subtraction is therefore performed at the level of the correction signals: the one sent to the MICH degree of freedom is also added, after passing through a

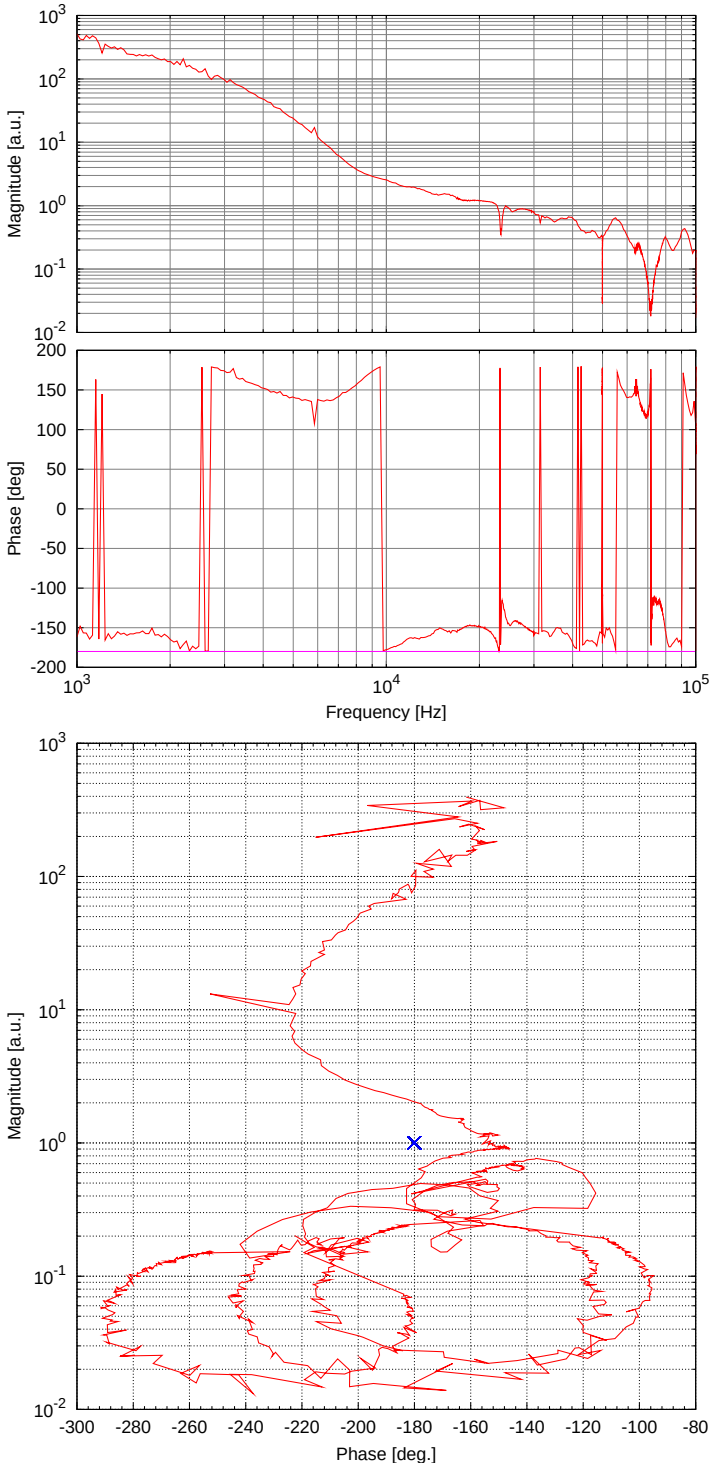

Figure 5.10: Open loop transfer function for the SSFS measured when the interferometer is locked in its final state.

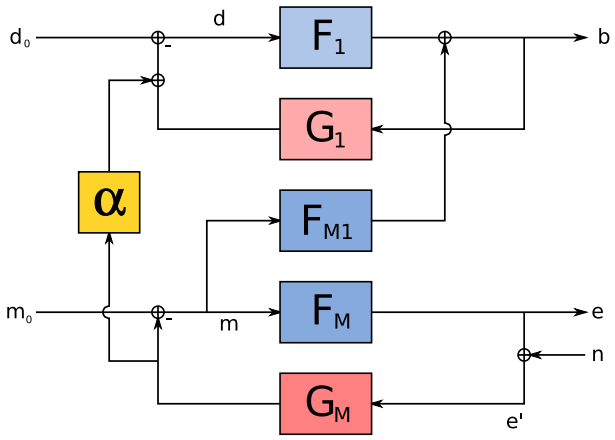

Figure 5.11: Scheme of the control loops involved in the measurement of the noise subtraction parameter, here α.

filter (denoted by α) to the differential mode one. This can be seen as a change in the way the differential and Michelson degree of freedom are driven. One advantage of this method is that the noise in the dark fringe signal is actually reduced. Moreover, if the noise which limits the MICH error signal comes from sensing noise instead of actuation noise, as it is the case, the correction signal subtraction is able to cancel it.

Therefore, assuming a noise subtraction at the level of the corrections, the effect on the dark fringe can be expressed as:

$$b = F_1 \left[d_0 - G_1 b - \alpha G_m \left(n + e \right) \right] + F_{M1} \left[m_0 - G_M (n + e) \right] \tag{5.6}$$

The contribution from the auxiliary loop can be written in terms of the corresponding correction, given by

$$m_z = G_M \left(e + n \right) \tag{5.7}$$

In this way, assuming that the noise coming from the auxiliary loop is dominant, the dark fringe signal is

$$b = -\frac{1}{1 + F_1 G_1} \left(\alpha F_1 + F_{M1} \right) \, m_z \tag{5.8}$$

This shows first of all that by using a suitable α it is indeed possible to cancel the noise contribution from the auxiliary loop. Moreover, if an external perturbation is added to this loop (to the error signal for example, as shown in fig. 5.11), the transfer function T from the correction signal to dark fringe can be measured. This also allows reconstructing the coupling F_{M1} between the two loops:

$$F_{M1} = -\alpha F_1 - T \left(1 + F_1 G_1 \right) \tag{5.9}$$

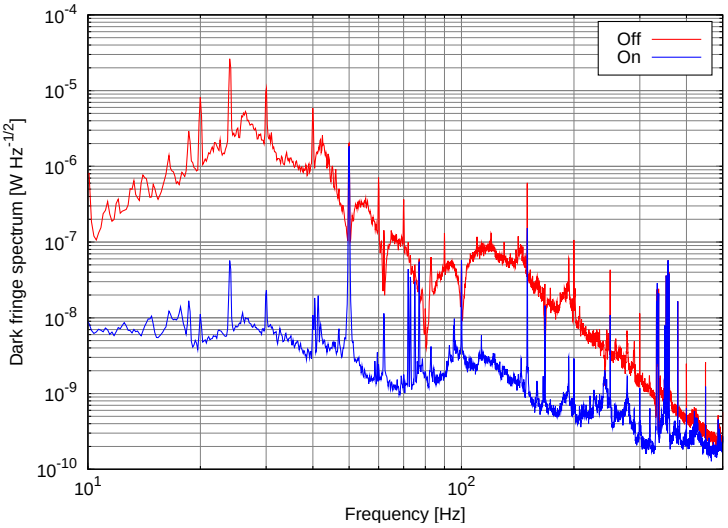

Figure 5.12: Performances of the MICH and PRCL noise subtraction (α and β techniques). The two curves compares the dark fringe noise with and without noise subtraction. The noise comes mainly from MICH below 80 Hz and from PRCL above the same frequency.

and gives a way to compute the correct shape of the α filter, as a function of the previous value of the filter itself and of the measured transfer function:

$$\alpha_{new} = \alpha + T\,\frac{1 + F_1 G_1}{F_1} \tag{5.10}$$

The only additional ingredient needed for this computation is the open loop transfer function of the DARM loop, which can be easily measured by injecting noise into the DARM loop itself, or modeled.

5.4.1 MICH noise subtraction: alpha technique

A typical example of the result of this kind of measurement for the MICH noise coupling is shown in fig. 5.13 together with the best α computed using eq. 5.10, compared to the noise subtraction filter used during the measurement. As it is visible there is a small mismatch between the running filter and the measured one, that can be easily solved by implementing a better filter.

The performances of MICH noise subtraction, usually called *alpha technique*, are very good. Indeed a reduction of the contribution of MICH noise to the dark fringe signal by a factor of roughly 50-100 can be normally achieved in a frequency range between 10 and 200 Hz (see fig. 5.12).

The long term stability of this noise subtraction has been studied in detail (see fig. 5.14). It turned out that the shape of the filter does not change

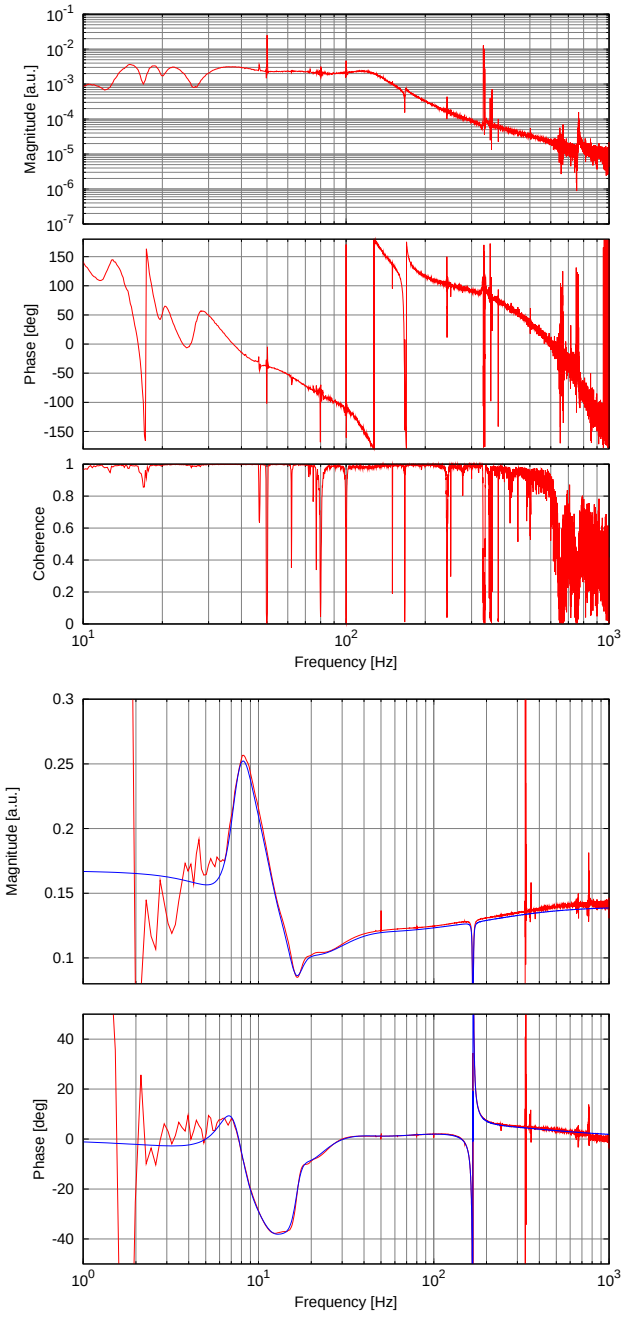

Figure 5.13: Example of the measurement of MICH noise coupling to the dark fringe signal. The top plot shows the transfer function from MICH correction to dark fringe, during the noise injection. The bottom plot shows instead the computed α transfer function (red) together with the one which was running at the moment of the measurement (blue).

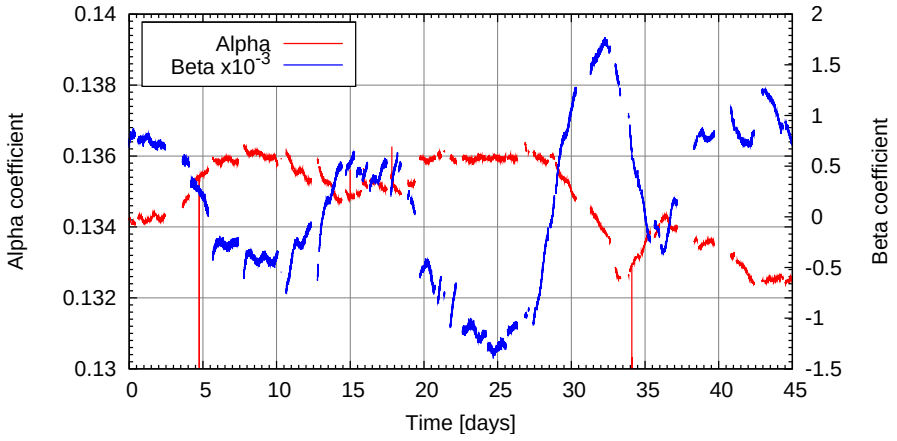

Figure 5.14: Trend of variation of the α and β coefficients over two months during the science run. The slow fluctuations are mainly driven by the arm cavity finesses.

significantly. This can be explained by the fact it should depend only on the difference in the BS and end mirrors actuators response. The overall gain of the filter changes slowly with time, following variations in the mean finesse of the two cavities, caused by temperature-driven Etalon effect in the two input mirrors [63, 64]. This change is compensated easily by a slow servo system.

5.4.2 PRCL noise subtraction: beta technique

The same subtraction technique has been applied to longitudinal control noise coming from PRCL. By injecting noise into the PRCL loop it is possible to measure the transfer function T between the correction and dark fringe signals. Eq. 5.10 can be used for computing a new value of beta knowing the one running at the moment of the measurement. Typical results are shown in fig. 5.15. The measured coherence between PRCL correction and dark fringe is not as good as for the MICH case. This is related to the fact that the coupling of PRCL noise is much lower than in the MICH case. This also implies that a very good cancellation of PRCL noise is not needed. For this reason so far only frequency independent noise subtraction has been used. Indeed the results shown in the figure agrees quite well with a constant beta within some percents, so there is no real need of a better subtraction.

This subtraction parameter also changes slowly with time and it is constantly adjusted by a servo system (see fig. 5.14).

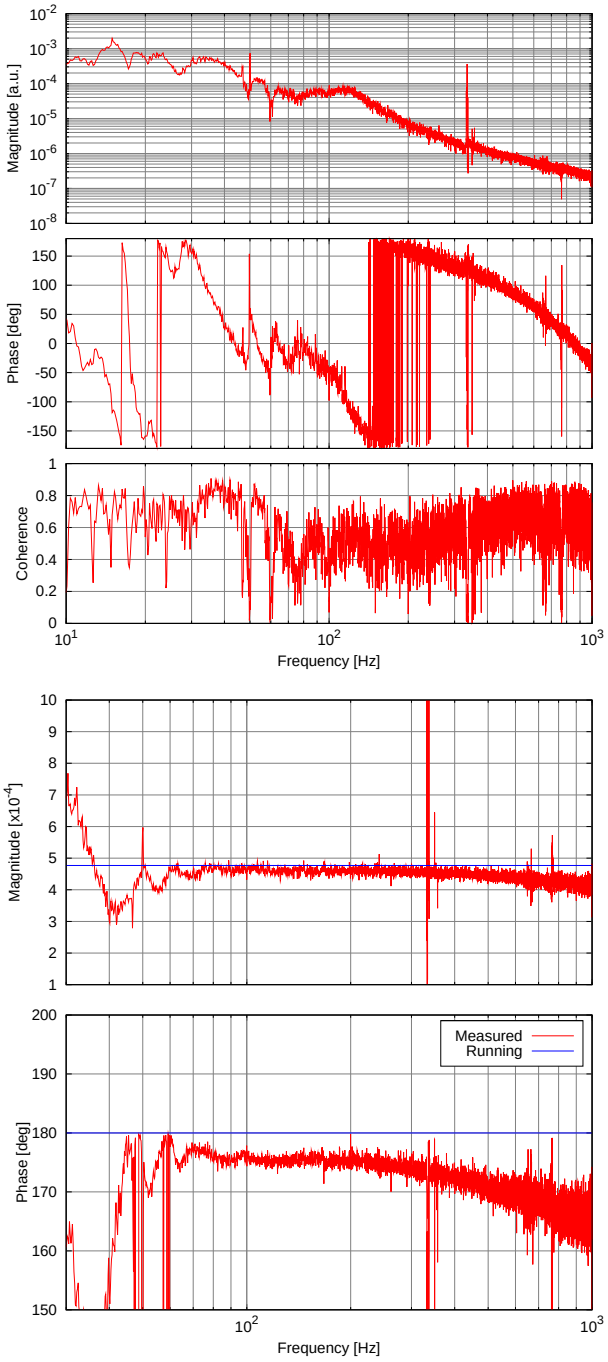

Figure 5.15: Example of the result of measurement of the PRCL noise coupling to the dark fringe signal. The left plot shows the transfer function from PRCL correction to dark fringe, during the noise injection in the PRCL loop. The right plot shows the measured β transfer function together with the one which was running at the moment of the measurement.

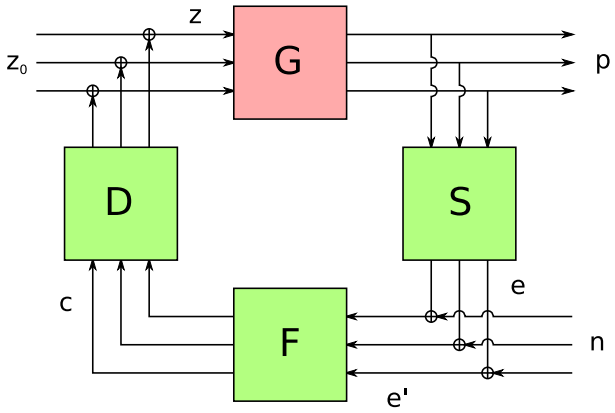

Figure 5.16: Scheme of the longitudinal sensing and control loops: **G** is the unknown optical matrix of the interferometer, **S** is the sensing matrix, **F** collects the corrector filter, **D** is the driving matrix. Refer to the text for more details.

5.5 Reconstruction of the optical matrix

Performing suitable noise injection in the longitudinal control loops, it is possible to derive an estimation of the interferometer optical transfer functions [65], which can be very useful for a better understanding and modeling of the system. In this analysis the two common mode loops has not been considered. The effect of the SSFS loop is indeed well decoupled, as already explained, because of its very high gain. Moreover, the error signal used for the CARM loop (the one acting on the common mode of the end mirror with low UGF, see Sec. B.2) is not sensitive to any other degree of freedom, since it senses only variations of the laser frequency, and therefore it is also decoupled from the other longitudinal degrees of freedom.

Referring to fig. 5.16, the *optical matrix* G of the system is the set of all transfer functions from the three physical d.o.f. (DARM, PRCL and MICH) to the photo-diodes used to reconstruct the error signals (`Pr_B1_ACp`, the mix of `Pr_B2_3f_ACp` and `Pr_B2_ACp`, `Pr_B5_ACq`). The measurement of this matrix is the goal of this procedure.

The longitudinal sensing and control system is modelled as follows. The photo-diode signals are mixed together using a *sensing matrix* S which reconstructs the three error signals. To these an external noise source can be added. The result is then passed through the three correction filters F. The correction obtained for each d.o.f. is sent to the different mirror actuators. This is described by the driving matrix D. All these matrices, except for the optical one, are known or can be measured independently from the locking loops.

5.5.1 Sensing matrix

This matrix simply takes the three photo-diodes signals and reconstruct three error signals multiplying by suitable gains. These are all set inside the digital global control system and therefore known. The signals are first normalized using suitable functions of the carrier and sidebands powers inside the recycling cavities. Afterward the DARM error signal is reconstructed from B1 alone multiplying it by the loop gain. Similarly the PRCL error signal is obtained from B2 alone, after normalization and multiplication by the loop gain. The MICH error signal comes instead from a mixing of B2 and B5, controlled by a cross-term gain. Since most of the locking parameters are controlled by the already described slow servo systems, the value of this sensing matrix changes slightly with time. A typical example is:

$$\begin{pmatrix} E_{DARM} \\ E_{PRCL} \\ E_{MICH} \end{pmatrix} = \begin{bmatrix} -9.6 \cdot 10^{-7} & 0 & 0 \\ 0 & 7.8 \cdot 10^{2} & 0 \\ 0 & -8.7 \cdot 10^{4} & 1.5 \cdot 10^{2} \end{bmatrix} \begin{pmatrix} B1\_ACp \\ B2\_ACp \\ B5\_ACq \end{pmatrix}$$

5.5.2 Filtering matrix

This matrix is in reality diagonal, since every degree of freedom has its own control filter and there is no mixing between different degrees of freedom at this stage. Therefore there are only three different filters, shown in fig. 5.17, together with the CARM one for reference.

5.5.3 Driving matrix

The driving matrix considered here is the one that converts the DARM, PRCL and MICH correction computed by the control system to real motions of these degrees of freedom. This is composed by three contributions.

The first one is a numerical matrix used by the global control system to convert from the computed d.o.f. corrections to the ones sent to the mirror actuators. This matrix is given by:

$$\begin{pmatrix} C_{NE} \\ C_{WE} \\ C_{PR} \\ C_{BS} \end{pmatrix} = \begin{bmatrix} 1 & \beta & \alpha \\ -1.1 & -1.1 \cdot \beta & -1.1 \cdot \alpha \\ 0 & -1 & -2 \\ 0 & 0 & \frac{1}{\sqrt{2}} \end{bmatrix} \begin{pmatrix} C_{DARM} \\ C_{PRCL} \\ C_{MICH} \end{pmatrix} \tag{5.11}$$

Here α and β are the coefficients that control the noise subtractions. As already explained, β is a constant value (typically about $-4.8 \cdot 10^{-5}$) and α is instead frequency dependent, with the shape shown in fig. 5.13 and a gain at low frequency of the order of 0.17. The global control part of the driving matrix includes also two notches for BS suspension violin modes at 167.05 Hz and 167.35 Hz.

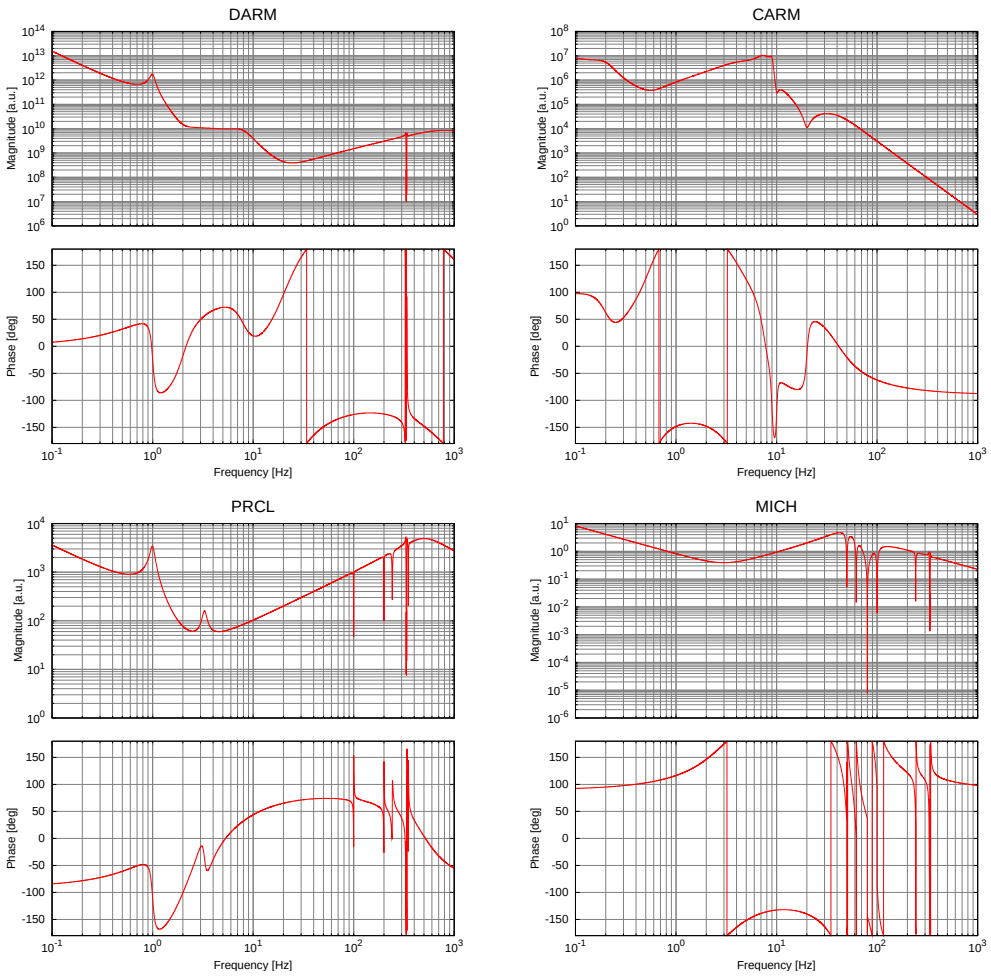

Figure 5.17: Bode plots of the filters used for the four longitudinal control loops.

Actuator	Gain ($\mu m/V$)
NE	12.1
WE	10.9
BS	78

Table 5.2: Actuators gains for longitudinal correction. All measurements have an uncertainty of about 5%.

The second contribution to the total driving matrix is given by the frequency response of the mirror actuators, from the applied correction to the resulting displacement. This response must be modeled differently for the end mirrors, where part of the locking force is re-allocated to the marionette, and for the BS and PR mirrors. For the last two the response can be described in first approximation as that of a simple pendulum, with resonance frequency at about 600 mHz. For NE and WE the transfer function must take into account the marionette mechanical transfer function and the compensator filters. The overall behavior is quite close to a simple pendulum, with some significant difference around the cross-over frequency. The low frequency gain of the actuators has been measured for NE, WE and BS [66, 67] and are listed in table 5.2. The gain for the PR actuators has not been measured yet, so the nominal value of 13 $\mu m/V$ is used here. An additional frequency dependence of NE and WE actuators has been measured. This is modeled using a pole at 100 Hz and a zero at 125 Hz.

Finally, the whole control chain must include a constant delay of about 600 μs coming from the data acquisition and control systems.

The third and last contribution to the total driving is given by a geometrical matrix that converts motions of the mirrors to the physical degrees of freedom. This has already been discussed in sec. 3.1 and can be summarized by

$$\begin{pmatrix} DARM \\ PRCL \\ MICH \end{pmatrix} = \begin{bmatrix} 1 & -1 & 0 & 0 \\ 0 & 0 & 1 & -\frac{1}{\sqrt{2}} \\ 0 & 0 & 0 & \sqrt{2} \end{bmatrix} \begin{pmatrix} z_{NE} \\ z_{WE} \\ z_{PR} \\ z_{BS} \end{pmatrix} \tag{5.12}$$

The total driving matrix is obtained by multiplication of these three parts. For a perfect driving the result should be diagonal. This is not the case for the present configuration of the Virgo locking system: the MICH and PRCL degrees of freedom are not completely decoupled. This might be improved in the future by measuring the PR actuator gain and computing the corresponding global control driving matrix.

5.5.4 Measured matrix

Referring to fig. 5.16, to perform the measurement necessary for reconstructing the optical matrix, noise is added to the error signals of the three locking loops at different times. For each noise injection, the transfer functions between the injected noise n and all three error signals e', taken after the addition of the noise, are measured, as well as the corresponding coherences. This gives a 3×3 matrix A of transfer functions. For each one of these, only frequency bins where the coherence is better than 0.5 are considered. All other bins are set to 0.

The measurement of the coupling from DARM noise to MICH and PRCL error signals has not been possible, since the coherence between the added noise and the error signals was always close to zero. The possible explanation is that the couplings factors are small and the intensity of the noise added to the DARM loop was not enough to generate an effect higher than the normal noise present in the error signals. For this reason in the following analysis the DARM noise coupling to other error signals has been assumed to be zero.

5.5.5 Optical matrix

The transfer function between the error signals e' and the noise n can be computed solving the feed-back system as in appendix E with additional care in maintaining the correct order of operands in matrix computations. Referring again to fig. 5.16, the error signals e' can be expressed by

$$e' = n + SGDFe' \tag{5.13}$$

and this equation can be inverted to obtain an analytical expression of the measured matrix A:

$$e' = A\, n = (1 - SGDF)^{-1}\, n \tag{5.14}$$

The unknown optical matrix G can be easily extracted since all other matrices are measured or known:

$$G = S^{-1} \left(A^{-1} - 1\right) F^{-1} D^{-1} \tag{5.15}$$

The results of this computation are shown in figures 5.18 and 5.19. The first figure shows the transfer functions to the dark fringe demodulated signal `Pr_B1_ACp`. As expected they are almost flat except for the arm cavities pole at about 500 Hz. The results compensated for the pole are shown in bottom panel of fig. 5.18. The residual frequency dependence can be well modeled with a simple pole at 3 kHz, which correspond to an anti-aliasing filter used inside the photo-diodes read-out system, and with a complex zero at 24 Hz with Q equal to one and a pole with the same Q at 28 Hz. This low frequency structure is related to a frequency dependence on the actuator response. The transfer function from the MICH d.o.f. is as expected the second most important one. Its magnitude is

about a factor 30 lower that that of the DARM transfer function. This ratio is of the order of magnitude of the expected one (see fig. 5.4), given by the resonant enhancement factor of the response to displacement in the Fabry-Perot cavities, given by

$$\frac{TF_{DARM\rightarrow DF}}{TF_{MICH\rightarrow DF}} \sim \frac{2\mathcal{F}}{\pi}$$

The transfer function of PRCL motion is instead higher than expected (see again fig. 5.4). The reason is that the driving is not perfectly diagonal and therefore the noise added to the PRCL error signal couples also to the MICH correction. Therefore the path followed by PRCL noise to reach the dark fringe signal passes through the MICH correction.

The plots of fig. 5.19 show the optical transfer functions to the demodulated signal from the beam in reflection of the interferometer `Pr_B2_ACp` (top) and to the one from the beam splitter pick-up beam `Pr_B5_ACq` (bottom). For these two photo-diode signals the measurements are not very good above roughly 100 Hz, mainly for the MICH transfer functions. This happens because the strong roll-off of the MICH control filter makes almost impossible to inject a significant amount of noise above that frequency.

The reconstruction of the optical matrix has been performed for several different noise injections, during different locks. The results of all these measurements are compatible within 10%, meaning that the optical configuration of the interferometer is reasonably constant in time. Since the transfer functions, after compensating for the cavity pole, are very close to be flat, the entire optical matrix G can be described with frequency independent coefficient. The mean values and uncertainties, given in W/μm are:

$$\begin{pmatrix} B1 \\ B2 \\ B5 \end{pmatrix} = \begin{bmatrix} 1.91 \pm 2\% & 2.2 \cdot 10^{-3} \pm 10\% & 7.86 \cdot 10^{-2} \pm 2\% \\ 0 & 1.0 \cdot 10^{-3} \pm 8\% & 1.90 \cdot 10^{-4} \pm 4\% \\ 0 & 0.61 \pm 8\% & 7.5 \cdot 10^{-2} \pm 10\% \end{bmatrix} \begin{pmatrix} DARM \\ PRCL \\ MICH \end{pmatrix} \tag{5.16}$$

5.6 Performances of the locking system

Starting from the measurement of the optical matrix, several other properties of the longitudinal sensing and control system can be obtained. First of all, the multiplication of the optical matrix with the sensing matrix gives the response of each longitudinal error signal to the motion of the different degrees of freedom (in arbitrary units):

$$S \cdot G = \begin{bmatrix} -1.8 \cdot 10^{-6} & -2.3 \cdot 10^{-9} & -7.7 \cdot 10^{-8} \\ 0 & 1.0 & 0.18 \\ 0 & 2.1 & -4.8 \end{bmatrix} \tag{5.17}$$

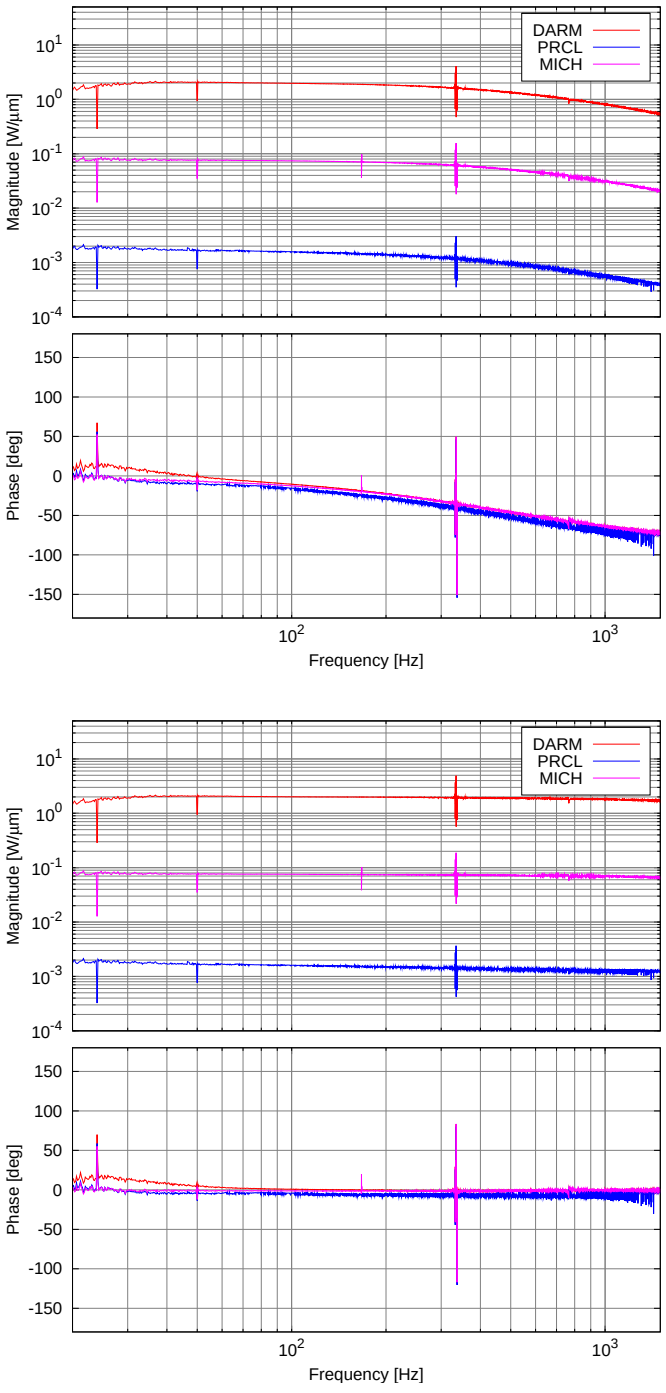

Figure 5.18: Plots of reconstructed optical matrix. The top plot shows the transfer functions from DARM, MICH and PRCL motion to the dark fringe signal `Pr_B1_ACp`. The bottom one shows the same transfer functions, corrected for the effect of the cavity pole at 500 Hz.

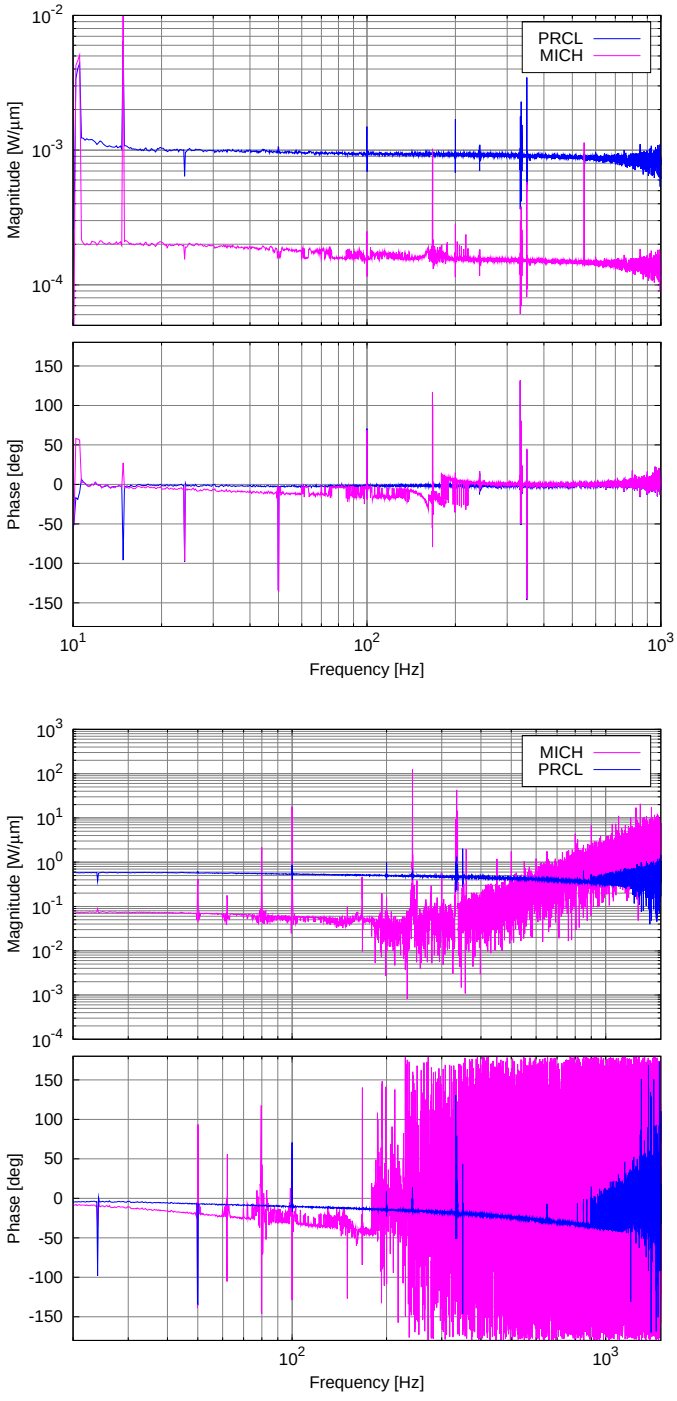

Figure 5.19: Plots of reconstructed optical matrix. The top plot shows the transfer functions to the reflected beam signal `Pr_B2_ACp` and the bottom one to the beam splitter pick-up signal `Pr_B5_ACq`.

This matrix also gives an estimate of the decoupling of different degrees of freedom in the error signals. Each row determines how much the corresponding error signal see an equal motion of the DARM, PRCL and MICH. Therefore if each row is normalized in order to have unity elements on the diagonal, the off-diagonal ones give estimates of the coupling to other motions:

$$\begin{bmatrix} 1 & 1/800 & 1/25 \\ & 1 & 1/5 \\ & 1/2 & 1 \end{bmatrix} \tag{5.18}$$

It appears clear that the DARM error signal, which by the way coincides with the dark fringe signal, has a good decoupling with respect to motions of MICH and PRCL, while the other two error signals has a much poorer decoupling. In particular the MICH error signal has only a decoupling of a factor of 2 with respect of PRCL motion.

From the matrix of eq. 5.17 a calibration of the error signals in μm can be obtained, by simple inversion:

$$\begin{pmatrix} z_{DARM} \\ z_{PRCL} \\ z_{MICH} \end{pmatrix} = \begin{bmatrix} -5.4 \cdot 10^5 & -1.8 \cdot 10^{-2} & 8.1 \cdot 10^{-3} \\ 0 & 0.93 & 3.5 \cdot 10^{-2} \\ 0 & 0.40 & -0.20 \end{bmatrix} \begin{pmatrix} e_{DARM} \\ e_{PRCL} \\ e_{MICH} \end{pmatrix}$$

This calibration matrix is clearly valid only at low frequencies, below 100 Hz, but this is the region where the residual motion of the mirrors are relevant. Using this matrix it is possible to reconstruct the real motion of the various degrees of freedom. The *locking accuracy* is usually defined as their residual RMS motions:

$$\begin{aligned} RMS_{DARM} &= 3.3 \cdot 10^{-12} \text{ m} \\ RMS_{PRCL} &= 2.8 \cdot 10^{-11} \text{ m} \\ RMS_{MICH} &= 8.4 \cdot 10^{-11} \text{ m} \end{aligned} \tag{5.19}$$

The actual motion of the DARM degree of freedom is much higher than what one should expect by considering the detector sensitivity to differential displacement (or gravitational waves). The reason is that the noise subtraction techniques operate in order to maintain the noise seen by the dark fringe signal as small as possible, at the price of introducing a larger differential motion of the end mirrors. This motion is exactly the one needed to cancel the contribution of PRCL and MICH from the dark fringe signal. In this way, even if the real motion of the end mirrors is much higher than what is expected, the sensitivity of the dark fringe signal to differential displacement is still given by the $(1,1)$ element alone of the matrix in eq. 5.16. Therefore once all contribution from other degrees of freedom are reduced as much as possible, the dark fringe signal can be considered as the limiting noise in sensing differential displacement.

5.7 Operating point

5.7.1 Definitions

The *locking point* can be defined as the point where all longitudinal control loops keep the interferometer locked, which correspond to the relative position of all mirrors that makes all the error signal simultaneously zero. One can distinguish the *operating point* which is the point where the best resonance conditions are obtained. These can be translated in terms of power signals:

- the carrier must be resonant inside the recycling cavity, meaning that `Pr_B5_DC` must be at its maximum;
- the sidebands must also be resonant in the recycling cavity, or in other words `Pr_B5_2f_ACq` must be maximum;
- the dark port must be tuned at destructive interference for the carrier: `Pr_B1_DC` must be at its minimum;
- finally, as a consequence of all the other conditions, the sidebands should be well balanced everywhere inside the interferometer, and in particular at the dark port.

For an ideal interferometer the locking point coincides with the operating point, since all error signals are zero exactly when the interferometer is at the best resonance condition. However, in a real interferometer there are many causes that can spoil this equivalence. For example the presence of higher-order Gaussian modes (for example due to mis-matching of the input beam with respect to the interferometer mode, or due to even small mis-alignments) can introduce relative offsets between error signals. In Virgo it is known that one of the main effects of the thermal transient is to change the curvature of the input mirror, therefore changing the resonance condition and mode of the sidebands in the recycling cavity. This is the main source of high-order modes and longitudinal offsets.

5.7.2 Map of locking point

This first technique to characterize the locking point was applied shortly after the beginning of the WSR program and gave very important information, that finally resulted in the implementation of the previously described offset servo for the balancing of the sidebands.

Since all longitudinal control loops are realized in the digital domain, it is quite easy to add constant offsets to their error signals. They must be maintained small to keep the locking point still inside the linear region of the error

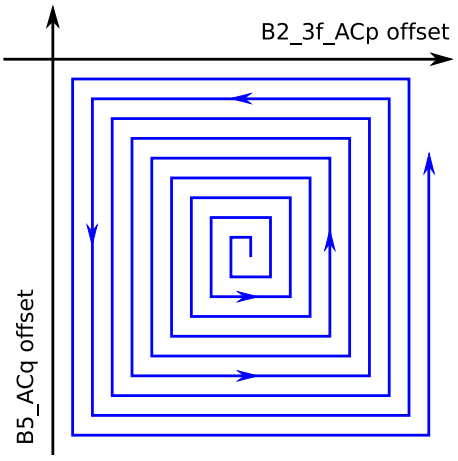

Figure 5.20: The two dimensional space of `Pr_B2_3f_ACp` and `Pr_B5_ACq` offsets is covered with a square spiral travelled at constant speed. In this way every region of the plan is sampled for a similar time.

signals and because too big offsets might move the locking point quite far from the optimal one, resulting in saturation of photo-diode signals.

For technical reasons the offsets were added not directly to the error signals, but to the demodulated output of the photo-diodes, immediately after the ADC boards. For the DARM and PRCL loops this makes no difference, since their error signals are reconstructed using only one photo-diode signal each. The MICH error signal instead is reconstructed from a combination of two signals: `Pr_B5_ACq` and `Pr_B2_3f_ACp` which is also used for PRCL. Therefore the addition of an offsets to this last signal results in a simultaneous motion of both MICH and PRCL.

The first observations showed that any offset added to the DARM or SSFS loops produced always a worsening of the interferometer performances, for example an increase of the power at the dark port and a decrease of the power in the recycling cavity. The effect was moreover symmetrical with respect to the zero offset. Therefore it is possible to conclude that the locking point of these two loops are coincident with the best operating point.

A similar experiment performed adding separately offsets to `Pr_B5_ACq` or `Pr_B2_3f_ACp` showed powers and noise levels changing in a non symmetrical way. This was a clear indication that the locking point was not correct, and that the two signals must be considered together in order to fully understand the position of the best operating point.

For this reason a scan of the two-dimensional offsets space has been performed. Technically, this has been obtained by starting from a given reference point and changing the two offsets separately with slow ramps in order to cover

the bi-dimensional plane with a square spiral (see fig. 5.20), with the offsets point moving at constant speed. This kind of measurements requires long times, typically of the order of hours, since the offsets must be moved slowly enough to avoid triggering instabilities of the interferometer.

After the measurement itself, a post-processing of the collected data is necessary to produce intelligible maps of interesting signals versus the value of the two offsets. The procedure is simple: the entire region covered by the two offsets are divided in square tiles to obtain a two-dimension histogram. Then every second the mean value of the offsets and of the analyzed signals are computed. The latter is stored in the tile which includes both values of the offsets. When all the measurement time has been processed, the values stored for each tile are averaged, to obtain an estimation of the mean value of the signal for that bin of the two-dimensional histogram.

Some results of this "mapping" of the operating point are shown in figures 5.21, 5.22 and 5.23. These maps are not centered around the zero offset position, since this gave by far not the best locking point. Actually the $(0, 0)$ position is close to the top left corner of the maps.

In fig. 5.21 the changes in some interferometer powers are shown. It is evident that moving away from the $(0, 0)$ position to the center of the plot, the carrier power (`Pr_B5_DC`) slightly change by about 5%, meaning that its overall recycling gain is decreasing. However at the same time also the power in the dark fringe is decreasing, and it has indeed a minimum near the center-right of the plot. If the ratio between the power inside the recycling cavity and the power at dark fringe is computed (see the lower right plot) it becomes evident that even if the recycling gain is decreased, the contrast of the interferometer becomes better. Finally, more or less in correspondence with the minimum of the dark fringe power, the recycling gain of the sidebands is maximum, as visible from the plot of `Pr_B5_2f_ACq` signal (bottom left). From these maps the conclusion can be drawn that the photo-diodes signals zero-crossing point does not give a good operating point: a better configuration is obtained by adding suitable offsets.

Moreover, the same conclusion can be drawn from the analysis of the maps shown in fig. 5.22, which plots the behavior of the carrier and sidebands fields at the dark port. These signals are obtained as already explained from a scanning Fabry-Perot cavity, and here they have been calibrated in watts so that the sum of carrier and sidebands powers is equal to the power read by the B1p photodiode. The top row maps show the expected behavior of the upper and lower sidebands, which should have their maximum gain at two different positions (this is an effect of the Schnupp asymmetry). From these values the sidebands imbalance can be computed, as

$$I = \frac{P_{USB} - P_{LSB}}{P_{USB} + P_{LSB}} \tag{5.20}$$

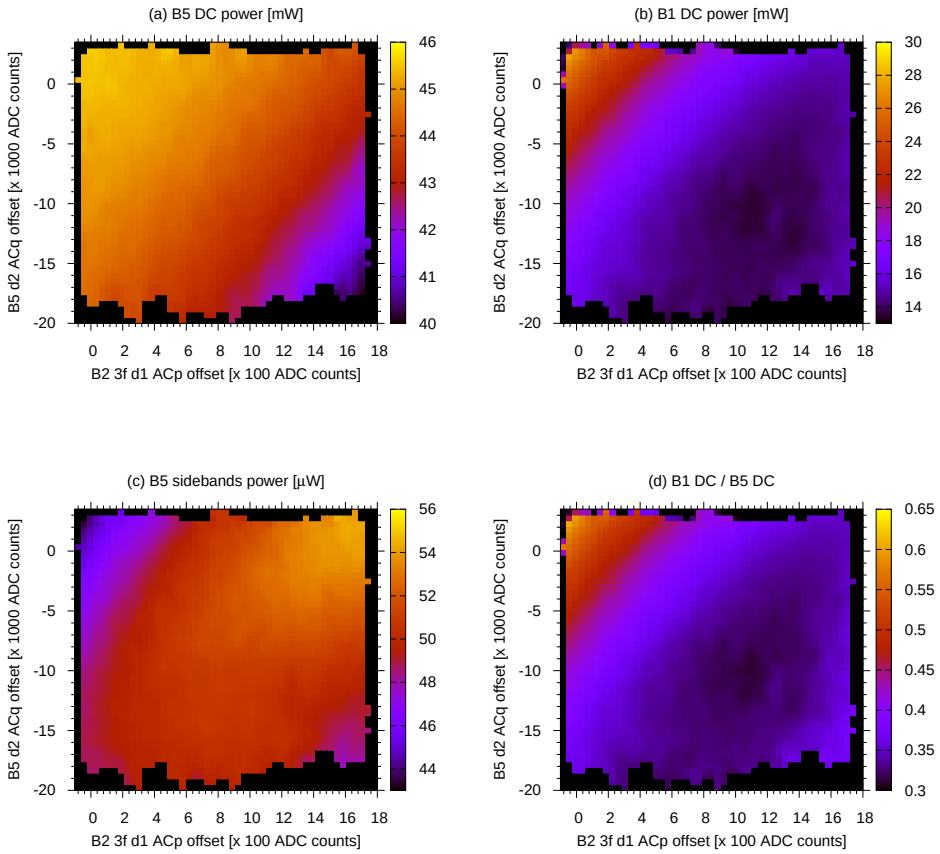

Figure 5.21: Effect of changing longitudinal offsets on interferometer powers. The axis represents the value of electronic offsets added to the two photo-diodes used to reconstruct MICH and PRCL error signals. **Top left:** Power inside the recycling cavity. **Top right:** Power at the dark port (after the output mode cleaner). **Bottom left:** Sidebands power inside the recycling cavity. **Bottom right:** Ratio of the power at the dark port and inside the recycling cavity. This gives an estimate of the "darkness" of the fringe.

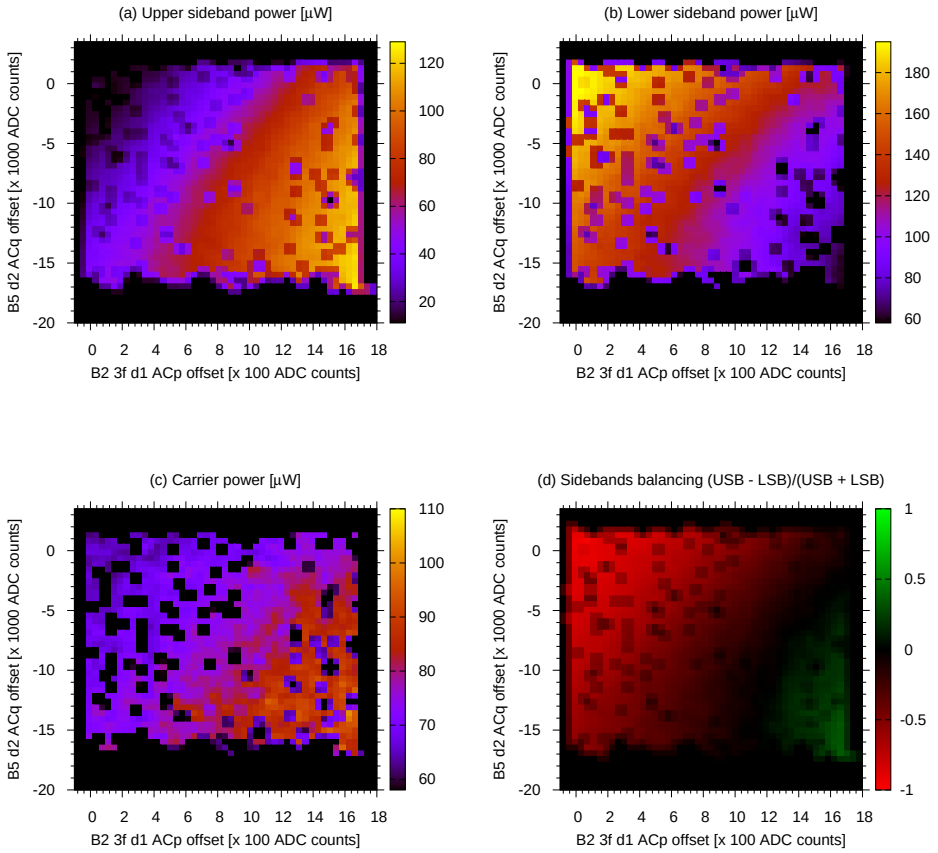

Figure 5.22: Effect of changing longitudinal offsets on carrier and sidebands powers at the dark port. The axis represent the value of electronic offsets added to the two photo-diodes used for reconstructing MICH and PRCL error signals. **Top left:** power in the upper sideband. **Top right:** power in the lower sideband. **Bottom left:** power in the carrier. **Bottom right:** sidebands imbalance, computed as the difference of the tow sidebands divided by their sum.

The region where this value is close to zero corresponds roughly to the previously identified one, which gives the best interferometer contrast. The sidebands should be balanced as better as possible, both for stability issues and to reduce the coupling of several noise sources [68].

Finally, the effect of changing the locking point on the detector sensitivity is shown in fig. 5.23. The top left plot shows the general improvement in the sensitivity, as measured by the NS-NS optimal oriented horizon. There is a significant improvement when the locking point is in the good region. A more detailed picture of the detector sensitivity can be obtained by looking at the noise level in different frequency bands, measured by mean of band-limited RMS (see sec. 8.1 for more details). The change in the BRMS of some bands is shown in the remaining plots of fig. 5.23.

In conclusion, this study allowed to prove that the locking point obtained without any careful tuning of the photo-diode offsets is not the best one, and that it is possible to greatly increase both the performances and the sensitivity of the detector by moving to a better point. The main outcome of this work has been the understanding of the necessity of a control of the locking offsets. Finally, after several experimental trials, the sidebands imbalance has been chosen as the error signal for the slow servo that changes only one of the two offsets. The use of a servo system has been necessary since the correct offsets to add to the photo-diode signals are strongly sensitive to the interferometer state: first, they can change quite a lot because of mirrors heating, even for about ten hours after the lock acquisition; second, they also depend strongly on the overall alignment condition of the interferometer; finally, as expected, they change accordingly to the demodulation phase of the photo-diodes. The offset long term evolution and accuracy are shown in fig. 5.24.

It is also interesting to convert the offsets so far expressed in terms of ADC counts to the equivalent displacement for the MICH and PRCL degrees of freedom. There are two steps in this conversion. The first one is to compute the correct combinations of `Pr_B2_3f_ACp` and `Pr_B5_ACq` that gives the MICH and PRCL error signals. The second one is the translation of error signals offsets to real displacement. Both these computations can be easily carried out. Some examples of the results are visible in fig. 5.25, where some of the maps already shown in figures 5.21, 5.22 and 5.23 are plotted against d.o.f. displacements. From this analysis it follows quite clearly that the most relevant effects are obtained by changing the MICH locking point, while the PRCL one plays a significant role only in changing the sidebands recycling gain, as visible from the $2f$ signal inside the recycling cavity.

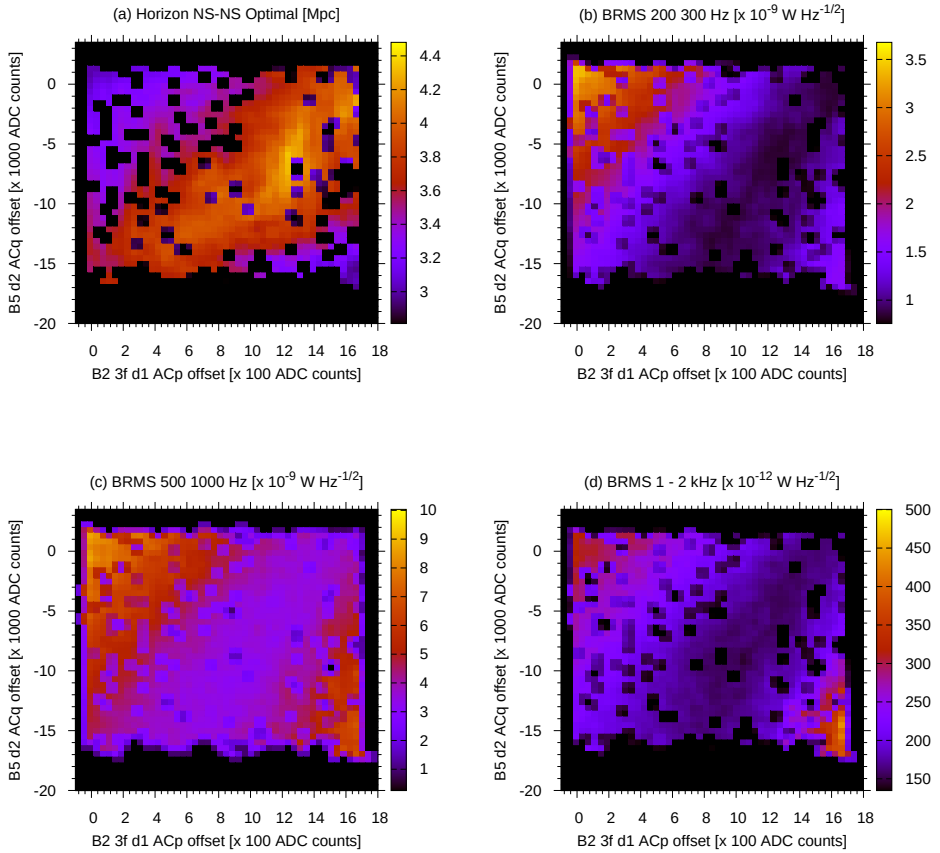

Figure 5.23: Effect of changing longitudinal offsets on interferometer sensitivity and noise. **Top left:** Maximum range for optimal oriented 1.4 solar masses coalescing neutron stars. **Top right:** Band-limited RMS of the dark fringe signal between 200 and 300 Hz. **Bottom left:** Band-limited RMS of the dark fringe signal between 500 and 1000 Hz. **Bottom right:** Band-limited RMS of the dark fringe signal between 1 and 2 kHz.

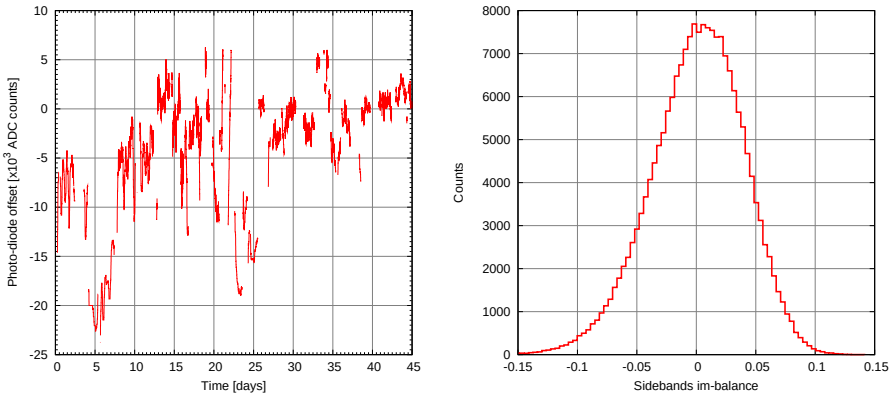

Figure 5.24: Performances of the sidebands balancing servo. The left plot shows the evolution of the added offset during one and a half months of the science run. Like the alpha and beta coefficients of fig. 5.14, the offset changes accordingly to variation of the cavity finesses. The right plot shows the residual im-balance of the sidebands, during a single lock of 90 hours. The accuracy in the balancing is of the order of 10% and is mainly limited by the error in measuring the sideband amplitudes.

5.7.3 Coupling of longitudinal noise to power signals

Another possible way to understand if the locking point gives the correct resonance conditions is to search for coupling of longitudinal noise into the signals that measure the power in different places of the interferometer. Powers should be maximum or minimum in correspondence of the operating point, and therefore any residual motion along the longitudinal degrees of freedom should not couple to power signals at first order, but only at the second and higher ones (see fig. 5.26). If instead the locking point is displaced from the maximum or minimum of the power, any motion of one d.o.f. can couple linearly to power signals.

As already explained calibration lines are permanently added to the error point of the longitudinal loops: 24 Hz to MICH, 62 Hz to PRCL, 379 Hz to DARM and 1111 Hz to the laser frequency. It is therefore possible to search for these lines in the spectra of all power signals. The best way to check if a line is visible, meaning that the corresponding longitudinal excitation couples directly into the power signal, is to check the coherence between the latter and the added excitation. If the coherence is not negligible, then a linear coupling between the longitudinal motion induced by the calibration line and the power signal is present, meaning that the locking point does not correspond to the top of the resonance peak.

In fig. 5.27 the results of this analysis, for the interferometer configuration of

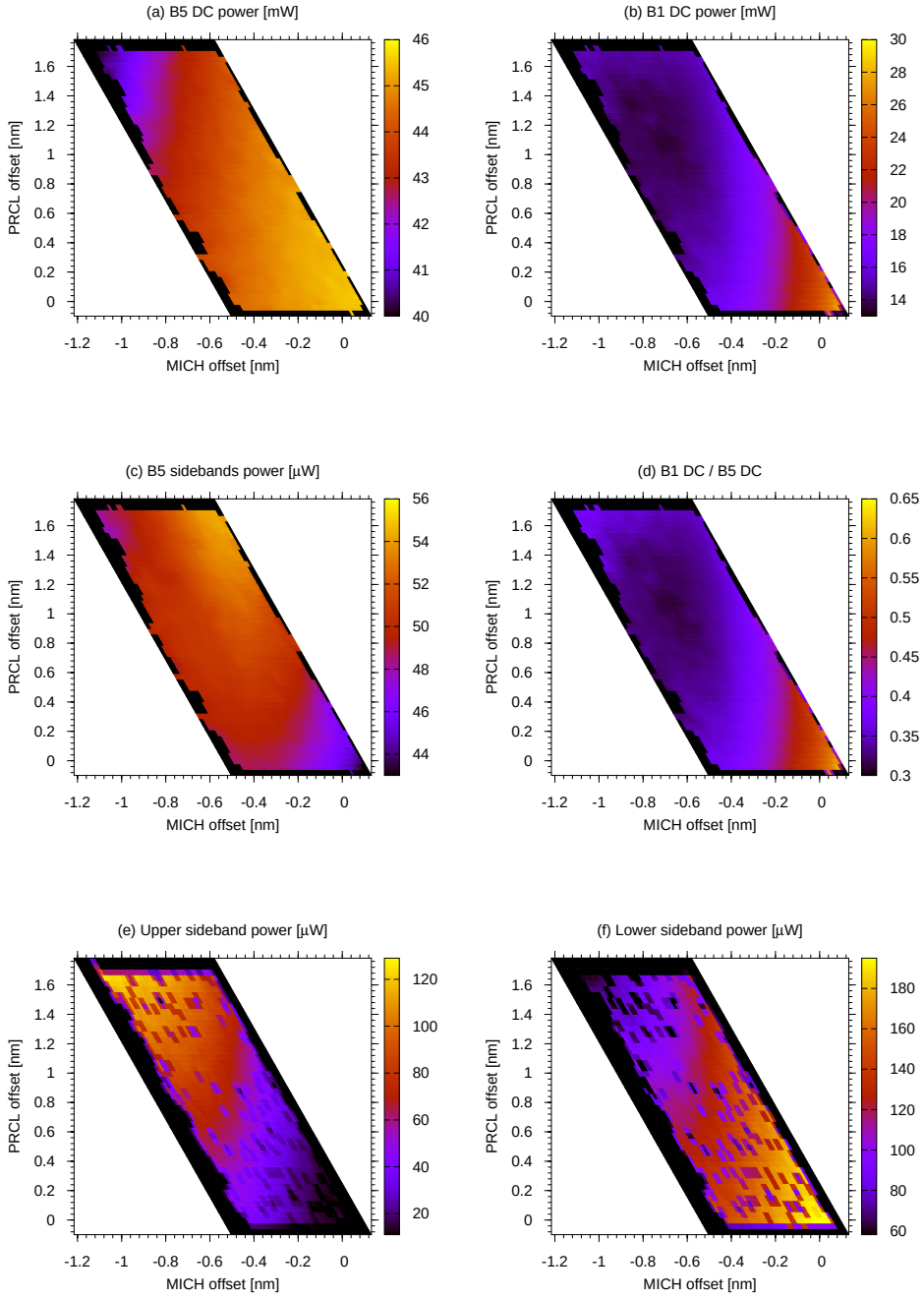

Figure 5.25: Map of operating point, re-expressed in terms of MICH and PRCL displacement in nanometers. In the first row the power inside the recycling cavity and at the dark port are shown; in the second row the sidebands power inside the recycling cavity and the fringe darkness; in the last row the two sidebands behavior.

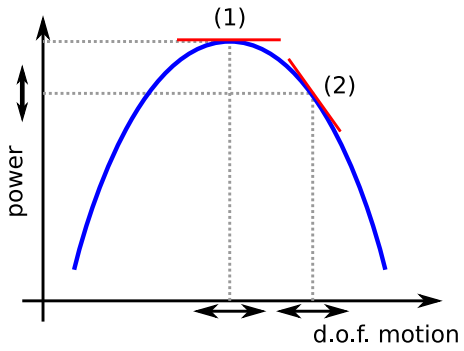

Figure 5.26: Scheme of the mechanism that couples longitudinal noise into power signals if the interferometer is not locked at the correct resonance condition.

the first part of the science run are shown. The plots in the first two rows refer to the MICH and PRCL degrees of freedom. The coherence of all powers with the longitudinal excitations are very close to 1, meaning that the linear relation is quite high and stable in time. This is also confirmed by the clear visibility of the calibration line in the spectra of powers. The plots in the last two rows instead does not show any significant coherence and the lines are not visible.

In conclusion this analysis shows that for what concern the differential mode and the frequency stabilization, the working point of the two control loops is indeed the good one, while MICH and PRCL are not yet optimal. This can in principle lead to a bigger coupling of longitudinal noise into the dark fringe signal.

These results suggest a possible procedure to find the good locking point and to maintain it. The power signals can be demodulated at the frequency of the calibration lines, in a way similar to what is done to reconstruct the unity gain frequency of the longitudinal loop, obtaining signals that can give information on the value of MICH and PRCL offsets. Since the coupling coefficient changes sign when passing the resonance, they give also information on the sign of the offsets, and therefore they can be used as error signals for a slow servo that changes MICH and PRCL longitudinal offsets to minimize the coupling of control noise into power signals. Using a servo instead of a fixed value will allow compensating for slow variations of the offsets.

5.8 Conclusions

In summary, a technique has been developed to reconstruct the optical response of the Virgo interferometer to longitudinal motion, using measurements based on (almost) white noise injections. The results confirm in the general behavior

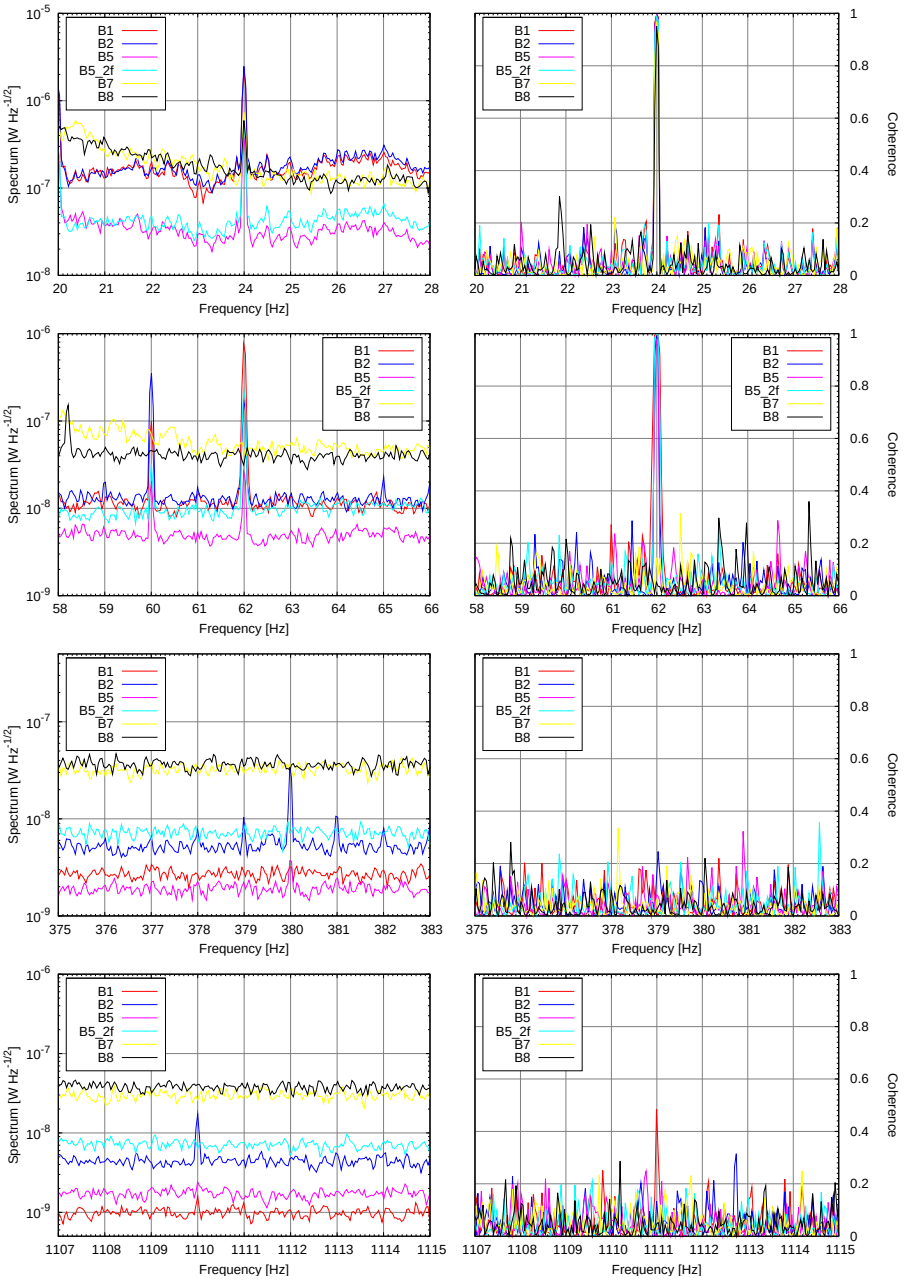

Figure 5.27: Coupling of longitudinal calibration lines into power signals. The left plots show the spectra of various power signals, while the right ones the coherence with the added excitation. From the top: MICH (24 Hz), PRCL (62 Hz), DARM (379 Hz), frequency stabilization (1111 Hz).

the expected transfer functions obtained from simulations. They moreover have been very useful to gain a better understanding of the detector and to develop noise projection, as is explained in chap. 7. There are several points that need a further development. More precise measurements would be useful to obtain better estimates of the optical matrix, mainly extending the results already obtained at lower and higher frequencies. A possible new measurement technique might replace the white noise with a *sweep sine*: a single line can be injected, with frequency slowing varying over a suitable frequency band. This method allows having a much higher amplitude of the excitation than with white noise, without perturbing too much the interferometer control and without saturating the dynamical range of the actuators. This will give a better signal-to-noise ratio in the measurement and will allow extending its validity range to lower frequencies. This method has not been used yet because of technical limitations of the present control architecture.

More efforts must also be devoted toward a better characterization of the longitudinal working point, to understand which is the best one and how to maintain it. The actual configuration is somehow defective, since the slow longitudinal offset servo uses only one error signal, given by the sidebands balancing, to control both MICH and PRCL locking offsets. It would be preferable to have two independent error signals to control these two offsets. A possible technique could imply the use of signals generated by demodulation of powers at the frequency corresponding to longitudinal calibration lines. Some work in this direction has already been started during the last period of the science run.

Finally, the task of improving the robustness and performances of the longitudinal control system is a priority one, since it is crucial to reduce the noise re-introduced at low frequency (see chap. 7). Some work has been done during the science run, mainly developing a better control filter for the CARM loop and studying the possibility of doing the same for MICH and PRCL. Moreover, the noise of the error signals is not yet completely understood and it is much higher than the expected sensor noise. Therefore the study of this noise might prove to be mandatory to reduce the longitudinal control noise at low frequencies.

Part II

Noise and sensitivity

Chapter 6

Noise sources and sensitivity

6.1 Sources of noise

The noise sources that limits a detector sensitivity or in general one interesting signal can be classified with respect to several different criteria. Given a time scale of interest, that can be minutes, hours or days, a noise source can be called *stationary* if its statistical properties do not vary significantly over the chosen time period. The most clear implication of this statement is that the contribution of the noise source to the signal power spectrum is constant in time. A noise source that does not fulfil this requirement is called instead *non-stationary*. There are many examples: noise sources that couple with a coefficient modulated by slow angular motion of the mirrors or by environmental conditions; micro-seismic residual motion of the suspensions that changes accordingly to the weather conditions, etc.

Another way to classify noises relies on their origin:

Fundamental noises. These are sources of noise which come from intrinsic limit of the detector. Examples can be seismic noise not completely filtered by the super-attenuators or shot-noise that limits the photo-diodes output depending on the level of power hitting them.

Control noises. These are those noises reintroduced in the system or amplified by the control loops used to maintain the correct operating point. They can be due for example to not optimal control filters or to noisy error signals or actuators.

Technical noise. More in general these are those noises coming not from fundamental limits but rather from the actual implementation of the detector. Examples are laser frequency and power noises.

Environmental noises, like electro-magnetic fields coupling to the detector

output or to the coils used for the actuation, or acoustic and seismic vibration outside the vacuum system that can re-enter the interferometer by means of diffused and scattered light.

Several different analysis methods can be used to discover and characterize noise sources:

Coherence analysis. A first method to have some indications of the probable origin of noise is to look at the coherence of the dark fringe with other signals. If there is some kind of linear relation between them this will be shown as a non zero coherence. This method however can not give any indication on the coupling mechanism. This will be discussed in the next section 6.2.

Stationary noises analysis. All noises coming from control system, technical limitations and similar are essentially constant over quite long periods of time. The main method used to study them is based on *linear noise projections*. These are active techniques, in the sense that the characterization of the noise source passes through a measurement that implies a perturbation of the system. First the coupling transfer function from a noise source to the dark fringe is measured, by adding an external perturbation to the system, and then the result is used to compute the contribution of this source to the total noise. Noise budgets are presented in chap. 7.

Slow non-stationary noises analysis. If part of the sensitivity is modulated with time scales going from seconds to several minutes and hours, the evolution in time of the noise power can be tracked and correlated to other monitoring channels coming from the interferometer. This method is passive, since no perturbation is done to the system. It often allows the identification of the sources of the noise power fluctuations. This analysis is the subject of chap. 8.

Fast transient analysis. This kind of analysis looks for transient events, which are short periods of time (fractions of second) when the noise power is sensibly higher than the usual value. These can be real transient events of fake events due to glitches in the data (wrong or missing samples for example). This is discussed in chap. 9.

6.2 Coherence analysis

If two signals are connected by a linear relation, the coherence[1] between them is not zero. Therefore a non-negligible coherence between for example the dark

[1] The definition of coherence is given in appendix D.

fringe and another detector channel in a given frequency band is a hint of a possible noise source limiting the main signal. This is however not conclusive, since coherence can not discriminate the direction of the coupling mechanism: supposing that signals A and B are coherent, it is not possible to tell if the noise in A is coupled to B or if it is the other way wrong, unless some other information are at disposal allowing to exclude one of the paths (for example if the dark fringe signal is coherent with an environmental channel like a microphone, it is reasonable to assume the coupling to be from acoustic to dark fringe). Moreover, A and B can be coherent because both are contaminated by a third source of noise C.

Even the lack of coherence is not a guarantee of uncoupled signals. Indeed, if the noise measured by a channel B couples to the main signal A, but the transfer function is non-stationary, meaning that it varies strongly with time, both in magnitude and phase, the averaging process involved in the coherence estimation can strongly under-estimate the linear relation between the two signal, resulting in a very small coherence even if the noise is dominant.

It is also important to consider that usually there is not only one source of noise that contributes to a given signal. Suppose that the coherence between a signal A and a possible noise source B is needed, but the first signal is also contaminated by another noise source C. The coherence that can be measured is given by

$$C_{A+C,B} = \frac{|S_{A+C,B}|^2}{S_{A+C,A+C}S_{B,B}} = \frac{|S_{A,B} + S_{C,B}|^2}{(S_{A,A} + S_{C,A} + S_{A,C} + S_{C,C})S_{B,B}}$$

and supposing that A and C are uncorrelated, as well as B and C, this simplifies to

$$C_{A+C,B} = C_{A,B}\,\frac{S_{AA}}{S_{AA} + S_{CC}}$$

and therefore if the noise coming from C is dominating A, the measured coherence can be decreased by a large factor, even if A and B are strongly related.

In conclusion, coherence analysis is for sure a valuable tool, since it can give hints on the origin of the dominant noise, but it is in general not conclusive and it usually can not give information about noises that are sub-dominant. An extension of coherence analysis to multiple channels, which can to some extent provide information on non-dominant noises, is obtained with the *multicoherence* techniques [69], which is not discussed here.

6.3 Detector sensitivity

Even if for commissioning purposes it is usually enough to analyze the spectrum of the dark fringe demodulated signal, for data analysis purposes and to gain a better knowledge of the detector sensitivity, it is necessary to convert it to

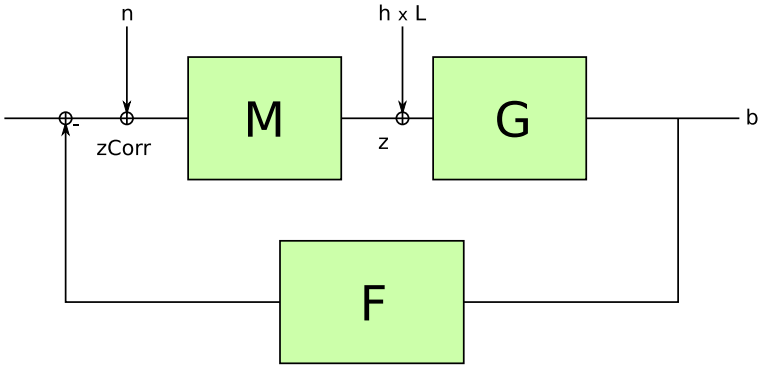

Figure 6.1: Scheme of the transfer functions involved in the measurement of the dark fringe signal calibration. Here M is the mechanical transfer function of the actuators, G the optical transfer function from differential motion to dark fringe and F the corrector filter of the DARM loop.

a calibrated gravitational wave signal. In this way the sensitivity is directly expressed in terms of differential strain.

The calibration factor that perform this conversion is frequency dependent: a first dependence comes from the optical response of the dark fringe signal to differential motion of the end mirrors, which is described by a simple pole at about 500 Hz; the second dependence comes from the longitudinal DARM control loop, which corrects differential displacements inside its bandwidth (roughly 100 Hz as discussed in section 5.2).

The standard way to recover the *calibration transfer function* is to mimic the action of a gravitational wave, adding a known source of white noise to one of the end mirrors longitudinal correction. This noise will produce both a differential and common mode motion of the end mirrors, but the latter is compensated by the action of the SSFS loop. Knowing the actuator gain, namely the transfer function from the correction signal to real displacement of the mirrors, it is possible to extract the needed calibration. The response of the dark fringe signal to the injected noise and to the strain given by a gravitational wave are given by (refer to fig. 6.1)

$$\begin{aligned} b_n &= \frac{MG}{1+MGF}\, n \\ b_h &= \frac{2}{L}\,\frac{G}{1+MGF}\, h \end{aligned}$$

Therefore the calibration can be recovered from the measured transfer function between the injected noise and the dark fringe signal if the frequency response of the actuators M is known:

$$\mathrm{TF}_{h\to df} = \frac{2}{L}\,\frac{1}{M}\,\mathrm{TF}_{n\to df}$$

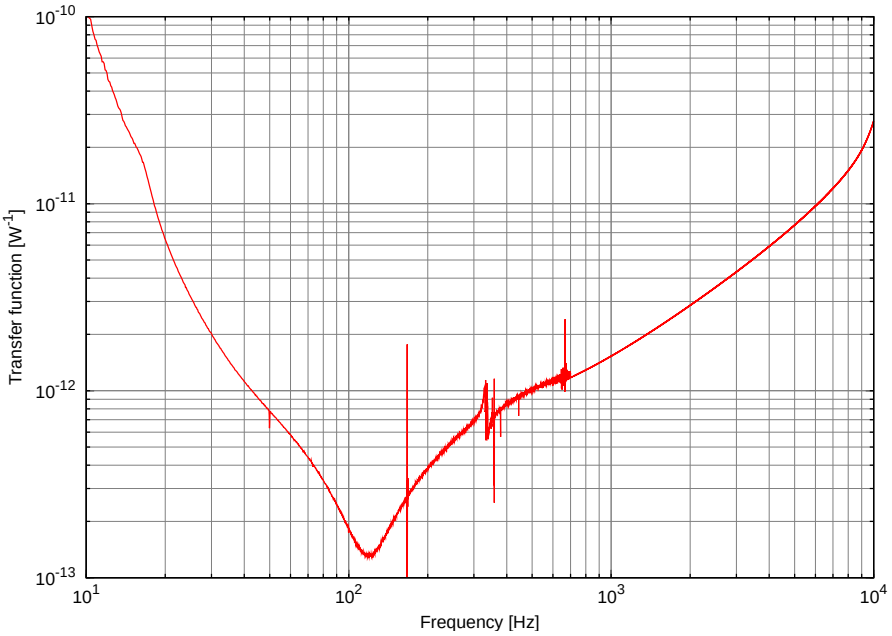

Figure 6.2: Measured calibration transfer function. The dark fringe spectrum, multiplied by this transfer function, gives the detector sensitivity.

This calibration includes both the frequency response of the optics and the effect induced by the DARM control loop. The typical result is shown in fig. 6.2. The calibration is measured below 700 Hz and fitted to a model at higher frequencies. This model includes the cavity pole and the effect of anti-aliasing filters. The structures below 400 Hz are related to the closed loop suppression of the DARM control.

The frequency response of the actuators is close to that of a simple pendulum, given by the last stage of the suspension system (see chap. 2). There are small deviations from this behavior that can be measured separately, for example by performing experiments in a free swinging Michelson configuration. The origin of these deviation are mainly ascribed to the frequency dependence of the electronic response.

The entire process of measuring the detector sensitivity takes about 10 minutes and it is used periodically to obtain reference calibrations.

The method discussed so far to measure Virgo sensitivity is based on frequency domain techniques. It is however important, mainly for data analysis purposes, to obtain a time domain calibrated version of the detector output, namely a signal that reconstruct as well as possible the differential strain. This is obtained using an adaptive algorithm that compensate on-line for the action of the longitudinal control system, tracking the amplitude of several calibration

lines to recover the variation of optical gains. The *h reconstruction* system is described in [70].

6.4 History of the detector sensitivity

The sensitivity of the Virgo detector has improved greatly over the past years. This section briefly outlines the story of the Virgo sensitivity, explaining the main actions that resulted in the improvements. The evolution is shown in fig. 6.3, starting from the first commissioning run in *recycling* configuration (C5) performed in December 2004. Between C5 and C6 the activity was mainly focused on reducing the longitudinal control noise, improving the frequency stabilization servo and implementing the automatic alignment system. The run C6 was the first one with the angular degrees of freedom controlled using slow servos in the *drift control* configuration. This helped a lot in improving the interferometer contrast and long term stability. The automatic alignment system has then been upgraded to a full bandwidth one, which operated during the C7 run. Other improvements between C6 and C7 were related to the reduction of actuator noise.

After the C7 run a long shutdown took place, with the two main goals of replacing the power recycling mirror and the suspended injection bench. The latter modification was necessary to be able to inject full power into the interferometer without suffering from back reflected light. After roughly one year of commissioning, the first *week-end science run* took place, with an improved high frequency sensitivity due to the increased input power.

Between WSR1 and WSR9 lots of commissioning activities has been performed: acoustic and seismic noise investigations to reduce the impact of scattered and diffused light; actuation noise reduction; implementation of the frequency dependent alpha technique to improve the low frequency sensitivity; modification of the second stage of frequency stabilization; improvements in the automatic alignment system. All these activities, together with many others, led to the detector sensitivity at the beginning of the first Virgo Science Run. During the run some smaller commissioning activities were performed, obtaining further sensitivity improvements at low frequency.

After the end of the run many other significant improvements have been attained, mainly at low frequencies. These are the results of improvements in the longitudinal and angular control systems and of the identification and mitigation of diffused light problems.

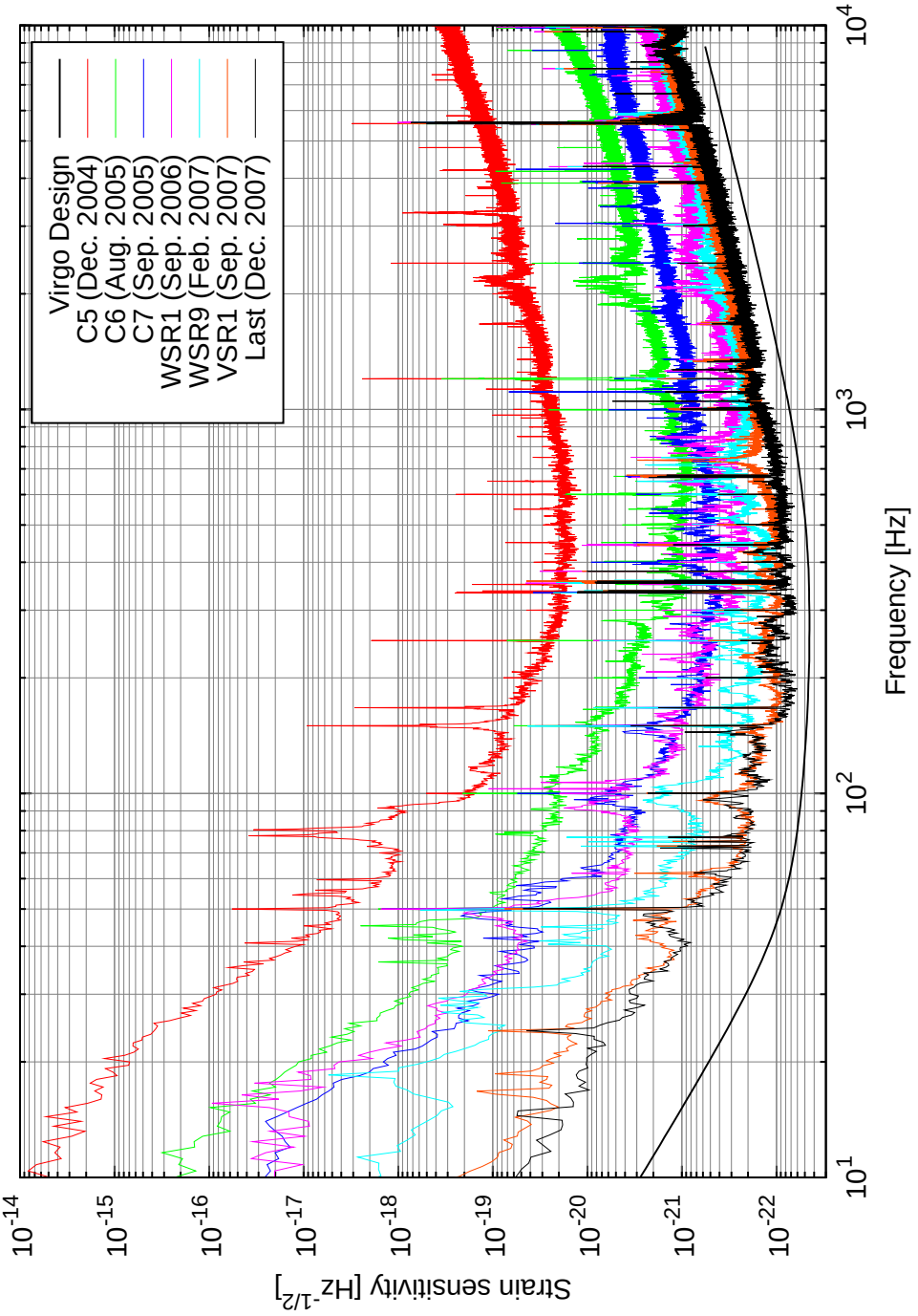

Figure 6.3: Evolution of the Virgo detector sensitivity during the last three years, since the first commissioning run in recycled configuration.

Chapter 7

Noise budgets

7.1 Linear noise projections

Once the lock is acquired, linear controllers are used to maintain it. Therefore control noises can be simply modeled with linear relations between the error signal of the loops and the dark fringe. This makes easy to identify this kind of noise, if it is the dominant one, using a simple coherence analysis. It is however useful to have a method to precisely measure the contribution of a loop noise to the dark fringe, even in the case of sub-dominant sources.

The *linear noise projection* technique [71] can be used to characterize the noise coming from a control loop. This method is made of two steps. First, an external perturbation is added inside the control loop to the error or to the correction signals. The noise level and spectral shape must be chosen in order to dominate the normal noise in the control loop at all the interesting frequencies. Using this *noise injection* it is possible to measure the transfer function between the error or correction signal and the desired main one (the dark fringe for example).

Indeed, referring to fig. 7.1, the effect of noise injections at the level of the error signal or of the correction can be easily computed:

$$\begin{aligned} s &= \frac{C}{1+FG}\,(z_0 - n_c - F\,n_e) \\ e &= \frac{G}{1+FG}\,(z_0 - n_c - F\,n_e) \end{aligned}$$

Considering only the case of noise added to the error signal (the other one being similar), at the frequencies where the added perturbation is dominant the

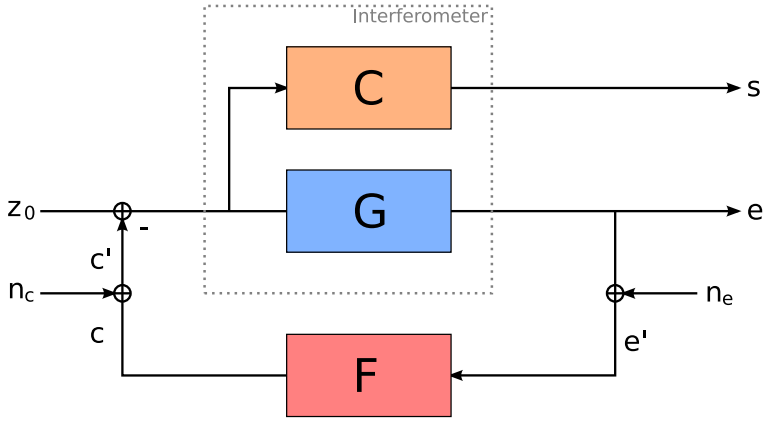

Figure 7.1: Scheme of one control loop and its noise contribution to another signal, used in the text for explaining the linear noise projection technique.

previous formulas simplifies to

$$\begin{aligned} s &= -\frac{CF}{1+FG}\, n_e \\ e &= -\frac{GF}{1+FG}\, n_e \end{aligned}$$

The error signal after the addition point of the noise is given instead by

$$e' = \frac{1}{1+FG}\, n_e$$

Therefore the transfer functions from the error signal before and after the noise addition to the dark fringe are given by:

$$\begin{aligned} \frac{s}{e} &= \frac{C}{G} \\ \frac{s}{e'} &= CF \end{aligned}$$

In a quiet period, when no noise is added, the dark fringe and error signals are given by

$$\begin{aligned} e_{quiet} &= \frac{G}{1+FG}\, z_0 \\ s_{quiet} &= \frac{C}{1+FG}\, z_0 \end{aligned}$$

The effect of the loop is two-fold. It reduces the motion of the controlled degree of freedom, but it can also introduce additional noise, coming from example from the sensing part. The residual motion of the d.o.f. can be estimated by

$$z = \frac{e}{G}$$

and its contribution to the dark fringe signals is given by

$$s = \frac{C}{G}\, e$$

This is indeed the transfer function measured between the error signal before the noise addition and the dark fringe. It gives an estimate of the contribution of the d.o.f. residual motion to the main signal. Indeed, inside the active bandwidth of the loop the correction applied is really needed to maintain the working position of the controlled degree of freedom. Therefore only the contribution of the residual motion to the dark fringe signal is interesting. This can be estimated multiplying the spectrum of the error signal (in quiet condition) with the absolute value of the transfer function between the point before the noise addition and dark fringe $TF_{e\to s}(f)$. This gives the *noise projection* of the control loop:

$$N_s^{\text{residual}}(f) = |TF_{e\to s}(f)|_{\text{with noise}} \cdot |ASD_e(f)|_{\text{without noise}} \tag{7.1}$$

On the other hand the loop can increase the motion of the d.o.f. through the correction it applies:

$$s = -C\, c = -CF\, e$$

and the link is given this time by the transfer function measured between the error signal after the noise addition and the dark fringe. Outside the active bandwidth of the loop, the applied correction has no effect in reducing the residual motion, but it can introduce additional noise in the dark fringe signal. This can be estimated in a way similar to eq.7.1, using this time the transfer function between the point after noise addition and the dark fringe:

$$N_s^{loop}(f) = |TF_{e'\to s}(f)|_{\text{with noise}} \cdot |ASD_e(f)|_{\text{without noise}} \tag{7.2}$$

Which one of the two noise projections should be used depends mainly on whether the frequencies one is interested in are inside of outside the active bandwidth of the loop.

Finally, it is worthwhile saying that even if in principle it would be much better to measure the noise transfer function with the feed-back loop open, to avoid suppression of the added noise, it is seldom possible to carry out such a measurement in complex systems like Virgo, since if one of the controls is not active, the interferometer is usually not stable at the operating point, and therefore the measurement, even if possible, is not performed in the correct state.

7.1.1 Subtle points and limits of linear noise projections

Even if this method for tracking the contribution of a control loop works well in most of the cases, there are some subtle points and some situation in which it might give wrong results. This section describes the most common issues.

In principle there should be no difference between computing a noise projection using the error or the correction signal, since in between the two there is only the control filter. However since both signal are somehow acquired and converted to digital format by some electronic board, they might be differently affected by unwanted noise. For example the error signal might be limited by some sensing noise n_e (for example shot noise, electronic noise, ADC noise) and therefore in some bands it might not describe correctly the residual motion of the system. If this happens outside the control bandwidth of the loop, this noise is usually re-injected into the system and if the corrector filter is not cleverly designed, it might increase the noise in the dark fringe.

A similar case is that of a loop with very high gain: inside its bandwidth the error signal is kept close to zero with great accuracy. The residual fluctuations might be smaller than the sensing noises n_e (typically ADC noise). In this case the error signal is no more a good estimate of the residual motion of the system, giving only an upper estimate. A solution to this limitation is to have another independent signal, sensitive to the same degree of freedom but not used for the feed-back. This avoids the problem of large loop suppression, and gives a good projection if the signal is not limited by sensing noise. This kind of solution is seldom applied mainly because it is not usual to have multiple signals than can be used for monitoring the same degree of freedom. Moreover, if the out-of-loop signal to be used for the projection has a better sensitivity than the one used for the feed-back, the role of the two will be soon switched: the most sensitive signal will be used as error signal, while the other one will be left out-of-loop, but likely blinded by sensing noise.

In summary whenever the error signal is dominated by some kind of sensing noise n_e, the corresponding noise projection must be considered with care.

Another difference between projections made with error or correction signals becomes clear when actuation noise n_c is considered: the correction sent to the actuators might be dominated at some frequencies by actuator noise. A typical example is DAC noise: since most of the control loops are digital, the output of the correction filter must be converted to an analog signal by a DAC board; if the amplitude of the correction is too small it can fall below the level of noise introduced by the conversion. In this case the projection of the correction signal gives a lower estimate of the real noise. For this reason it is always a better idea to use, if possible, the error signal of the loop for the projection, since it takes automatically into account the possible excess of noise re-injection due to actuation noise.

Moreover, while the error signal, if well reconstructed, gives a real estimate of the residual motion, the correction, inside the control bandwidth at least, contain also information on other noise sources that enters after the signal read-out and that are corrected by the loop: this means that the correction might be

much higher than the real motion of the system. A simple example is the locking of a single cavity: the error signal is taken from the transmission photo-diode and the actuation is done by applying a force to the end mirror. If the input mirror is strongly excited, the effective length of the cavity would have large variations. Since the loop has no way to damp the input mirror, it simply acts with a large correction applied to the end one, which is moved in order to keep the distance between the two mirrors constant. Therefore even if the correction is large the residual motion and the re-injected noise are small.

The last point to discuss is the effect of multi-dimensional control systems, which is the case of interferometric detectors. If the loops that control different degrees of freedom are not perfectly decoupled (which is usually the case), the same noise can be counted multiple times in different loops. For example if the error signal used for controlling A is contaminated by a large amount of noise coming from residual motion of B, when projecting its noise also a contribution from B will be considered. But this contribution is also taken into account when projecting B itself. In conclusion, the total sum of all noise projection can give an under or over estimate of the total amount of noise, depending on the relative coupling of noises in the various loops.

7.2 Summary of Virgo noise budget during VSR1

The typical sensitivity and the total noise budget during the first two months of the Science Run are shown in fig. 7.2. The various contributions are explained in details in the following sections.

At low frequencies, below roughly 50 Hz, the limiting source of noise comes from longitudinal controls (sec. 7.3), with a contribution from angular noise (sec. 7.5) between 30 and 40 Hz. Between roughly 50 and 100 Hz the noise comes from different sources, mainly actuation (sec. 7.3.1) and noise coming from eddy currents in the metallic reference masses. Between 100 and 1000 Hz, the noise floor is well described by shot noise (sec. 7.10) and still actuator and eddy currents noises, but there are many structures not completely understood. Part of these has been identified and cured during the last month of the science run. They were originated by longitudinal noise in the IMC cavity caused by noisy piezo-electric actuators mounted on the suspended injection bench. The most likely origin of the remaining structures is environmental noise (sec. 7.11) that can couple through diffused light or input beam jitter (sec. 7.6.1). Above 1 kHz the main sensitivity limitation comes from the dark fringe shot-noise and in a small frequency band around 6 kHz from frequency noise (sec. 7.4). This bump was also caused by the noisy piezo-electric actuators and it disappeared after the intervention.

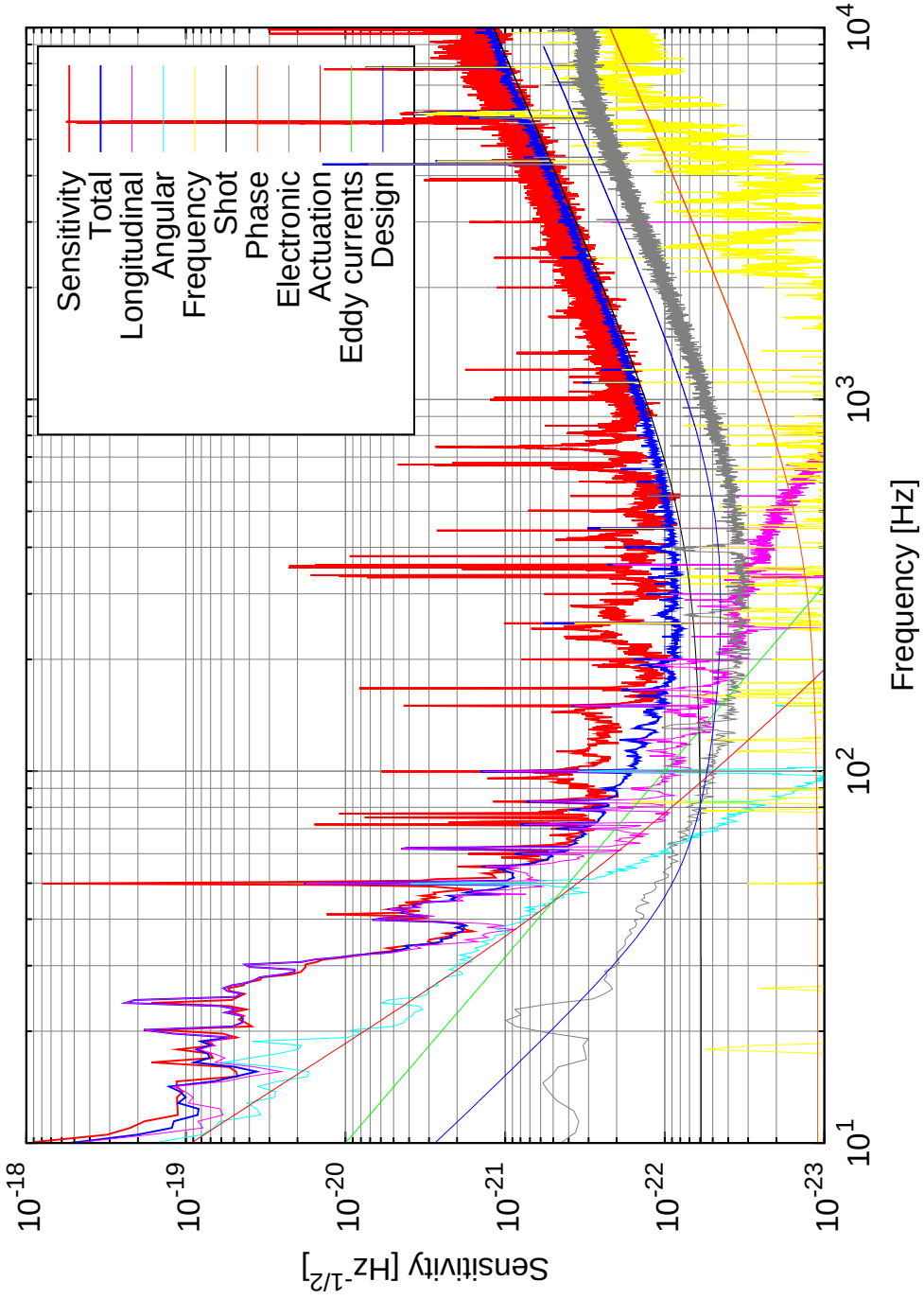

Figure 7.2: Summary of the detector noise budget for the configuration running during the first two months of VSR1. Refer to the text for more details.

7.3 Longitudinal control noise

Since the noise of DARM is the gravitational channel itself, and the effect of the DARM loop is taken into account during the calibration of the dark fringe signal, the contributions of longitudinal control noise that are relevant are those of MICH, PRCL and CARM loops.

An automatic procedure [72] has been implemented and periodically used during all the run to measure the longitudinal noise budget. This procedure performs the required noise injections, computes the transfer functions from the error signals after the noise addition to the dark fringe and uses them to obtain the control noises projection. Since the error signals are used, the projections are valid only if they are not limited by sensing noise. This is true for the error signals used for the longitudinal sensing and control system. Moreover, the computed projections include the effects of actuation noise.

A typical result of the longitudinal noise budget measurement is shown in fig. 7.3. Both the coherence and the transfer function from the longitudinal loop error signals (after the adding point of the noise) to the dark fringe are computed. The transfer functions are used, at frequencies where the coherence is good, to project the normal level of noise. The typical results for the first part of the science run are shown in fig. 7.4. The noise coming from the PRCL loop is about a factor 10 below the actual sensitivity, but it is strongly variable with time. The CARM control noise is one of the two concurrent sources that limits the sensitivity below 20-30 Hz. The MICH control noise is very close to the sensitivity below 20 Hz and limiting between 20 and 40 Hz roughly. The steep roll-off of the control filter above about 50 Hz ensures that this loop does not affect the sensitivity above that frequency.

In order to improve the low frequencies sensitivity, the control noise coming from CARM and MICH had to be reduced. For what concerns the first degree of freedom, this has been obtained in two steps. First, any mis-balancing of the actuation at the end mirrors results in a leaking of the CARM correction to the differential mode and this couples directly with the dark fringe signal. By simply tuning the balancing of the CARM actuation of the end mirror it has been possible to reduce the coupling of this control noise by roughly a factor ten. The second action has been the implementation of a better control filter with a steeper cut-off at about 9 Hz (shown in fig. 5.17). The total effect of these two modification brought the CARM control noise well below the actual sensitivity, and even below the design one above 30 Hz.

7.3.1 Actuation noise

An important contribution to the noise in the dark fringe signal comes from actuation noise. For what concerns the beam splitter and power recycling mirror

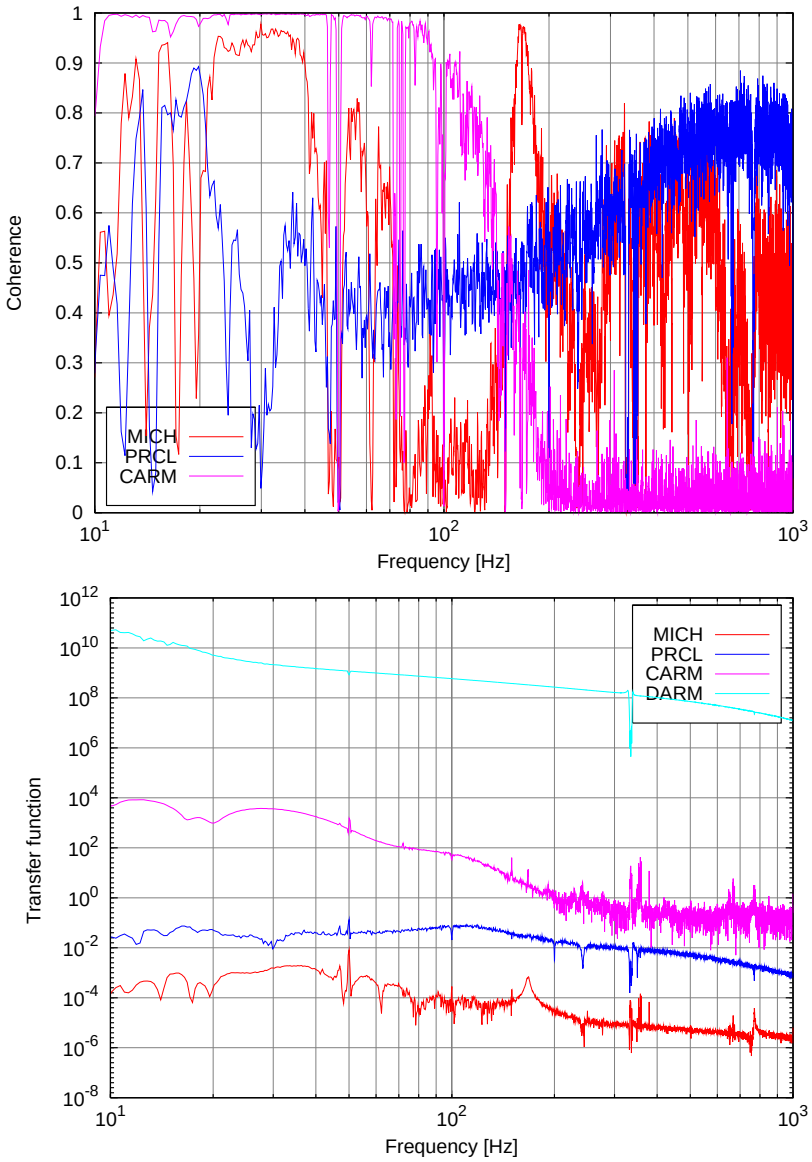

Figure 7.3: Example of the measurements performed to compute the longitudinal noise projections. The top plot shows the coherence between the error signals and the dark fringe during the corresponding noise injection. The bottom plot shows the obtained transfer functions.

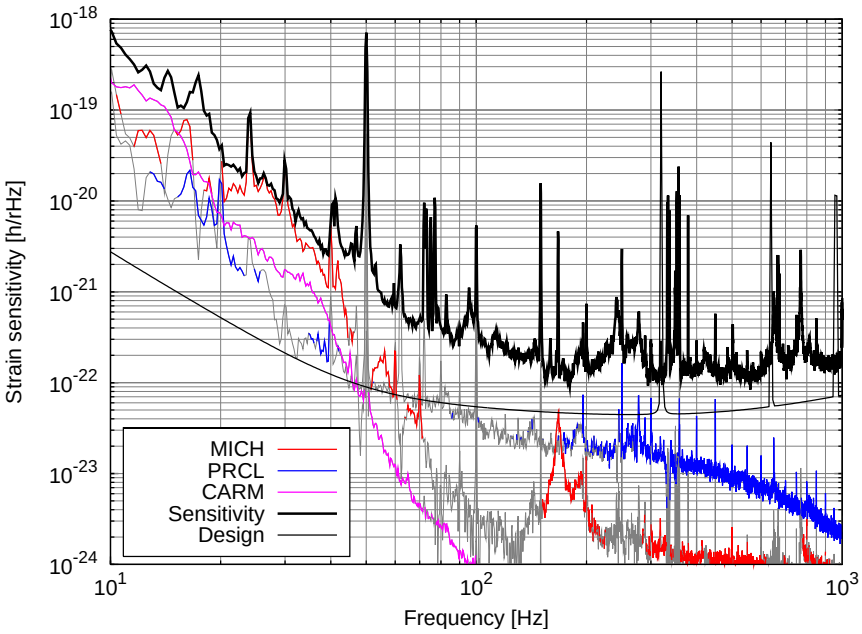

Figure 7.4: Projection of longitudinal noise in the dark fringe signal, calibrated in units of strain sensitivity, measured during VSR1. The color of the lines is grey when the measurement of the corresponding transfer function showed low value of coherence, meaning that the projection is not meaningful. The thick black line is the measured sensitivity of the detector while the thin black one is the design one.

this is already taken into account by the longitudinal budget, but it is still interesting to understand what fraction of the noise introduced by the MICH and PRCL loop can be ascribed to actuation noise. Instead the contribution of the end mirrors actuators must be considered separately.

A scheme of the coil driver low-noise section, responsible of converting the digital correction to the actual current flowing in the coil actuators, is shown in fig. 7.5. The main source of actuation noise comes from the digital-to-analog converter. The boards used in Virgo have a peak-to-peak range of 10 V and a floor noise that can change accordingly to the input signal. For null or sinusoidal input it was measured to be of about 300 $nV/\sqrt{Hz}$. If a signal that mimic the correction applied during normal operations is used, the noise introduced has a $f^{-1/2}$ shape and a value of about $1.5\mu V/\sqrt{Hz}$ at 100 Hz.

In the science mode low noise configuration the maximum value of the force that it is necessary to actuate using the reference mass coils is small. This allows the use of two tricks to reduce the impact of the DAC noise. The correction is first digitally amplified (by a factor 600 for the end mirrors) before the

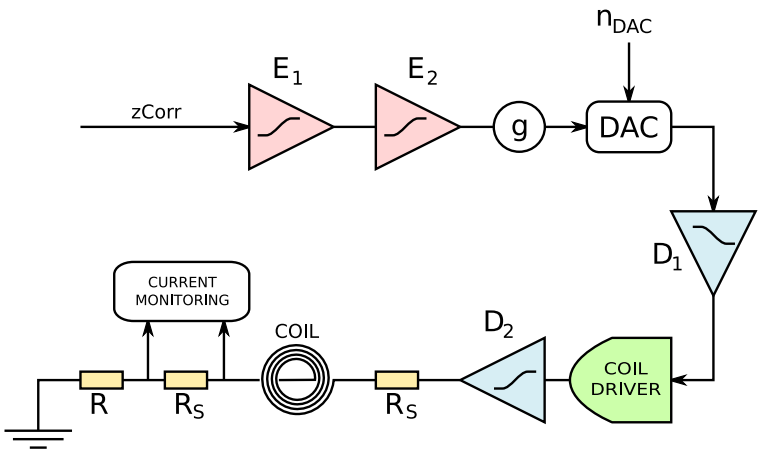

Figure 7.5: Scheme of one of the coil drivers used to convert the longitudinal correction to the current to be applied to the coil actuators.

DAC, thus enhancing the signal-to-noise ratio. The amplification is compensated analogically adding a resistor in series with the coil. Moreover, the high frequency part of the correction is amplified by *emphasis filters*, compensated after the DAC by analog counterparts. In this way a further improvement of the signal-to-noise ratio of the correction is obtained at high frequencies. For the end mirrors these filters are made by a couple of real poles at 3 and 20 Hz and a couple of real zeros at 80 and 100 Hz. A similar configuration is also used for the BS, while the PR has no emphasis/de-emphasis filters.

The contribution of the DAC noise to the dark fringe signal can be estimated as follows. First, the DAC noise can be expressed in terms of equivalent noise at the level of the longitudinal correction dividing it by the emphasis filter and the gain:

$$n_{zCorr} = \frac{n_{DAC}}{g\, F_{emph}} \tag{7.3}$$

The corresponding mirror displacement can be computed using the known frequency response of the mechanics:

$$n_z = F_{mech}\, \frac{n_{DAC}}{g\, F_{emph}} \tag{7.4}$$

This noise estimate refers to one single coil. Therefore for each mirror the total displacement noise is given by the incoherent sum of the one coming from each coil (there are two of them for end mirrors and power recycling, and four for the beam splitter). Assuming the same level of noise for each coil and similar filters, this gives an additional factor $\sqrt{2}$ for end mirrors and power recycling, and a factor 2 for the beam splitter.

For the two end mirrors, the displacement noise translates directly in a DARM motion and it can be expressed in units of sensitivity dividing by the

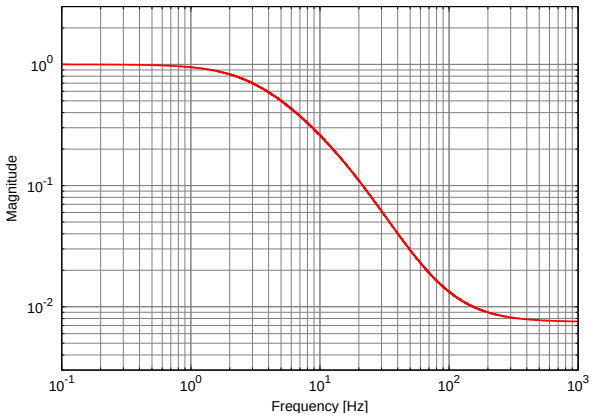

Figure 7.6: Typical shape of the analog de-emphasis filters used to reduce the actuation noise. This allows a reduction of more than a factor 100 at higher frequencies.

arms mean length and by the cavity response:

$$h_{end} = \frac{\sqrt{n_{zNE}^2 + n_{zWE}^2}}{LF_{cav}} \tag{7.5}$$

The displacement noise from the beam splitter and the power recycling mirror can be recombined in terms of MICH and PRCL noise, using the geometrical driving matrix described in sec. 3.5. The PRCL displacement noise can be propagated to the gravitational channel using the measured optical matrix (see sec. 5.5), since the effect of the noise subtraction technique can be neglected. The same is not true for the MICH noise, since α can give cancellation factors up to 100 in the relevant frequency band. The predicted actuation noise projection uses a theoretical factor to convert from MICH motion to dark fringe signal [73, 74]. The real transfer function can be obtained taking into account the effect of the noise subtraction or more easily with a direct measurement injecting noise directly at the level of the BS actuators. The two projections are compatible.

The level of actuation noise in the Science Run configuration is shown in fig. 7.7. The total is about a factor 2 below the detector sensitivity between 10 and 80 Hz. This plot also shows an estimation of the noise due to *eddy currents* induced in the metallic reference mass [75]. This is an intrinsic limitation for the current payload configuration and it is indeed close to the actual sensitivity. The long term plans for Virgo+ include the replacement of the metallic reference mass with dielectric ones.

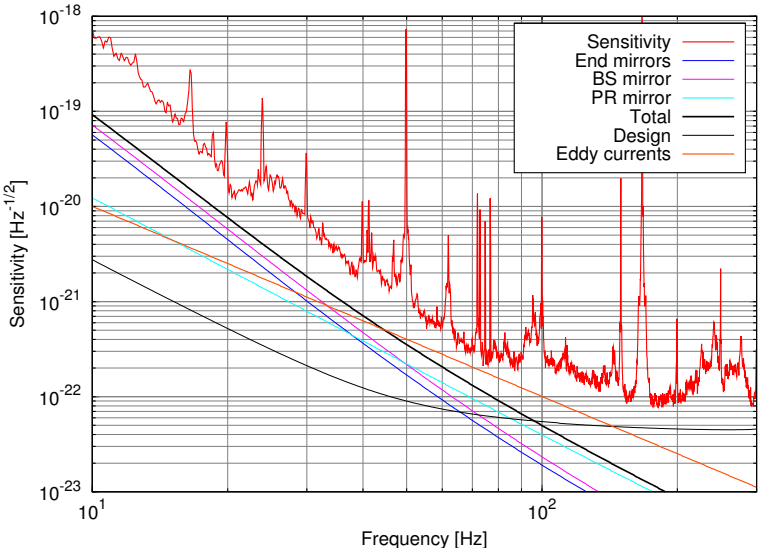

Figure 7.7: Projection of actuation noise in the gravitational wave signal. The total noise is about a factor 2 below the actual sensitivity up to roughly 80 Hz. An upper limit for the noise coming from reference mass eddy currents is also shown.

7.4 Frequency noise

Since the unitary gain frequency of the second stage of frequency stabilization is higher than the observational bandwidth, a noise budget for frequency noise must take into account the coupling of residual frequency noise to the dark fringe signal. The measure is performed by adding noise to the error signal of the SSFS and measuring the transfer function from the signal before the addition to the dark fringe. The result is shown in fig. 7.8. This transfer function does not give directly the optical coupling between the SSFS error signal and the dark fringe, since it is necessary to correct for the effect of the DARM loop which reduces the effect of frequency noise like any external disturbance. If a constant transfer function is considered as the real coupling of frequency noise between the two signals, the effect of the DARM loop can be easily computed using the open loop transfer function described in sec. 5.2. The result is shown in fig. 7.8. The agreement with the measurement is very good above about 30 Hz. Below this frequency the measured transfer function shows some un-expected sharp features, which are likely the effect of cross-coupling with some other longitudinal control loops.

In any case, using the modeled transfer function, the residual noise in the error signal can be projected in the dark fringe. The result is shown in fig. 7.9. The contribution of frequency noise to the detector noise is negligible for almost

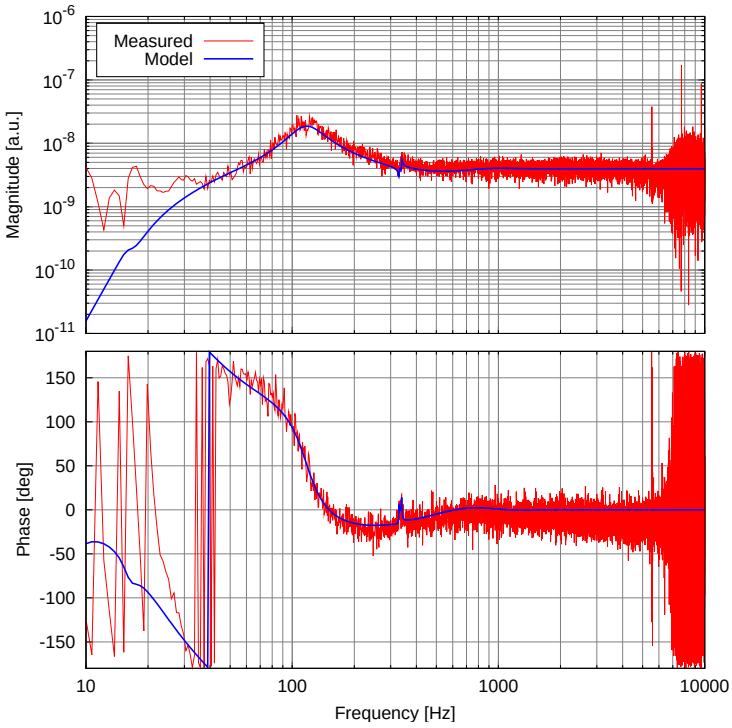

Figure 7.8: Measured transfer function for frequency noise, from the error signal of the second stage of frequency stabilization to the dark fringe demodulated signal. The measurement agrees very well with the expected model (refer to the text for details).

all frequencies, excluding a narrow region between 5800 and 5950 Hz, where it is the limiting source of noise.

The level of frequency noise has been strongly decreased by the modification in the control of the suspended injection bench piezo-electric actuators. In particular, the noise bump at about 6 kHz has completely disappeared.

7.5 Angular control noise

As explained in chapter 4 all angular degrees of freedom of the interferometer are controlled by using global servo systems, most of them with a bandwidth of the order of 3 Hz. The control noise coming from these global loops can be estimated using an automatic procedure similar to that implemented for the longitudinal degrees of freedom. The angular control of the two input mirrors and of the θ_y degree of freedom of the beam splitter are controlled using only local controls. Since the error signals for these loops are local, a coherence

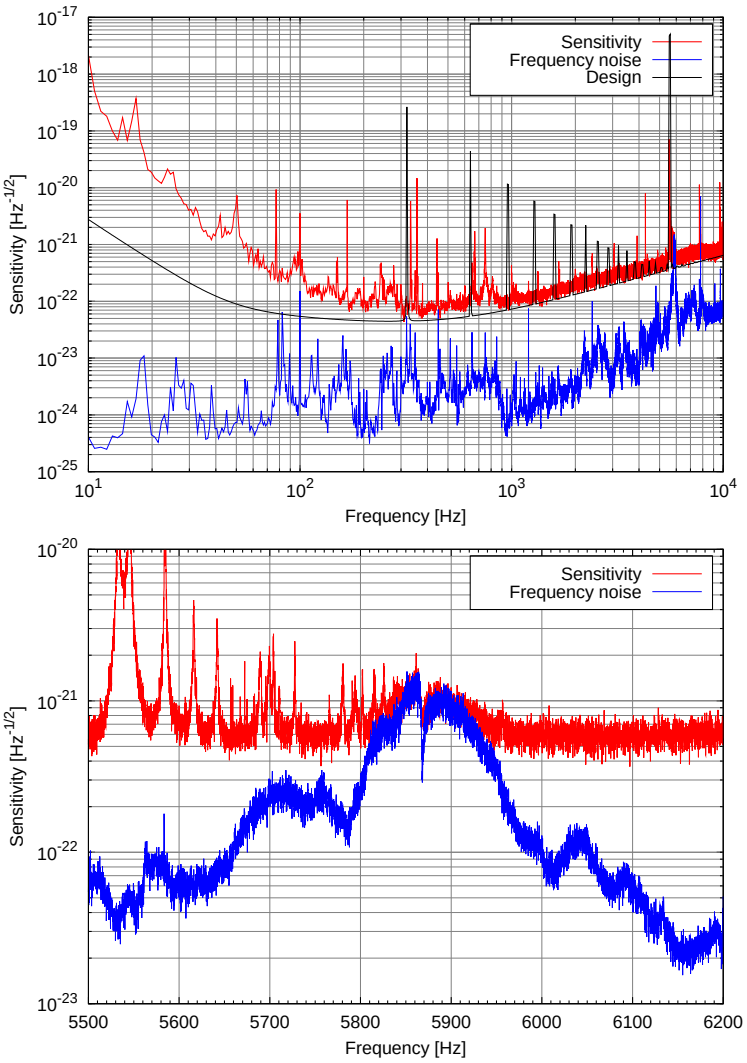

Figure 7.9: Projection of the residual frequency noise into the gravitational channel signal, during VSR1. The bottom plot is a zoom around a narrow region where this noise is actually limiting the sensitivity.

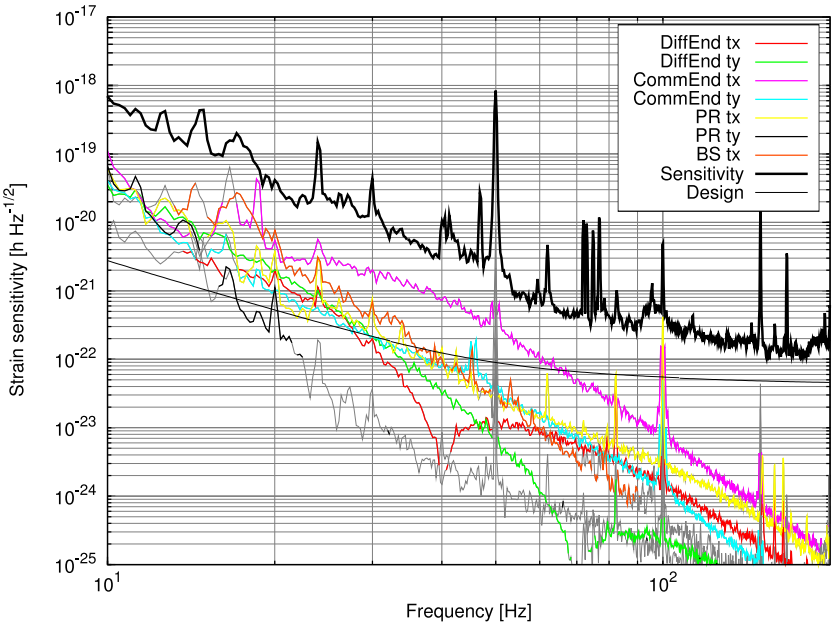

Figure 7.10: Projection of angular noise in the dark fringe signal, calibrated in units of strain sensitivity, measured during VSR1. The color of the lines is grey when the measurement of the corresponding transfer function showed low value of coherence, meaning that the projection is not meaningful. The thick black line is the measured sensitivity of the detector while the thin black one is the design. This angular noise budget includes only those degrees of freedom controlled in automatic alignment configuration.

analysis is enough to see if they are contributing to the dark fringe noise. This is not the case. It might be anyhow interesting to add them to the noise budget, but this has not been done yet.

The noise budget for the global angular control system, measured in the VSR1 configuration, is shown in fig. 7.10. The end mirror common mode θ_x control is one of the two dominant sources of noise in a small region between 30 and 40 Hz. Excluding this d.o.f., all other noise contributions are even below the design sensitivity above 30-40 Hz. At lower frequencies they are one of the sources that concur to give the measured noise, even if not the dominant one.

7.6 Other sources of control noises

There are many other control loops working during the normal detector operation of the Virgo interferometer, and most of them do not affect the sensitivity with control noise. The most critical ones are perhaps those linked with the

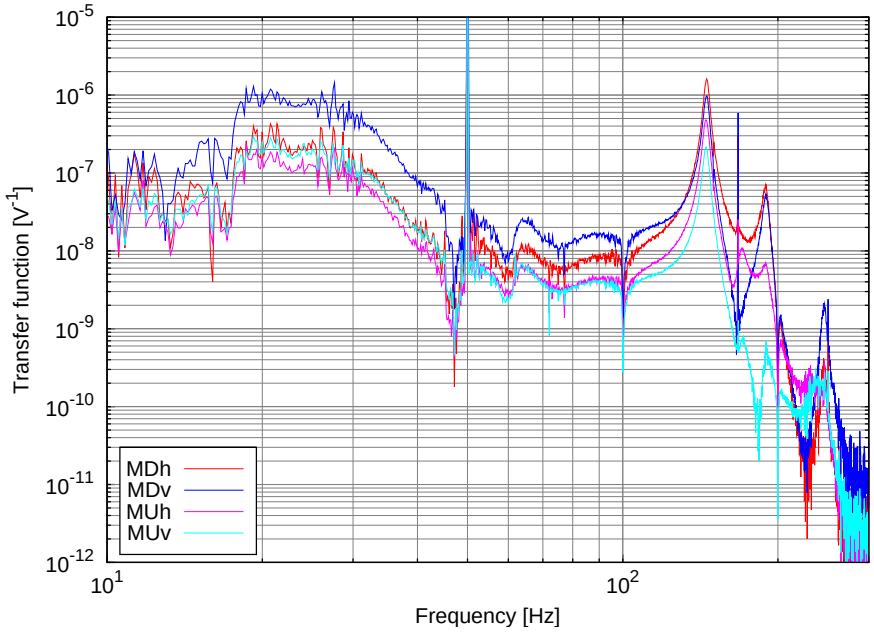

Figure 7.11: Transfer functions from the four BMS correction signals to the dark fringe. Several resonant structures are visible above 100 Hz.

injection system, mainly with the angular and length control of the input mode cleaner. These are mainly relevant if the modulation frequency is not well tuned with respect to the IMC length, as explained in sec. B. However, even by artificially increasing the noise in the loops more then a factor 10 no effect was visible in the dark fringe signal. Therefore it is safe to conclude that these loops are not relevant.

There are at least other two sources of control noise that has proved to be relevant. The first is the Beam Monitoring System (see sec. 2.2) which can generate input beam jitter than couples with the dark fringe signal [76]. The second source is linked with the local controls of the suspended detection bench.

7.6.1 Beam Monitoring System

The BMS system (see sec. 2.2) uses two quadrant photo-diodes places on the external injection bench to extract error signals for stabilizing the position of the beam before the IMC. The four error signals (two quadrants, both vertical and horizontal signals) are combined together with a reconstruction matrix to control two mirrors mounted on piezo-electric actuators.

The projection of BMS control noise into the dark fringe signal has been performed adding noise between roughly 20 and 300 Hz to each of the four

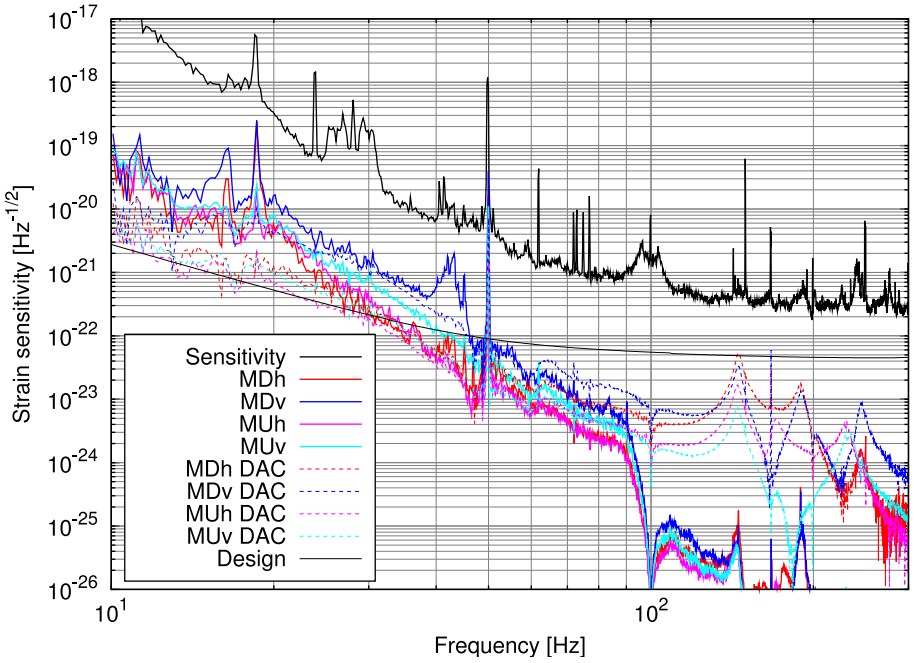

Figure 7.12: Projection of the BMS correction signals in the detector sensitivity. The dotted lines represent the projection of the DAC noise.

correction signals and measuring the transfer functions to the dark fringe. The results of this measurements are shown in fig. 7.11. Above 100 Hz all transfer functions show several structures, which are related to internal resonances of the mirror mounts and of the actuators: they are mainly at 145 Hz, 170 Hz, 190 Hz, 230 Hz and 245 Hz.

Using these transfer functions it is possible to compute the projection of the four correction signals in the detector sensitivity (see fig. 7.12). However it is necessary to take into account DAC noise, which turns out to be much higher than the requested correction signal above 100 Hz (the DAC noise is dotted in fig. 7.12). However even considering the DAC noise, it might seem that the BMS contribution is completely negligible.

However, projecting the correction signal it is not possible to correctly recover the contribution of any source of actuation noise that comes after the read-out of the correction. For the BMS system this means not counting any additional motion of the beam steering mirrors: for example noise introduced by the piezo-actuators themselves or seismic noise that can excite directly the resonant modes of the mirror mounts. The only way to take into account the contribution from these sources of noise is to compute the projections using the error signals as starting point. The transfer functions from error signals to dark

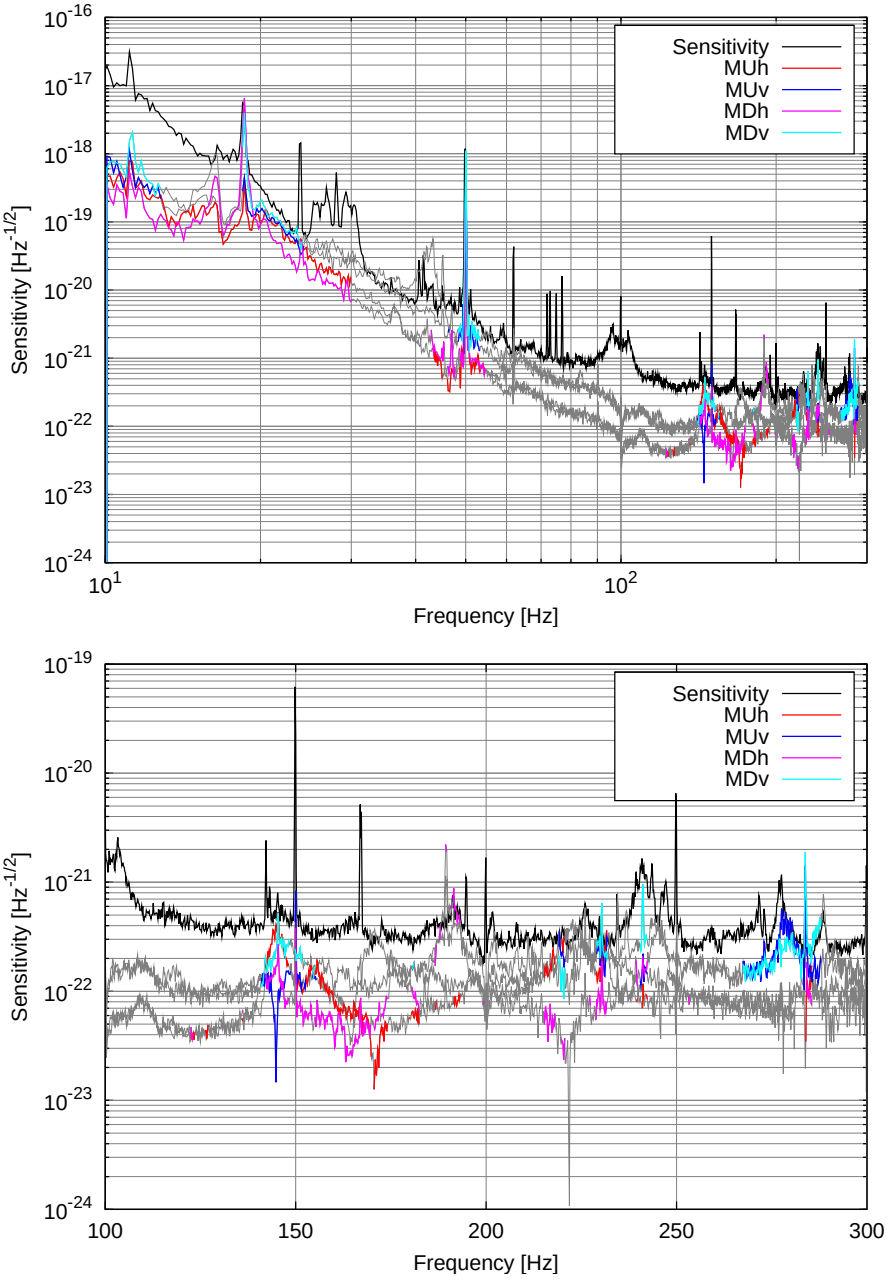

Figure 7.13: Projection of the BMS error signals in the detector sensitivity. The lines are grey where the signals are dominated by sensing noise. At those frequencies the projections are not meaningful. The bottom plot is a zoom at higher frequencies.

fringe can be easily computed knowing the one already measured and the matrix used to reconstruct the corrections. These projections are however valid only at frequencies where the error signals are not dominated by sensing noise. Its level can be easily measured when there is no light impinging on the photo-detectors and assuming that the level of this *dark noise* does not change with the amount of light hitting the detector. For the quadrant photo-detectors used for the BMS system unfortunately the dark noise is almost dominant above few tens of Hz. Only some small frequency regions, corresponding to the mounts resonances, show a signal significantly higher than the dark noise.

The result of projecting the BMS error signals is shown in fig. 7.13. Where the lines are grey the error signals are dominated by sensing noise, and therefore the projections are not meaningful. However there are some frequency regions, around the BMS mount resonances, that are meaningful: in these regions the beam jitter introduced by the BMS system is very close to the sensitivity. This is consistent with a coherence analysis: the BMS error signals are coherent with the dark fringe around the resonant frequencies. Moreover they are coherent with seismic and acoustic sensors on the optical benches, proving that the origin of this noise is likely seismic motions of the mirror mounts. A further proof that beam jitter noise coming from the BMS system is limiting the sensitivity comes from the analysis of fast non-stationarities or *glitches* (see chap. 9): around the resonance frequencies of the mounts, several glitches are found in coincidence with ones in the BMS error signals.

In conclusion, even if a complete noise projection for these degrees of freedom is not possible because the error signals are dominated by sensing noise, there are strong indications that beam jitter into the input mode cleaner is contributing to the dark fringe noise in the region between 100 and 300 Hz.

7.6.2 Suspended Detection Bench

The position of all suspended benches must be controlled, at least at low frequency, to maintain their correct orientation. The local control loops implemented for the suspended detection bench have a unitary gain frequency of about 1 Hz, therefore any correction sent to the coil actuators above this frequency can introduce spurious motions of the bench. These couple to the dark fringe signal in a complex and not completely understood way: the main candidate is some form of clipping of the main beam.

The control noise coming from the output bench was indeed limiting the sensitivity in a quite wide region between 20 and 40 Hz, even if the coherence between the dark fringe signal and bench correction was quite poor, since as expected the coupling of such noise can be strongly modulated in amplitude and phase.

After the suspicion of noise coming from the bench controls arose, improve-

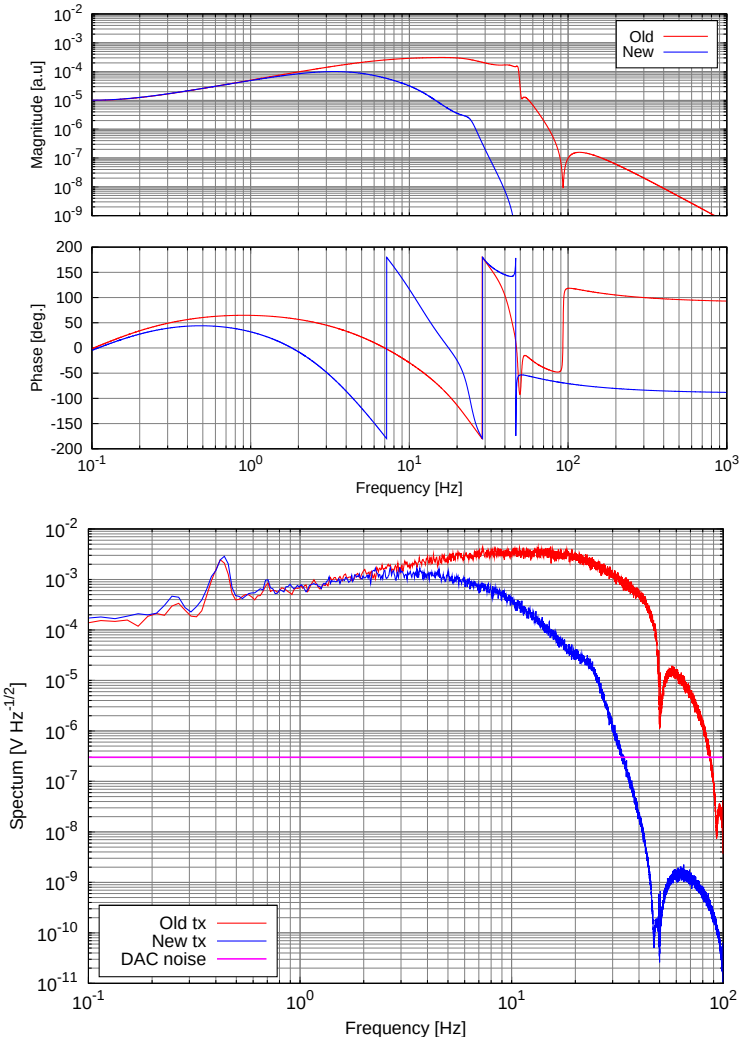

Figure 7.14: Improvements in the suspended detection bench controls. The top plot shows a comparison between the two corrector filters, while the bottom one shows the corresponding reduction in the correction signal. These plots refers to the θ_x degree of freedom. The results for the others are similar. The pink line shows the level of DAC noise.

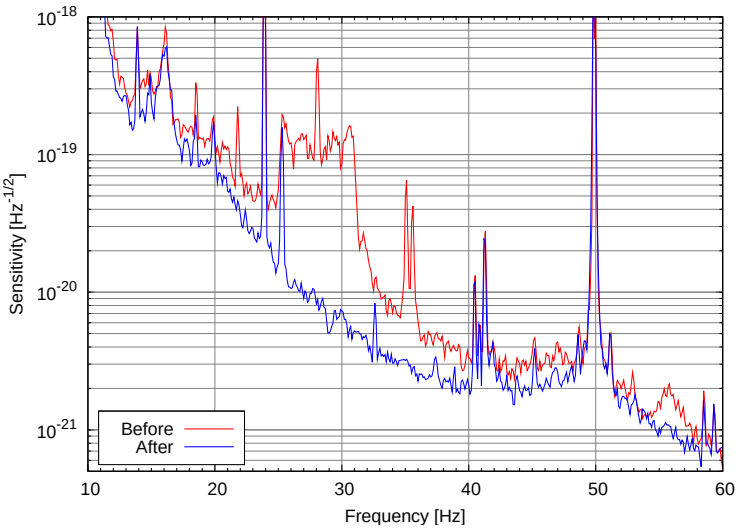

Figure 7.15: Improvements in the detector sensitivity after the implementation of the improved control filters for the suspended detection bench.

ments were introduced implementing more efficient control filters, capable of maintaining the same accuracy in the bench control while reducing the correction above 10 Hz by at least a factor 10 (see fig. 7.14). The computed correction actually falls below DAC noise above about 30 Hz.

The effect on the detector sensitivity is quite impressive and it is shown in fig. 7.15. The most striking structure that has disappeared is a quite big line at 28 Hz with several sidebands around it. This is a further proof that the noise coupling was strongly modulated. From the result it is clear that the bench control was a quite strong limiting source of noise in the entire region between 20 and 50 Hz.

7.7 Laser intensity noise

Fluctuations of the input laser intensity have a component at the modulation frequency which is not stabilized by any control system, but the intrinsic relative intensity noise of the free laser at 6 MHz is of the order of

$$\frac{\delta P_{6\ MHz}}{P} < 9 \cdot 10^{-9}\ \mathrm{Hz}^{-1/2} \tag{7.6}$$

and this does not give a relevant contribution to the dark fringe noise [73].

The component at low frequency of the laser intensity noise, inside the detector observational bandwidth, is much higher for the free laser and therefore it is stabilized using the *power stabilization loop* described in sec. 2.2. This

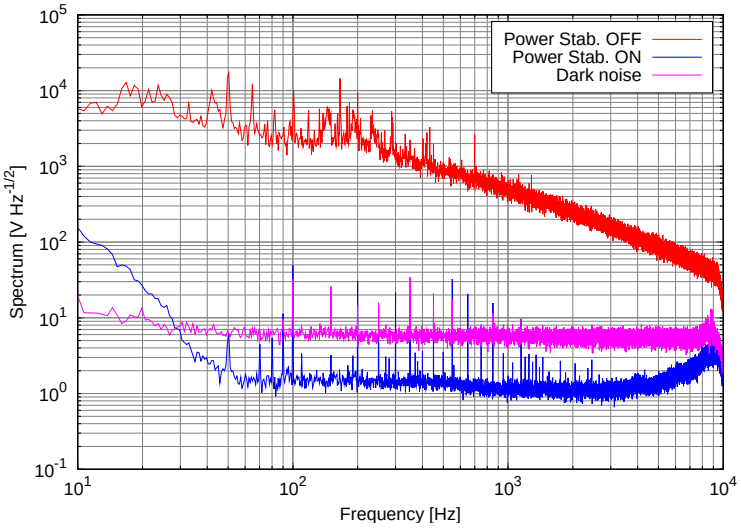

Figure 7.16: Plot of the power stabilization error signal in three different conditions: when the loop is on, when it is off, and when no light is reaching the photo-detector. This last curve shows the *dark noise* of the detector.

intensity noise can couple to static or RMS fluctuations of the DARM degree of freedom around the operating point. The simplest possible model gives [73]:

$$S_h \simeq \frac{RMS_{DARM}}{L} \frac{S_{\delta P}}{P} \tag{7.7}$$

where L is the mean arm length, P the dark fringe power, RMS_{DARM} gives the RMS fluctuations of the dark fringe signal expressed in terms of equivalent DARM noise and $\mathcal{S}_{\delta P}$ is the laser intensity noise spectrum. The contribution coming from the input laser power fluctuations can be estimated substituting in the above equation the dark fringe power with the input one (fig. 7.17).

So far no complete measurement of the real transfer function from power noise to the dark fringe has been performed, mainly due to the lack of a good out of loop sensor measuring the residual intensity noise when the high frequency power stabilization loop is engaged. Indeed, as shown in fig. 7.16, the very high gain of the loop reduces the noise in the error signal below the level of dark noise. For this reason it can not be used reliably to perform a noise projection. However, a simple upper limit to the contribution of power noise can be obtained by comparing the dark fringe spectrum when the stabilization is on and off. The increase of noise in the sensitivity is almost null: only between 300 Hz and some kHz there is an increase of the order of 10%. Therefore an upper limit can be set by lowering the dark fringe spectrum by an amount given by the ratio of the power stabilization error signal when the loop is on and off. The results is shown in fig. 7.17, when both the dark noise and the spectrum of the signal in

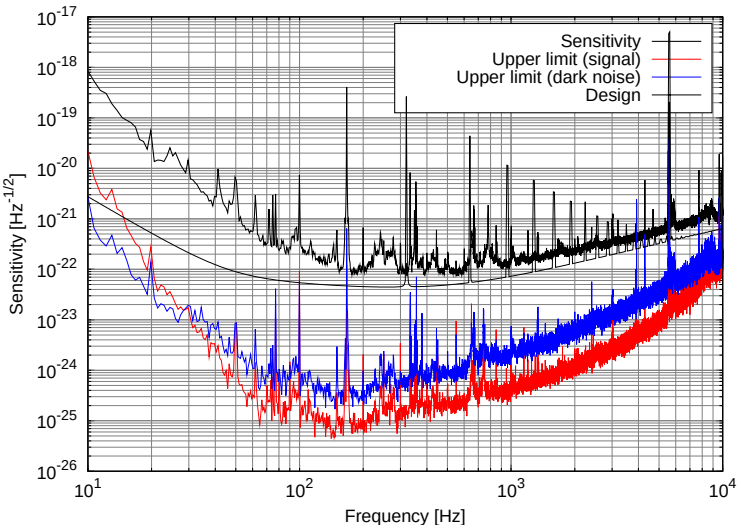

Figure 7.17: Upper-limit to the contribution of laser intensity noise to the sensitivity. The two curves uses the spectrum of the power stabilization error signal with the loop closed and its dark noise to obtain the estimate.

normal condition are used. This shows that the residual laser intensity noise is almost everywhere a safe factor below the actual and design sensitivities.

7.8 Oscillator phase noise

If the reference oscillator that generate the 6 MHz signal used for the demodulation process has a small amount of phase jitter, the in-phase demodulated signal of the dark fringe can be contaminated by a small contribution from the quadrature one. This can be estimated as [73]:

$$S_s \simeq \delta\varphi \cdot \mathrm{ACq} \cdot \mathrm{TF}_{df \to h} \tag{7.8}$$

where $\delta\varphi$ is the spectral density of phase noise, ACq is the RMS power in the quadrature signal and $TF_{df \to h}$ is the calibration transfer function, that converts the dark fringe signal to the gravitational wave strain. The level of phase noise of the signal generator used presently in Virgo has been estimated to be about $0.15\mu\mathrm{rad}/\sqrt{Hz}$, using data from a period when big fluctuations of the quadrature signal were present. In this way a linear relation between the level of high frequency noise and the value of the dark-fringe quadrature signal has been found.

This gives the estimation of contribution of phase noise to the sensitivity shown in fig. 7.18. The projection is safely below the actual sensitivity and in

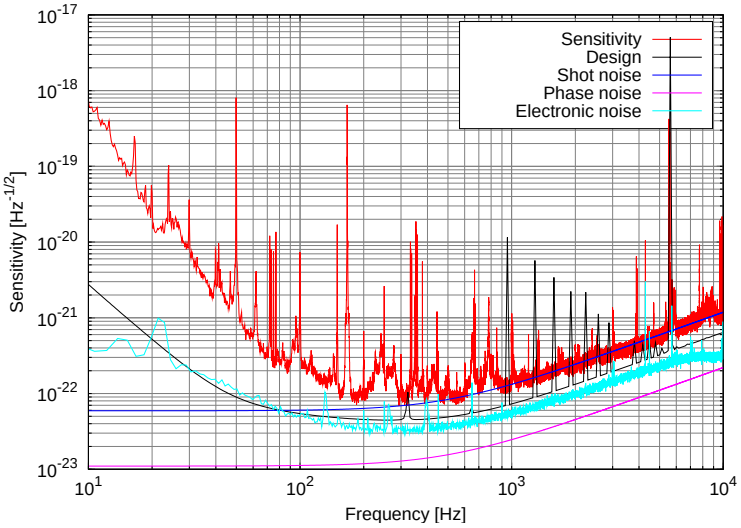

Figure 7.18: Summary of noises relevant at high frequencies: shot noise, oscillator phase noise and dark fringe photo-detector electronic noise.

any case no indication of phase noise contamination of the dark fringe signal has been found so far. For this reason there has not been strong efforts in the direction of a full measurement of the coupling of phase noise.

7.9 Electronic noise

The name *electronic noise* usually indicates all the noises introduced by the photo-diode itself and by the entire read-out chain. Therefore it can include dark noise of the photo-diode, additional noise introduced by the read-out and demodulation board and finally also ADC noise. The sum of all these noises are easily estimated by measuring the output signal during a period when there is no light impinging on the detector. The implicit assumption is that this noise does not change significantly when there is light.

The most relevant electronic noise is that coming from the dark fringe diode itself. It was measured, with no light impinging on the diode, to be $4 \cdot 10^{-11} WHz^{-1/2}$. The corresponding contribution to the strain sensitivity, shown in fig. 7.18, is well below the actual detector sensitivity. Contribution from other photo-diodes can enter through longitudinal and alignment loops. They are therefore already taken into account by the corresponding noise budgets and in any case they are negligible.

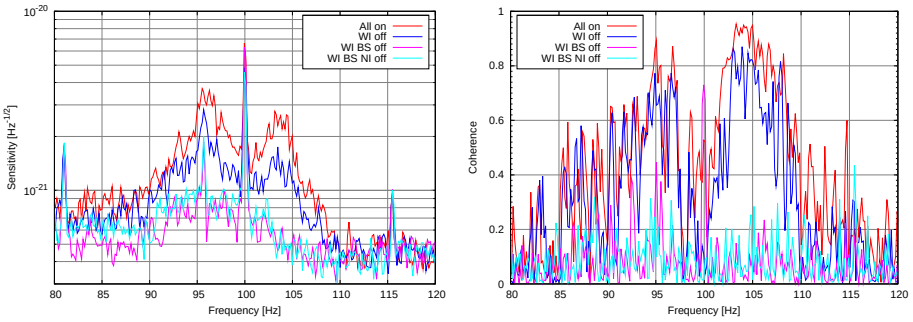

Figure 7.19: Example of noise of electro-magnetic origin. The field was generated by simple power supplies used for the local control illuminators. The two plots show the effect of switching them off on the sensitivity (left) and on the coherence between dark fringe signal and a magnetic probe (right).

7.10 Shot noise

The actual limitation at high frequency is shot noise. Assuming that the power reaching the dark fringe is dominated by the contribution of the sidebands, the shot noise level can be estimated as a function of the power measured on the B1 diode [73, 74, 77]:

$$S_h = \mathrm{TF}_{df \to h} \cdot \left(\sqrt{\frac{3}{2}} \sqrt{2} \sqrt{2 h_P \nu P_{B1}} \right) \tag{7.9}$$

where $TF_{df \to h}$ is the calibration transfer function and P_{B1} is the power impinging on the dark fringe photo-diode. This gives the result shown in fig. 7.18, which explains well the floor noise level above some kHz.

7.11 Environmental noise

7.11.1 Electro-magnetic noise

The electromagnetic fields generated by electrical and electronic components can couple to the main detector output through some electro-magnetic pick-up in the read-out or actuation electronic, or through direct coupling to the magnets used for the mirror control. This kind of noise is very difficult to find and debug, since the electro-magnetic field can change significantly in space and it is usually very difficult to find any coherence between the dark fringe signal and magnetic probes. Even if a coherence is found, therefore indicating that the source of the noise is electro-magnetic, it is usually difficult to identify the origin of the disturbance and to cure it.

An example of noise coming from fields irradiated by electronic devices is shown in fig. 7.19. The source was tracked down to power supply boxes used for the local control illuminators. These boxes were placed close to each tower, just outside the vacuum tanks. A first experiment was performed by switching off the boxes one by one. As clearly visible in fig. 7.19 the largest noises came from the power supplies placed inside west input and beam splitter ovens.

This noise coupled directly with the magnets used for the mirror control. This high coupling is explained by the fact that for the two input mirrors and for the beam splitter these coils have been attached with the wrong relative polarity: therefore the total magnetic dipole momentum is significantly different from zero.

This source of electro-magnetic noise was finally strongly reduced by displacing of several meters the power supplies from the towers.

7.11.2 Acoustic noise

Even if all the mirrors and the main optics of the detector are suspended to seismic attenuators and placed in vacuum, all injection and detection components are mounted on benches in air and sitting on the ground. Seismic motions of the benches and of the components mounted on them can introduce noise into the dark fringe. To distinguish from the seismic motion of the mirrors, which is completely filtered by the super-attenuators (see sec. 2.4), this noise is usually called *acoustic noise*, since it is important mainly in the acoustic range of frequencies (between some Hz and some thousands Hz) and because one of the main origin is real acoustic noise close to the benches.

A mirror or a lens mounted on an optical bench can vibrate and introduce a phase modulation on the beam reflected or transmitted. For a moving mirror the effect can be described in terms of the reflected electric field:

$$E_R(t) = e^{2ikx(t)} = e^{4\pi i \frac{x(t)}{\lambda}}$$

where $x(t)$ is the mirror displacement with respect to a fixed reference, as a function of time. Its spectral component are usually concentrated in the acoustic region. The depth of the phase modulation depends on the amplitude of the mirror motion. If the amplitude of $x(t)$ is much smaller than the laser wavelength, the exponent in eq. 7.11.2 is small and the effect is roughly linear. The noise introduced in the detector output will resemble the spectral structures of the mirror motion which usually is larger in correspondence of mechanical resonances of the mount or of the optical bench. On the other hand, if the amplitude of the motion is larger than one wave-length, the non-linear nature of eq. 7.11.2 is dominant and the detector noise spectrum can be very different from the one of the optics motion.

The modulation depends also on the laser frequency. This means that carrier and sidebands will be affected in a different way:

$$\begin{aligned} E_{CAR}^{REF} &= e^{2i\frac{\omega}{c}t}E_{CAR} \\ E_{SB}^{REF} &= e^{2i\frac{\omega}{c}t}e^{\pm 2i\frac{\Omega}{c}t}E_{CAR} \end{aligned}$$

The common term between the three fields is not relevant for the main interferometric beams: it cancels out in any power or demodulated signal measured by a photo-detector, since they depends on the produxct of the field with its complex conjugate (see for example eq. A.2). The additional dephasing of the sidebands affects instead all demodulated signals. Assuming a mirror motion of the order of one wave-length for reference, the dephasing has an amplitude of the order of 10^{-8} radians. The effect on the demodulated signal can be estimated from eq. A.3 for example:

$$AC_P(t) \sim \cos\left(\frac{2\Omega}{c}x(t)\right) AC_p^0(t) \sim \left(1 - \mathcal{O}(10^{-16})\right) AC_p^0(t)$$

where AC_P^0 is the signal that would be there without the effect of the moving optics. This contribution is usually neglegible.

The common de-phasing becomes important if the reflected beam is a spurious one which might enter again the interferometer with a superposition of Gaussian modes that may have large low order components. These can resonate and be transmitted to the dark port with some small amplitude and a phase carrying information about the mirror motion:

$$E_{DF} = E_0(t) + \varepsilon e^{i\phi(t)}E_1(t)$$

being E_0 the main field amplitude and E_1 the one of the original beam before scattering. This additional component will add spurious noise to the detector output. A typical example of this situation comes from the arm cavity end benches: if the transmitted beam hits a lens perpendicular to it, part of the beam is scattered back inside the cavity, with exactly the geometry of the resonant mode.

Of course the amount of noise reintroduced by these mechanisms depends directly on how much the optical elements move. The origin of these motions can be tracked down to essentially two categories: seismic motion of the ground, both of natural and human origin or acoustic noise that directly excites lenses and mirrors. In both cases it is possible to reduce the motion having better seismic and acoustic isolation of the benches or making the mounts more rigid. In particular it is important to avoid that an optical element has a resonance below 1-2 kHz since this might enhance the motion at that frequency.

Analysis techniques

Noise from diffused and scattered light is very difficult to identify by means of coherence analysis with acoustic and seismic sensors. The main reason is the highly non-stationary and non-linear coupling. Moreover, the real motion of the scattering element might be very different from what is recorded by seismometers and microphones, unless they are placed exactly on top of it. In the worse case one can imagine for example to have the seismic sensor placed on a node and the optical element on a maximum of the resonance pattern of a bench: therefore the element can move with a large amplitude and the sensor will not be able to detect it.

The simplest, and often the only, way to study the coupling of acoustic noise is to increase as much as possible the environmental disturbances and look at the effect on the dark fringe signal. One possibility is to use loudspeakers to "inject" acoustic noise at different places. This method has usually been very effective in exciting almost all optical components. However it is intrinsically not selective: it is not possible to clearly identify which is the particular object that is coupling the noise to dark fringe. Another similar method consists in using a shaker attached to the benches: in this way it is possible to excite seismically without coupling to acoustic noise. Like loudspeakers, this method is not selective. The only way to better identify the culprit between all the optical components in a bench is to perform *tapping tests* hitting directly single objects. Even if this is not a precise quantitative method, it can give useful information on which element is the most critical one.

All these techniques have been widely used in Virgo to characterize the contribution of acoustic noise and to identify the sources. Acoustic and seismic noise injections have been performed around all optical benches in air: the laser and external injection benches in the laser laboratory, the external detection bench in the detection laboratory and the two terminal benches in the end stations. Moreover there are at least two in-vacuum optical elements that can play a significant role in re-introducing seismic noise. Indeed, the injection and detection suspended benches are separated from the remaining of the vacuum system by means of two *Brewster windows*, namely anti-reflection coated windows placed at the Brewster angle with respect to the beam. The reason of these two separations is that the vacuum inside the detection and injection towers is not as good as the one in the main part of the interferometer. The optical elements mounted on the two suspended benches can pollute the vacuum and therefore they must be separated from the main area to avoid any contamination of the mirrors. Since these windows are attached to the vacuum tube, they can move because of the ground seismic motion. These two Brewster windows have also been excited using the shaker to measure their contribution to the dark fringe noise.

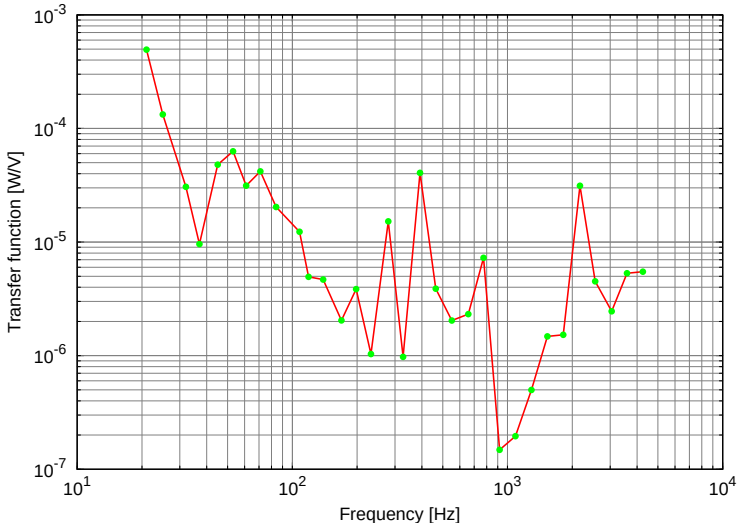

Figure 7.20: Transfer function from seismic excitation of the detection Brewster window to the dark fringe signal, measured using single lines.

In all stations acoustic and seismic lines at different frequencies have been injected, with the main goal of understanding the non-linear properties of the couplings:

- The coupling of acoustic and seismic noise depends strongly on the line frequency (see fig. 7.20). The coupling coefficient of a line can change of orders of magnitude with relatively small (tens of Hz) shifts in frequency. This is expected since the coupling passes mainly through the excitation of mirrors mounts and optical components resonances, which can be quite narrow.

- Even using a very strong line, only the linear coupling term is important: effects in the dark fringe signal are visible only around the line frequency and not at multiples of it.

- The coupling is strongly non-stationary on quite fast time-scales, up to tens of Hz. This is clearly seen in the dark fringe signal: the effect of a single line is not limited to the line frequency, but instead it is spread on a bump, composed of strong sidebands around the central frequency (see fig. 7.21). The width of the noise bump is strongly varying depending on where the acoustic or seismic excitation is applied and also on its frequency. This non-stationarity is not surprising when dealing with noise coming from diffused and scattered light, since the noise is modulated by the power in the beam which is diffused.

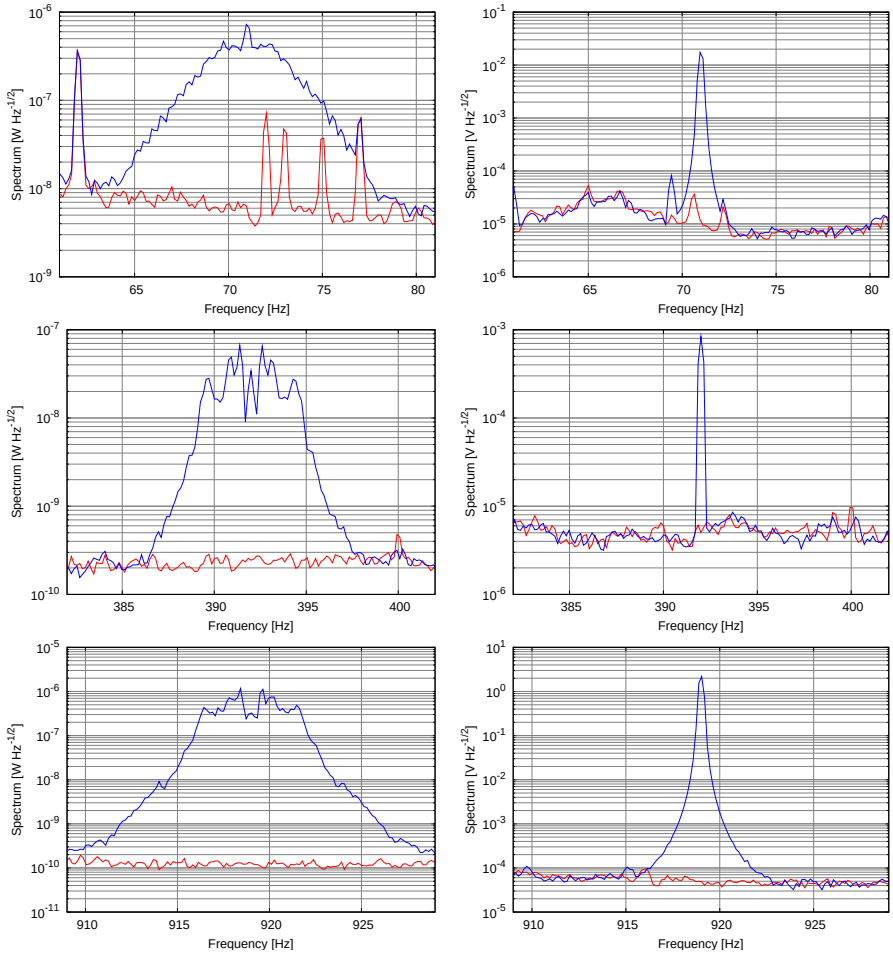

Figure 7.21: Injection of seismic lines on the detection Brewster window. The plots in the left column show the effect on the dark fringe signal, while the right column ones show the lines as detected by a seismometer. The red curves show the ambient noise with no injections.

This last point explains the difficulties in characterizing acoustic and seismic noise. The strong non-stationarity spoils the coherence between dark fringe and seismometers or microphones, even if the noise is dominant. Moreover, the environmental sensors can not usually be placed exactly on top of the source of the scattering, since it is usually not known a priori. This means that what is measured by the sensor can be quite different from the real motion of the scattering element, because of the intrinsic non-localized nature of acoustic and seismic waves. For these two reasons it turned out to be quite difficult to produce accurate projections of the contribution of this kind of noise to the gravitational signal.

Projections of the environmental noise in the two end stations and in the central area laboratories have been measured using white noise acoustic and seismic injections. Since the coherence between any environmental sensor and dark fringe is in any case poor, the transfer function have been estimated using the ratio between the power spectra of dark fringe and sensor signals. Clearly the projection should be considered meaningful only when there is a visible increase of the dark fringe noise during the measurement. It happens sometimes that the projection obtained in this was gives an estimate of the noise higher than the real one. This might indicate that the microphone or seismometer is more sensitive than the scattering element to the injected noise.

The results of this analysis for the Virgo detector are shown in plots from fig. 7.22 to 7.27. These projections refer to the situation in the period just before the start of the science run. Several interventions had already been performed: acoustic isolation enclosures were placed around the two laser laboratory optical benches, the two end ones and the external detection bench; several optical mounts were replaced with more rigid one.

In figures 7.22 and 7.23 the contribution of the acoustic noise in the two terminal optical benches is shown. After the installation of the two acoustic enclosures around the benches, the level of noise that could be injected using loudspeakers has proved to be barely sufficient to introduce visible effects in the dark fringe signal. Therefore for most frequencies only an upper limit can be computed: assuming that no effect is visible in the dark fringe when noise is injected, it is given by the actual sensitivity reduced by a factor equal to the increase of noise in the environmental sensor. For both west and north end stations, the estimated contribution from the acoustic noise is well below the actual sensitivity.

Similar noise projections for the optical benches in the detection and laser laboratories are shown in figures 7.24 and 7.25. At some frequencies, corresponding to resonances of optical mounts on the benches, there are some visible effects on the dark fringe signal. At these frequencies it is possible to compute a real noise projection, while at other ones only an upper limit can be obtained.

The contribution of acoustic noise in the laser laboratory is negligible, mainly because of the good performances of the acoustic enclosure installed around the optical benches. For what concern the detection laboratory the noise projection can be computed only for some small frequency regions, where it turns out to be quite close to the actual sensitivity: mainly around 110 Hz, between 400 and 500 Hz, around 600 Hz and 1600 Hz. For all other regions only upper limits could be computed. Not all of them are significant, because the noise injected could not dominate by a large factor the normal environmental noise.

Finally, the results of the seismic noise injections on the two Brewster windows are shown in figures 7.26 and 7.27. The contribution from the injection Brewster is well below the actual sensitivity. On the contrary, the projection of the detection Brewster seismic noise is close to the actual sensitivity in several bands between 100 and 1000 Hz: between 240 and 260 Hz, around 300 Hz, 390 Hz, 470 Hz, 500 Hz, between 580 and 780 Hz, between 1480 and 1780 Hz and between 1930 and 2200 Hz. In some of these bands the projection is higher than the actual noise. This might be caused by some of the effects already discussed before: the high non-stationarity and non-linearity of the noise coupling and the fact that the environmental sensors might not read exactly the motion of the diffusing element.

In conclusion, it is very difficult to state accurately which elements are the most relevant ones for introducing acoustic noise through diffused light. However it seems possible to conclude that at least some of the structures visible in the sensitivity between 100 and 1000 Hz are likely to be generated by diffused and scattered light, coming from the detection laboratory and neighbouring optical elements. The most likely candidates are however the Brewster window between the main vacuum and the detection tower and the tower itself.

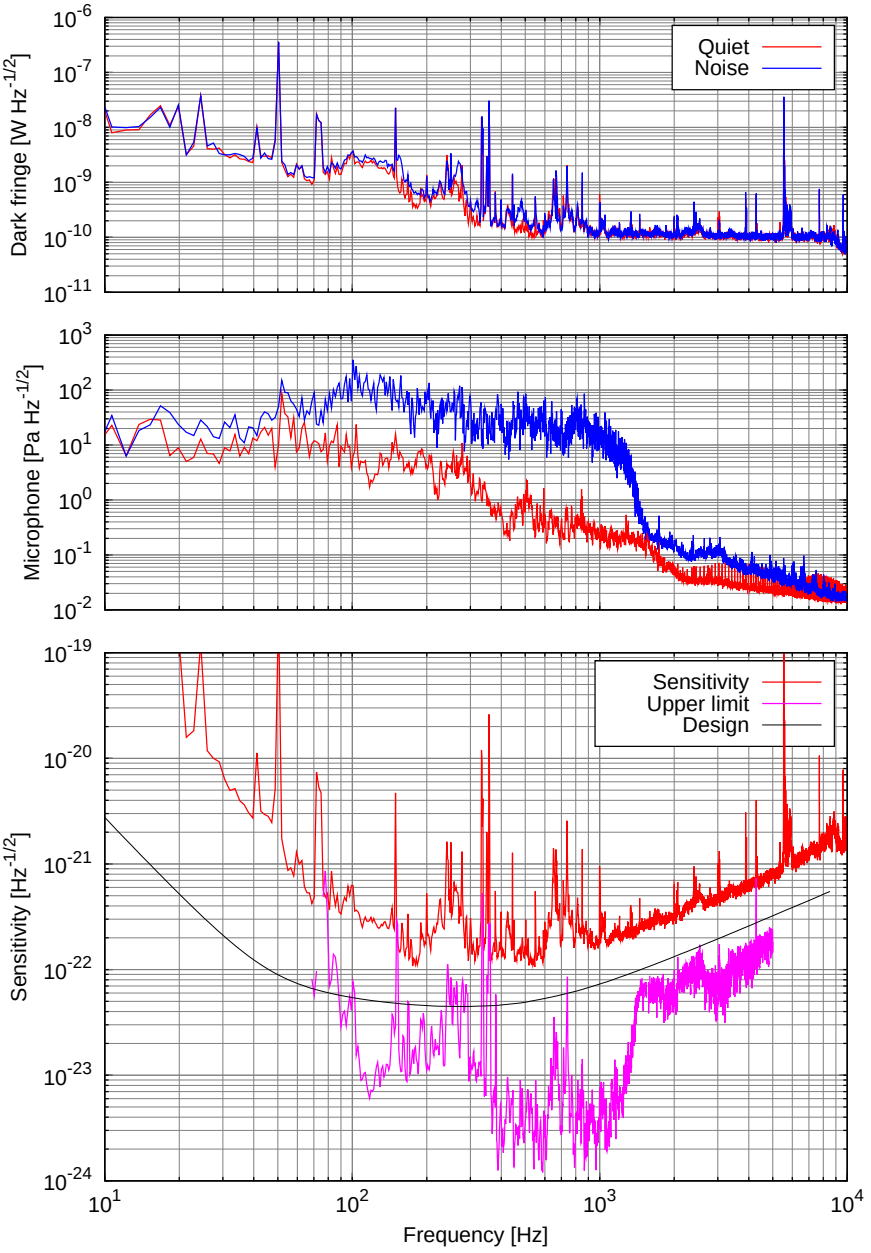

Figure 7.22: Projection of acoustic noise in the north terminal station. The two top plots compare the spectra of the dark fringe signal and of a microphone inside the north terminal optical bench in quiet condition and during the noise injections. The bottom plot shows the computed upper limit on the contribution of acoustic noise to the sensitivity.

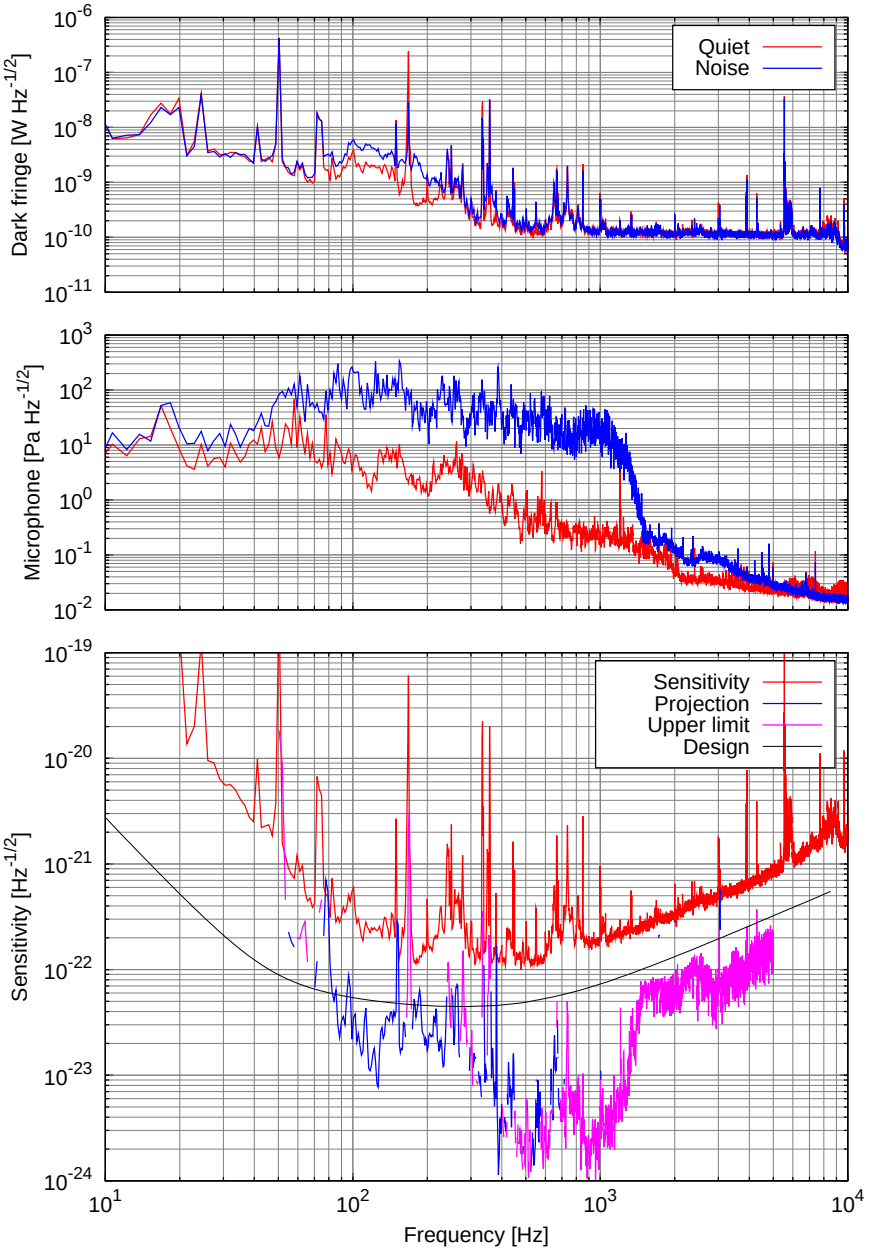

Figure 7.23: Projection of acoustic noise in the west terminal station. The two top plots compare the spectra of the dark fringe signal and of a microphone inside the west terminal optical bench in quiet condition and during the noise injections. The bottom plot shows the computed projection and upper limit on the contribution of acoustic noise to the sensitivity.

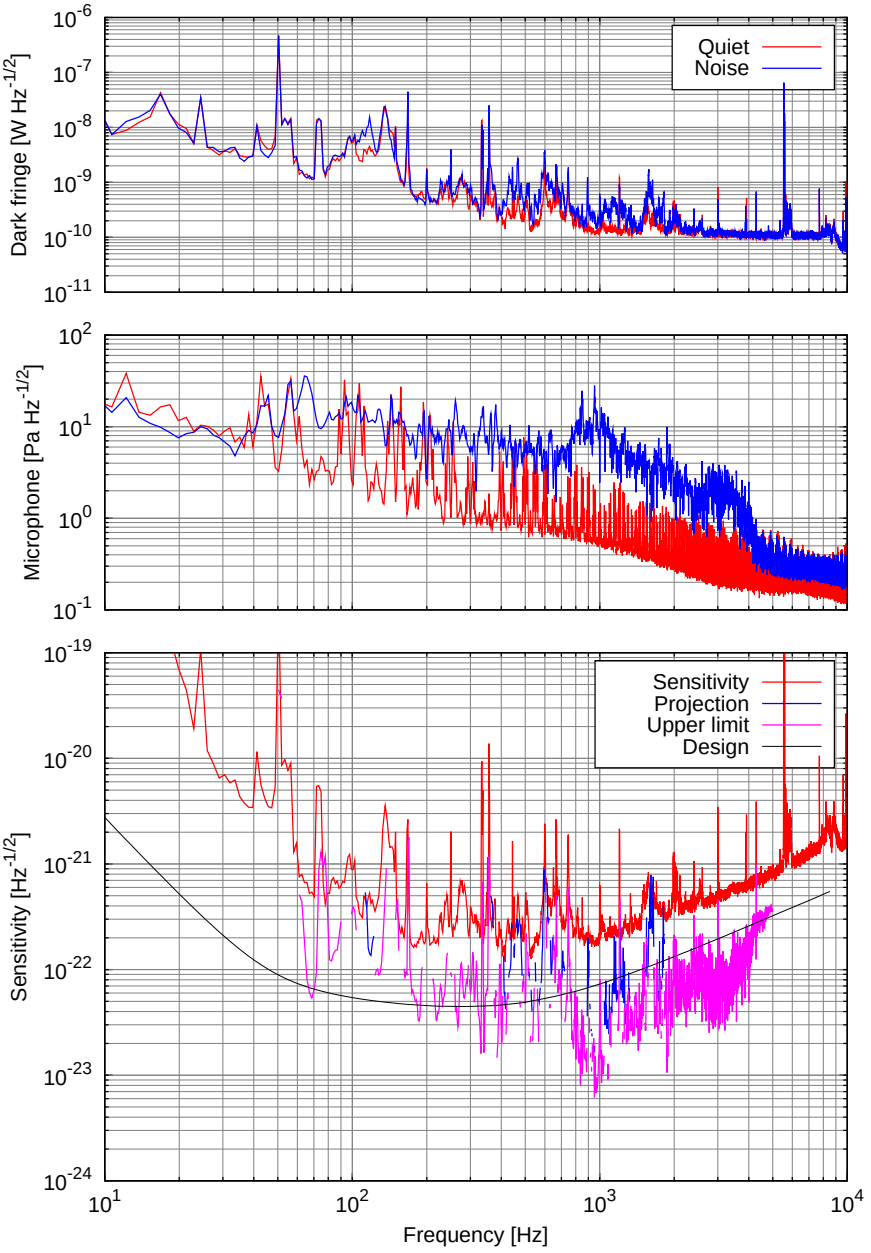

Figure 7.24: Projection of acoustic noise in the detection laboratory. The two top plots compare the spectra of the dark fringe signal and of a microphone inside the external detection bench in quiet condition and during the noise injections. The bottom plot shows the computed projection and upper limit on the contribution of acoustic noise to the sensitivity.

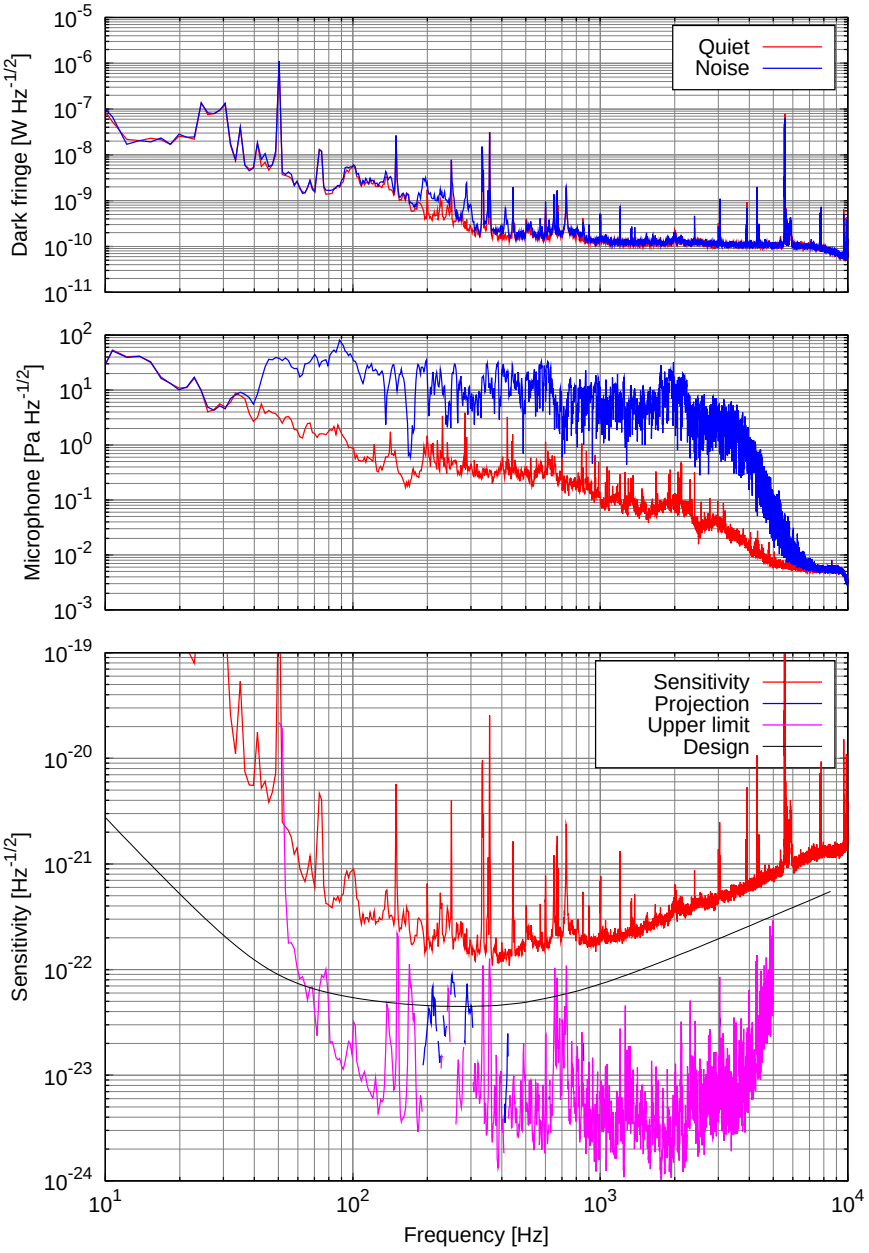

Figure 7.25: Projection of acoustic noise in the laser laboratory. The two top plots compare the spectra of the dark fringe signal and of a microphone inside the external injection bench in quiet condition and during the noise injections. The bottom plot shows the computed projection and upper limit on the contribution of acoustic noise to the sensitivity.

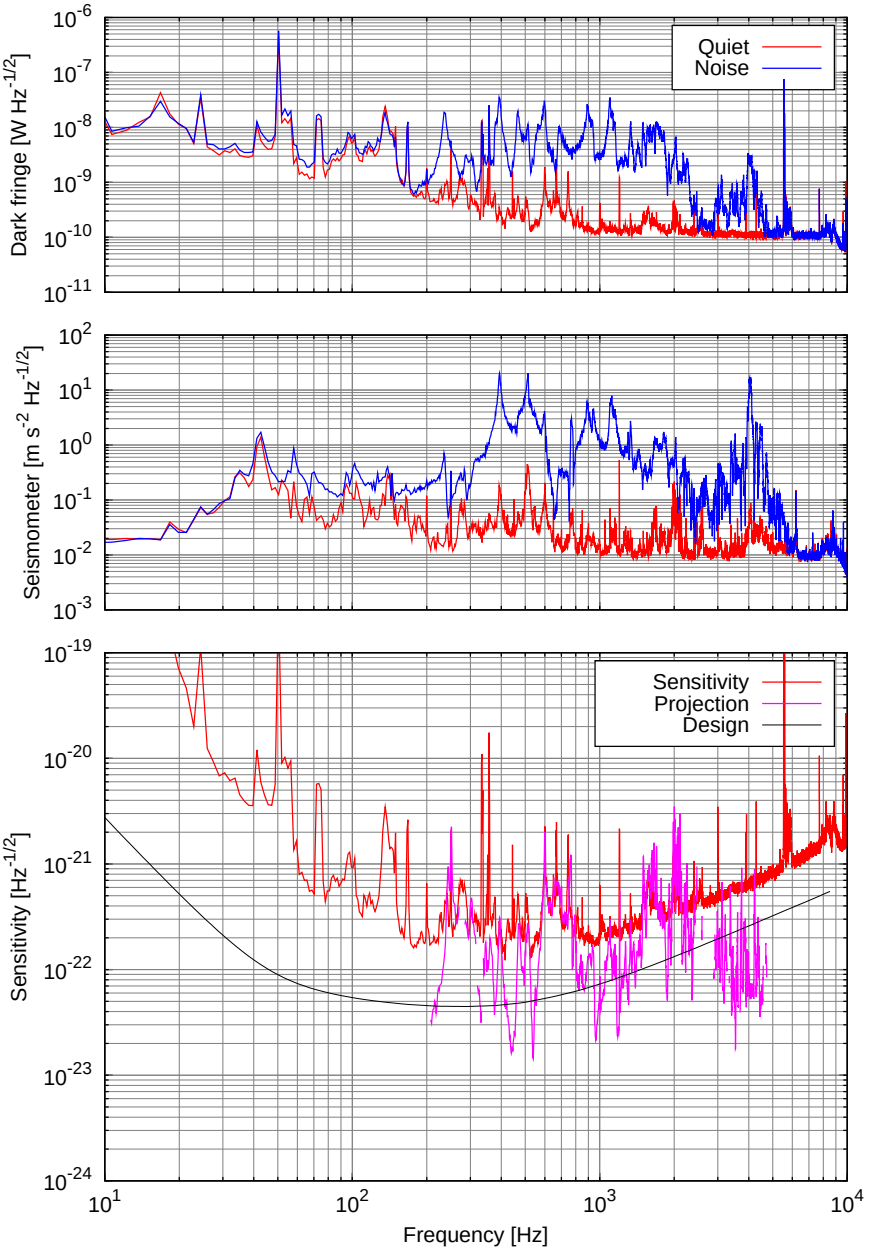

Figure 7.26: Projection of seismic noise of the detection Brewster window. The two top plots compare the spectra of the dark fringe signal and of a seismometer attached to the window in quiet condition and during the noise injections. The bottom plot shows the computed projection and upper limit on the contribution of seismic noise to the sensitivity.

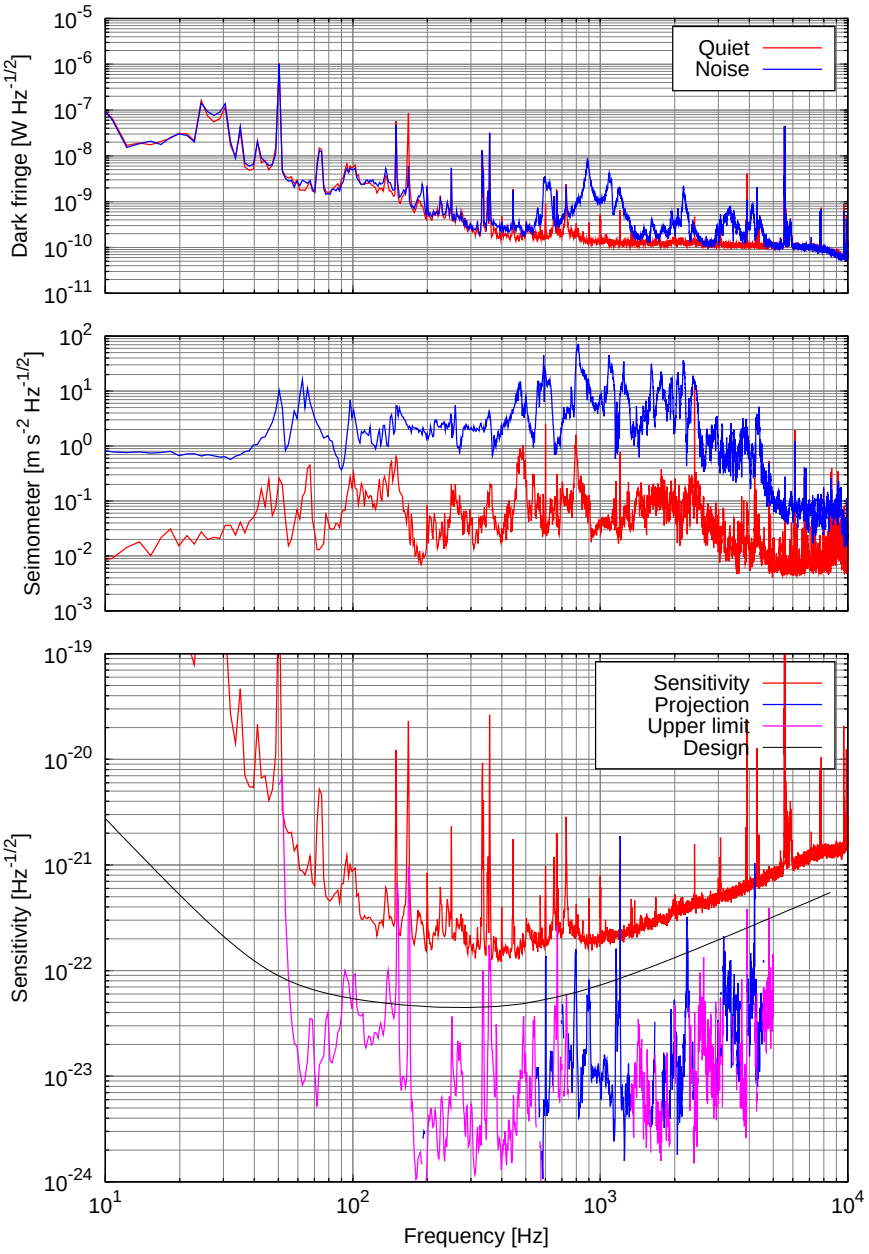

Figure 7.27: Projection of seismic noise of the injection Brewster window. The two top plots compare the spectra of the dark fringe signal and of a seismometer attached to the window in quiet condition and during the noise injections. The bottom plot shows the computed projection and upper limit on the contribution of seismic noise to the sensitivity.

7.12 Conclusions and latest development

The linear noise projection technique has proved to be very important to gain a full understanding of the noise sources limiting the detector, even if it has been deeply applied only to longitudinal and angular degrees of freedom and to laser frequency noise. There are still many sources of control noise that might profit from a similar analysis, even if they are known to be non dominant: for example suspended benches local controls, input beam jitter, laser power noise, modulation amplitude and phase noise. The automation of noise budget measurements is very important, since it provides a very powerful and simple tool to obtain quantitative indications of the improvements brought by commissioning activities.

The analysis of noise coming from diffused and scattered light has been a very active item in the months immediately before the beginning of the run, and it is likely to maintain its importance even afterward. The technique developed for the characterization of this noise and the estimation of projection on the detector sensitivity have been and will be useful, even if they are intrinsically not very precise. In any case these methods have been widely used to compare the situation before and after actions devoted to diffused light mitigation.

After the end of the scientific run the commissioning activities brought many improvements to the detector sensitivity, mainly at low frequency (fig. 7.28):

- the longitudinal sensing and control system has been strongly optimized, improving the performances of the noise subtraction techniques and improving the error signal noise. In this new configuration control noise coming from these loops is a factor 3 to 5 lower than the sensitivity;
- the angular controls have been improved also, mainly developing better corrector filters and centering better the beam on all mirrors. Also angular control noise is no more limiting the sensitivity;
- an extensive campaign of diffused light investigation and mitigation helped removing many structures up to some hundred Hz.

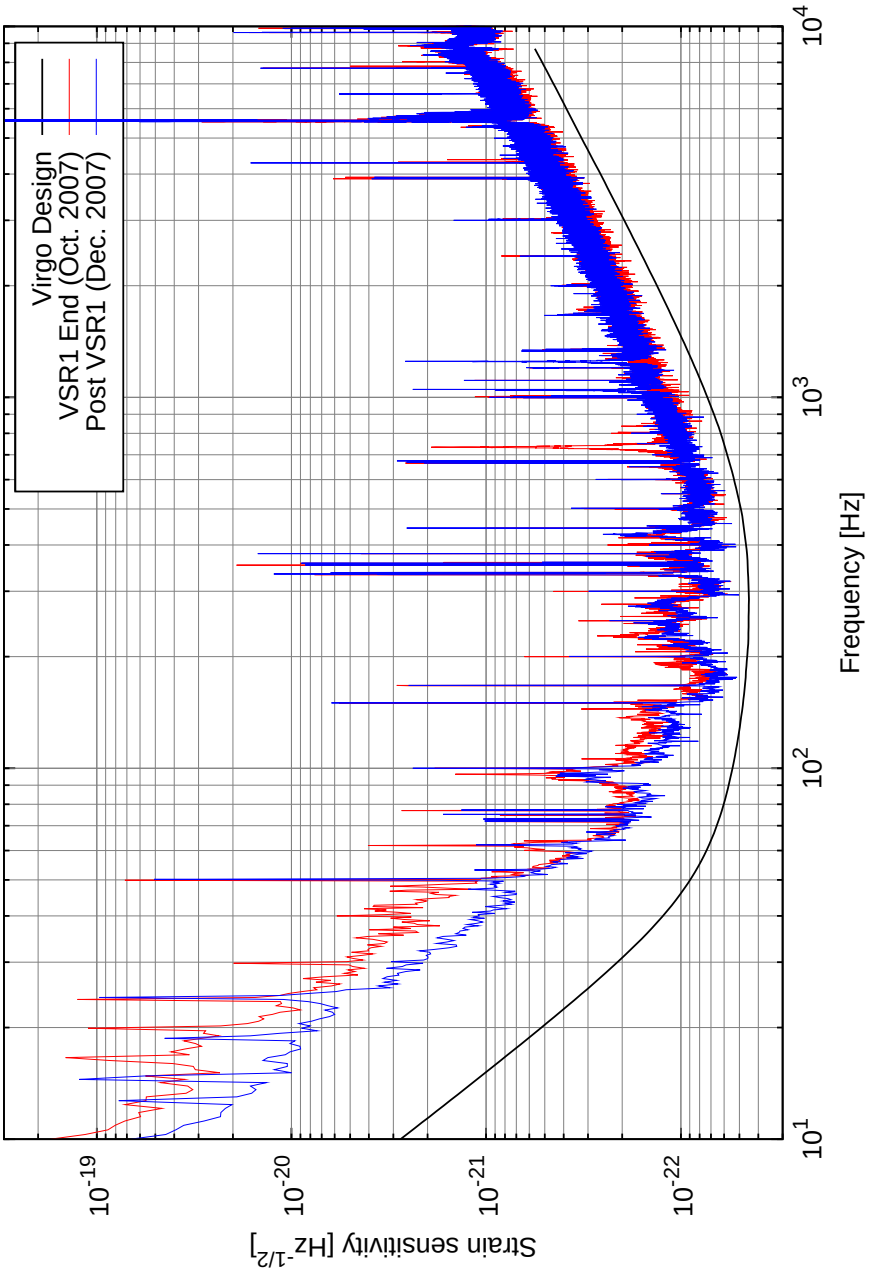

Figure 7.28: Improvements in the detector sensitivity obtained in the two months following the end of VSR1.

Chapter 8

Non-stationary noises

The level of noise in the dark fringe spectrum is not constant in time: there are normally variations over different time scales, from seconds to hours and days. The study of these variations is useful to characterize the long term behavior of the detector and to understand their origin, with the goal of reducing them as much as possible.

8.1 Computation of band-limited RMS

To easily perform quantitative analysis on the dark fringe noise variations over time, it is useful to compute the *band-limited RMS*, which is the total power of the noise in a limited frequency band. If this computation is performed periodically it is possible to track the time evolution of the noise.

There are at least two methods that can be used to compute band-limited RMS. First, given the edge frequencies of the desired band $[f_1; f_2]$, the signal can be processed using a tuned band-pass filter. If the filter roll-off is steep enough (usually a second order one is sufficient), the total RMS of the output, averaged over a suitable time window, gives the total power in the band. The second method consist in estimating the power spectrum of the signal and summing the power of all bins inside the frequency band. The two methods are clearly equivalent, since summing only bins into a band in frequency domain amounts to multiplying the spectrum by a square window, which is equivalent to time domain band-pass filtering. The first method requires less computational time for a single band. The by-product of the second method is an estimate of the full power spectrum. If the same signal has to be monitored in multiple bands, which is usually the case, the second method is better.

In summary, whatever method is used for estimating the BRMS, given the dark fringe signal and a list of frequency bands

$$\left\{ \left[f_1^{min}, f_1^{max} \right], \ldots, \left[f_n^{min}, f_n^{max} \right] \right\}$$

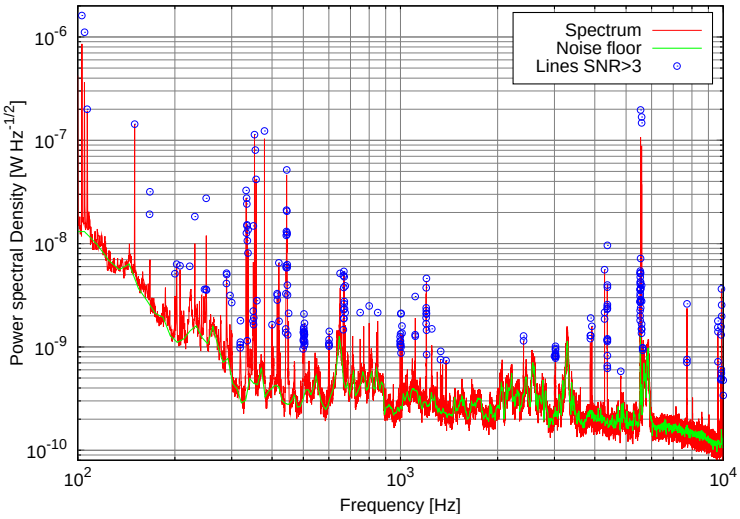

Figure 8.1: Result of the line identification algorithm applied to the dark fringe signal. The red curve is the full spectrum while the green one is the reconstructed noise floor. The blue circles are the lines found with SNR greater than 3.

and chosen a suitable time window T for the averaging or the computation of the power spectrum, the results are n new signals, sampled at $F = 1/T$, which give the noise power in each band as a function of time. It is possible to obtain these signals at a larger sampling rate using overlapping time intervals for the computations: for example it is possible to use 10 s of data for each estimation, with an overlapping of 90%, meaning that every second the last 10 s of data are used for the computations. This is useful to have a better frequency resolution. Indeed, considering the case of power spectrum estimation, if a time window of T seconds is used for the estimation, using n_{av} averages with 50% overlap, the length of each single Fourier transform is given by

$$\Delta T = \frac{2T}{n_{av} + 1} \tag{8.1}$$

and therefore the frequency resolution of the Fourier transform is

$$\delta f = \frac{n_{av} + 1}{2T} \tag{8.2}$$

Therefore, the use of longer overlapped intervals allows gaining a better frequency resolution and moving the monitored bands to lower frequencies.

8.1.1 Contribution of narrow spectral lines

If a signal contains a strong sinusoidal contribution at a given frequency (called in brief *spectral line* or simply *line*), the BRMS of a band containing it might

be completely dominated by the power in the line itself. Every fluctuation of the noise floor is hidden by the line amplitude. This situation is quite common when analyzing signals coming from interferometric detectors, because strong lines are usual and often added for calibration and monitoring purposes. An algorithm has been developed to separate the contribution to the BRMS coming from the noise floor and from lines [78].

The algorithm works in two main steps: first it estimates the noise floor and afterward it searches for lines and estimates their parameters[1]:

1. The starting point is an estimate of the power spectrum S_k. Its logarithm is computed $L_k = \log S_k$. This logarithmic transform is applied to reduce the contribution of strong lines in the computation of mean values and standard deviations.

2. The full frequency range, between the minimum frequency f_{min} and the maximum f_{max}, is divided into N segments (typically 200 between 1 and 10 kHz). In each of these segments, the minimum value of L_k is found and associated with the central frequency of the segment. All the N points obtained in this way are linearly interpolated to all frequencies between f_{min} and f_{max}, obtaining a first lower estimate LF_k of the logarithm of the noise floor.

3. The difference between the real logarithm of the spectrum and the latter estimate is computed $D_k = L_k - LF_k$. This has the effect of flattening the noise floor over the entire frequency range.

4. The mean value and standard deviation of the difference D_k is computed over all the frequency range. All points which are more than three time the standard deviation far from the mean value are discarded. Then the mean value and standard deviation are computed again and the process iterated a couple of times.

5. The lower estimate is corrected adding the computed mean value to obtain the final estimate of the noise floor: $F_k = \exp\left(LF_k + \overline{D_k}\right)$

6. All local maxima of the spectrum are found and their signal-to-noise ratio (SNR) computed dividing their peak value by the value of the noise floor at the corresponding frequency. Only those with SNR higher than a given threshold SNR_{min} are considered.

7. For each of these maxima, side bins are inspected to find the frequencies where the spectrum stop to decrease. These are defined as the limit frequencies of the peak

[1] A different algorithm for extracting lines is described in [79]

8. Adjacent peaks are merged together if the ratio of their amplitudes are below the SNR threshold. This is done to avoid counting a peak with small sidebands multiple times. The line frequency is defined as the one of the strongest peak

9. For each of the surviving lines the frequency and peak amplitude are computed, as well as the SNR, defined as before as the peak value over the noise floor value.

This algorithm can be used to separate the contribution of lines to the BRMS from the noise floor, therefore allowing to track separately the evolution in time of the power in lines and in the bulk of the noise spectrum. It is also used for on-line high resolution search of lines in the dark fringe spectrum.

8.2 Analysis of dark fringe non-stationarities

During all the science run the dark fringe signal has been monitored by an on-line process, called *NonStatMoni* [80], which performed the computation of band-limited RMS every second, with different time windows, and saved the results in the main data stream. The list of all the monitored bands is reported in table 8.1.

Two different strategies has been adopted for the analysis of noise non-stationarities. The typical duration of a continuous segment of science mode data is of the order of several tens of hours. This time window is enough to perform a Fourier analysis of the BRMS values. This allows the identification of periodicities in the noise variations, that can afterward be studied to understand their origin. The typical frequencies are between 1 and 500 mHz.

The noise level in different bands however shows also slower and non-periodic fluctuations, that are more easily studied in the time domain, by looking for correlation with other auxiliary channels.

8.2.1 Spectral analysis

Using the data from a single continuous science mode data segment, the main periodical non-stationarities can be studied computing the power spectrum of the time series given by the value of the BMRSs for each second. In this way the maximum detectable frequency of the fluctuations is given by half the inverse of the time shift between two consecutive windows:

$$f_{MAX} = \frac{1}{2S} \tag{8.3}$$

which in the case of Virgo science run data is 500 mHz. The minimum frequency, which correspond also to the spectrum resolution, is given by a formula similar

Minimum frequency	Maximum frequency	Time window
0 Hz	10 Hz	10 s
10 Hz	30 Hz	10 s
30 Hz	50 Hz	10 s
50 Hz	100 Hz	10 s
100 Hz	200 Hz	5 s
200 Hz	300 Hz	5 s
300 Hz	400 Hz	5 s
400 Hz	500 Hz	5 s
500 Hz	600 Hz	5 s
600 Hz	700 Hz	5 s
700 Hz	800 Hz	5 s
800 Hz	900 Hz	5 s
900 Hz	1000 Hz	5 s
500 Hz	1 kHz	1 s
1 kHz	2 kHz	1 s
2 kHz	3 kHz	1 s
3 kHz	4 kHz	1 s
4 kHz	5 kHz	1 s
5 kHz	6 kHz	1 s
6 kHz	7 kHz	1 s
7 kHz	8 kHz	1 s
8 kHz	9 kHz	1 s
9 kHz	10 kHz	1 s

Table 8.1: List of all the bands monitored during the Science Run by the NonStatMoni process. The output sampling rate is 1 Hz.

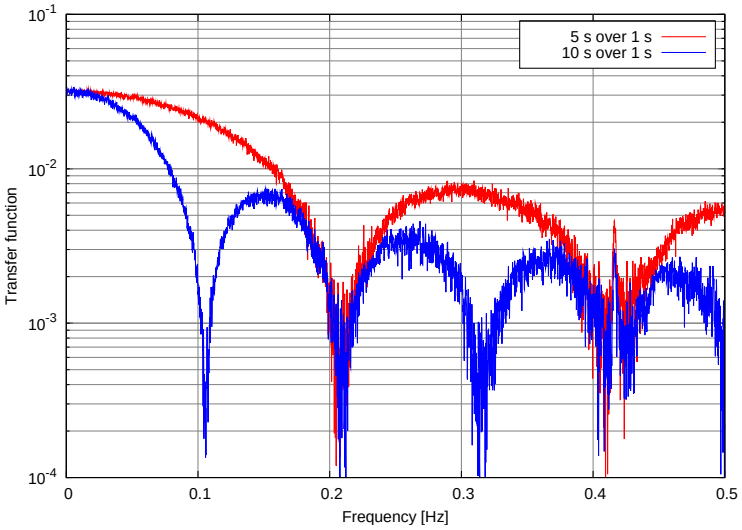

Figure 8.2: Example of the ratio between spectra of BRMS estimated with different time interval. This is the measured ratio between values computed with 10 s and 1 s and between 5 s and 1 s.

to eq. 8.2, where now T is the duration of the data segment and n_{av} is the number of averages: for example a single stretch of data 50 hours long, taking 20 averages, the frequency resolution is about 70 μHz.

There is one subtle point in this estimation of the fluctuation spectrum, if the overlap of the time intervals is not zero. In this case two consecutive samples for BRMSs are not completely independent, and it might seem not possible to recover information on frequencies higher than $1/2T$. However using overlapped intervals is not really equivalent to over-sampling the time series. Indeed, the operation of estimating the BRMS can be seen as an average of the instantaneous power in the band over the time interval used for the computation of the spectrum. This is equivalent to a time convolution with a rectangular window function: therefore the effect on the spectrum is simply the multiplication by the Fourier transform of this window, which is the well-known *sinc* function. In conclusion, given the BRMS values of a signal, computed with two different windows T_1 and $T_2 > T_1$, the ratio of the spectra of the two time series is given by (see fig. 8.2):

$$TF(f) = \left| \frac{\mathrm{sinc}\pi f T_2}{\mathrm{sinc}\pi f T_1} \right| \tag{8.4}$$

Once the frequencies of the main "fast" non-stationarities have been identified, it is interesting to correlate the variation of the BRMS in different bands with global variables, like environmental conditions (temperatures, seismic activity, etc.), laser power levels at different output ports, alignment conditions,

etc. One possible way to do this is to compute the coherence between the BRMS values and slow signals monitoring the detector: a high value of the coherence indicates that the dominating sources of noise in that particular band is modulated like the fluctuations of the considered monitoring signal. If the BRMS taken into account is computed using overlapped segments, the coherence is not affected by the transfer function of eq. 8.4, since a linear transformation does not change the coherence between two signals.

These frequency-domain analysis are performed automatically by an off-line analysis tool, which reads the output data from NonStatMoni, computes spectra and coherences with a large set of auxiliary interferometer channels. The results are organized as web pages [81].

Analysis of the science run data

An example of the results obtained for a long stretch of data during the science run is shown in figures 8.3, 8.4 and 8.5. These spectra are almost all very similar and does not show many relevant structures. The main difference concerns the band 5-6 kHz where the BRMS is dominated by strong lines corresponding to mirror internal resonant modes. The other spectra are, with some exception, quite smooth, as expected for noise without strong non-stationarities.

The coherence analysis of these BRMSs shows some important relations in different frequency regions:

- referring to fig. 8.3,8.4 and 8.5, the very low frequency non-stationarities (below 100 μHz) are coherent with variation in the seismic activity, as measured by the RMS of seismometers in different bands, and also with the mode cleaner terminal mirror angular motions. The two things are likely related: high seismic motion excites more the short MC suspension;

- referring to fig. 8.3,8.4 and 8.5, the fluctuation at frequencies between 1 mHz and 10 mHz are coherent with angular motions of the beam splitter and west arm mirrors. This has also an effect visible on the dark fringe power and in the sidebands amplitudes at the dark port, before the output mode cleaner;

- referring to fig. 8.3, the narrow line at about 20 mHz is due to angular motion of the PR and BS mirrors in the ϑ_y degree of freedom;

- referring to fig. 8.3 and 8.4, the structure between 25 and 30 mHz is also related to beam splitter and west input mirror motions, but in the ϑ_x degree of freedom;

- referring to fig. 8.4, the structures visible between 100 and 200 mHz are coherent with the angular motion of PR and BS in the ϑ_x degree of freedom

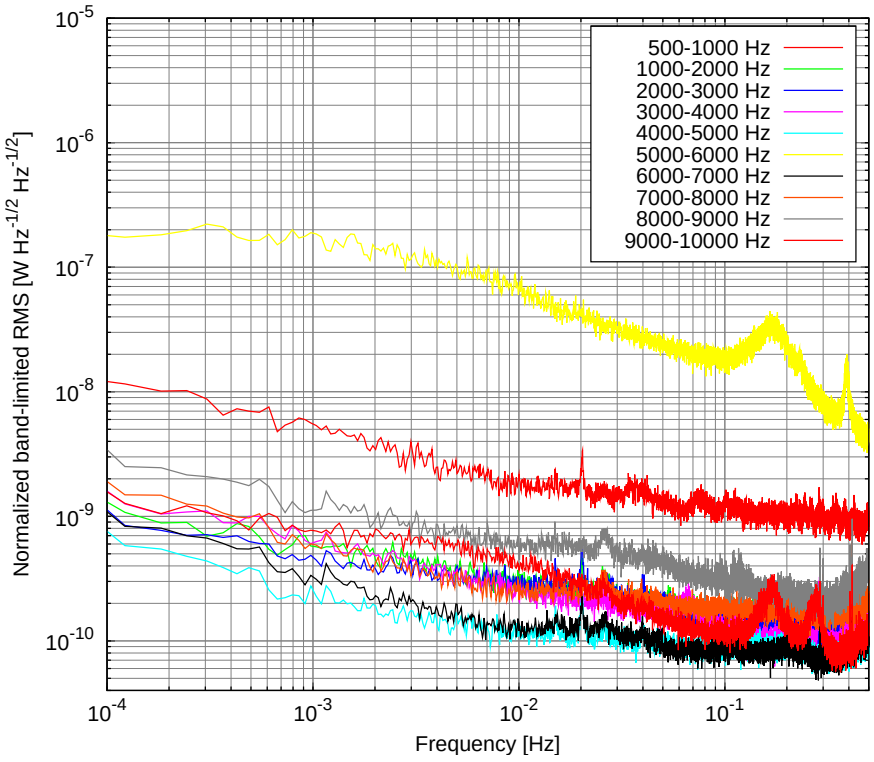

Figure 8.3: Spectrum of dark fringe band-limited RMS variation for high frequency bands.

In summary, on the timescale of one hour or less, the detector noise is quite stable and the main sources of semi-periodic non-stationarities are linked to residual angular motions.

8.2.2 Time domain analysis

The non-stationarities on long time scales (typically days) are more easily analyzed in time-domain. For the first three months of the run, all the science mode segments of data have been analyzed, computing the root mean square value of the BRMS over time windows of 100 s. In this way only the slower fluctuations are taken into account. Moreover, the final 100 seconds of each science segment has been discarded, to avoid possible perturbation of the BRMS values by pre-unlock transient. Also the first 3000 seconds of each lock has been discarded since several frequency bands are dominated by damping resonances, like violin and mirror internal modes, that are excited during the lock acquisition.

An example of the BRMS variations over the long period is shown in fig. 8.6. It is important to correlate these fluctuations with changes in the detector con-

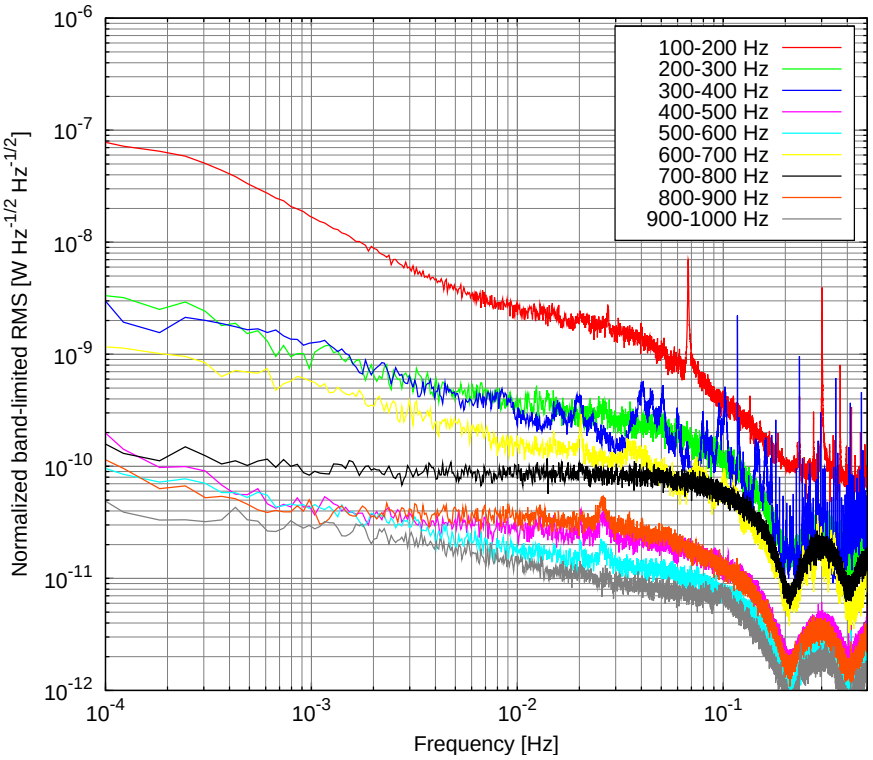

Figure 8.4: Spectrum of dark fringe band-limited RMS variation for intermediate frequency bands.

ditions. For this reason the mean value of several auxiliary channels has been computed over the same 100 s periods used for the BRMS:

- signals concerning the length sensing and control system: the DARM, MICH and PRCL loops electronic gains, the value of the sensing cross term between MICH and PRCL, the alpha and beta coefficients, the offset added to balance the sidebands (see chap. 3);
- the powers detected by all photo-diodes: B1, B1p, B5, B7 and B8 as well as the signal used to estimate the sidebands power inside the recycling cavity B5_2f;
- the power transmitted by the input mode cleaner;
- the amplitude of carrier and sidebands at the dark port, as detected by the scanning Fabry-Perot system (see sec. 2.5 and B.6.3);
- the total RMS of angular corrections for all six main mirrors and for the injection and detection suspended benches;

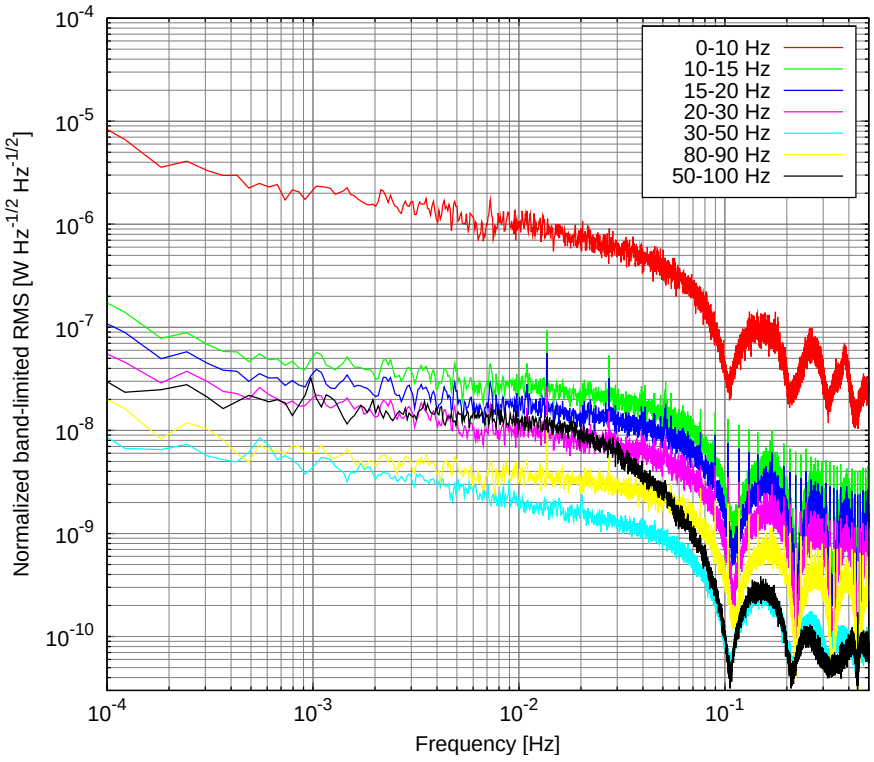

Figure 8.5: Spectrum of dark fringe band-limited RMS variation for low frequency bands.

- the seismic activity in different frequency bands between 30 and 4000 mHz;
- the seismic noise measured on top of the detection Brewster window (see sec. 7.11.2);
- the motion of the top stage of the mirror suspensions;
- the vertical position of all main mirrors and of the two suspended benches;
- the external temperature as well as those measured inside the main buildings, the optical benches and the towers;
- the centering signals of all alignment quadrants (see chap. 4);
- the beam position measured with respect to the output mode cleaner by quadrants mounted on the suspended detection bench, as well as the OMC locking signals;
- the input beam position measured by the BMS system as well as the corresponding RMS motions;

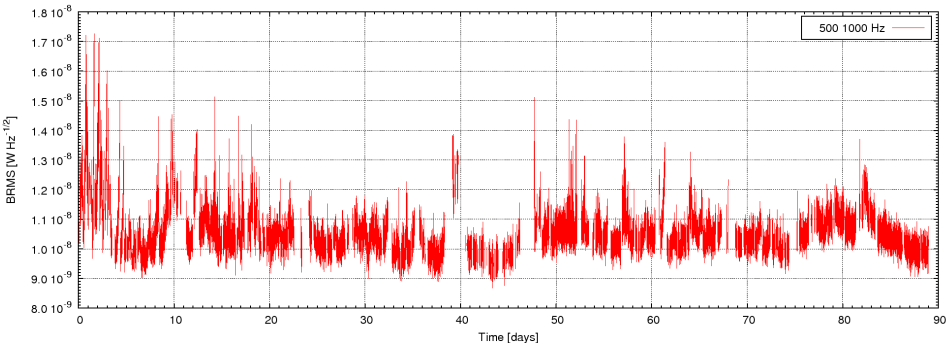

Figure 8.6: Typical example of the variation over long period of the band-limited RMS, in this case computed between 500 and 1000 Hz.

- the optical gains measured on-line by the calibration process, which track the dark fringe response to mirror motions at specific frequencies.

This makes a total of about 100 auxiliary channels to search for correlation with the dark fringe noise.

8.2.3 Multi-dimensional linear regression

The task of finding the possible correlations between the time evolution of the BRMS in a given band and a set of auxiliary channels can be tackled with statistical methods, in particular applying a *multi-dimensional linear regression* [82]. The values at n different times y_i of the BRMS in a given band can be viewed as the noisy version of a linear combination of the k auxiliary channels measured at the same times $x_{1\ldots k,1\ldots n}$:

$$y_i = \beta_0 + \beta_1 x_{1,i} + \cdots + \beta_k x_{k,i} + \varepsilon_i \tag{8.5}$$

Here β_j are the unknown coefficients to be estimated and ε_i is a source of additional noise, that can be considered as coming from the measurement of the y_i or also from the auxiliary channels. In other words, the analysis starts from the hypothesis that the input x signals are deterministic and that the output is a random variable given by an unknown linear combination of the x plus some random noise. This noise is assumed to be normally distributed, with zero mean, uncorrelated for different times and with constant unknown variance σ. These hypothesis are reasonably satisfied in the case analyzed. Under these assumption the *Gauss-Markov* theorem [83] states that the best un-biased estimate of the β coefficients can be obtained with a least square method.

It is easier to carry out the computation in matrix form. With the following

definitions:

$$
\begin{aligned}
Y &= \begin{pmatrix} y_1 \\ \vdots \\ y_n \end{pmatrix} \\
X &= \begin{pmatrix} 1 & x_{1,1} & \dots & x_{1,k} \\ \vdots & \vdots & & \vdots \\ 1 & x_{n,1} & \dots & x_{n,k} \end{pmatrix} \\
\beta &= \begin{pmatrix} \beta_1 \\ \vdots \\ \beta_k \end{pmatrix} \\
\varepsilon &= \begin{pmatrix} \varepsilon_1 \\ \vdots \\ \varepsilon_n \end{pmatrix}
\end{aligned}
$$

equation 8.5 can be rewritten in a more compact form:

$$Y = X\beta + \varepsilon$$

and the sum of squared errors is

$$
\begin{aligned}
S &= \sum_{i=1}^{n} (y_i - \beta_0 - \beta_1 x_{1,i} - \cdots - \beta_k x_{k,i})^2 = (Y - X\beta)^T (Y - X\beta) \\
&= Y^T Y - 2\beta^T (X^T Y) + \beta^T (X^T X)\beta
\end{aligned}
$$

The best estimate of the β coefficients is obtained by minimization of this quantity, or in other words by solving the equation:

$$0 = \frac{\partial S}{\partial \beta^T} = -2X^T Y - 2(X^T X)\beta$$

If all the auxiliary signals are linearly independent, the X matrix has maximum rank and $X^T X$ is invertible. Therefore the solution of the previous equation is

$$\hat{\beta} = (X^T X)^{-1} X^T Y \tag{8.6}$$

and the predicted output signal is

$$\hat{Y} = X\hat{\beta}$$

The estimated parameters are linear combination of the measured Y which is a realization of a normal random variable. It follows that also β is normally distributed, and its covariance matrix is given by

$$C(\hat{\beta}) = \left[(X^T X)^{-1} X^T\right] \sigma^2 \left[(X^T X)^{-1} X^T\right]^T = \sigma^2 (X^T X)^{-1}$$

Therefore the variance of the parameters $\hat{\beta}$ can be computed if the value of σ is known. An un-biased estimator can be found analyzing the probability distribution of the sum of squared *residuals*, defined as

$$\widehat{SSR} = (Y - \hat{Y})^T (Y - \hat{Y}) = (Y - X\hat{\beta})^T (Y - X\hat{\beta}) \tag{8.7}$$

Some algebraic computations yield

$$Y - X\hat{\beta} = \left(1 - X(X^T X)^2 X^T\right) Y$$

From the geometrical point of view the operator inside brackets is an orthogonal projection into the subspace complementary to the one spanned by the columns of X. Therefore its dimension is exactly $n - k - 1$. Eq. 8.7 represent therefore a sum of $n - k - 1$ squared normal random variables, each one with variance given by σ. In other words the following variable

$$\frac{\widehat{SSR}}{\sigma^2} = \frac{(Y - X\hat{\beta})^T (Y - X\hat{\beta})}{\sigma^2} \tag{8.8}$$

is distributed like a $(n - k - 1)$-dimensional χ^2. This finally gives the needed un-biased estimator of σ as

$$\hat{\sigma}^2 = \frac{(Y - X\hat{\beta})^T (Y - X\hat{\beta})}{n - k - 1} \tag{8.9}$$

Using this the variance of the $\hat{\beta}$ parameters can be computed:

$$\hat{s}(\hat{\beta}_j) = \hat{\sigma} \sqrt{(X^T X)^{-1}_{j,j}}$$

Finally the variable

$$T = \frac{\hat{\beta}_j - \beta_j}{\hat{s}(\hat{\beta}_j)}$$

follows a Student's t distribution with $n - k - 1$ degrees of freedom and it allows the determination of confidence intervals for the estimated $\hat{\beta}_j$ as

$$\hat{\beta}_j - t_{\alpha/2} \hat{s}(\hat{\beta}_j) < \beta_j < \hat{\beta}_j + t_{\alpha/2} \hat{s}(\hat{\beta}_j) \tag{8.10}$$

where the confidence level is $1 - \alpha$.

8.2.4 Application of the technique

Since the linear regression technique is quite sensitive to out-layers, all channels have been scanned for periods of bad behavior, and these have been excluded from the analysis. At the end about 50000 data points remained, covering the first three month of the science run. All auxiliary channels have been normalized using their mean, standard deviation and the number of points:

$$x_j^N = \frac{1}{\sqrt{N_P}} \frac{x_j - \mu_j}{\sigma_j} \tag{8.11}$$

In this way all the signals have similar order of magnitude. Moreover, in this way numerical problems due to the high number of multiplications of signals in the computation of the $X^T X$ matrix are reduced.

The result of the analysis is a set of about 100 coefficients for the BRMS in each frequency band. The confidence intervals of these estimations can be obtained as explained before. However, given the very high number of degrees of freedom involved in this linear regression, the Student's distribution can be very well approximated by a normal one. The confidence intervals have therefore been computed at the 3σ level, corresponding to a confidence of 99.7%. Afterward all coefficients compatible with zero were discarded. The number of surviving $\hat{\beta}_j$ is still high, of the order of 60. Therefore a method to identify the less significative ones has been constructed as follows: the standard deviation of a given channel contribution to the predicted BRMS is divided by the standard deviation of the residual. This gives an estimation of the importance of that signal for the prediction. All signals with this ratio lower than a given threshold were discarded. The best value has been found esperimentally to be 1/10. This procedure left a number of coefficients of the order of 20-30 for each band-limited RMS.

Finally, the linear regression analysis has been performed again for each band using only the relevant channels identified as explained above. In this way the prediction of the BRMS values improved.

The results are shown in figures from 8.7 to 8.11 for all the analyzed bands. The agreement between the real variations of the BRMS and the predicted values is good for all bands, except for the 5-6 kHz. This is expected since this BRMS is dominated by very large mirror internal resonance peaks, which are quite stable with time.

A further check of the obtained models can be performed by plotting the histogram of the residuals. Supposing that the model could completely describe the non-stationarities, the residuals should be distributed like the normal noise of eq. 8.5. Some of the histograms are shown in fig. 8.12. Their distribution is usually not too far from a normal one, with frequent tails on the high values side. This is an indication that not all the non-stationary behavior can be explained on the simple basis of the chosen set of auxiliary channels.

Although this technique is very useful to understand which amount of the total noise non-stationarity can actually be predicted from a given set of auxiliary channels, it is quite difficult to extract a small number of channels that can give some useful information for the detector characterization and commissioning. The main reason is that the auxiliary channels are indeed independent, otherwise the analysis would fail, but they are not orthogonal, in the sense that there are close relationship between them. For example the seismic activity at very low frequency can affect the interferometer sensitivity by spoiling the

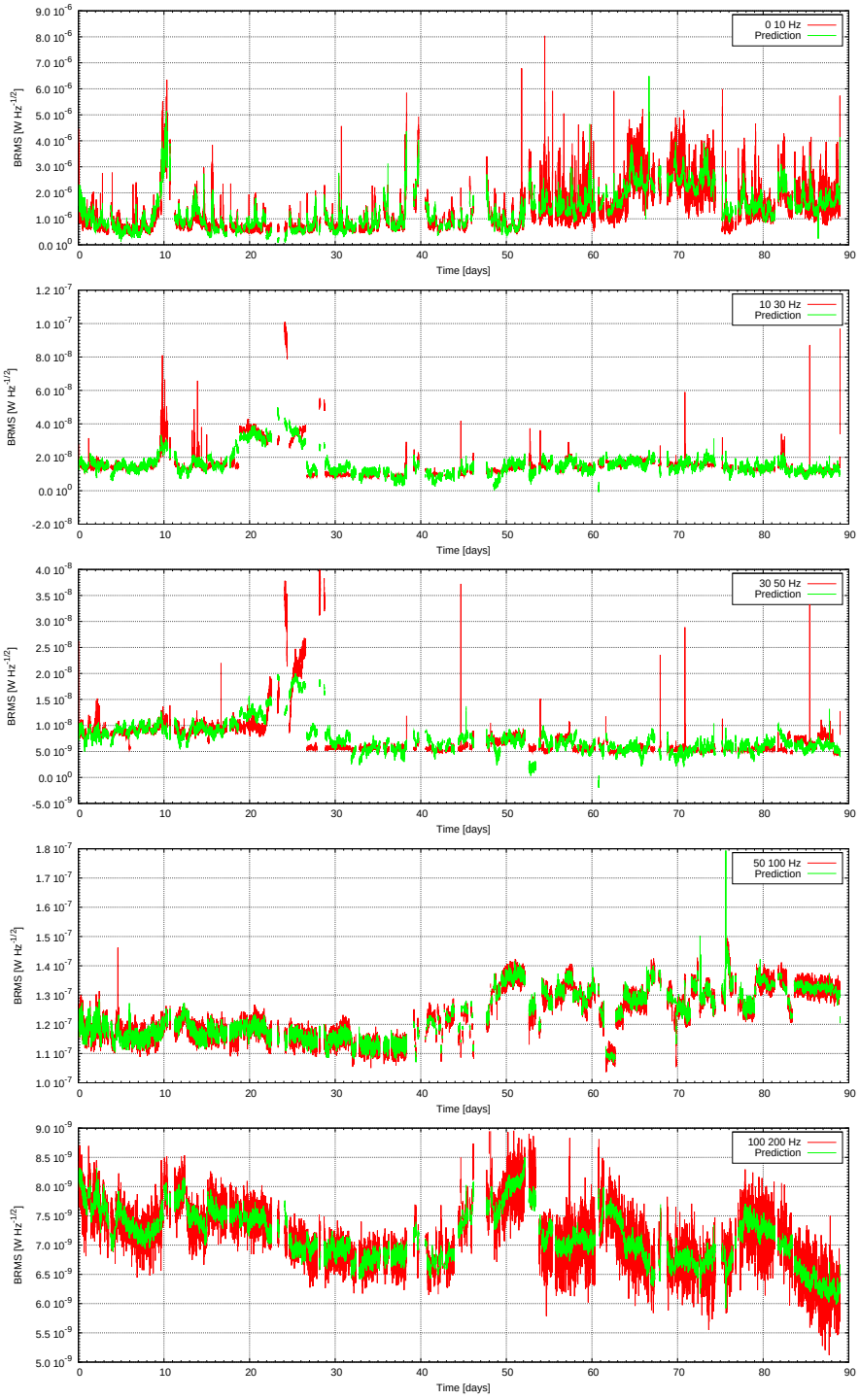

Figure 8.7: Variation of the BRMS in low frequency bands and predicted values from the linear regression analysis.

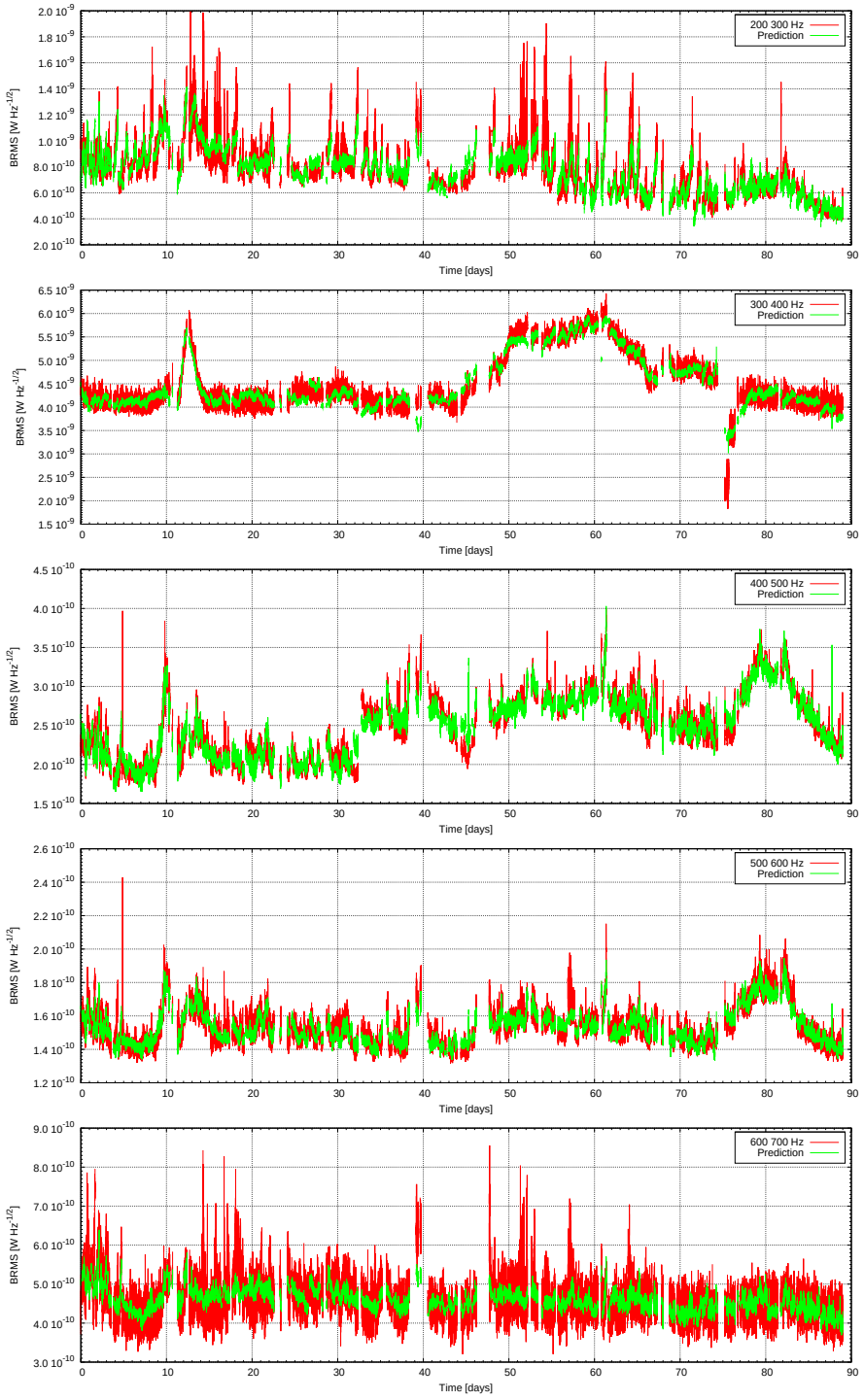

Figure 8.8: Variation of the BRMS in intermediate frequency bands and predicted values from the linear regression analysis.

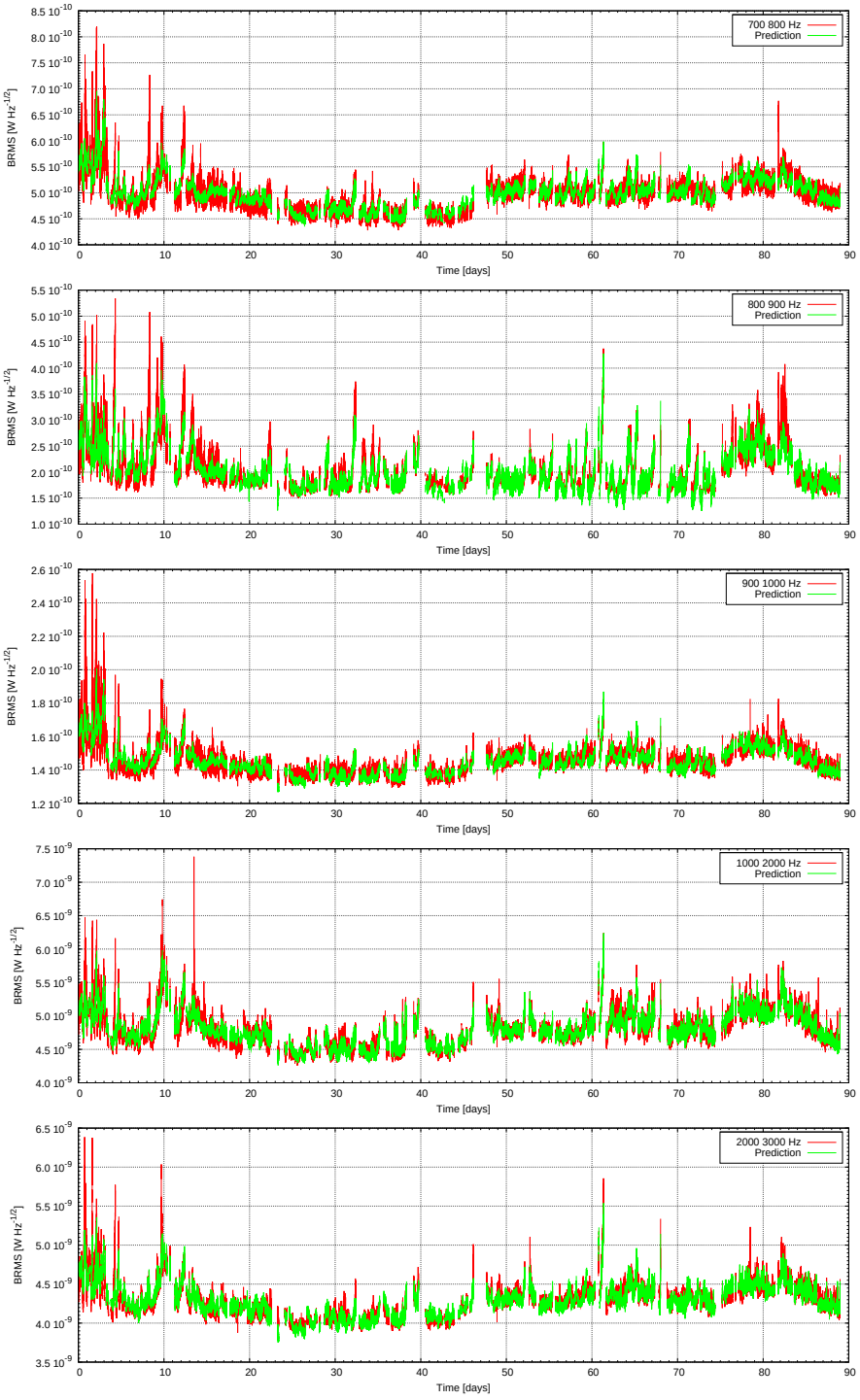

Figure 8.9: Variation of the BRMS in intermediate frequency bands and predicted values from the linear regression analysis.

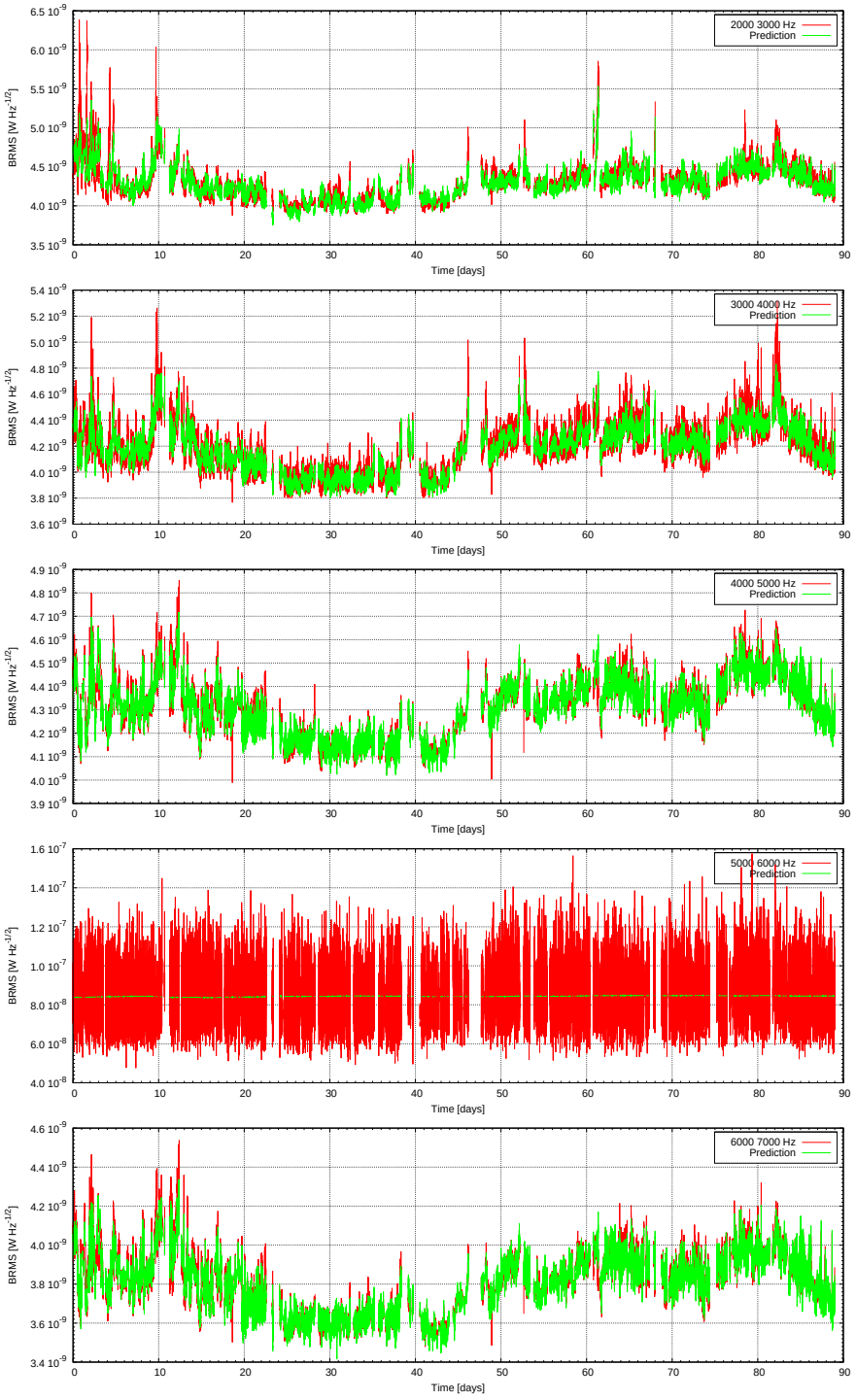

Figure 8.10: Variation of the BRMS in high frequency bands and predicted values from the linear regression analysis.

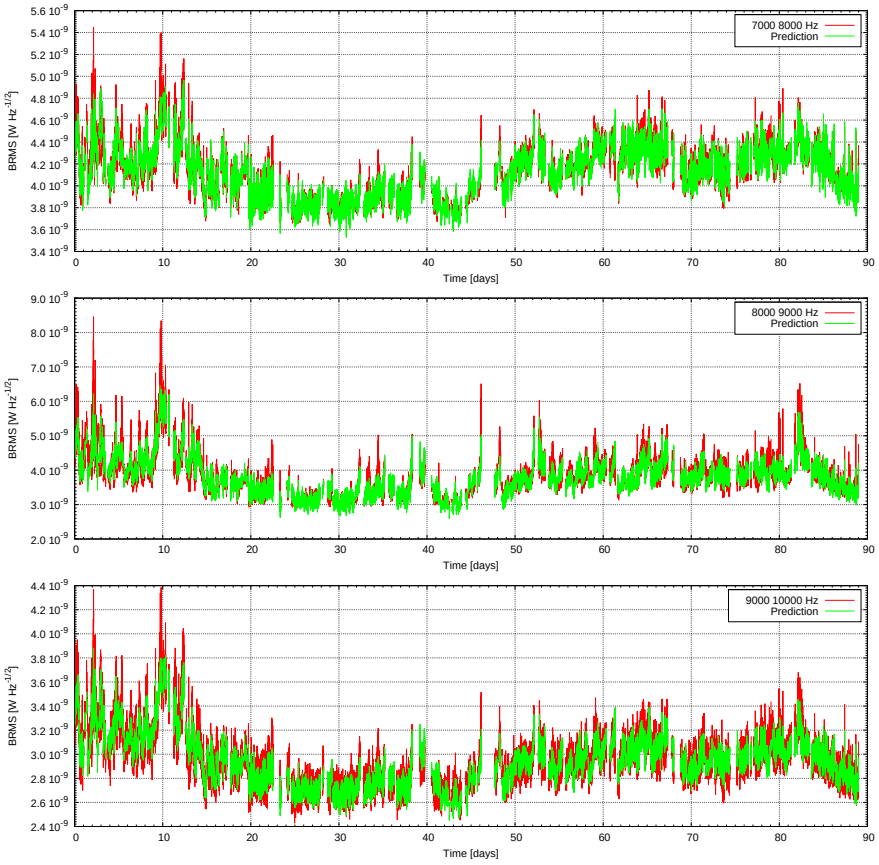

Figure 8.11: Variation of the BRMS in high frequency bands and predicted values from the linear regression analysis.

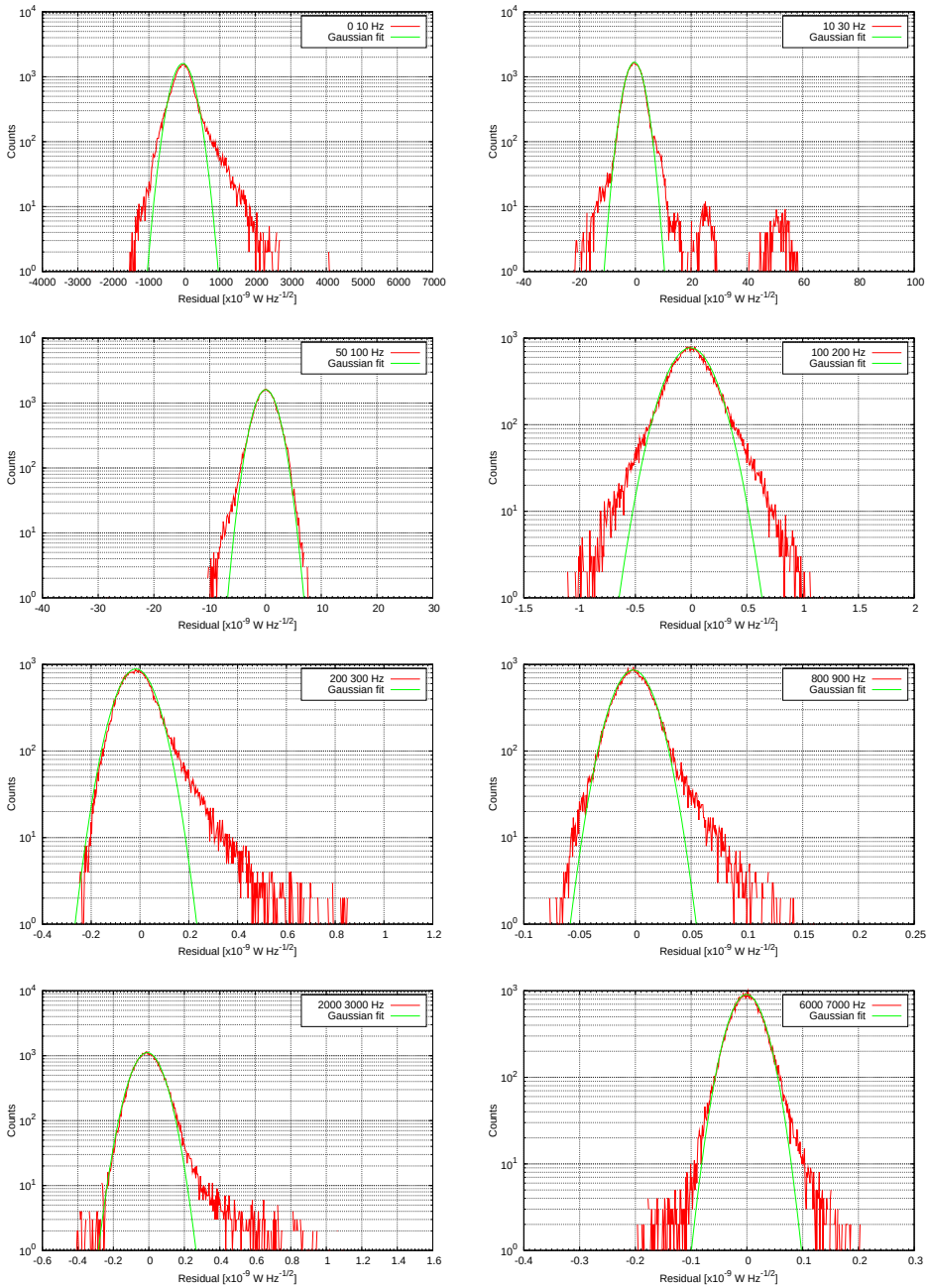

Figure 8.12: Some example of histograms of the residuals in some frequency bands.

accuracy of the alignment loops. Therefore both the seismic sensors and the RMS of angular corrections are good signals and even if the original cause is the micro-seism, the multi-dimensional regression might end up with using only the alignment signal.

To overcome all these difficulties, a different approach has been developed to be able to "sort" the auxiliary channels in order of relevance for the prediction of the BRMS in a given band. The first step is a one-dimensional linear regression analysis of the BRMS time series with each auxiliary channel separately. The one that minimize the residual standard deviation is then chosen and its predicted contribution is subtracted from the BRMS values. Starting from this subtracted time series the analysis is re-iterated, taking every time into account only the auxiliary channel that minimize the residual standard deviation. In this way the final prediction is not the optimal one and not as good as the one obtained with the full linear regression, but at least it is possible to extract a reduced number of channels (usually 5) that can reconstruct most of the slowest trends of the BRMS. This analysis usually fails to reproduce the fastest variations or the shortest events.

With this technique it has been possible to determine, for each frequency band, those auxiliary channels that are most relevant to explain the non-stationarities. Some of these channels can be pointed out as the real origin of the noise variation, like for example an increase of some correction RMS which can be tracked down to a real increase of the residual motion of one degree of freedom. Some other channels are not likely to be the direct culprit of the noise increase, but simply an indicator of something changing inside the detector. A typical example are the powers detected by photo-diodes.

In summary, the non-stationarities are linearly depending on several different channels. The noise at high frequencies, above 1 kHz, is changing accordingly to

- the power in the dark fringe, as detected before the OMC. This is an indication of changes in the interferometer contrast due to higher order modes, usually due to small alignment drifts off the operating point. Moreover there is a linear dependence on the dark fringe quadrant centering signals, meaning that the beam might be moving in front of the quadrants and of the OMC. This is further confirmed by the dependence on the signals coming from the suspended detection bench quadrants, used for the alignment of the bench telescope;

- the RMS of angular corrections of the suspended injection and detection benches. The first couple to the main interferometer as beam jitter;

- some temperature inside the central and terminal buildings, that might cause drifts in the quadrant centering that worsen the overall alignment

of the interferometer.

The noise at intermediate frequencies, between roughly 100 and 1000 Hz is instead changing like

- the RMS of suspended injection bench angular controls, even more than in the high frequency bands;
- the vertical position of several main mirrors, mainly the arm cavity ones;
- the RMS of the angular corrections of the end mirrors. This is directly related to micro-seismic conditions: when the seismic noise at very low frequency is higher, the accuracy of the angular controls is reduced;
- the dark fringe power before the OMC;
- the variation of some length sensing and control signals, like the optical gains and the sensing cross term. It is unlikely that there is a direct relation between the values of these signals and the noise in the 100-1000 Hz band. It is more likely that these signals are indicators of something changing inside the interferometer, like for example the arm cavity finesses, due to changes in the input mirror temperature.

Finally the noise at low frequency, roughly below 100 Hz, known to come mainly from controls (see chap. 7), changes accordingly to

- mainly the micro-seismic conditions at the lowest frequencies;
- the vertical position of several payloads, both mirrors and the suspended detection bench;
- the values of the noise subtraction coefficients alpha and beta (see chap. 5.4), which directly affect the noise in this region;
- the power transmitted by the arm cavities, which is likely to indicate a dependence on the finesse variations;
- the RMS of angular corrections of both the injection suspended bench and the input mode cleaner terminal mirror.

8.3 Conclusions

The study of noise non-stationarities gives a different perspective on the detector sensitivity than other kind of analysis. The computation of band-limited RMS from on-line data has been running since a couple of years even before the run, and has been widely used when a quantitative measurement of the noise level

was needed and a simple comparison of spectra at two different time was not enough.

The study of semi-periodic non-stationarity allowed to identify several sources of noise fluctuation, mainly linked to residual angular motions of the mirrors, and it gave the necessary indications to trigger improvements. Indeed the stationarity of the noise during the run was very good and there were few periodical modulation still present, and all quite small.

The time domain analysis of the noise level during long periods has been first carried out during the science run, since this was the right occasion to collect long stretches of data in controlled and stable conditions. The linear regression analysis is only the starting point of a deeper investigation, and showed very interesting results. Indeed most of the noise level variations can be explained with simple linear relations with several interferometer monitoring and auxiliary channels. The foreseen and natural evolution of this analysis is not the blind attempt to add more and more channels to reconstruct every noise non-stationarity, but instead a deeper investigation of the results already obtained. The goal is to understand the relations between a given BRMS and some relevant auxiliary channel, to be able to kill the noise source or to control the suitable interferometer degree of freedom in order to minimize the coupling. Moreover, this linear regression analysis should be extended to include quadratic coupling with auxiliary channels, since these might be the dominant one in the hypothesis that the detector working point is the optimal one.

Finally, the understanding of a large number of sources of non-stationarities is the first step toward the subtraction of their contribution and the study of the remaining noise level variation. The most interesting analysis is for sure the search for noise modulation with a period of one sidereal day, which might indicate a non-terrestrial origin, for example from a gravitational wave astrophysical galactic background [19].

Chapter 9

Fast transient noises

Another kind of non-stationary noises that can appear in interferometric detectors consists in fast transients: brief periods of time, lasting usually less than one second, of increased noise in the full frequency band or in a restricted one. The origin of this kind of events are many: brief instabilities in some control loops, real glitches in the signals, dust falling in front of photo-detectors, fast-varying noise couplings, environmental noise, etc. As a matter of nomenclature, in the following these transient events will be called *clusters*.

9.1 The HACR algorithm

There are lots of different algorithms that can be used to detect such events, most of them developed in the context of impulsive gravitational wave sources (bursts) analysis. The algorithm implemented as part of this work and described here is based on HACR (*hierarchical algorithm for curves and ridges*) [84] developed inside the GEO600 collaboration. This algorithm is quite fast, allowing a simultaneous monitoring of tens of channels. This characteristic makes it very useful to perform coincidence analysis.

The idea behind this algorithm is to to search for times and frequencies where there is an excess of power with respect to the mean statistics. Given an input signal $x(t)$, the algorithm first compute short windowed Fourier transforms (using for example 50 ms of data) without averages. In this way a time-frequency map $F(t, f)$ of the signal is created using the squared values of these transforms, with good time and quite low frequency resolutions (see fig. 9.1a). The second step is the computation of a mean value of the spectrum, by running a decay average for each frequency bin: the result is a map of the mean values of the signal power spectrum over the past seconds (see fig. 9.1b) for each time:

$$M(t, f) = \overline{F(t - \Delta t < \tau < t, f)} \tag{9.1}$$

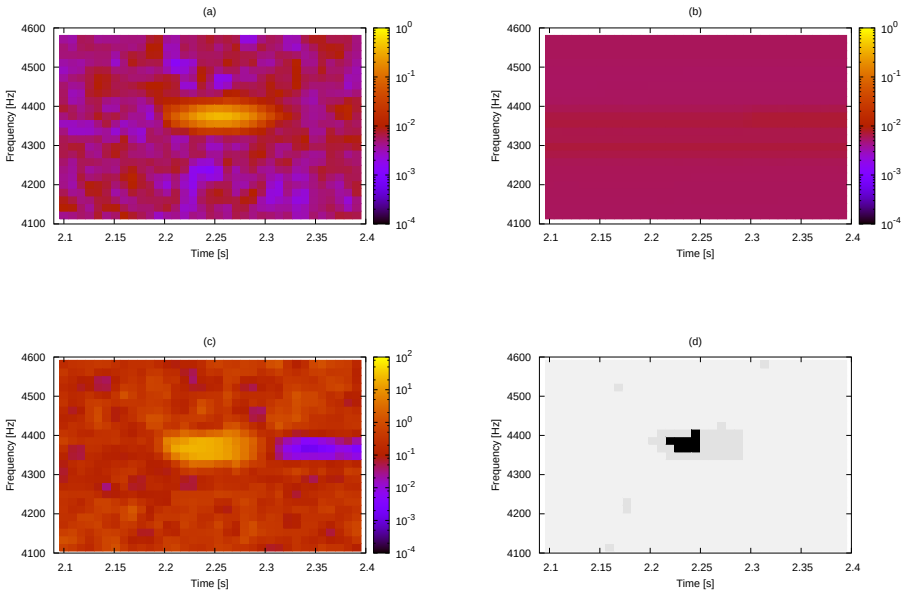

Figure 9.1: Example of how the HACR algorithm works, using simulated data made of white noise plus a sine-Gaussian burst. Top left (a) is a time-frequency map of single short Fourier transforms of the signal. Top right (b) is the mean value of the power spectrum obtained by time averages from the previous map. Bottom left (c) is the significance map computed from the previous ones. Bottom right (d) is the corresponding triggers map, with $T_{HIGH} = 20$ and $T_{LOW} = 3$: black bins are those with significance above T_{HIGH}, grey one with significance above T_{LOW}.

At the same time also the variance of each frequency bin is computed in a similar way:

$$\sigma^2(t,f) = \overline{(F(t,f) - M(t,f))^2} \tag{9.2}$$

The mean value is recomputed excluding bins with deviations greater than 3σ. At this point the *significance* of each time-frequency bin is computed as the deviation from the mean value in units of σ:

$$s(t,f) = \frac{|F(t,f) - M(t,f)|}{\sigma(t,f)} \tag{9.3}$$

This significance map (see fig. 9.1c) is the starting point for finding regions with excess of power: the algorithm triggers every time the significance of a bin exceeds a given high threshold T_{HIGH}. All these triggers are then analyzed one by one. Given one of them, all neighbouring bins are considered: if their significance exceed a lower threshold T_{LOW} they are clustered together with the

triggering bin. This procedure is iterated for all the bins in this newly formed cluster in order to recover all adjacent bins with significance above the lower threshold. The reason for this operation is that a transient event usually spreads its power over more than one bin and therefore a clustering is necessary to be able both to recover the full event power and to avoid multiple counting of the same event.

For each of these clusters several quantities are computed. The mean time and frequency are obtained with weighted averages based on bin powers:

$$t = \frac{\sum_{i \in C} t_i \, F(t_i, f_i)}{\sum_{i \in C} F(t_i, f_i)} \tag{9.4}$$

$$f = \frac{\sum_{i \in C} f_i \, F(t_i, f_i)}{\sum_{i \in C} F(t_i, f_i)} \tag{9.5}$$

Similarly the total power is computed summing over all bins in the cluster:

$$P_{TOT} = \alpha \sum_{i \in C} F(t_i, f_i) \tag{9.6}$$

where α is a normalization parameter depending on the window function used and on the overlapping of subsequent segments used in computing the spectrum map.

The maximum and mean significances are also computed. An estimation of the signal-to-noise ratio (SNR) is given dividing the power in the cluster with the one in the mean spectrum (which is what would have been measured without any transient):

$$SNR = \frac{\sum_{i \in C} F(t_i, f_i)}{\sum_{i \in C} M(t_i, f_i)} \tag{9.7}$$

Other interesting parameters are the number of points in the cluster and its time and frequency widths:

$$\Delta t = \sqrt{\frac{\sum_{i \in C} (t_i - t)^2 \, F(t_i, f_i)}{\sum_{i \in C} F(t_i, f_i)}} \tag{9.8}$$

$$\Delta f = \sqrt{\frac{\sum_{i \in C} (f_i - f)^2 \, F(t_i, f_i)}{\sum_{i \in C} F(t_i, f_i)}} \tag{9.9}$$

All these results are saved in lists of events than can be used for various analysis:

- The number of clusters per minute can give a quantitative indication of the stability of the detector and on the data quality.
- Looking at the time and frequency distributions of the clusters it is often possible to identify periodicities and particular frequency bands that generate classes of transients.

- The use of this algorithm for commissioning purposes can help in identifying the origin of not understood noises. For example frequent clusters can be difficult to discover looking only at spectra, since they can be easily mistaken by a stationary incoherent noise.
- From the data analysis point of view, list of triggers of this kind can be useful to set up statistical veto procedures, making coincidence analysis between different channels [85].

9.2 Analysis of dark fringe clusters

During the science run the HACR algorithm has been running on-line [86], looking for clusters in several channels: the dark fringe in-phase and quadrature, the longitudinal corrections and errors, the laser frequency and power stabilization errors, the beam monitoring system (BMS) errors. All the results have been stored in a centralized database. This was periodically mined by an automatic script to produce short reports about some of the analyzed channels. These reports are available via a web page [87].

The analysis of HACR results starts naturally from the clusters detected in the dark fringe in-phase demodulated signal. In the following the analysis is described for two different periods of science data[1]: the main difference between the two is the disappearance of clusters generated by the beam monitoring system, due to the replacement of a broken piezo-electric actuator.

Time-frequency maps are shown in fig. 9.2 for the dark fringe signal. These give a global overview of the number of clusters in the analyzed channel, allowing the identification of variations over time and of the most interesting frequencies. The distribution in SNR, shown in fig. 9.3 allows to identify two classes of clusters: the main part of the distribution has SNR greater than 9, while a different population has lower SNR, even below 1. One should remember that the HACR algorithm does not consider any cut in the clusters SNR, but only on their maximum significance: therefore these low SNR clusters must in any case have high significance, meaning that they are actually regions of the time-frequency power map where there is a large fluctuation of the noise. A deeper investigation showed that this class of clusters are related to strong lines in the dark fringe spectrum: calibration lines or thermal modes of wires and mirrors. Therefore in the following only clusters with SNR greater than 9 are considered.

In fig. 9.4 the frequency distribution of the cluster is shown. It is possible to distinguish several classes of clusters depending on their frequency (see table 9.1). The clusters between 7.8 and 9.3 kHz are a relevant fraction of the total and correspond to a structure well visible in the dark fringe spectrum, which is

[1] The first one spans from GPS time 867827080 to 868066580, the second one from 869885490 to 869932490.

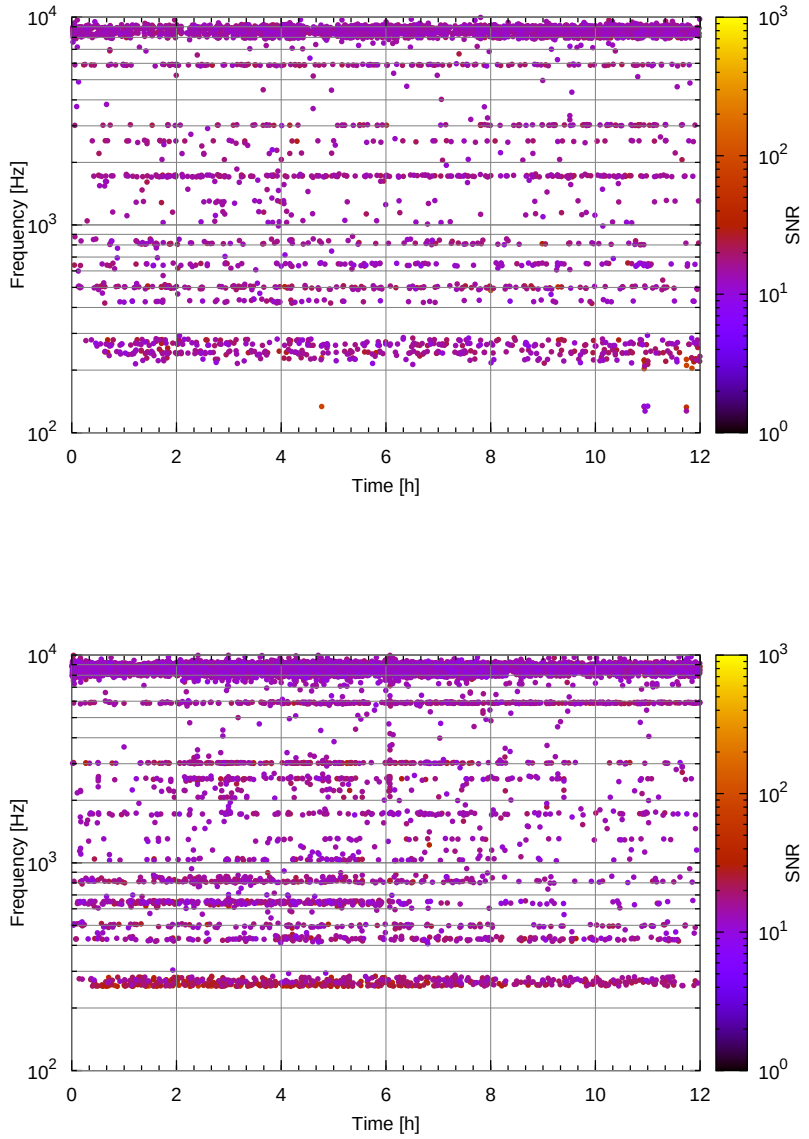

Figure 9.2: Time-frequency map of clusters in the dark fringe in-phase demodulated signal during 12 hours of two different science mode periods. The color of the dots represent the reconstructed SNR of the clusters. The top plot refers to the first period, before repairing the BMS system, the bottom one to the second period.

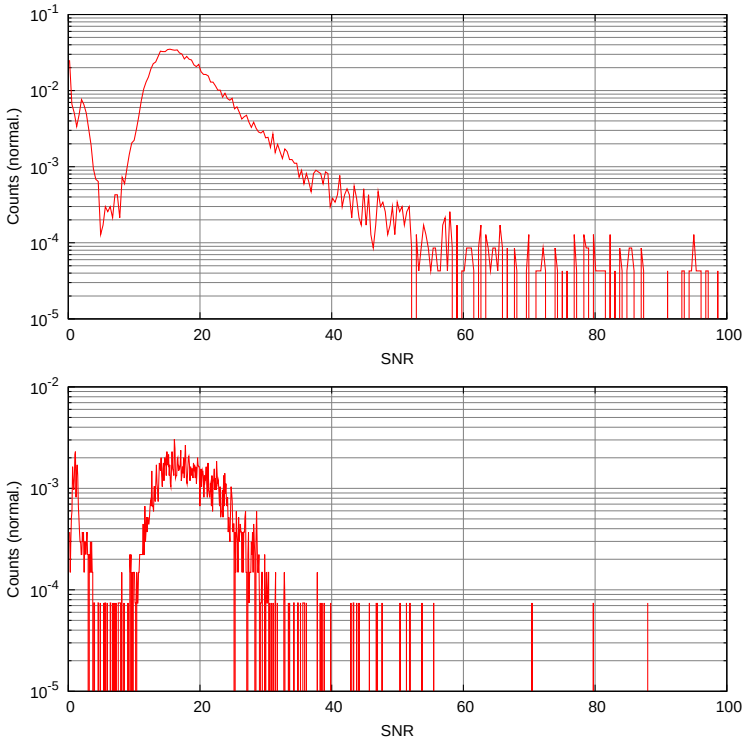

Figure 9.3: SNR distribution of the clusters detected in the dark fringe in-phase demodulated signal. The top plot refers to the first period and the bottom to the second. Note that the time length of the two periods is not the same.

believed to be electro-magnetic noise coming from the main power supplies. The clusters between 5.8 and 5.96 kHz corresponds to the frequency noise bump (see sec. 7.4). All other cluster classes correspond to structures in the dark fringe whose origin is not well identified. The classes at lower frequencies, namely below 300 Hz were mainly related to the BMS malfunctioning: the number of clusters detected in this region is indeed strongly reduced after the replacement of the broken actuator.

It is interesting to investigate if the detected clusters are distributed randomly in time or if there is some periodicity in their presence. This possibility can be studied computing an *auto-correlogram*: for each cluster the time difference with all later ones is computed and organized in an histogram. The results for all the clusters and for those in some selected frequency bands are shown in fig. 9.5 for the second period of science data. While the glitches at low frequencies does not show any significant periodicity, those in the first class (between 7.8 and 9.3 kHz) shows a clear repetitive structure with a period of about 2 s. This means that the source of noise coupling responsible for these

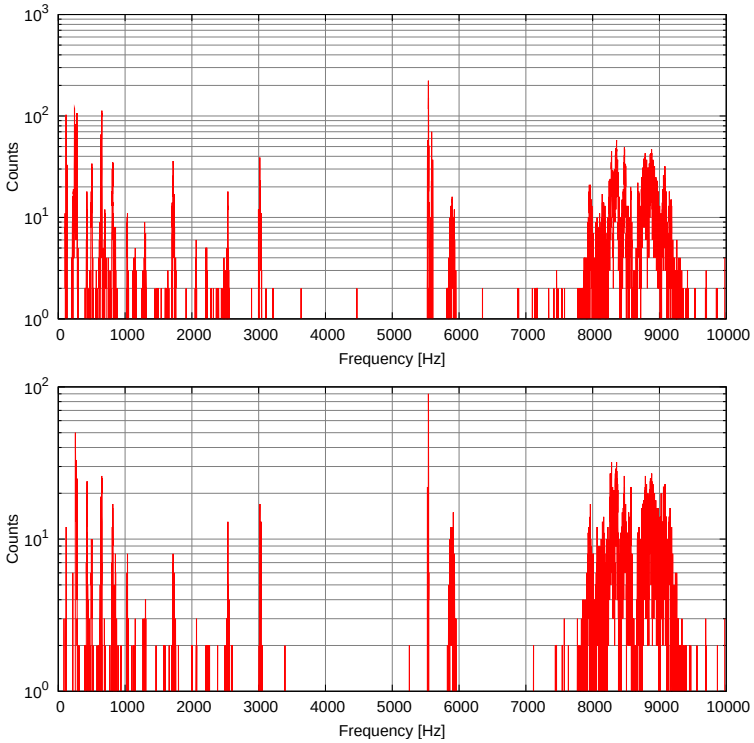

Figure 9.4: Frequency distribution of the clusters detected in the dark fringe in-phase demodulated signal. The top plot refers to the first period and the bottom to the second. Note that the time length of the two periods is not the same.

glitches is modulated with a frequency of about 500 mHz.

9.3 Analysis of coincidence with auxiliary channels

A powerful method to investigate the origin of the dark fringe clusters is to correlate them with those detected in other auxiliary channels. In general, given two lists of clusters for two channels, a first analysis can look for time coincidences. Given a time window δt (usually of the order of 100 ms), two clusters are considered coincident if their times differ less than δt. However, if the number of clusters is large enough, even with small time window, some of them might be considered accidentally coincident. To discriminate this possibility, the coincidence analysis is repeated several times with different time shifts added to one of the two series of clusters. If the coincidences have a physical meaning,

Class no.	Min. freq. [Hz]	Max. freq. [Hz]	Description
1	7800	9300	Power noise
2	5800	5960	Frequency noise
3	2990	3050	
4	2520	2550	
5	2200	2230	
6	2050	2070	
7	1700	1760	
8	1280	1320	
9	1020	1040	
10	800	860	
11	600	710	
12	480	510	
13	410	440	
14	200	300	BMS
15	120	140	BMS

Table 9.1: List of cluster classified depending on their frequency.

the *time-shift histogram*, built counting the number of coincidences found for each time shift, should have a large peak around zero. Moreover the number of coincidences for large time shift gives an estimate of the accidental rate. Finally, the width of the peak around zero gives a estimate of the best time window to be used for catching the largest number of real coincident clusters and the smallest number of accidental ones.

Since the clusters detected by HACR have both a mean time and frequency information, it is possible to study the simultaneous coincidence both in time and frequency, with different window sizes (100 ms for time and 200 Hz for frequency). This usually further restricts the number of coincidences found, removing all those pairs of clusters which are not centered around the same frequency. This is normally a desired feature if the coupling mechanism of the noise is known to be linear. Otherwise a more general analysis can be performed by adding simultaneous time and frequency shifts to one of the two series of clusters and building a *double-shift histogram*.

9.3.1 Coincidences with beam monitoring system error signals

As already anticipated, during the first period of science mode most of the clusters detected at frequencies below 600 Hz were identified to be caused by the bad behavior of the beam monitoring system. For this reason it is interesting

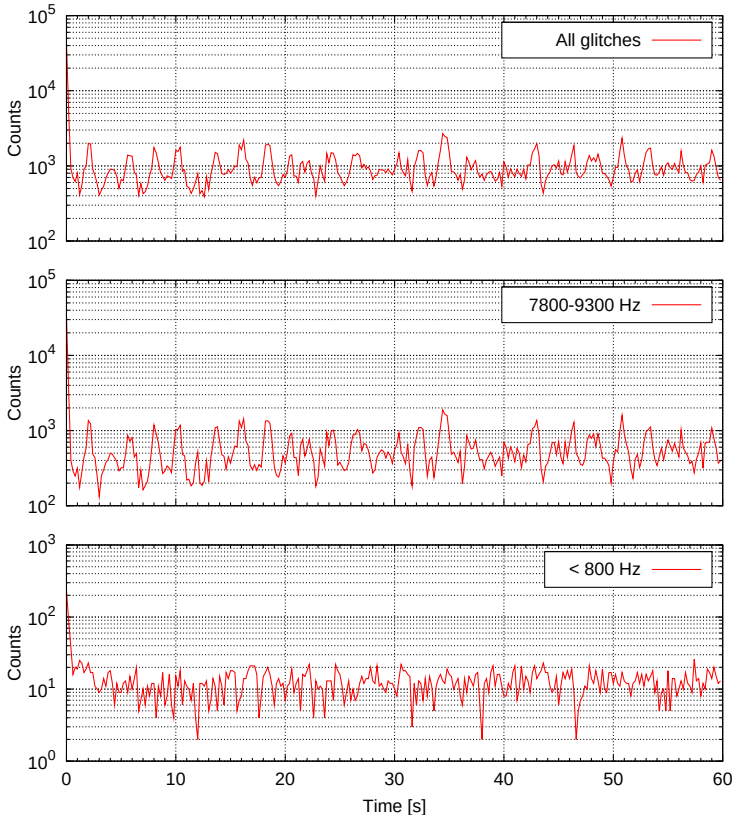

Figure 9.5: Auto-correlogram of the dark fringe in-phase signal clusters, for some selected frequency bands.

to carry out a coincidence analysis between the dark fringe clusters and those detected in the four BMS error signals. The result of the time-shift analysis is shown in fig. 9.6. The coincidences found at zero time-shift are physical, even if their number is not large. The coincidences both in time ($\delta t = 100\ ms$) and frequency ($\delta f = 500\ Hz$) are concentrated at frequencies below 250 Hz, mainly in correspondence of the BMS mount resonances (see sec. 7.6.1). However, comparing the frequency distribution of dark fringe clusters before and after the BMS repairing (see fig. 9.7), it appears that also clusters at higher frequencies, up to 800 Hz, are less frequent, suggesting a non-linear propagation of BMS noise to the dark fringe.

9.3.2 Coincidences with quadrature signal

Since the quadrature demodulated signal of the dark fringe beam is almost completely not sensitive to gravitational waves, it is interesting to analyze the

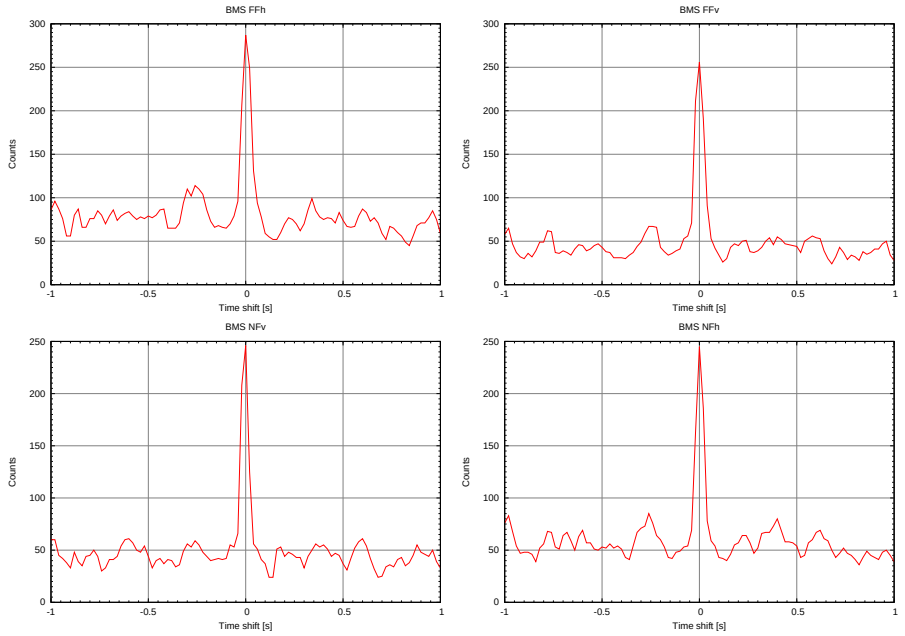

Figure 9.6: Time shift plots for coincidences between the dark fringe signal and the four BMS error signal.

coincidence between clusters in the main in-phase signal and in the quadrature one. The result of the time-shift analysis is shown in fig. 9.8. The distribution is indeed strongly peaked, showing that the coincidences found have physical meaning, but the maximum is not found for zero time shift, and the distribution appears significantly asymmetric. However, if also frequency coincidence is required, this asymmetry disappears. A double time and frequency shift analysis gave the result shown in fig. 9.9. The distribution shows at least three peaks:

- the expected one at zero shifts;
- a big and wide peak centered around $\Delta t = 70$ ms and $\Delta f = 8100$ Hz;
- a smaller one centered around $\Delta t = 60$ ms and $\Delta f = 2500$ Hz;

The last two peaks mean that low frequency clusters in the quadrature demodulated signal are coincident with high frequency ones in the phase signal (see fig. 9.10). In particular almost all clusters detected in the 7.5-9.5 kHz region in the in-phase signal are coincident with quadrature clusters below 900 Hz. Similarly the in-phase signal clusters around 2 and 3 kHz are coincident with some in the quadrature between 400 and 900 Hz.

In conclusion a relevant part of the clusters detected in the dark fringe signal in the low frequency region (below 1 kHz) are coincident in both time

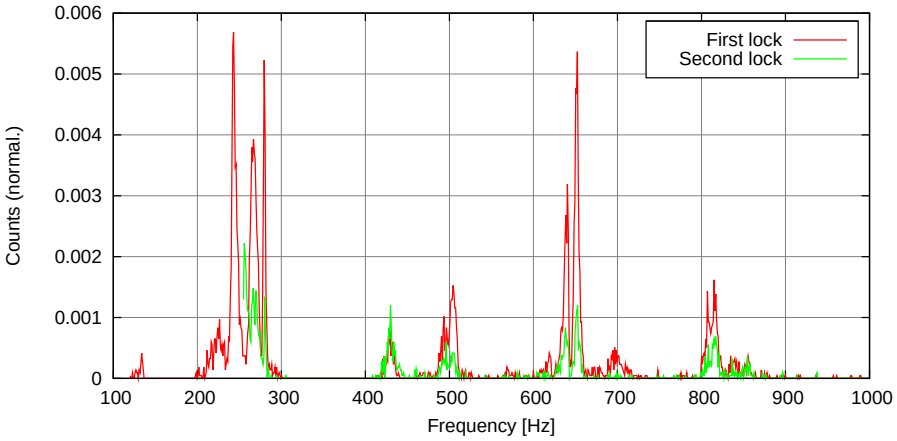

Figure 9.7: Comparison of the normalized frequency distribution of dark fringe clusters before and after the repairing of the BMS actuator.

and frequency with similar clusters in the quadrature signal. Instead, those around 2 and 3 kHz are coincident in time with clusters in the quadrature signal, but the frequency must be shifted by 2.5 kHz to have double coincidence: the quadrature clusters below 1 kHz are coincident with the in-phase one at higher frequency. The same is true for almost all the in-phase clusters in the 8-9 kHz region: they are coincident with quadrature clusters in the same low frequency region.

The mechanism that creates this non-linear relation between in-phase and quadrature clusters is still under investigation.

9.4 Conclusions

The strength of the HACR algorithm is its speed: it is possible to simultaneously analyze tens of channels without the need of large computing power. This makes it very useful for commissioning purposes, since it can give quick and quantitative indications of the signals glitchiness. Moreover the results can be used to perform coincident analysis. This gives another perspective on the detector noise characterization. It is not unlikely for example that a noise which is normally not limiting the sensitivity, and therefore is not considered important by a linear projection analysis, can couple in a highly non-stationary way and generate clusters in the main signal as well as in other ones.

During the science run, the periodic report web pages gave a valuable data quality tool, since it allowed to easily compare the number and distribution of cluster during different locks and periods, pointing out possible problems in the detector.

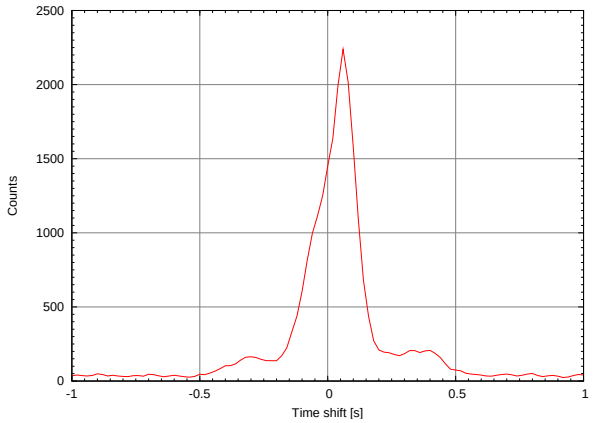

Figure 9.8: Time shift plot for coincidences between the dark fringe in-phase and quadrature signals.

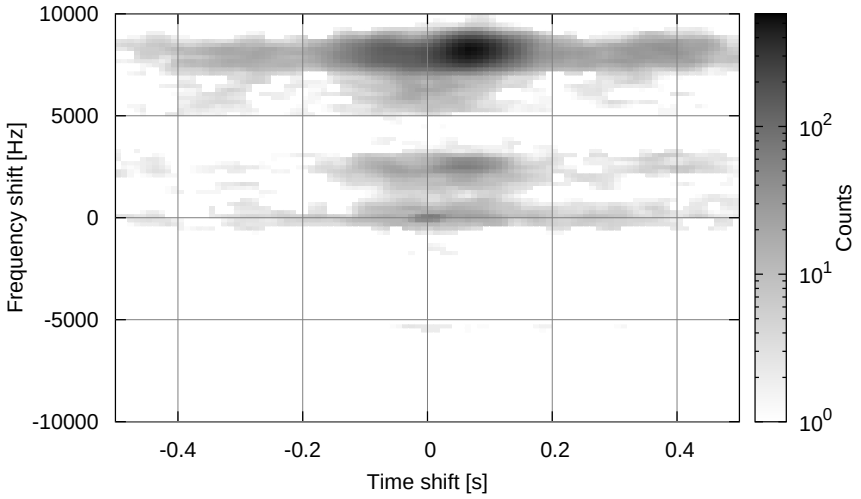

Figure 9.9: Time and frequency shifts histogram for double coincidences between the dark fringe in-phase and quadrature signals.

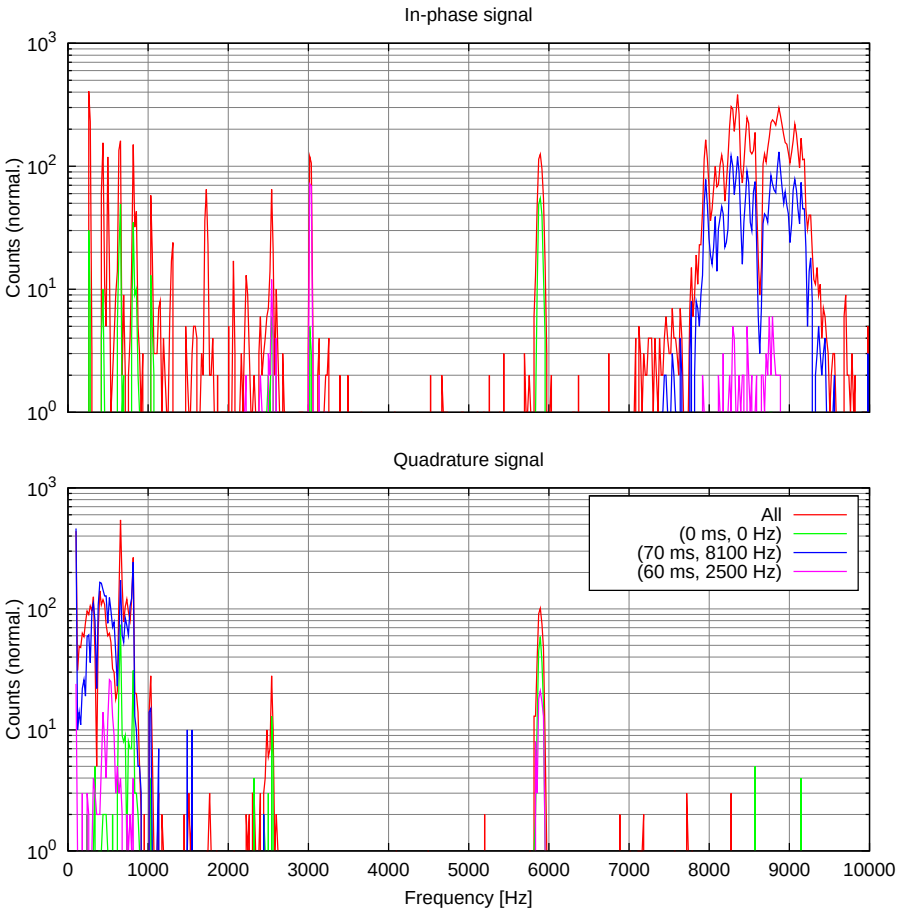

Figure 9.10: Frequency distribution of the in-phase and quadrature signal clusters found to be coincident with different time and frequency shifts, corresponding to the peaks in fig. 9.9.

Part III

Conclusions

Conclusions

The work done for the commissioning of the Virgo interferometer in the last three years, since the first lock of the recycled configuration, has brought the detector to a remarkable sensitivity, comparable with those of the LIGO scientific collaboration (see fig. 9.11). The duty cycle of science mode data during the first Virgo science run has been higher than 80%, with stable sensitivity.

During the time spent working in the Virgo project I have been involved mainly in commissioning work, under several different aspects.

Angular sensing and control system. I worked for one year with the alignment group to the first implementation of the angular control of the mirrors in the full recycled configuration of the interferometer, before the C6 an C7 commissioning runs (see chap. 4).

Length sensing and control system. The main part of my commissioning work was carried out together with the locking group, for the re-implementation of the control system after the increase of the input power. After the first re-locks of the detectors I have been strongly involved in the development of better control strategies to improve the stability and performances of the locking: the slow servo systems to stabilize on the long term the unitary gain frequencies of the loops and other locking parameters; control filters improvements to reduce the noise re-injected in the dark fringe signal (see chap. 3). Moreover I worked on locking characterization: to the reconstruction of the longitudinal optical matrix (see sec. 5.5); to the identification of the correct operating point which lead to the implementation of the sidebands balancing servo system, acting on the longitudinal locking point (see sec. 5.7). These studies made possible to further improve the performance of the longitudinal control system, bringing it to the level of being no more a limiting source of noise at any frequency.

Control noise studies. I started a systematic campaign of characterization of the contribution to the dark fringe noise coming from control systems. The main outcomes of this work have been: the implementation of an auto-

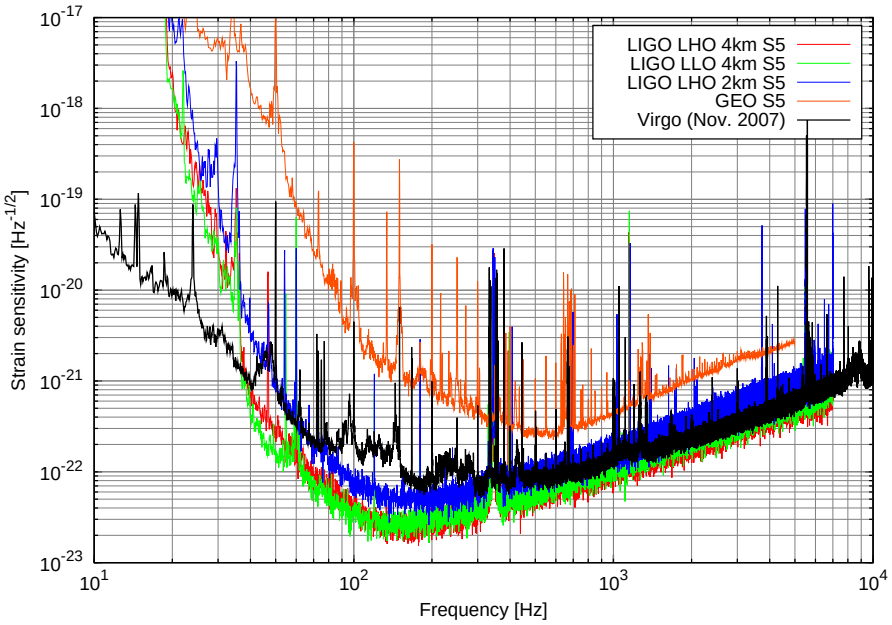

Figure 9.11: Comparison of the typical Virgo sensitivity during the first science run with that of the LSC detectors during the S5 run.

matic procedure for the measurement of longitudinal and angular control noise budgets (see sec. 7.3 and 7.5), now routinely used during the science run; the estimation of the contribution of frequency noise to the sensitivity and the measurement of the transfer function between frequency noise and dark fringe signal (see sec. 7.4); the implementation of improved control filters to reduce the noise coming from some servos (see chap. 7).

Noise studies. I focused mainly on the implementation of tools and analysis techniques for the characterization of non-stationary noises (see chap. 8). To this goal I developed several noise analysis tools that are providing on-line data during the run: *NonStatMoni* to monitor the variation with time of band-limited RMS of the dark fringe and environmental signals, together with an off-line analysis tool that can periodically generate web reports; *LineMonitor* (see sec. 8.1.1), which computes the spectrum of a signal and identify the main narrow lines, writing the results in the main data stream; *VirgoHACR* to detect short transient noises on many different channels (see chap. 9). I also developed several techniques to analyze the results of these tools, like the non-stationarity studies explained in sec. 8.2.2.

Environmental noise. I collaborated with the environmental studies group

to characterize the coupling of acoustic and seismic noise through diffused and scattered light, implementing analysis techniques to better understand the non-linear behavior of these noise couplings (see sec: 7.11).

In terms of the maximum detection range for coalescing neutron stars, in the last three years the detector sensitivity has improved enormously, passing from 80 kPc during the C6 commissioning run (September 2005) to more than 5 MPc in the months after the end of VSR1 (December 2007). There is still a lot of work to be done to improve the detector sensitivity: the main source of noise below some hundreds Hz is understood to be of environmental origin, coupling through diffused light. Moreover the sensitivity is close to be limited by actuation noise at the lowest frequencies (10-30 Hz).

In the near future major upgrades of the detector is planned, moving toward the Virgo+ project [88]. The lase power will be increased from 20 to 50 W. This implies that thermal effects in the input mirrors will increase accordingly. For this reason a thermal compensation system in under development, and it will be installed and commissioned before the increase of input power. Other upgrades are foreseen: the entire digital data acquisition and control system will be replaced; the two arm cavity mirrors will also be replaced with the goal of increasing the finesse from 50 to 150. Finally it is foreseen to install monolithic suspensions to reduce the thermal noise at low frequencies. This should increase the design coalescing binary horizon up to about 50 MPc [88, 89].

Part IV

Appendices

Appendix A

Fields inside optical systems

This appendix collects several computations of fields and signals in different kind of optical systems. All the computations are carried out in the plane wave approximation, without considering the effect of higher order modes. More general computations can be found also in [90].

A.1 Basic conventions

In the plane wave approximation, the beam entering in an optical system can be described by its (complex) amplitude and its frequency:

$$E(t) = E_0 \, e^{i\omega t} \tag{A.1}$$

In general the frequency $\omega/2\pi$ can be that of the main laser (which will be indicated simply by ω) or of one of the radio-frequency sidebands generated by frontal modulation, namely $\omega \pm \Omega$.

The effect of the reflection on a mirror can be described as follows (see fig. A.1). If the mirror is still, the amplitude of the transmitted and reflected beams can be written as

$$\begin{aligned} E_T &= t \, E_0 \\ E_R &= ir \, E_0 \end{aligned}$$

where t and r are real amplitude transmission and reflection coefficients and the conventions used here are those of [12].

Any motion of the mirror can be described as a displacement $x(t)$ from a fixed reference point. If this displacement is constant, the effect on the reflected beam would be simply a dephasing given by

$$E_R = ir \, e^{2ikx} \, E_0$$

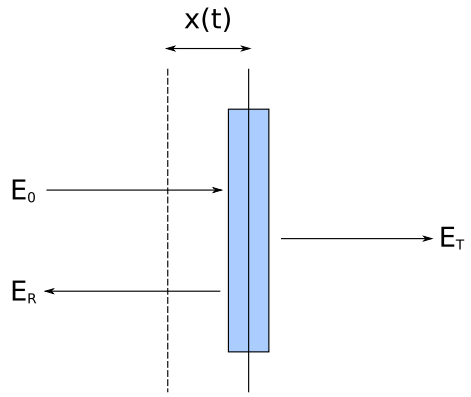

Figure A.1: Conventions for transmitted and reflected beams by a semi-reflecting mirror.

where $k = \frac{\omega}{c}$. This results is still true if the variation of the displacement is small in the time the light needs to cover it, which is equivalent to the requirement that the speed of the mirror must be much less than the speed of light. This is of course true with very good accuracy. Therefore the effect of a moving mirror is a time varying dephasing:

$$E_R(t) = ir\ e^{2ikx(t)}\ E_0$$

If the displacement of the mirror is smaller than the wave-length of the laser beam, namely $\frac{|x(t)|}{k} \ll 1$, then the previous expression can be approximated to first order:

$$E_R(t) \approx ir\ \left[1 + 2ikx(t)\right]\ E_0$$

To compute transfer function from mirror motions to optical signals, it is useful to consider monochromatic motions given for example by

$$x(t) = x_0\ \cos(2\pi\omega_x t) = \frac{x_0}{2}\left(e^{2i\pi\omega_x t} + e^{-2i\pi\omega_x t}\right)$$

In conclusion to completely characterize an optical system (at the linear order) it is sufficient to consider an input field with two components: one oscillating at the main frequency ω and one at $\omega+\omega_x$ and to compute the transmission coefficients of both components to the output port, taking into account the effect of the perturbation added inside the system. If the fields are described by bi-dimensional vectors, this can be expressed in matrix notation:

$$\begin{pmatrix} E_0 \\ E_x \end{pmatrix}_{out} = \mathbf{M} \begin{pmatrix} E_0 \\ E_x \end{pmatrix}_{in}$$

where $\mathbf{M}$ is a two by two matrix. For example the effect of a moving mirror is

given by[1]

$$\mathbf{M} = ir\left(\mathbf{1} + \begin{bmatrix} 0 & 0 \\ 2ikx_0 & 0 \end{bmatrix}\right)$$

and the propagation over a distance L by

$$\mathbf{P}(L) = \begin{bmatrix} e^{ikL} & 0 \\ 0 & e^{i(k+k_x)L} \end{bmatrix}$$

where $k_x = \frac{\omega_x}{c}$.

A.2 Powers and demodulation

The input field can be decomposed in a carrier and two RF sidebands. For small modulation index m

$$E_{IN}(t) = E_0(t)e^{i\omega t}\left[\left(1 - \frac{m^2}{4}\right) + i\frac{m}{2}e^{i\Omega t} + i\frac{m}{2}e^{-i\Omega t}\right]$$

where the amplitude $E_0(t)$ can vary slowly (with respect to ω and Ω) to take into account a possible perturbation added to the input, like amplitude, phase or frequency noise. In general the output field can be written in similar way

$$E_{OUT}(t) = e^{i\omega t}\left[A_0(t) + A_+(t)e^{i\Omega t} + A_-(t)e^{-i\Omega t}\right]$$

where the A coefficients can be computed given the system matrix defined above $M_{ij}(k, k_x)$ as a function of the field and perturbation frequencies:

$$\begin{aligned}
A_0(t) &= \left(1 - \frac{m^2}{4}\right) E_0(t)\left[M_{11}(k,0) + M_{12}(k,k_x)e^{i\omega_x t}\right. \\
&+ \left. M_{12}(k,-k_x)e^{-i\omega_x t}\right] \\
A_+(t) &= i\frac{m}{2}E_0(t)\left[M_{11}(k+k_\Omega,0) + M_{12}(k+k_\Omega,k_x)e^{i\omega_x t}\right. \\
&+ \left. M_{12}(k+k_\Omega,-k_x)e^{-i\omega_x t}\right] \\
A_-(t) &= i\frac{m}{2}E_0(t)\left[M_{11}(k+k_\Omega,0) + M_{12}(k-k_\Omega,k_x)e^{i\omega_x t}\right. \\
&+ \left. M_{12}(k-k_\Omega,-k_x)e^{-i\omega_x t}\right]
\end{aligned}$$

A photo-diode placed at the system output port detects a total power given by:

$$\begin{aligned}
P_{OUT}(t) &= |E_{OUT}(t)|^2 \\
&= |A_0|^2 + |A_+|^2 + |A_-|^2 \\
&+ e^{i\Omega t}\left(A_0^* A_+ + A_0 A_-^*\right) + e^{-i\Omega t}\left(A_0^* A_- + A_0 A_+^*\right) \\
&+ e^{2i\Omega t}A_-^* A_+ + e^{-2i\Omega t}A_+^* A_-
\end{aligned}$$

[1] This is not the most general form of this matrix. Indeed, the $(1,2)$ off-diagonal matrix element could be different from zero, introducing a down-conversion effect of the field at ω. However, this is neglected here since, assuming the field at ω to be small, it would give a second order effect. Moreover, this form of $\mathbf{M}$ is enough to compute all optical transfer functions from mirror displacement to any field.

As usual the mean power, or *DC signal*, can be extracted, neglecting all component with oscillatory behavior:

$$DC(t) = |A_0|^2 + |A_+|^2 + |A_-|^2 \tag{A.2}$$

and the in-phase and quadrature demodulated signals can be obtained by mixing with a sine or cosine wave at the modulation frequency Ω and taking only the low frequency part of the result:

$$AC_p(t) = P_{OUT}(t) \cdot \cos\Omega t = \frac{1}{2}\mathrm{Re}\left[A_0 A_-^* + A_0^* A_+\right] \tag{A.3}$$

$$AC_q(t) = P_{OUT}(t) \cdot \sin\Omega t = \frac{1}{2}\mathrm{Im}\left[A_0 A_-^* + A_0^* A_+\right] \tag{A.4}$$

More in general the demodulation can be done with a cosine wave shifted by an arbitrary phase ϕ and the result will be

$$AC_\phi(t) = \frac{1}{2}\mathrm{Re}\left[e^{-i\phi}\ \left(A_0 A_-^* + A_0^* A_+\right)\right] \equiv \mathrm{Re}\left[e^{-i\phi} AC\right] \tag{A.5}$$

where the complex demodulated signal has been defined[2].

In a similar way the frequency response of the output demodulated signal to a perturbation added inside the system can be computed by specialization of the above formulas:

$$\begin{aligned} AC(\omega_x) = -\frac{im}{4}\left(1-\frac{m^2}{4}\right)\Big[& -M_{12}^*(k,k_x)M_{11}(k-k_\Omega,0) \\ & -M_{11}(k,0)M_{12}^*(k-k_\Omega,-k_x) \\ & +M_{12}^*(k,-k_x)M_{11}(k+k_\Omega,0) \\ & +M_{11}^*(k,0)M_{12}(k+k_\Omega,k_x)\Big] \end{aligned} \tag{A.6}$$

If the perturbation is added to the input beam instead of inside the system, this result is slightly different. The input field can be given in general by

$$E_{IN}(t) = \left(1+\alpha e^{i\omega_t t} + \beta e^{-i\omega_x t}\right)\ E_0(t)e^{i\omega t}\left[1 + i\frac{m}{2}e^{i\Omega t} + i\frac{m}{2}e^{-i\Omega t}\right]$$

and the frequency response of the demodulated signals is given by

$$\begin{aligned} AC(\omega_x) = -\frac{im}{4}\left(1-\frac{m^2}{4}\right)\Big[& -\alpha M_{22}^*(k,k_x)M_{11}(k-k_\Omega,0) \\ & -\beta M_{11}(k,0)M_{22}^*(k-k_\Omega,-k_x) \\ & +\beta M_{22}^*(k,-k_x)M_{11}(k+k_\Omega,0) \\ & +\alpha M_{11}^*(k,0)M_{22}(k+k_\Omega,k_x)\Big] \end{aligned}$$

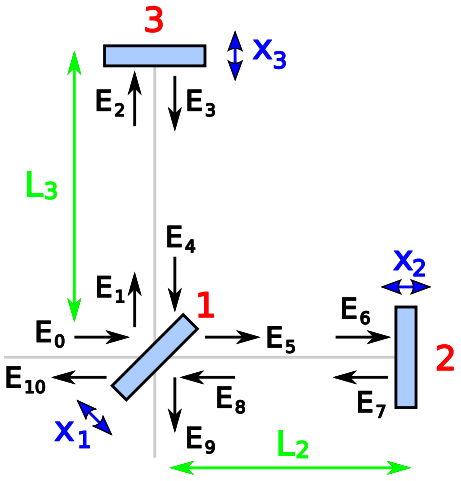

Figure A.2: Scheme of a simple Michelson interferometer, with the names conventions used and explained in the text.

A.3 Simple Michelson interferometer

Referring to fig. A.2, the beam splitter is the mirror number 1 and its transmission and reflection coefficients are denoted by t_1 and r_1 (they are usually both equal to $1/\sqrt{2}$). Similarly the two arm mirrors are denoted by 2 and 3 and their distance from the beam splitter by L_2 and L_3. All three mirrors are allowed to move at the signal frequency ω_x, with amplitudes given by x_i. The naming convention for fields are shown in fig. A.2.

The two interesting fields are at the interferometer reflection E_{10} and at the dark port E_9. Let the propagation matrix along the two arms be P_2 and P_3 and the reflection matrices for the three mirrors be

$$\begin{aligned} \hat{R}_1 &= ir_1\left(1 \pm \sqrt{2}R_1\right) \\ \hat{R}_2 &= ir_2\left(1 + R_2\right) \\ \hat{R}_3 &= ir_3\left(1 + R_3\right) \end{aligned}$$

where the factor $\sqrt{2}$ for the beam splitter is necessary to take into account its 45 degrees orientation and the sign depends on the direction the incoming beam is hitting the mirror from. The R_i matrices are simply given by

$$R_i = 2ikx_i \begin{bmatrix} 0 & 0 \\ 1 & 0 \end{bmatrix}$$

[2]Note that in this expression the field amplitudes are used. In the case of a single cavity, the carrier can be treated as a real field, while the two sidebands are pure imaginary numbers. The complex conjugation then introduces a sign difference between the two terms in eq. A.5.

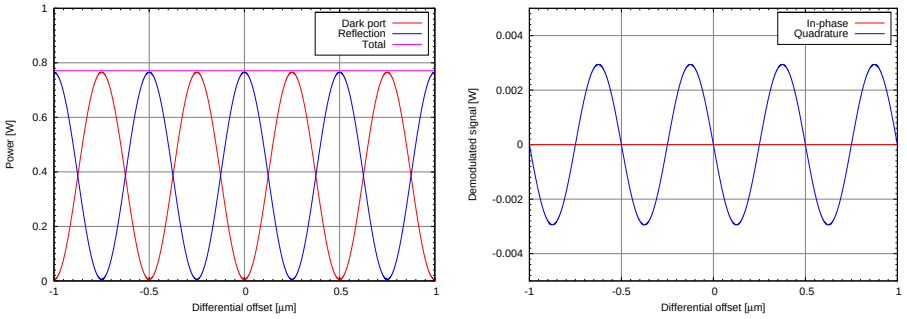

Figure A.3: Example of output signals from a simple Michelson interferometer. The parameters have been chosen as follows: $r_1 = t_1 = 1/\sqrt{2}$, $r_2 = 0.8$, $r_3 = 0.95$, $L = 3000$ m, $\Delta L = 1.2$ m, $\lambda = 1$ μm, $m = 0.1$, $\Omega = 2\pi \cdot 6.2 \cdot 10^6$ rad/s. The input power is 1 W. On the left the powers reflected and transmitted to the dark port are shown. On the right the in-phase and quadrature demodulated signals at the dark port are plotted.

With these conventions, the fields reflected and transmitted by the interferometer are given by

$$\begin{aligned} T_{MICH} = \frac{E_9}{E_0} &= -r_1 r_2 t_1 (1 - \sqrt{2}R_1) P_2 (1 + R_2) P_2 \\ &\quad -r_1 r_3 t_1 P_3 (1 + R_3) P_3 (1 + \sqrt{2}R_1) \\ R_{MICH} = \frac{E_{10}}{E_0} &= -i r_1^2 r_3 (1 + \sqrt{2}R_1) P_3 (1 + R_3) P_3 (1 + \sqrt{2}R_1) \\ &\quad +i t_1^2 r_2 P_2 (1 + R_2) P_2 \end{aligned}$$

Since all mirror motions are considered small and only linear effect are to be considered, the above expressions can be simplified by keeping only terms containing at most one R operator:

$$\begin{aligned} T_{MICH} &= -r_1 r_2 t_1 \left(P_2^2 + P_2 R_2 P_2 - \sqrt{2} R_1 P_2^2 \right) \\ &\quad -r_1 r_3 t_1 \left(P_3^2 + P_3 R_3 P_3 + \sqrt{2} P_3^2 R_1 \right) \qquad \text{(A.7)} \\ R_{MICH} &= -i r_1^2 r_2 \left(P_2^2 + P_2 R_2 P_2 \right) \\ &\quad -i r_1^2 r_3 \left(P_3^2 + P_3 R_3 P_3 + \sqrt{2} R_1 P_3^2 \right) \qquad \text{(A.8)} \end{aligned}$$

From these equations the full expression of the two operators can be easily computed. It is customary to define *common mode* and *differential mode* lengths

and motions by

$$\begin{aligned} L_2 &= L + \frac{\Delta L}{2} \\ L_3 &= L - \frac{\Delta L}{2} \\ x_2 &= x_c + \frac{x_d}{2} \\ x_3 &= x_c - \frac{x_d}{2} \end{aligned}$$

Equations A.7 and A.8 have to be specialized in different ways for carrier and sidebands, since the frequency and the interference conditions are different. The carrier is usually kept near destructive interference at the dark port. Its transmission coefficient can be derived form the $(1,1)$ element of eq. A.7:

$$-e^{-ik(\Delta L-2L)}r_1\left(e^{2i\Delta Lk}r_2+r_3\right)t_1$$

The destructive interference is obtained when $e^{2i\Delta L_0 k} = -1$. Therefore the differential mode length can be expressed as a displacement from this value $\Delta L = \Delta L_0 + D$. In a similar way the value of the common mode length can be expressed as the displacement C from the point defined by $e^{2iL_0k} = 1$. These displacements are often called *offsets*. Afterward, some approximations can be considered. First of all $k_x \ll k$ can be used everywhere except inside the exponents, where some care is necessary. Indeed it is possible to assume $k_x D \approx 0$, $k_x C \approx 0$. For the sidebands, the same conditions must be used, with the approximation $k_\Omega \ll k$. The final expressions for the transmission and reflection matrices are quite long and are not reported explicitly here.

Using the approximated version of eq. A.7 and the expressions found in the previous section for DC and demodulated signals (eq. A.2 and A.3) it is possible to compute the power reaching the dark port and the one reflected as a function of the common and differential mode offsets. From eq. A.2 the transmitted and reflected powers can be computed:

$$\begin{aligned} DC_{REF} &= P_{IN}\left[r_1^4 r_3^2 + r_2^2 t_1^4 + r_1^2 r_2 r_3 t_1^2 \cos(2Dk)\right. \\ &\quad \left.\left(2 - m^2 + m^2\cos(2\Delta L k_\Omega)\right)\right] \qquad \text{(A.9)} \\ DC_{TRA} &= P_{IN}\left[r_1^2 t_1^2\left(r_2^2 + r_3^2 + r_2 r_3 \cos(2Dk)\right.\right. \\ &\quad \left.\left.\left(m^2 - 2 - m^2\cos(2\Delta L k_\Omega)\right)\right)\right] \qquad \text{(A.10)} \end{aligned}$$

The power at the dark port is indeed minimum when the differential mode offset is zero (see fig. A.3). In this condition the reflected power is of course maximum. The residual power at dark fringe has both a carrier component determined by the asymmetry in the arm end mirror reflections and a sidebands component, determined mainly by the *Schnupp asymmetry* ΔL_0. Both reflected and transmitted powers are independent of the common mode offset C.

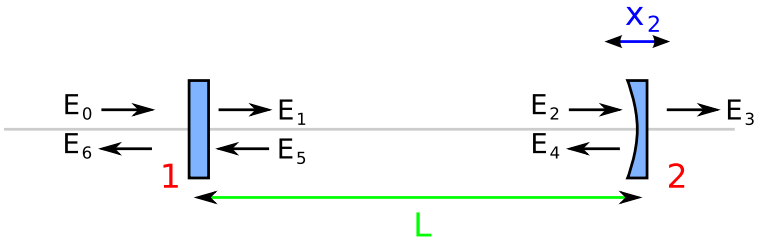

Figure A.4: Scheme of a Fabry-Perot resonant cavity, with the names conventions used and explained in the text.

Similarly, from eq. A.3 and eq. A.5 the demodulated signals at the dark port can be obtained:

$$AC = -\frac{1}{8} e^{-ik_\Omega(\Delta L - 2L)} \left(-1 + e^{2i\Delta L k_\Omega}\right) m(m^2-4) r_1^2 r_2 r_3 t_1^2 \sin(2Dk)$$

This signal is zero both when the ITF is tuned at dark or bright fringe (destructive or constructive interference at the dark port), but the crossings have different slopes, see fig. A.3. This signal has a constant phase, therefore there is one demodulation phase for which the in-phase component is zero and the quadrature contains all the information.

Using eq. A.6 the transfer function from a differential mode motion to the dark fringe signal can be computed:

$$\begin{aligned} TF &= \frac{1}{8} e^{-\frac{i(\Delta L - 2L)(ck_\Omega + f\pi)}{c}} \left(-1 + e^{2i\Delta L k_\Omega}\right) \\ &\quad \left(1 + e^{\frac{2i\Delta L f \pi}{c}}\right) km(m^2-4) r_1^2 r_2 r_3 t_1^2 \end{aligned}$$

This transfer function is almost flat in amplitude up to a frequency which depends only on the asymmetry in the arm lengths (for an asymmetry of 1.2 m this frequency is about 40 MHz).

A.4 Fabry-Perot resonant cavity

Referring to fig. A.4, let 1 and 2 denote the input and end mirrors, and r_i, t_i the corresponding reflection and transmission coefficients. The length of the cavity is denoted by L. It is sufficient to consider only motions of one of the mirrors, for example the end one. First of all the field inside the cavity E_1 must be computed. It can be expressed in terms of the following matrix equation:

$$E_1 = t_1 E_0 - r_1 r_2 P_L (1 + R_2) P_L E_1$$

which can be solved, with some care in the order of the operands, obtaining the following result:

$$E_1 = t_1 [1 + r_1 r_2 P_L (1 + R_2) P_L]^{-1} E_0 \tag{A.11}$$

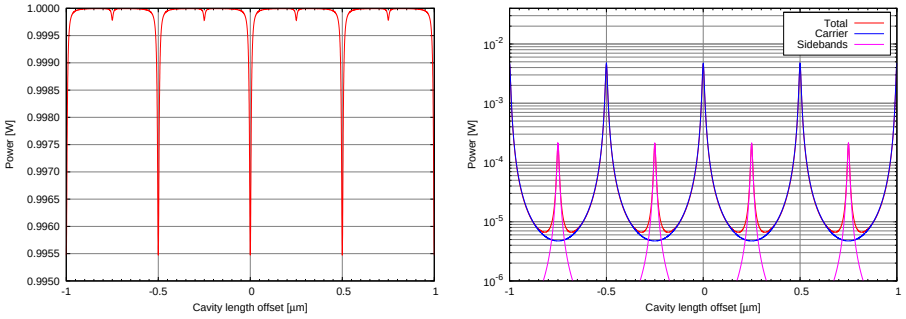

Figure A.5: Power reflected (left) and transmitted (right) by a Fabry-Perot cavity with parameters similar to those of Virgo arm cavities: $L = 3000$ m, $r_1 = 0.93883$, $r_2 = 0.99992$, $m = 0.3$.

From this the transmitted and reflected fields can be easily derived:

$$\begin{aligned} E_T &= t_1 t_2 P_L [1 + r_1 r_2 P_L (1 + R_2) P_L]^{-1} \, E_0 \\ E_R &= i \left[r_1 + r_2 t_1^2 P_L (1 + R) P_L \right. \\ &\quad \left. [1 + r_1 r_2 P_L (1 + R_2) P_L]^{-1} \right] \, E_0 \end{aligned}$$

The carrier and sidebands fields have different resonance conditions inside the cavity. Typically the cavity length is tuned in order to have the carrier at resonance. The modulation frequency is chosen in order to have the sidebands anti-resonant. The $(1,1)$ component of the matrix in eq. A.11 is:

$$\frac{t_1}{1 + r_1 r_2 e^{2ikL}}$$

Therefore the correct resonance conditions are obtained choosing for the carrier $e^{2ikL_0} = -1$ and for the sidebands $e^{2i(k \pm k_\Omega)L_0} = 1$. The previous equations can therefore be simplified and the cavity length can be expressed as an offset from the resonance. Approximations similar to the one adopted for the Michelson interferometer can be applied also here. The final expression for the transmission an reflection matrices are quite long and are not reported here.

The transmitted and reflected powers can be computed, using eq. A.2, as a function of the offset from resonance:

$$P_{TRA} = P_{IN} \left[\frac{t_2^2 t_1^2 \left(1 + r_2^2 r_1^2 - 2\left(-1 + m^2\right) r_2 r_1 \cos\left(2\delta L k\right)\right)}{2 + 2 r_2^4 r_1^4 - 4 r_2^2 r_1^2 \cos\left(4\delta L k\right)} \right]$$

$$\begin{aligned} P_{REF} &= P_{IN} \left[r_1^2 + t_1^2 + \frac{t_1^2 \left(-1 + r_2^2 (r_1^2 + t_1^2)\right)}{1 + r_2^4 r_1^2 - 2 r_1 r_2 \cos(2\delta L k)} \right. \\ &\quad \left. - m^2 \frac{2 r_1 r_2 t_1^2 \left(-1 + r_2^2 (r_1^2 + r_2^2)\right) \cos(2\delta L k)}{1 + r_2^4 r_1^4 - 2 r_1^2 r_2^2 \cos(4\delta L k)} \right] \end{aligned}$$

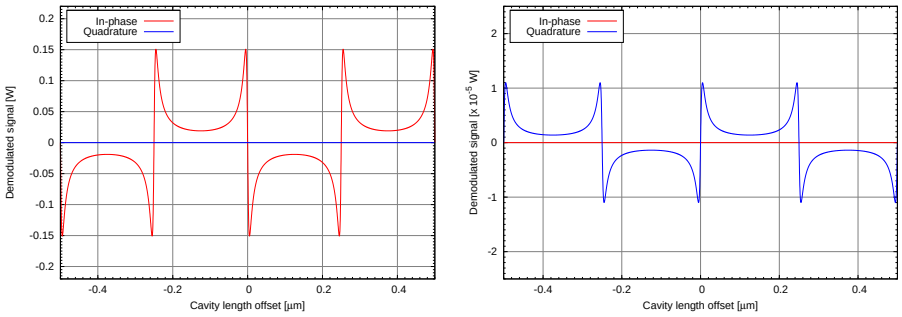

Figure A.6: Demodulated signals in reflection (left) and transmission (right) of a Fabry-Perot cavity with the same parameters of fig. A.5.

The transmitted power is maximum when the cavity is resonant for the carrier, see fig. A.5. A second smaller peak is visible when the sidebands are resonant. The distance between two different resonant peaks is called *free spectral range* (FSR) and it can be expressed both in terms of a change in the cavity length or in the laser frequency:

$$\begin{aligned} \delta L &= \frac{\lambda}{2} \\ \delta\nu &= \frac{c}{2L} \end{aligned}$$

It is customary to define the *finesse* of the cavity as

$$\mathcal{F} = \frac{\pi\sqrt{r_1 r_2}}{1 - r_1 r_2}$$

With these definition the width of the resonance peak (at half height) is given by

$$\delta\nu_{FWHM} = \frac{\delta\nu}{\mathcal{F}}$$

For the Virgo arm cavities the finesse is about 50.

The demodulated signals in reflection and transmission can be computed using eq. A.3 and eq. A.5:

$$AC_{REF} = \frac{m}{4}(m^2-4) r_1 r_2 t_1^2 \frac{\left(1 + r_2^2(r_1^2 + t_1^2)\right)\sin(2\delta Lk)}{1 + r_1^4 r_2^4 - 2 r_1^2 r_2^2 \cos(4\delta Lk)} \tag{A.12}$$

$$AC_{TRA} = i\frac{m}{4}(m^2-4) \frac{r_1 r_2 t_1^2 t_2^2 \sin(2\delta Lk)}{1 + r_1^4 r_2^4 - 2 r_1^2 r_2^2 \cos(4\delta Lk)} \tag{A.13}$$

These are the well known *Pound-Drever-Hall signals* that can be used to control the cavity length (see fig. A.6 and chapter E).

Finally, using eq. A.6 the transfer function from a motion of the end mirror to the transmitted signal can be computed:

$$TF_{TRA} = -i\frac{m(m^2-4)}{2\left(r_1^2 r_2^2 - 1\right)} e^{\frac{4\pi i L f}{c}} \frac{r_1 r_2 t_1^2 t_2^2}{1 - e^{\frac{8\pi i L f}{c}} r_1^2 r_2^2} \tag{A.14}$$

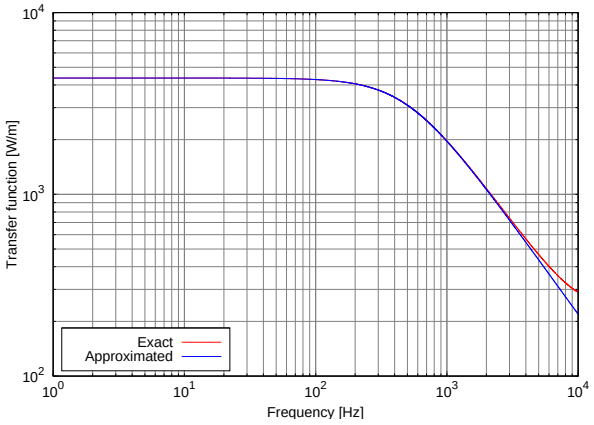

Figure A.7: Transfer function from longitudinal motion of the cavity end mirror to the transmitted demodulated signals, for a Fabry-Perot cavity with the same parameters of fig. A.5. The red curve is the exact expression, while the blue one is the usual one-pole approximation.

For small enough frequencies, the exponential can be approximated at first order and the transfer function is given by a simple pole (see fig. A.7):

$$TF_{TRA}(f) = i\frac{km(m^2-4)r_1 r_2 t_1^2 t_2^2}{2(r_1^2 r_2^2 - 1)^2}\,\frac{1}{1 - i\frac{f}{f_p}}$$

The pole frequency is given by

$$f_p = \frac{1}{2\pi}\frac{c}{2L}\frac{1 - r_1^2 r_2^2}{1 + r_1^2 r_2^2} \approx \frac{c}{4L\mathcal{F}}$$

For a Fabry-Perot cavity like Virgo arms, this pole is at about 500 Hz.

The main feature of a Fabry-Perot cavity, that can be deduced from eq. A.12 or A.14, is that the optical response of the reflected field to a cavity length change is amplified, with respect to a simple mirror, by a factor

$$G = \frac{2\mathcal{F}}{\pi}$$

This is the reason why resonant cavities are used as "optical amplifier" for gravitational wave signals. For the Virgo arm cavities, this amplification factor is about 32.

Appendix B

Lock acquisition technique during VSR1

This appendix describes in details the lock acquisition technique used in Virgo during all the science run. This is the result of the work of the entire locking, alignment and commissioning teams during the last years. After the end of VSR1 it has further evolved, gaining in speed, robustness and noise performances. This is not discussed here, see for example [91].

The full locking acquisition sequence in Virgo is composed of 12 steps, each leaving the interferometer in a stable state. The following sections describe all the actions performed during the procedure. Please refer to [92] and [93] for a more technical description.

B.1 Locking and pre-alignment of the two cavities

B.1.1 Locking of the arm cavities and MICH

The standard state of the uncontrolled Virgo interferometer is with all mirrors roughly aligned except the power recycling one, which is intentionally misaligned by 150 μrad in order to prevent its reflected beam to interfere inside the optical system. In the first step of the locking acquisition procedure, due to this misalignment, the two cavities are locked independently using the in-phase demodulated signals in transmission (`Pr_B7_ACp` and `Pr_B8_ACp`, see fig. B.1) with a standard Pound-Drever-Hall technique. In order to increase the linear range of the error signals, they are normalized using the power transmitted by the

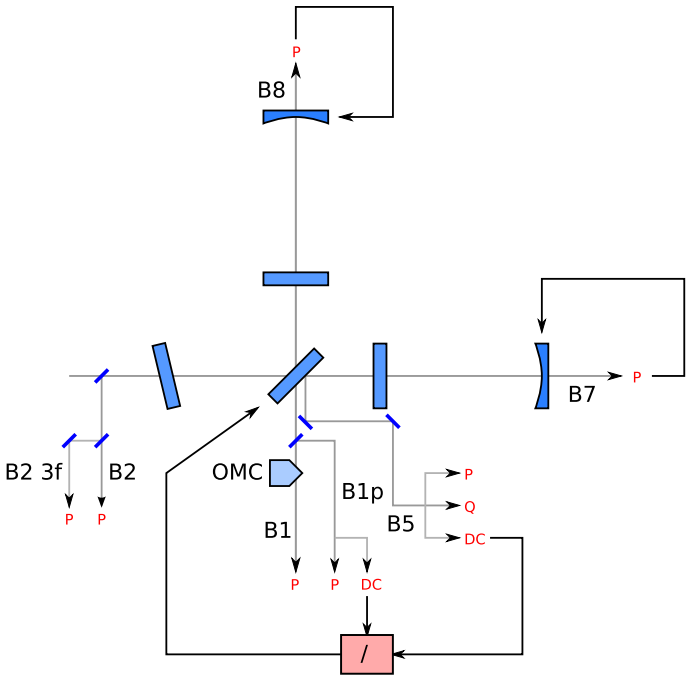

Figure B.1: Scheme of the control strategy for the first step of the lock acquisition procedure. See the text for more explanations

cavities themselves [46]:

$$E_N = \frac{\texttt{Pr\_B7\_ACp}}{\texttt{Pr\_B7\_DC}}$$
$$E_W = \frac{\texttt{Pr\_B8\_ACp}}{\texttt{Pr\_B8\_DC}}$$

The resonance condition at the dark port is chosen on order to be at *half fringe*: the power transmitted there is half of the maximum possible. This condition is well outside the linear range of the demodulated signal, even with normalization. For this reason a *DC locking* is used: the fringe is locked directly to the amount of power which is transmitted to the dark port, normalized by the maximum possible power which is estimated using the power reflected by the north arm and by the secondary face of the beam splitter. In other words, the error signal is given by

$$E_{MICH} = \alpha \frac{\texttt{Pr\_B1p\_DC}}{\texttt{Pr\_B5\_DC}} - \phi$$

where the dark fringe beam used is the one which does not pass through the output mode-cleaner, which is not on resonance yet. In the previous formulas α is a normalization constant which depends essentially on the reflectivity of the

secondary face of the BS mirror and on the fraction of the beam that hits the photo-detectors and ϕ is the *fringe offset* which is set to 0.5 in this step and afterward it is reduced down close to 0 which corresponds to the dark fringe condition. The response of this signal to MICH motions becomes smaller and smaller as the fringe offset decreases, since the dark port power has a typical cosine dependence on the MICH offset.

The PR mirrors does not need to be controlled yet, since it is misaligned.

B.1.2 Fine pre-alignment

After the two cavities and MICH are locked, a *fine pre-alignment* procedure is run with several goals: to align the input beam in order to center it in the north arm cavity; to align the beam splitter to center the reflected beam in the west arm cavity; to align the input and end mirror of both cavity in order to superimpose the beam and cavity axes. To do this, a global automatic alignment system is engaged for the two cavities separately. This system, which will be explained more in details in *chapter 4*, uses the demodulated signals obtained from wave-front sensors placed in transmission of the cavities to reconstruct suitable error signals for the angular position of the input and end mirrors. The misalignment of the PR mirror ensures that the two cavities are independent. These error signals are passed through pure integrator filters to remove their high frequency component and then used as set-points for the local angular control systems of the mirrors. The bandwidth of this *drift control system* is of the order of few tens of mHz. Its main advantage is that the high frequency motion of the mirrors are still controlled by the local systems, easily providing enough gain to damp the suspension angular resonances, while ensuring that the cavity is well aligned with respect to the laser beam.

While this system keeps the cavities aligned, the position of the transmitted beams are measured by cameras and the pointing of the input beam and the BS position are changed accordingly to meet fixed reference position.

All this pre-alignment procedure takes in normal condition few minutes and afterward the drift control system is dis-engaged, since it cannot work with the same error signals during all the lock acquisition sequence. Therefore the mirrors are controlled by the local systems alone keeping them close the correctly aligned position.

B.1.3 Check of main modulation frequency

The main modulation frequency Ω must be precisely tuned to match the resonant peak of the input mode cleaner. The carrier is always kept on resonance by the locking servos of the IMC. If the modulation frequency is chosen in order to match exactly an integer multiple of the IMC free spectral range (about

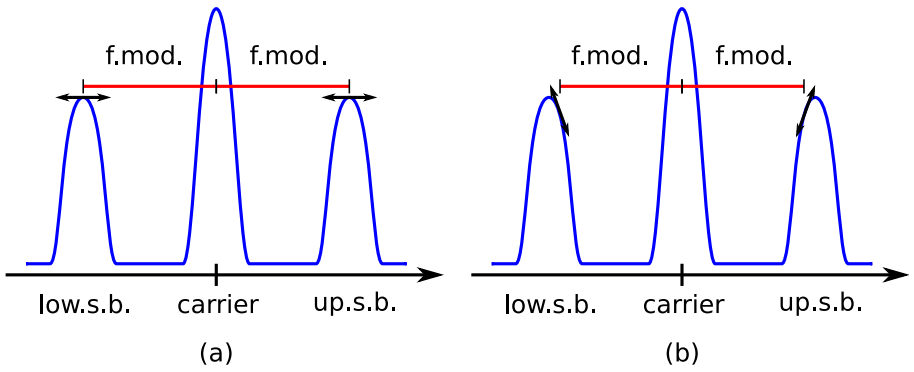

Figure B.2: Effect of a mis-tuning of the main modulation frequency with respect to the IMC length. (a) the frequency is tuned to make the two sidebands exactly resonant (b) the sidebands are not perfectly resonant in the IMC.

1 MHz), then any length variation of the cavity does not couple linearly to a change in amplitude of the sidebands transmitted into the main interferometer (see fig. B.2a). If instead the matching is not perfect (see fig. B.2b), any change in the length of the IMC can couple linearly and differentially to the sideband amplitudes. In other words if the modulation frequency is not well matched to the length of the IMC, any length noise of this cavity can couple directly to the dark fringe signal.

For this reason, during the pre-alignment procedure, a check of the relative matching of the IMC length and modulation frequency is performed. In normal condition a calibration line at 1111 Hz is always added as an external perturbation to the laser frequency. For the IMC cavity this line is equivalent to length noise and it affects the sidebands only if the modulation frequency is not exactly tuned. A fraction of the beam transmitted by the IMC is sent to a photo-detector and demodulated first at Ω and then at 1111 Hz. This signal gives the amplitude of the calibration line as seen by the beating between the carrier and the first order sideband fields. It is therefore directly related to the mis-match between Ω and the IMC length and it can be used as an error signal to tune the modulation frequency.

If the mismatch is small, it is corrected simply changing the modulation frequency. Otherwise the length of the IMC is changed, by unlocking it, moving the top suspension point of the end mirror of the needed amount and re-locking it. After this operation is performed, the lock acquisition can be started again.

The needed accuracy for this tuning, at the present Virgo sensitivity, is a bit less than one Hz, and it can be easily obtained by only checking the matching at the beginning of each lock.

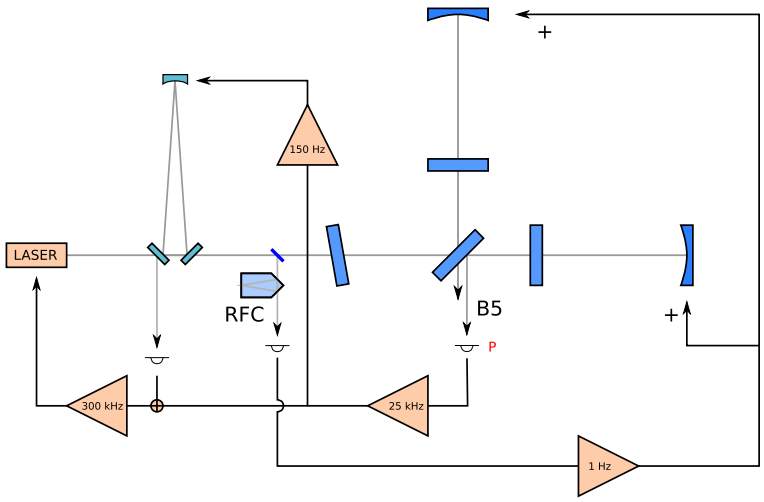

Figure B.3: Control scheme for the laser frequency and the common mode of the interferometer when the second stage of frequency stabilization (SSFS) is engaged

B.1.4 Force reallocation to top suspension point

Another action performed during this first step of lock acquisition is the reallocation of the very low frequency part of the longitudinal corrections to the top stage of the suspensions. This *tidal control*, engaged at the first step for the BS mirror, consist in using the longitudinal correction as set point for the top stage local control after passing through an integrator filter with unity gain around 1 mHz. In this way it is possible to reduce strongly the force applied directly to the mirror and the necessary dynamical range of the lower stage actuators.

For the NE and WE mirror the longitudinal correction is not used for adjusting the set point, but it completely replaces the local control error signals coming from position sensors: the longitudinal correction is therefore mixed with the accelerometer signal, with cross-over frequency at 70 mHz. In this way the same effect of the tidal control is obtained, plus the advantage of avoiding the use of noisy local signal for the suspension control. This particular system is called *global inverted pendulum control* (GIPC).

B.2 Second stage of frequency stabilization

In the second step of the lock acquisition procedure the control strategy for the two arm cavities is modified. As already stated, a change in the laser frequency is equivalent to a change in the length scale. The most sensitive degrees of freedom are those related to the long arm cavities: in particular a change in

their mean length (CARM) is equivalent to a change in laser frequency (eq. 3.6). Moreover the residual frequency noise, with only a stabilization on the IMC and RFC active, is still too high for reaching a good sensitivity. A further stage of stabilization is needed and the only better possible reference available is the mean length of the arms itself.

Therefore during the second step of lock acquisition the *second stage of frequency stabilization* (SSFS) is engaged (see fig. B.3). It uses the error signal coming from the reflection of the north arm (as seen by the `Pr_B5_ACp` signal). The correction is obtained by a suitable control filter to give a unity gain frequency (UGF) which varies between 100 Hz and 25 kHz depending on the state of the interferometer. This is then added to the error signal of the first stage of frequency stabilization (coming from the reflection of the IMC). It also replaces the reference cavity signal for the lock of the input mode cleaner. Indeed, due to the very high gain of the first stage of stabilization, the sum of the IMC reflection and of the SSFS correction signal can be assumed to be zero in the active band of the second stage of frequency stabilization. Therefore the IMC reflection and the SSFS signal can be considered to be equal and opposite. In other words summing these two signal is equivalent to using the IMC reflection for the IMC locking, with the usual unity gain frequency of about 100 Hz.

In this way the laser frequency is kept locked to the mean length of the long arms below some tens of kHz (by the SSFS loop) and the input mode cleaner is simultaneously locked on the laser frequency. In this way however the reference cavity is no more locked and the common mode of the arm cavities is free to swing at low frequency, mainly in correspondence of resonances of the suspensions. This results in an equivalent change in the laser frequency, which can be seen for example by the reference cavity error signal. Therefore this is used, with a bandwidth of about 1 Hz, to feed back a common mode correction to the end mirrors. In this way the mean length of the cavities and finally the laser frequency are still locked to the reference cavity below 1 Hz. This last control loop is usually called the *CARM loop*, since it acts directly on the mechanical common mode of the end mirrors. It must be distinguished from the *SSFS loop* which is the one controlling the laser frequency with high unity gain frequency.

This control scheme is completed by the control of the differential mode of the end mirrors (DARM). A suitable error signal is given by the transmission of one of the two cavities, since any common mode motion is no more visible there due to the action of the SSFS. Actually the demodulated signal coming from the west arm transmission is used to control differentially the end mirrors.

The switch to common and differential mode control and the engagement of the SSFS is done quickly, without any mixing or blending of error signals. At the same time the fringe offset is reduced from 0.5 to 0.4.

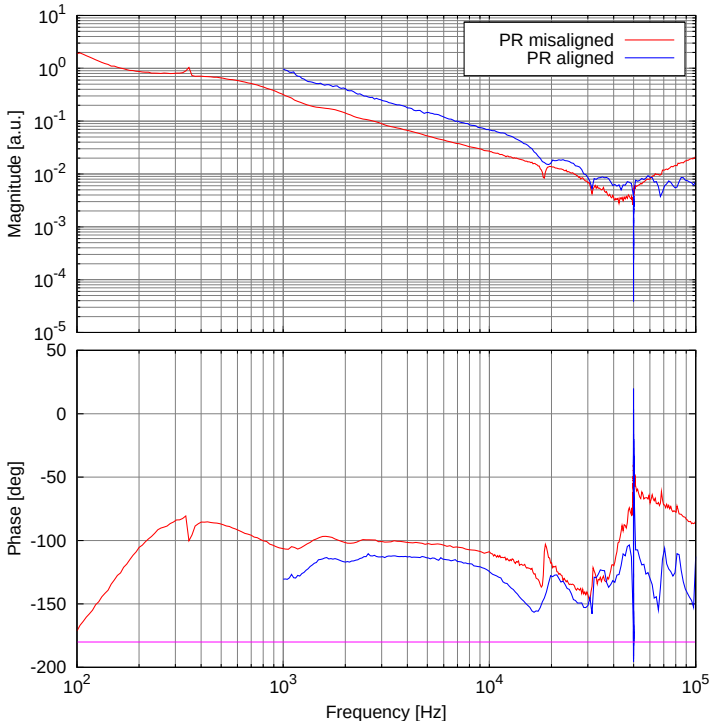

Figure B.4: Measured open loop transfer function of the SSFS loop during the second step of the lock acquisition sequence, when the PR mirror is still misaligned (red) and during the third step, after the re-alignment of the PR mirror (blue).

The SSFS control loop is implemented by means of analog electronics, since due to its high unity gain frequency it must be able to operate up to some hundreds of kHz. This electronic system includes a limited remote control of the gain which is necessary to cope with the great increase in the optical gain during the different steps of the lock acquisition sequence. Indeed when the SSFS is first engaged its unity gain frequency is around 160 Hz (see fig. B.4) while at later steps it increases up to tens of kHz.

B.3 Re-alignment of power recycling mirror

After the engagement of the SSFS control loop the power recycling mirror is realigned from its position at 150 μrad in 15 seconds. During this transition the circulating power inside the interferometer increases by a large amount due to the recycling action of the aligned PR mirror (see fig. B.5 right). Therefore all signals undergo a large change in their optical gain, which is almost completely

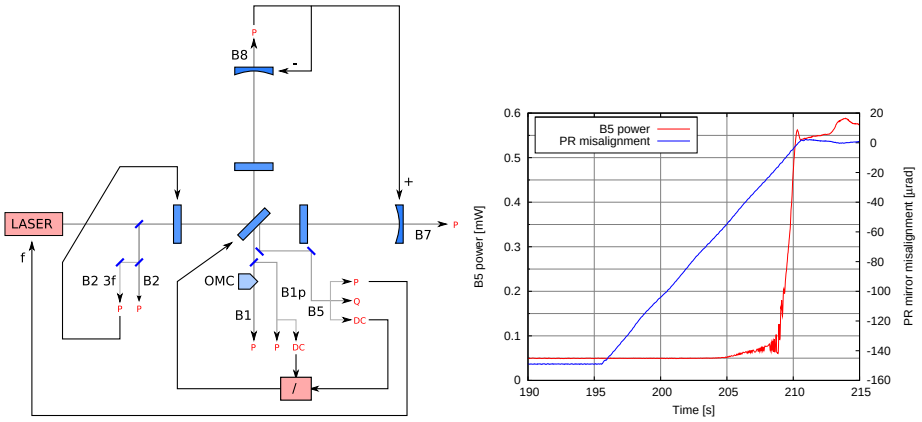

Figure B.5: **Left:** scheme of the interferometer controls at step 3, after the re-alignment of the power recycling mirror. **Right:** change in the power inside the recycling cavity, as measured by a photo-diode on the B5 beam, during the power recycling mirror re-alignment.

compensated by the use of suitable normalizations, as explained in the previous sections. The only exception is the SSFS analog loop: the gain of the corrector filter is changed to compensate the increase in the optical gain, and the new UGF is set around 1 kHz (see fig. B.4). The corrector gain of the SSFS is changed again during later steps to cope with the further increase of circulating power.

At the same time the longitudinal control of the PR mirror is engaged using the in-phase signal coming from the demodulation at 3Ω of the interferometer reflection `Pr_B2_3f_ACp` (see fig. B.5 left). The choice of this particular signal instead of the normal demodulated one is motivated by the fact that the former is robust against changes in the interferometer state, in particular against a change in the fringe offset [46]. The normal demodulated signal strongly changes the gain and even the sign of its response to PRCL motion and it is therefore much more difficult to use it during all the lock acquisition sequence.

This error signal is normalized using the value of the power inside the recycling cavity, as read by `Pr_B5_DC`. In this way the change in optical gain due to the increase of the recycling gain during later steps of lock acquisition is almost completely compensated.

This is the first condition of the interferometer with all mirror aligned and all longitudinal degrees of freedom controlled. Moreover during this step different control filters are engaged for the MICH and PRCL loops to have more gain at low frequency, allowing to obtain a better locking accuracy. Finally the tidal control is engaged also for the PR mirror.

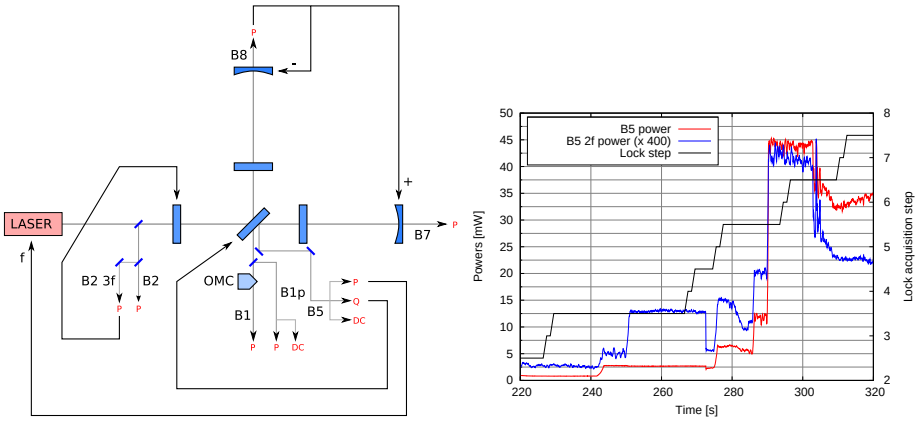

Figure B.6: **Left:** scheme of the interferometer controls at step 6, after the transition to dark fringe. **Right:** Evolution of total and sidebands power (see by the `Pr_B5_2f_ACq` signal) inside the recycling cavity during the lock acquisition sequence.

B.4 Fine pre-alignment of PR mirror

At this point the fringe offset is decreased to 0.2, and the control filter for the DARM loop is changed in order to obtain more gain at low frequency. Also the input mirror coil drivers (see section 2.4) are switched to the low noise configuration, even if they are not used for the control.

Afterward a pre-alignment of the power recycling mirror is performed, by using global signals in a similar way to what is done at step 1 for the arm cavities. The error signals used for these control loops (which have a bandwidth of about 3 Hz) come from wave-front sensors placed on the B5 beam (see chapter 4 for more details). These alignment loops are kept active until the power of the sidebands inside the recycling cavity (measured by the `Pr_B5_2f_ACq` signal) goes above a suitable threshold. At the end of this pre-alignment procedure the PR angular control is switched back to the local sensors.

The fringe offset is then decreased to 0.1 and a fine tuning of several loop gains is performed to maintain the stability of the interferometer. In this configuration the demodulated signals coming from the B5 beam are obtained by using the photo-diode which receive a lower fraction of the total power (usually called *low power diode*), to avoid saturation due to the still large offset from zero of the Pound-Drever-Hall signal for the MICH loop.

B.5 Transition to dark fringe

The locking point of the MICH loop is finally moved to the dark fringe condition, therefore setting the fringe offset to zero. This is done in two steps. The first one changes the fringe offset from 0.1 to 0.05, still using as error signal the ratio of the powers measured by photo-diodes placed in the B1p and B5 beams. However as the locking point approaches the dark fringe condition, the slope of this signal decreases more and more as B1p power becomes closer and closer to its minimum. At the dark fringe this slope would be zero, and therefore this error signal could not be used any more. The last change in the offset from 0.05 to 0 is therefore obtained by using the quadrature demodulated signal of the B5 beam (`Pr_B5_ACq`) instead of the ratio of powers. This is done smoothly by mixing the two signals with a time dependent ramp (this method is usually called *blending* of the two signals). After reaching the dark fringe, there are no more risks of saturating the B5 demodulated signal and therefore they are reconstructed using the high power and *low noise* diode.

After all these actions the interferometer is locked close to its final operating point, with the arm cavities resonant as well as the power recycling one, and the dark point tuned at dark fringe (see fig. B.6). However the error signals used for the longitudinal control loops are not yet the final one:

- the laser frequency is controlled by using the in-phase signal of the B5 beam, still using the low power photo-diode;
- the common mode is controlled by using the reference cavity signal (this remains the same even in later steps);
- the differential mode is controlled using the in-phase demodulated signal obtained from the beam transmitted by the west arm;
- the power recycling cavity length is controlled by the in-phase signal coming from the reflection of the interferometer, demodulated at 3Ω;
- the Michelson d.o.f. is controlled by using the quadrature signal from the beam splitter secondary face reflection (this remains the same even in later steps).

B.6 The thermal transient

B.6.1 Description

After reaching the dark fringe condition, the power build-up inside the recycling cavity is close to its maximum: about 210 W are stored inside the recycling cavity and more than 4.5 kW inside the two Fabry-Perot cavities. In particular the

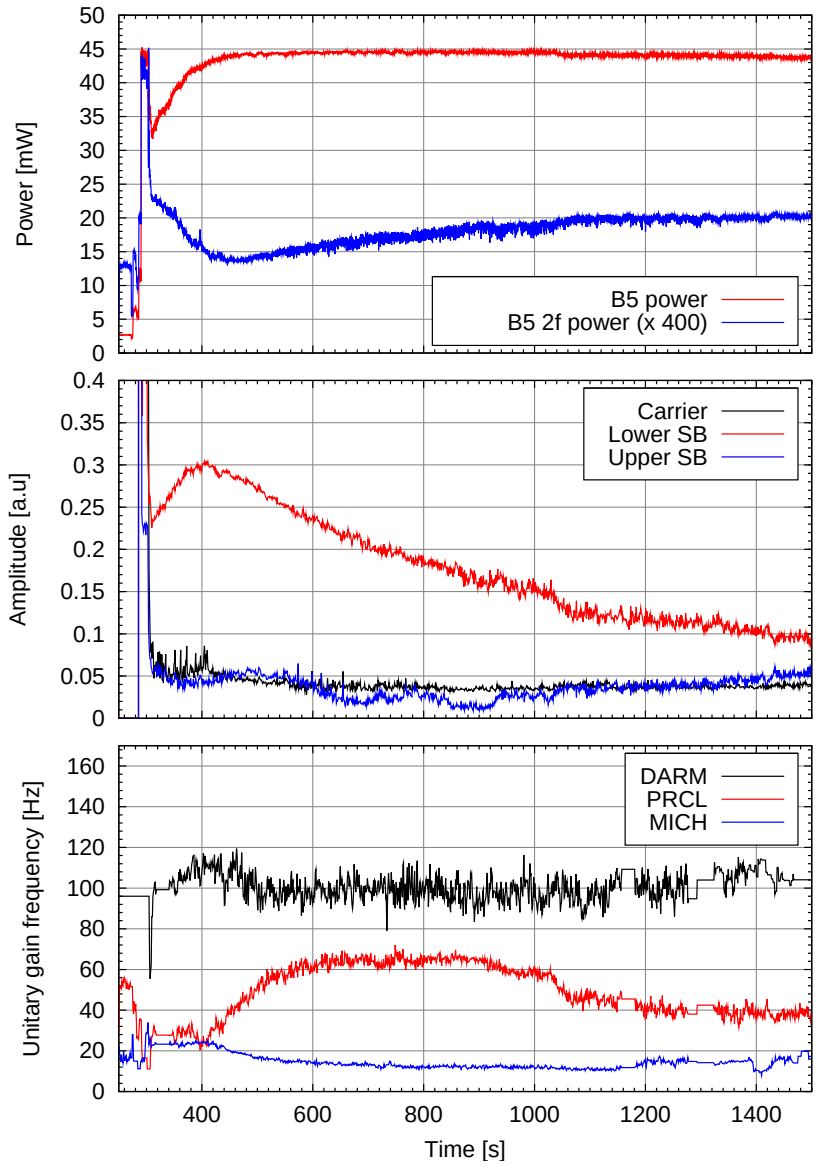

Figure B.7: Evolution of interferometric signals during the thermal transient period. **Top:** powers of carrier and sidebands inside the recycling cavity, as measured by the `Pr_B5_DC` and `Pr_B5_2f_ACq` signals. **Middle:** carrier and sidebands amplitudes at the dark port. These signals are obtained by elaboration of a scanning Fabry-Perot system output (see section 2.5). **Bottom:** unity gain frequency of the three main longitudinal control loops, reconstructed using a suitable calibration line.

power that is transmitted through the input mirrors is high and even assuming low losses in the substrate the absorption can be of the order of 20-30 mW (from simulations [94] and fit to mirror temperature change [95]).

The heating of the input mirrors produce a thermal lensing effect which changes the geometry of the power recycling cavity and in conclusion the resonance conditions of both carrier and sidebands (see fig. B.7). Initially, when the ITF is moved to the dark fringe, the power inside the recycling cavity suddenly increase to its maximum value (around 44 mW on `Pr_B5_DC`). After some seconds the system jumps down to a lower power state (around 30 mW). This change is induced moving the demodulation phase of the signal used to control PRCL. If this jump is not performed, the ITF remains locked on the high power state, but systematically unlocks after few minutes. Otherwise the detector switch to the different lock state, where both carrier and sidebands are not at the best resonance condition. The recycling gains for carrier and sidebands, together with several other interferometric signals, evolve slowly with time, following the heating of input mirrors. After a period of time of the order of half an hour all signals have reached a stable value, with again a high recycling gain of the carrier.

B.6.2 Simulations

The reason of this behavior has been understood by means of careful simulations, both computing the effect of thermal absorption in the mirror substrate [95] and the induced change in the resonance conditions [94]. The main effect of the power absorption is a thermal lensing in both the mirror substrate and coating. These have two different effects on the carrier and sidebands resonance conditions. The carrier power, as measured by `Pr_B5_DC`, returns to its maximum value with a time constant of about 200 s. The sidebands instead show a quite different behaviour, as it is well visible both looking at their power inside the recycling cavity or at their amplitude at the dark port. After a longer period (of the order of 10 minutes) the sidebands power inside the recycling cavity reaches a stable value, which is however lower by a factor 2 with respect to the maximum. At the dark port the carrier amplitude stabilizes with a similar time constant. Moreover the sidebands start being strongly un-balanced, with the upper one almost vanishing. They tend to naturally balance with a time constant of the order of several hours.

During the same period the response of all locking error signals also changes strongly. In particular the `Pr_B2_3f_ACp` signal (used to control PRCL) deviates a lot from a standard Pound-Drever-Hall signal (see fig. B.8). Indeed, the zero crossing point at the beginning of the thermal transient, when the input mirrors are still "cold", slowly disappears as the energy absorbed by the mirrors increases: this explain why the initial high power state of the interferometer can not be

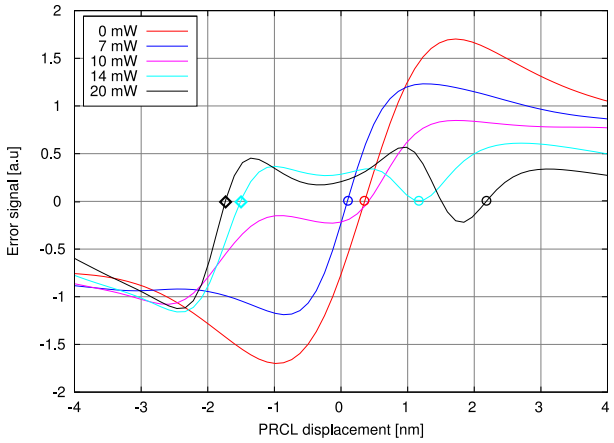

Figure B.8: Evolution of the `Pr_B2_3f_ACp` error signal dependence on PRCL motion, at different moments during the thermal transient, corresponding to different power absorption in the input mirrors. The circles show the evolution of the zero crossing point corresponding to the high power state of the interferometer. The squares show the point where the interferometer is locked during the thermal transient. These results [94] has been obtained by mean of frequency domain simulation using Finesse [61].

maintained for a long time. If the demodulation phase of the error signal is changed by a sensible amount (about 30-40 degrees) another zero crossing point with the correct sign appears during the transient. This is the point where the interferometer jumps after reaching the dark fringe. It slowly moves toward the correct resonance condition for the carrier with the increase of the energy absorbed by the input mirrors.

B.6.3 Locking strategy

The thermal transient period is maybe the most critical one for the stability of the interferometer, since it is mandatory to bring and keep it in the correct state. Moreover the sensitivity of all error signals to the longitudinal degrees of freedom changes strongly during this period. Therefore the first ten minutes of the thermal transient are spent mostly waiting for the mirrors to heat up and only few actions are performed.

The first one is to change the error signal used to control the differential degree of freedom. The demodulated transmission of the west arm is too noisy and a better signal can be extracted from the dark fringe itself. Since the output mode cleaner is usually not yet in resonance at this point of the lock acquisition procedure, the in-phase demodulated signal from the dark fringe beam (B1p)

that does not pass through it is used. The switch is performed blending together the two signals.

One of the most important actions performed in the early part of the thermal transient is the engagement of the automatic alignment control of the angular differential motion of the cavity end mirrors (for more details about this alignment strategy refer to chapter 4). The error signals are extracted from the dark fringe beam B1p itself by using wave-front sensors, similarly to the pre-alignment of the arm cavities. The bandwidth of these two control loops are of about 3 Hz. Their engagement strongly stabilizes the dark fringe and power recycling cavity powers and has proved to be crucial for the stability of the system.

During the thermal transient other alignment controls are engaged, using different error signals and bandwidths: the input beam is controlled using signals from wave-front sensors placed in reflection of the interferometer, in drift control configuration, which means with a bandwidth of some tens of mHz; the end mirror common mode is controlled with full bandwidth (3 Hz) using a combination of signals coming again from the wave-front sensors placed on the reflected beam; the power recycling mirror is controlled using signals from the B5 beam, as during the pre-alignment procedure (with 3 Hz bandwidth); finally the BS mirror is controlled using signals from the beam transmitted by the west arm, with full bandwidth for pitch motions and drift control configuration for yaw. The remaining input mirror degrees of freedom are controlled only starting from later steps. See chapter 4 for more details.

Afterward the normalization of all error signals is changed from `Pr_B5_DC` to `Pr_B5_2f_ACq`, which measures the sidebands power inside the recycling cavity. This has experimentally proved to be the best choice to compensate for the change in optical gains of the signals used for the control of the central part of the interferometer.

Even with this normalization the optical gains of all longitudinal control loops change strongly during the transient period, as can be expected because of the varying resonance conditions of both carrier and sidebands. For the DARM loop, this variation proved to be too large: without any compensation the overall gain soon changes more than the stability margin of the control system. For this reason a slow servo has been implemented with the aim of reconstructing the unity gain frequency of the DARM control loop and stabilizing it to the desired value. The same strategy is used for reconstructing the UGF of all longitudinal loops. A permanent calibration line is added to each one of the error signals at a frequency slightly outside the bandwidth of the control loop (at 24 Hz for MICH, at 62 Hz for PRCL and at 379 Hz for DARM). Using a demodulation technique the ratio between the line amplitude in the error signal before and

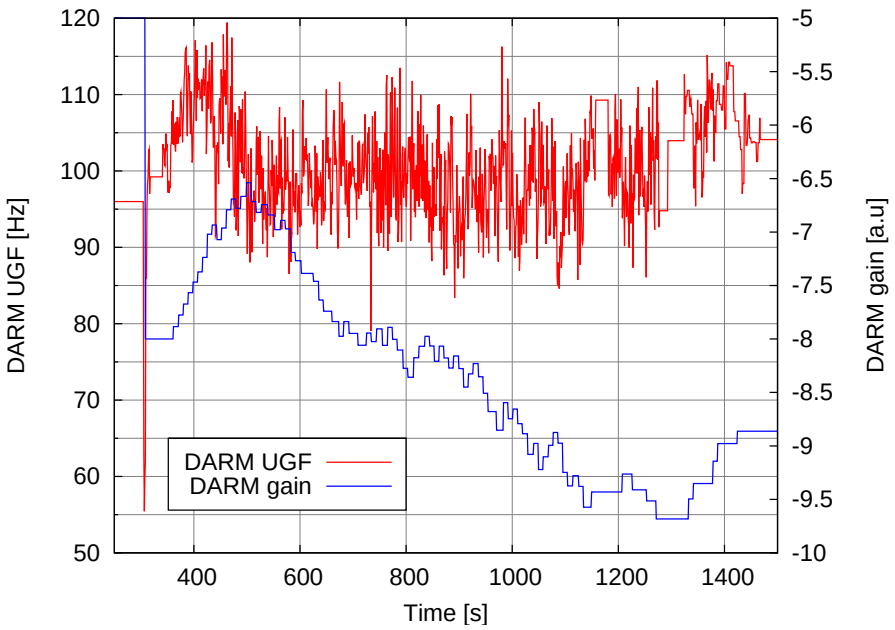

Figure B.9: Evolution during the thermal transient of the reconstructed UGF of the DARM loop and of the corrector filter gain. The former is the error signal for the slow UGF servo, while the latter is the correction.

after the noise addition can be computed:

$$g(f) = \frac{\text{Amplitude before}(f)}{\text{Amplitude after}(f)}$$

As explained in sec. E.1 this ratio gives the open loop gain at the line frequency. Knowing the shape of the transfer function the UGF of the loop can be easily computed. The evolution during the thermal transient for the three main longitudinal loops is shown in fig. B.7. During the first part of the thermal transient only the DARM loop UGF is stabilized. This is obtained with the action of a slow servo system. It computes the UGF of the loop averaging over 30 s and compares it with the desired value (100 Hz for DARM). If the difference is greater than a fixed threshold, the gain of the corrector filter is modified accordingly (there is also a maximum allowed relative change in the gain, to avoid too big changes in a single step). The gain is then updated in the global control parameters, where it is actually applied only after passing it through a low pass filter to have a smooth transition. The total effect is a slow servo system that can maintain the unity gain frequency of the loop at any desired value, with a bandwidth of the order of 10 mHz (see fig. B.9).

At intermediate steps during the transient the way error the signals for MICH and PRCL are reconstructed is changed. The matrix which reconstruct

the error signals from the photo-diode demodulated outputs is initially diagonal: the PRCL error signal is reconstructed only from `Pr_B2_3f_ACp` while the one for MICH only from `Pr_B5_ACq`. An off-diagonal term is added with the aim of minimizing the contribution of PRCL motion to the MICH error signal. For this reason the MICH error signal is given by

$$E_{MICH} = g_{MICH} \left(\frac{\texttt{Pr\_B5\_ACq}}{N_1} + c_{MP} \frac{\texttt{Pr\_B2\_3f\_ACp}}{N_2} \right) \tag{B.1}$$

where N_i are normalization coefficients build with powers. The off-diagonal term c_{MP} is initially set to a fixed value, close to the optimal one and afterward a servo is engaged to keep it as close as possible to the good value, which may change slowly with time. The error signal for this servo is obtained by demodulating E_{MICH} in correspondence of the PRCL calibration line (62 Hz). If the off-diagonal term is optimal, the PRCL line should not be visible in the MICH signal, and therefore the demodulation should return zero. If the term is not perfectly tuned, some signal is visible at the line frequency, and the demodulation contains both amplitude and sign information.

Close to the end of the waiting period, the global alignment control of the input mirrors in engaged. This is a drift control system which uses the position of the beams transmitted by the two arm cavities, as seen by cameras, as a reference.

The final action performed during the thermal transient waiting time is to digitally add an offset to the error signal used for PRCL control, changing the locking point for this degree of freedom. This is done in order to reduce the sidebands imbalance, since as will be shown in section 5.7 this depends strongly on the operating point. At a later step another slow servo is engaged to control the sidebands balancing at the dark port.

B.7 Locking of output mode-cleaner

During the waiting period of the thermal transient, the shutter in front of the output mode cleaner is opened, and the servo which finds and maintains its resonance is activated. In this way at the end of the transient the OMC is reasonably close to its resonance and the DARM loop control can be switched from B1p (which is the dark fringe beam pick-up before the OMC) to the demodulated signal obtained from the beam transmitted by the OMC, namely `Pr_B1_ACp`. This signal is much better since the OMC filters out all non-Gaussian modes which are usually modulated by mis-alignments. Moreover this beam contains 99% of the dark port power and therefore it has a much better signal-to-noise ratio for differential motion of the end mirrors. Initially a low power diode is used.

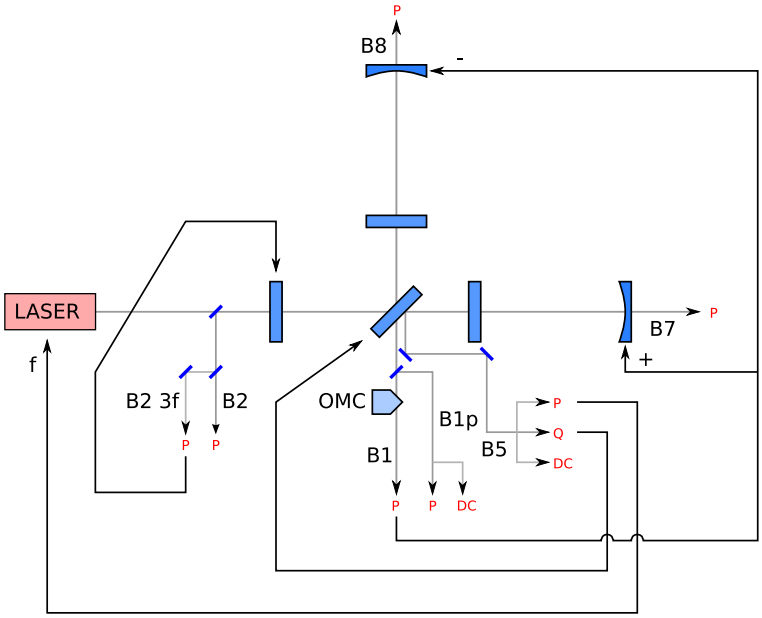

Figure B.10: Scheme of the longitudinal control system after the thermal transient. The DARM loop is controlled using the beam transmitted by the OMC.

This switch also improves the interferometer contrast. It has indeed been observed that there is a relative offset between the locking point obtained with B1p and with B1: this might be due to the contamination of the first by higher-order modes generated for example by a mismatch between the laser beam spatial mode and the cavities resonant mode.

B.8 Low noise control filter

From this point on the interferometer is locked in a robust configuration and the operating point is very close to the final one, the only difference being the evolution due to the final part of the thermal transient. Therefore all action performed in the later steps of the lock acquisition procedure are focused to improve as much as possible the sensitivity of the detector by moving to the so-called *low noise configuration*.

The first actions are devoted to reduce the noise re-introduced by the control loops in the dark fringe signal. It has been experimentally found that the most relevant limiting control noise source is the MICH loop. At this step of the lock acquisition a new corrector filter is engaged. It implements a steep roll-off at about 50 Hz which strongly reduces the noise re-introduced outside the active bandwidth of the feed-back system (see fig. B.11).

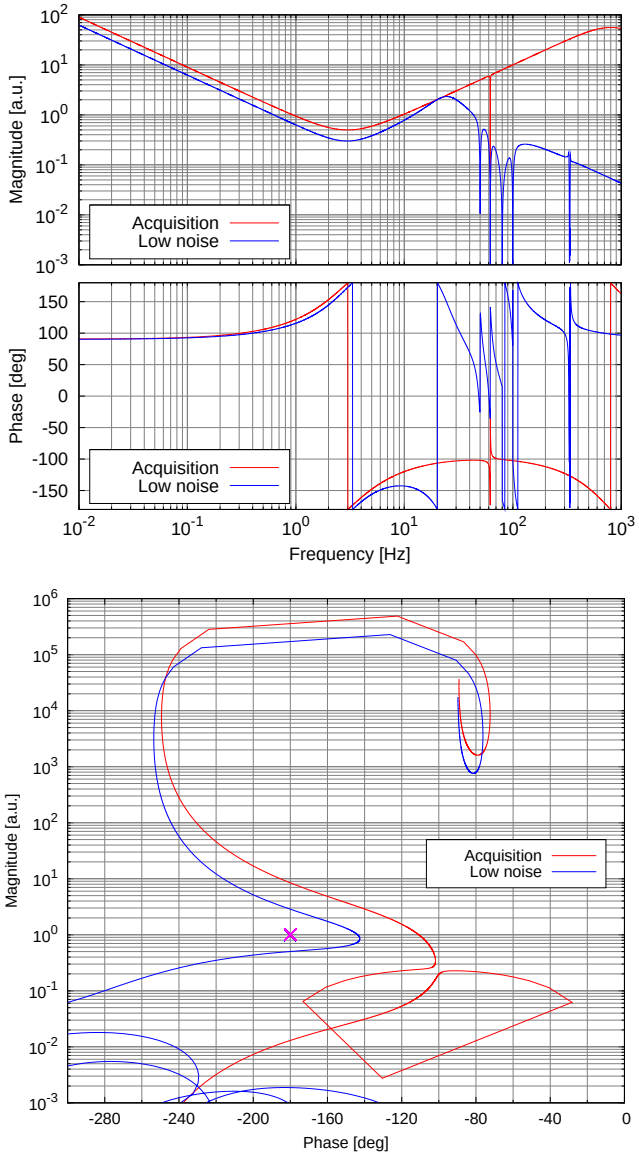

Figure B.11: Comparison of the MICH control filter used during the lock acquisition with the low noise filter. **Top:** Bode plot. **Bottom:** Nichols plot of the open loop transfer function assuming a flat optical response and the simple pendulum mechanical model.

In order to reduce even further the noise re-introduced by the MICH loop, without making the control loop unstable, a noise-subtraction technique is used. The correction signal of the MICH loop is sent, after proper filtering, to the end mirrors in differential configuration. This is the so-called *alpha technique* and it is discussed in more details in section 5.4. A similar noise subtraction technique is also implemented for the reduction of PRCL noise: the correction computed for the PRCL d.o.f. is also added to the differential correction of the end mirrors. This is called *beta technique*. The overall gains of these two noise subtraction paths are adjusted continuously by slow servos which uses as error signals the demodulation of the dark fringe at the frequency of PRCL and MICH calibration lines.

The sidebands balancing servo, described in section B.6.3 is engaged at this point, together with the unity gain frequency servos for MICH and PRCL. The requested UGF are 100 Hz for DARM, 40 Hz for PRCL and 15 Hz for MICH.

B.9 Low noise actuators

A possible source of noise in feed-back control systems can come from the actuation noise, in particular the DAC noise introduced by the electronic boards that converts the digital correction signals to the actual current applied to the coils actuators.

At this step of the lock acquisition procedure, several actions are performed to reduce this noise. First, the longitudinal correction applied to the end and input mirrors is partially reallocated to the marionette actuators. To summarize, the longitudinal correction is split in several parts. The very low frequency component of the correction is sent both to the reference mass actuators and to the inverted pendulum controls. In this way the large low-frequency component of the force is applied at the top level, greatly reducing the needed dynamical range at the level of mirror. Moreover, the correction in the frequency region below roughly 7 Hz is reallocated to the marionette actuators. This is obtained by using suitable low and high pass filters, which compensate also for the transfer function from marionette to mirror due to the additional pendulum stage. This re-allocation is performed for two main reasons: first it reduces even further the dynamical range needed for the reference-mass actuators; secondly any actuation noise at the level of the marionette is filtered by the additional pendulum stage. Finally the components of the correction above 7 Hz is still applied using the reference-mass actuators.

Since the dynamical range of the force that must be applied from the reference mass is greatly reduced in this way, the corresponding coil-drivers can be switched to *low noise* mode (see section 2.4 for more details).

Finally the dark fringe signals are reconstructed using the sum of the outputs

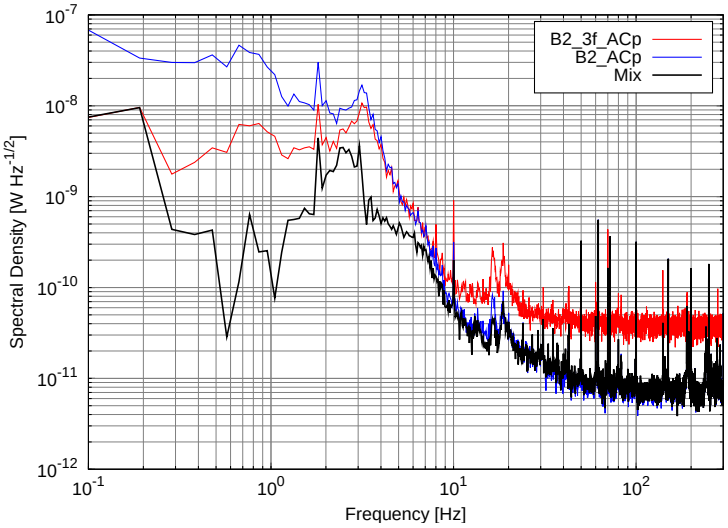

Figure B.12: Comparison of three different signals for the PRCL control. `Pr_B2_3f_ACp` is the signal usually used during lock acquisition. The mix signal is obtained by combining this signal at low frequency (below 5 Hz) with `Pr_B2_ACp` (above 5 Hz). The difference at low frequency is due to the fact that the mixed signal is in-loop while the other two are not.

of two photo-diodes which receives each half of the beam transmitted by the output mode cleaner. In this way the shot noise limit is strongly decreased.

B.10 Last low noise steps

After the change in the MICH control filter the dominant source of noise is the PRCL loop. The main reason is that the error signal used during lock acquisition (`Pr_B2_3f_ACp`) is very noisy at high frequencies, since it is limited by sensing (shot and ADC) noise above 30 Hz (see fig. B.12). Another signal which senses the same degree of freedom in a similar way is `Pr_B2_ACp`. Therefore the two signals are mixed together: `Pr_B2_3f_ACp` is low-passed through a first order filter with corner frequency at 5 Hz; the complementary high-pass filter is applied to `Pr_B2_ACp` and the two signals are summed together. In this way the behavior of the control loop is the same at low frequency and the noise re-injected at high frequency is lowered by about one order of magnitude.

B.11 Science mode configuration

In conclusion, the state of longitudinal sensing and control in the final configuration can be summarized as follows:

- the DARM degree of freedom is controlled using the dark fringe itself as error signal (`Pr_B1_ACp`) with unity gain frequency at 100 Hz;
- the PRCL degree of freedom uses the `Pr_B2_3f_ACp` signal below 5 Hz and `Pr_B2_ACp` above. The unity gain frequency of this loop is at 40 Hz.
- the MICH degree of freedom is controlled using `Pr_B5_ACq`. Its control loop has a unity gain frequency at 15 Hz and a strong roll-off above 50 Hz;
- the gains of these three longitudinal loops are stabilized by slow servo using as error signal the demodulation of calibration lines;
- the laser frequency is stabilized on the mean length of the arm cavities, using `Pr_B5_ACp` as error signal and with unity gain frequency at about 25 kHz; at the same time the common mode of the arm cavities is locked on the demodulated reflection of the reference cavity, with a bandwidth of about 1 Hz;
- all longitudinal actuators are in low-noise configuration: the very low frequency part of the correction is applied also at the top stage of the suspension, while for the two cavity end mirrors the correction is re-allocated at intermediate frequencies to the marionette;
- the re-injection of MICH and PRCL noise in the dark fringe signal is reduced by using noise subtraction techniques.

Appendix C

Linear systems

The simplest model of a physical system with one single input and one output is a linear transformation:

$$y(t) = \int_{-\infty}^{t} h(t,\tau)\, x(\tau)\, d\tau$$

where the requirement of causality has been already taken into account. In general the integral kernel $h(t,\tau)$ is a function of two variables, since the behavior of the system can vary with time. If this is not the case, the system being time-invariant, the above expression can be simplified considering that it is possible to write $h(t,\tau) = h(t-\tau)$ and therefore

$$y(t) = \int_{-\infty}^{0} h(\tau)\, x(t-\tau)\, d\tau \tag{C.1}$$

This is the most general expression of a *linear time-invariant system*. The vast majority of the systems involved in interferometric detectors are well described by this kind of models.

A very convenient way to describe linear transformations, widely used in the theory of control systems for example, is the Laplace transform [56]. Given a signal $x(t)$, null when $t < 0$, its Laplace transform is defined as

$$\tilde{x}(s) = \int_{0}^{\infty} x(t)\, e^{-st}\, dt$$

Laplace transform	Time function (for $t > 0$)
$\frac{1}{s}$	1
$\frac{1}{s-s_0}$	$e^{s_0 t}$
$\frac{\omega_0^2}{s^2+\frac{\omega_0}{Q}s+\omega_0^2}$	$\frac{\omega_0}{\sqrt{1-\frac{1}{4Q^2}}} e^{-\frac{\omega_0 t}{2Q}} \sin\left(\omega_0 t\sqrt{1-\frac{1}{4Q^2}}\right)$

Table C.1: List of anti-transform of common second order rational functions.

It can be shown that this function of the variable s can be extended to a complex function with s varying in a defined domain of the complex plane. Applying the Laplace transform to eq. C.1 one obtains

$$\tilde{y}(s) = \tilde{h}(s)\,\tilde{x}(s) \tag{C.2}$$

where the new function $\tilde{h}(s)$ is usually called the *(Laplace) transfer function* of the linear system. The Laplace transform is an extension of the Fourier transform, which can be recovered putting $s = i\omega$, if the imaginary axis is contained in the domain of existence.

In most cases the transfer function of a linear system can be described using rational functions

$$F(s) = \frac{P(s)}{Q(s)} = \frac{b_m s^m + b_{m-1} s^{m-1} + \cdots + b_1 s + b_0}{a_n s^n + a_{n-1} s^{n-1} + \cdots + a_1 s + a_0}$$

If both numerator and denominator are factorized, the function can be described as a list of poles and zeros. Moreover, if $F(s)$ is the transfer function of a physical system, all complex poles and zeros appear together with their complex conjugate, since in the time domain the integral kernel $h(\tau)$ must be real, being both $x(t)$ and $y(t)$ physical real signals.

A rational function is characterized by its poles and can therefore be written as:

$$F(s) = \sum_i \frac{K_i}{(s - p_i)^{n_i}}$$

where n_i are the pole multiplicities and K_i the corresponding residuals. The anti-transform of each of these terms in time-domain is proportional to an exponential $e^{p_i t}$ (see table C.1). This result is very useful when considering the response of a system to a step function or to an impulse (usually called *step response* and *impulse response*). In the latter case, being the Laplace transform of an impulse at $t = 0$ a constant, from eq. C.2 follows that the impulse response of the system is given simply by the anti-transform of the transfer function. Therefore it will contain oscillating terms at frequencies given by the imaginary part of each pole. If one pole has negative real part the oscillation is damped, otherwise it has constant amplitude if the pole is purely imaginary, or it grows up exponentially if the pole has positive real part. Therefore a system is stable, in the sense that its response to an impulse is asymptotically decreasing, if its transfer function has only poles with negative real part.

In developing feed-back control system and in describing the properties of mechanical and optical systems, it is customary to describe transfer functions in terms of pole and zero frequencies and quality factors. A real (simple) zero at a frequency f_0 is given by

$$Z_1(s) = s - 2\pi f_0$$

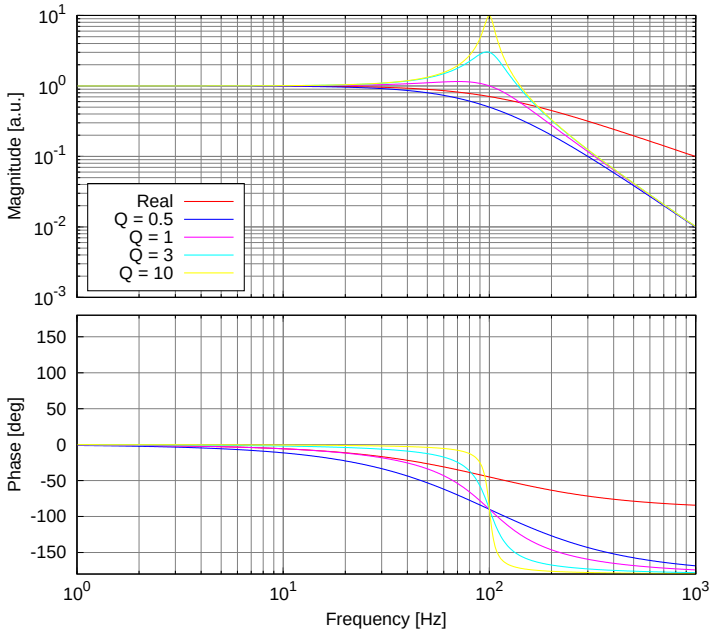

Figure C.1: Transfer function of systems described by a simple real pole or one complex pole with different quality factors Q.

while a real pole is given by the inverse of this expression. A complex (double) zero at frequency f_0 and with quality factor Q is given by

$$Z_2(s) = s^2 + \frac{2\pi f_0}{Q} s + (2\pi f_0)^2$$

The inverse of this formula gives the transfer function of a complex double pole (see fig. C.1): this correspond to a system whose impulse response is a damped oscillation at frequency $f = f_0\sqrt{1 - 1/4Q^2}$, with time constant $\tau = \frac{Q}{\pi f_0}$: the higher the Q, the longer the oscillation will last. An example of such a system is a simple mechanical pendulum with friction.

Appendix D

Signal analysis

D.1 Random processes

The main part of the work in commissioning and characterizing an interferometric detector deals with the analysis and interpretation of digital signals. In general any physical quantity can be defined as a random variable depending on time $X(t, S)$ (a *random process* [96]) where S describes the state of the physical system. A digital signal is a sampled version of this $\mathbf{X}(s) = (X(t_1, s), X(t_2, s), \ldots, X(t_n, s))$. At a fixed time t the *cumulative probability distribution* of the system can be defined as

$$F_X(x, t) = P\left(\{X(t) < x\}\right)$$

and the *probability density* as its derivative

$$f_X(x, t) = \frac{\partial F_X(x, t)}{\partial x}$$

Similar definitions hold for probability distributions of the values of the random variable at multiple times:

$$\begin{aligned} F_{XX}(x_1, t_1; x_2, t_2) &= P\left(\{X(t_1) < x_1\} \wedge \{X(t_2) < x_2\}\right) \\ f_{XX}(x_1, t_1; x_2, t_2) &= \frac{\partial^2 F_{XX}(x_1, t_1; x_2, t_2)}{\partial x_1 \partial x_2} \end{aligned}$$

In general the probability density at two times is not simply given by the product of the two at single times, unless the two random variables obtained at two different times are *independent*:

$$\begin{aligned} F_{XX}(x_1, t_1; x_2, t_2) &= F_X(x_1, t_1)\, F_X(x_2, t_2) \\ f_{XX}(x_1, t_1; x_2, t_2) &= f_X(x_1, t_1)\, f_X(x_2, t_2) \end{aligned}$$

It is possible to define *statistical moments* for the signal, at fixed time. The mean value:

$$\mu_X(t) = E\left[X(t)\right] \equiv \int x\, f_X(x, t)\, dx$$

The standard deviation:

$$\sigma_X^2(t) = E\left[(X(t) - \mu_X(t))^2\right] = \int (x - \mu_X(t))^2 \, f_X(x,t)\, dx$$

The auto-correlation:

$$R_{XX}(t_1, t_2) = E\left[X(t_1)X(t_2)\right] = \int\int x_1 x_2 \, f_{XX}(x_1, t_1; x_2, t_2)\, dx_1 dx_2$$

The auto-covariance:

$$\begin{aligned} C_{XX}(t_1, t_2) &= E\left[(X(t_1) - \mu_X(t_1))\,(X(t_2) - \mu_X(t_2))\right] \\ &= R_{XX}(t_1, t_2) - \mu_X(t_1)\mu_X(t_2) \end{aligned}$$

In a similar way the correlation and covariance of two signals can be defined:

$$\begin{aligned} R_{XY}(t_1, t_2) &= E\left[X(t_1)Y(t_2)\right] = \int\int x_1 y_2 1, f_{XY}(x_1, t_1; y_2, t_2)\, dx_1 dy_2 \\ C_{XY}(t_1, t_2) &= R_{XY}(t_1, t_2) - \mu_X(t_1)\mu_Y(t_2) \end{aligned}$$

A zero-mean, *normal distributed* or *Gaussian process* $\{X_i : i = 1, \ldots, n\}$ is specified by the following probability density:

$$f(X_1, \ldots, X_n) = \frac{1}{\sqrt{(2\pi)^n \det\Sigma}} \exp\left(-\frac{X^T \Sigma^{-1} X}{2}\right)$$

where Σ is the *covariance matrix* that completely characterize the process. If this matrix is diagonal, random variables obtained at different times are independent.

D.2 Stationarity and ergodicity

A random process is called *stationary* if all its moments are independent of time: this means that the statistical properties of the random variables at two different times are equal. For first order statistics this implies that the mean is constant in time. For second order ones, the auto-correlation is a function of the time difference only.

A moment of the process at a time t can be estimated by averaging over several different realizations of the process, for example

$$\mu_X(t) \simeq \int X(t, s)\, dP(s)$$

This is usually not possible, since a detector output consists in one single signal, which is one particular realization of the random process. If the process is stationary, one can imagine to substitute the average over different realizations with an average over time. In general the equivalence of the two means is not

true, unless the process is *ergodic*. In the following all random processes are assumed to be ergodic, therefore averages over realizations can be exchanged with averages over time. For reference, the definitions of mean, standard deviation and auto-correlation are given by:

$$\begin{aligned} \mu_X &= \lim_{T\to\infty} \int_{-T}^{+T} X(t)\,dt \\ \sigma_X^2 &= \lim_{T\to\infty} \int_{-T}^{+T} (X(t)-\mu_X)^2\,dt \\ R_{XX}(\tau) &= \lim_{T\to\infty} \int_{-T}^{+T} X(t)X(t+\tau)\,dt \end{aligned}$$

D.2.1 Power of a signal

The *mean power density* of a signal, also called *root mean square value* (RMS) is defined as

$$RMS_X = \lim_{T\to\infty} \int_{-T}^{+T} X^2(t)\,dt$$

It can be easily shown that this is equal to the auto-correlation function at zero delay and also that

$$RMS_X = R_X(0) \geq |R_X(\tau)|$$

It often turns out to be useful to separate the contribution to the signal power coming from different frequencies. For this reason the *power spectral density* (PSD) or *power spectrum* of the signal can be defined as the Fourier transform of the auto-correlation:

$$S_{XX}(\omega) = \int_{-\infty}^{+\infty} e^{-i\omega\tau}\, R_{XX}(\tau)\,d\tau \tag{D.1}$$

The physical units of the power spectrum are $[X]^2/\text{Hz}$. If the signal $X(t)$ is real, the power spectrum is even $S_{XX}(\omega) = S_{XX}(-\omega)$.

It is customary to define the *amplitude spectral density* (ASD), or simply *spectrum*, of the signal as

$$\tilde{X}(\omega) = \sqrt{S_{XX}(\omega)}$$

whose units are $[X]/\sqrt{\text{Hz}}$. This is not the Fourier transform of the signal, nor a simple average of Fourier transforms.

The *band-limited root mean square value* (BRMS) of a signal in a frequency band $[\omega_1, \omega_2]$ is simply the integral of the power spectral density in that band:

$$BRMS_X[\omega_1,\omega_2] = \int_{\omega_1}^{\omega_2} S_{XX}(\omega)d\omega$$

It is also possible to define the *cross power spectrum* of two signals:

$$S_{XY}(\omega) = \int_{-\infty}^{+\infty} e^{-i\omega\tau}\, R_{XY}(\tau)\,d\tau$$

Another definition of power spectrum can be given as the following limit

$$S(\omega) = \lim_{T\to\infty} \frac{1}{2T} \left| \int_{-T}^{+T} X(t) e^{-i\omega t}\, dt \right|^2$$

This is equivalent to eq. D.1 if the signal satisfies the condition

$$\int_{-\infty}^{+\infty} |\tau R(\tau)| d\tau < \infty$$

which is usually true for most physical signals.

D.3 Linear transformation of signals

If a given signal $X(t)$ is transformed in $Y(t) = H[X(t)]$ with a time-invariant linear transformation

$$Y(t) = \int_{-\infty}^{+\infty} h(\tau) X(t-\tau)\, d\tau$$

the *(Fourier) transfer function* is defined as follows

$$H(\omega) = \int_{-\infty}^{+\infty} h(t) e^{-i\omega t}\, dt$$

since it is the function that connects X and Y Fourier transforms:

$$\tilde{Y}(\omega) = H(\omega)\, \tilde{X}(\omega)$$

The effect on correlations is easily expressed in terms of convolution integrals

$$\begin{aligned} R_{XY}(\tau) &= R_{XX}(\tau) \otimes h^*(-\tau) \\ R_{YX}(\tau) &= R_{XX}(\tau) \otimes h(\tau) \\ R_{YY}(\tau) &= R_{XX}(\tau) \otimes h^*(-\tau) \otimes h(\tau) \end{aligned}$$

and from these formulas the power spectra can be computed:

$$\begin{aligned} S_{YY}(\omega) &= |H(\omega)|^2\, S_{XX}(\omega) \\ S_{XY}(\omega) &= H^*(\omega) S_{XX}(\omega) \\ S_{YX}(\omega) &= H(\omega) S_{XX}(\omega) \end{aligned}$$

In particular the amplitude spectral density of the transformed signal is simply the one of the input signal multiplied by the modulus of the transfer function.

From these definition it follows that the transfer function between two signals, supposed to be linearly related, can be estimated by the following ratio

$$TF_{X\to Y}(\omega) = \frac{S_{YX}(\omega)}{S_{XX}(\omega)} = H(\omega)$$

Another useful quantity is the *coherence*:

$$C_{XY}(\omega) = \frac{|S_{XY}(\omega)|^2}{S_{XX}(\omega)S_{YY}(\omega)}$$

If X and Y are linearly related, this is equal to 1. Therefore coherence is a good indicator of the amount of linear relation between two signals.

D.4 Estimators

Since almost all signals are acquired digitally, the previous equations must be translated in the discrete time domain. The *discrete Fourier transform* (DFT) can be defined coherently with the continuous time version as:

$$\tilde{x}_k = DFT(x, \omega_k) = \frac{\Delta T}{N} \sum_{n=0}^{N-1} x_n \, e^{-\frac{2\pi i}{N} kn} \tag{D.2}$$

where ΔT is the length of the interval used for the computation and $\omega_k = \frac{k}{N\Delta T}$. The discrete Fourier transform is periodic with period equal to N and for real signals it has the *reflection property*:

$$DFT(x, \omega_k) = DFT(x, \omega_{-k})^* \tag{D.3}$$

Therefore only the first half of the discrete Fourier transform gives independent results.

It is common to use *window functions* for the estimation of DFTs, to improve the frequency resolution by reducing leakage between adjacent bins and to have a better convergence of the estimator [97]: the signal is multiplied by the window function before computing the transform:

$$DFT_w(x, \omega_k) = \frac{\Delta T}{N} \sum_{n=0}^{N-1} w_n \, x_n \, e^{-\frac{2\pi i}{N} kn}$$

This is equivalent to convolution in the frequency domain with the Fourier transform of w_n. A commonly used window is the *Hann* one:

$$h_n = A \, \frac{1}{2} \left[1 - \cos\left(\frac{2\pi n}{N-1} \right) \right]$$

where A is a normalization constant chosen in order to have

$$\sum_{j=0}^{N-1} w_n^2 = 1$$

To estimate the power spectrum it is in principle possible to use its definition (eq. D.1), but this is quite a computationally heavy operation, and it is also not a good estimator, since it converges very slowly to the real value [98].

A more widely used method to estimate the power spectrum of a signal is the *Welch modified periodogram* [99]. The time average of eq. D.1 in the limit with $T \to \infty$ is replaced by an average over M different segments, possibly overlapping. The discrete Fourier transform is then computed for each segment, typically using dedicated algorithms like the *Fast Fourier Transform* (FFT) [100] which is particularly optimized for segments of data with a number of samples given by a power of two. The Welch estimator of the power spectrum is given by:

$$S(\omega_k) = \frac{1}{M} \sum_{n=0}^{M-1} \frac{1}{\Delta T_n} \left| \frac{\Delta T_n}{N_n} \sum_{j=0}^{N_j-1} w_n \, X(t_{n,j}) e^{-\frac{2\pi i}{N} kn} \right|^2$$

where ΔT_n and N_n are the length and the number of samples of the $n-$th data segment.

The generalization of this method to the estimation of cross power spectrum, transfer function and coherence is straightforward.

D.5 Digital filters

Since almost all signals are acquired digitally, it is important to have a mean of applying linear transformation to discrete time signals. This kind of transformation are usually called *digital filters* and are at the basis of signal analysis and of most of the control systems commonly used in interferometric detectors (see chapter E).

Given a digital signal x_n, the most general linear transformation can be expressed by the following difference equation [101]:

$$\sum_{p=0}^{N} \alpha_p y_{n-p} = \sum_{q=0}^{M} \beta_q x_{n-q} \tag{D.4}$$

or in a equivalent way:

$$y_n = \frac{1}{\alpha_0} \left[-\sum_{p=1}^{N} \alpha_p y_{n-p} + \sum_{q=0}^{M} \beta_q x_{n-q} \right]$$

The output signal at the n-th sample is computed from the previous M values of the input signal x and from the previous $N-1$ values of the output signal itself. This kind of digital filters are usually called *infinite impulse-response* (IIR) filters, since their response can be asymptotically not zero even when the input is constantly null after a given time.

In dealing with continuous time system it is useful to define the Laplace transform. In discrete time system instead the z-transform is defined:

$$X(z) = \sum_{n=0}^{\infty} x_n \, z^{-n} \tag{D.5}$$

	Time domain	z domain
Linearity	$ax_n + by_n$	$aX(z) + bY(z)$
Time shift	x_{n-k}	$z^{-k}X(z)$
Scaling	$a^n x_n$	$X(z/a)$
Time reversal	x_{-n}	$X(1/z)$
Conjugation	x_n^*	$X^*(z^*)$
Differentiation	nx_n	$-z\frac{dX(z)}{dz}$
Convolution	$x_n * y_n$	$X(z)Y(z)$

Table D.1: Some properties of the z-transform.

This has several properties similar to those of the Laplace transform (see table D.1). In particular using the linearity and time shift properties, the difference equation in eq. D.4 can be written in the form of a transfer function connecting the two z-transforms:

$$H(z) = \frac{Y(z)}{X(z)} = \frac{\beta_0 + \beta_1 z^{-1} + \beta_2 z^{-2} + \cdots + \beta_M z^{-M}}{\alpha_0 + \alpha_1 z^{-1} + \alpha_2 z^{-2} + \cdots + \alpha_N z^{-N}}$$

The typical situation in digital filter designs is to search for a discrete time system that best approximates a continuous time specification of the desired frequency response of the filter, given in terms of a Laplace transfer function. The most commonly used procedure is to employ the *bi-linear transform*, which is a conformal mapping of the s-plane to the z-plane.

The starting point is the exact mapping of the s-plane to the z-plane, given by the complex exponential:

$$z = e^{sT} \tag{D.6}$$

where T is the time interval between samples (the reciprocal of the sampling frequency f_s). This expression can be approximated to first order by

$$z = e^{sT} = \frac{e^{sT/2}}{e^{-sT/2}} \approx \frac{1 + \frac{sT}{2}}{1 - \frac{sT}{2}}$$

and in a similar way the inverse of eq. D.6 can be approximated by:

$$s = \frac{1}{T}\log z \approx \frac{2}{T}\left[\frac{z-1}{z+1} + \frac{1}{3}\left(\frac{z-1}{z+1}\right)^3 + \ldots\right] \approx \frac{2}{T}\frac{1-z^{-1}}{1+z^{-1}}$$

The bi-linear transform uses this last first order approximation to obtain the z-domain transfer function $H_d(z)$ from the Laplace transform $H_c(s)$ of the system, by substituting

$$s \to \frac{2}{T}\frac{1-z^{-1}}{1+z^{-1}} \tag{D.7}$$

or in other words

$$H_d(z) = H_a\left(\frac{2}{T}\frac{1-z^{-1}}{1+z^{-1}}\right) \tag{D.8}$$

To determine the effect of this approximation on the frequency response of the discrete time system, the resulting z-domain transfer function can be evaluated at points on the unitary circles that corresponds to physical frequencies $z = e^{i\omega T}$:

$$\begin{aligned} H_d(e^{i\omega T}) &= H_a\left(\frac{2}{T}\frac{e^{i\omega T}+1}{e^{i\omega T}-1}\right) \\ &= H_a\left(\frac{2}{T}\frac{e^{i\omega T/2}-e^{-i\omega T/2}}{e^{i\omega T/2}+e^{-i\omega T/2}}\right) \\ &= H_a\left(i\frac{2}{T}\tan\left(\frac{\omega T}{2}\right)\right) \end{aligned}$$

This means that the imaginary axis of the Laplace plane, corresponding to physical frequencies, is mapped to the unitary circle in the z-plane with a *warping* of the frequencies. The discrete time filter behaves at a frequency ω exactly like the continuous time filter at a frequency given by

$$\omega_a = \frac{2}{T}\tan\left(\frac{\omega T}{2}\right) \tag{D.9}$$

For frequencies much smaller than the sampling one this shift is negligible, but it becomes more and more relevant as the frequency approaches the Nyquist one. This behavior can be corrected by *pre-warping* the frequencies of poles and zeros of the continuous time filter according to eq. D.9.

Appendix E

Feed-back control systems

In an interferometric gravitational wave detector like Virgo, there are tens of degrees of freedom (mirror positions and pointing, input beam position, etc.) that must be kept close to well determined working points in order to maintain the detector in the correct operating condition within the needed accuracy. This is a typical problem of developing suitable *control systems*, the most common ones being those working in feed-back configuration. This appendix introduces the basics concepts of control system theory. The treatment is restricted to linear control systems, since they cover virtually all of those used in gravitational wave interferometers as long as the residual fluctuations of the controlled degrees of freedom are small enough.

E.1 Simple feed-back system

The simplest situation in a problem of control is a physical object (see fig. E.1), usually called *plant*, which can be described as a linear system with one single input (for example a Fabry-Perot cavity and its length) and one single output, the *error signal* (a photo-diode demodulated output for example). This system is usually called in engineering books SISO (single-input single-output).

The goal of the control system is to keep the input degree of freedom as close as possible to a given function of time, the *reference*. Being the system linear, this can be taken as the value 0, and therefore controlling the input degree of freedom is equivalent to keeping the error signal close to zero. The response of the plant can in general be described using a linear transfer function $G(s)$ depending on the Laplace variable s. The error signal can be affected by some sensing noise which can be related to the sensor itself (for example shot noise for photo-diodes, ADC noise, etc.) or can be injected on purpose to measure the features of the system.

The feed-back is obtained passing the error signal through an ad-hoc *correc-*

tor $F(s)$ and feeding the result (*correction signal*) back to the plant by means of *actuators* whose response is modeled by $A(s)$. For example the length of a Fabry-Perot cavity is controlled sending currents to coils attached to one of the mirrors. In general the actuators themselves can introduce some additional noise, called *actuation noise*, or as before an external excitation can be added on purpose to the correction signal. There is a general convention that put a minus sign at the summation point of the correction and the system free motion. In this way the correction signal is in-phase with the motion that the feed-back suppresses.

The behavior of the full linear system can be easily computed:

$$\begin{aligned} e(s) &= G(s)\left[z'(s) - n_a(s) - A(s)\left(n_c + F(s)n_s + F(s)e(s)\right)\right] \\ z(s) &= z'(s) - n_a(s) - A(s)\left(n_c + F(s)n_s + F(s)e(s)\right) \end{aligned}$$

where $e(s)$ and $z(s)$ are the error and input signal respectively. These implicit equations can be solved to obtain:

$$\begin{aligned} e(s) = {} & \frac{G(s)}{1+G(s)F(s)A(s)}\, z'(s) - \frac{G(s)}{1+G(s)F(s)A(s)}\left(n_a(s) + A(s)n_c(s)\right) \\ & - \frac{G(s)F(s)A(s)}{1+G(s)F(s)A(s)}\, n_s(s) \end{aligned} \tag{E.1}$$

$$\begin{aligned} z(s) = {} & \frac{1}{1+G(s)F(s)A(s)}\, z'(s) - \frac{1}{1+G(s)F(s)A(s)}\left(n_a(s) + A(s)n_c(s)\right) \\ & - \frac{F(s)A(s)}{1+G(s)F(s)A(s)}\, n_s(s) \end{aligned} \tag{E.2}$$

The fact that the output of the system is used also as part of the input justifies the name feed-back and also explains why it is customary to refer to feed-back control system as *loops* and to distinguish between the *open loop* configuration when the feed-back signal is disconnected from the input and the *closed loop* configuration.

For simplicity the actuator transfer function can be considered as a part of the plant transfer function $G(s)$ and the correction and actuation noise can be treated on the same basis.

All signals that are measured inside a feed-back loop are called *in-loop* (for example the error and correction signals) while those measured outside or added from outside are called *out-of-loop* (for example the free motion of the system or any external added perturbation). As an effect of the feed-back all in-loop signals are reduced, with respect to the free system, by an amount given by the *suppression factor*

$$G_{CLTF} = \frac{1}{1+G(s)F(s)}$$

also called *closed-loop transfer function* (CLTF) to differentiate from the *open-loop transfer function* (OLTF) given by

$$G_{OLTF} = G(s)F(s)$$

Usually the value of the open loop transfer function at a given frequency is called the *gain* at that frequency. A change in the overall gain of the transfer function is simply a multiplication by a frequency independent coefficient. The frequency (usually unique) where the gain is equal to one is called *unity gain frequency* UGF or *band-width* of the loop.

One widely used method to measure the open-loop transfer function of a system consists in adding a known source of noise $n(s)$ for example to the error point. If this noise dominates all the signals, in equations E.1 and E.2 only terms proportional to $n(s)$ are relevant:

$$\begin{aligned} e(s) &= -\frac{G(S)F(S)}{1+G(S)F(s)}\, n(s) \\ e'(s) &= \frac{1}{1+G(s)F(s)}\, n(s) \end{aligned}$$

The OLTF is given by the opposite of the transfer function between the error signal measured after and before the addition of the noise.

Both the error and correction signals contain information on the residual motion of the system. At frequencies where the open-loop gain is higher than one, the error signal gives a good estimate of the residual motion of the system, apart from a calibration factor given by the plant transfer function.

At the same frequencies instead the correction signal is not a good estimate of the motion. For example consider a resonant Fabry-Perot cavity with its length controlled by applying a force to one of the two mirrors, using the demodulated transmission as error signal. If the input mirror is moving a lot, the correction signal must be large enough to induce a motion of the end mirror such that the cavity length is constant. Therefore the correction can be quite large even if the error signal and the residual fluctuation of the cavity length are small.

E.2 Response to variations of the input signal

One of the most interesting properties of a control system is the ability to track a varying input signal. This performance of a linear system, described by a transfer function $F(s)$, can be studied by analyzing the response to an input step:

$$x(t) = \begin{cases} 0 & \text{if } t < 0 \\ 1 & \text{if } t \geq 0 \end{cases}$$

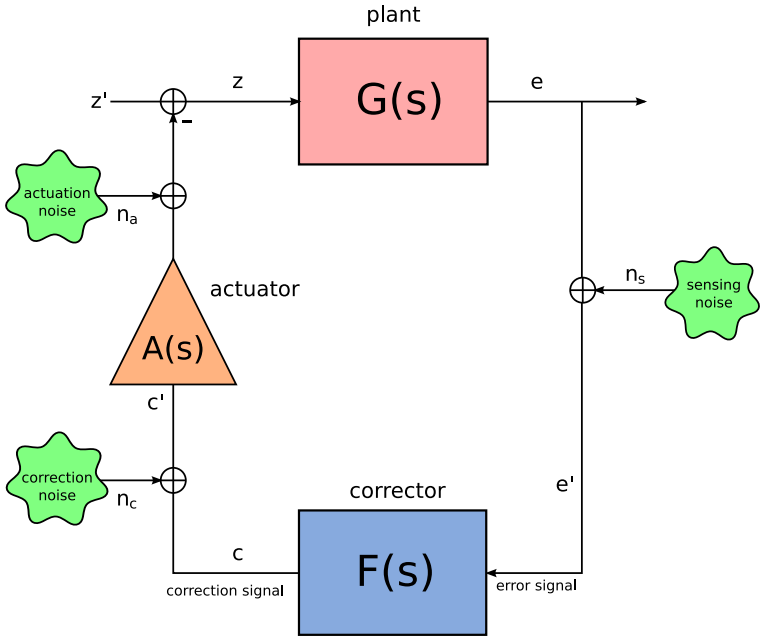

Figure E.1: Scheme of a simple feed-back loop. See the text for details.

The Laplace transform of this signal is $\tilde{x}(s) = \frac{1}{s}$ and therefore the system output is given by

$$\tilde{y}(s) = \frac{F(s)}{s}$$

The behavior of the anti-transform of this expression for large times can be obtained, assuming the system to be stable, by using the *final value theorem* [56]:

$$\lim_{t \to +\infty} y(t) = \lim_{s \to 0} s\, \tilde{y}(s)$$

In particular the response of the linear system to the input step for large times is given by:

$$\lim_{t \to \infty} y(t) = F(0)$$

Therefore the output of the system goes to zero only if its transfer function includes a zero at $s = 0$.

In terms of feed-back systems, the input signal is an external disturbance added to the controlled d.o.f. and the output is for example the residual motion of the system. Therefore the transfer function of the system is given by

$$F(s) = \frac{1}{1 + G_{OLTF}(s)}$$

and it has a zero at the origin only if $G_{OLTF}(s)$ includes a pole for $s = 0$ (a *pure integrator*). This is the reason why real poles at zero frequency are usually added to the controller filter.

The simplest case is that of a system with open loop transfer function given by a simple pure integrator with unity gain at ω_0:

$$\begin{aligned} G_{OLTF}(s) &= \frac{\omega_0}{s} \\ F(s) &= \frac{1}{1+G_{OLTF}(s)} = \frac{s}{s+\omega_0} \end{aligned}$$

Its response to a input unity step is given by the anti-transform of

$$\tilde{y}(s) = \frac{F(s)}{s} = \frac{1}{s+\omega_0}$$

which is exponentially decaying:

$$y(t) = e^{-\omega_0 t}$$

From this equation it is also possible to extract the *time constant* of the system, which is the typical time scale of its response to variations of the input signal

$$\tau = \frac{1}{\omega_0} = \frac{1}{2\pi f_0}$$

where f_0 is the unity gain frequency of the system.

In a similar way the behavior of a system with two real poles at the origin can be studied.

$$\begin{aligned} G_{OLTF}(s) &= \frac{\omega_0^2}{s^2} \\ F(s) &= \frac{1}{1+G_{OLTF}(s)} = \frac{s^2}{s^2+\omega_0^2} \\ \tilde{y}(s) &= \frac{F(s)}{s} = \frac{s}{s^2+\omega_0^2} \end{aligned}$$

and the anti-transform of the last expression gives the time response to an input step:

$$y(t) = \cos(\omega_0 t)$$

which is not exponentially decreasing in time. Therefore the response of this system does not converge to zero when the input is perturbed, but rather a persistent oscillation at the unity gain frequency is present. This introduces the subject of stability of a feed-back system.

E.3 Stability

From the general point of view, a linear system described by a transfer function $G(s)$ is *proper* if $G(i\infty)$ is finite and strictly proper if $G(i\infty) = 0$. This is usually true for all physical system, since for very high frequency the response is always small.

Moreover, a system is *stable* if its transfer function is analytic in the closed right half plane $s \geq 0$ or in other words if it has no poles in that region. It is *asymptotically stable* if there are also no poles on the imaginary axis.

As explained in chapter D, the anti-transform of the transfer function gives the response of the system to an impulse (usually called *impulse response* of the system). Any pole in the half right plane will anti-transform to an oscillation with exponentially increasing amplitude and any pole on the imaginary axis to a constant amplitude oscillation. In the first case the response of the system to an impulse is therefore growing exponentially, while in the second case it remains constant with time. This explains the given definitions of stability: a stable system responds to an input impulse with a limited output signal, while an asymptotically stable system with an output which goes to zero when time tends to infinite. Since the system is linear, the behavior with any input is completely characterized by the impulse response.

Therefore any control system, in order to be able to maintain the controlled d.o.f. close to the desired value must be stable or better asymptotically stable. Otherwise any disturbance to the input will we amplified and will soon diverge exponentially. The control will fail to work as soon as the motion is larger than the linearity range of the system.

For a feedback system, the requirements of stability and asymptotical stability translate in requirements on the closed loop transfer function: a feedback system is asymptotically stable if and only if the closed loop transfer function

$$G_{CLTF} = \frac{1}{1 + F(s)G(s)}$$

has no pole for $\mathrm{Re}\, s \geq 0$.

E.3.1 Nyquist stability criterion

Usually the study of a system transfer function is carried out in the frequency domain rather than in the Laplace domain, mainly because the values of the transfer function on the imaginary axis $s = i\omega$ are the only one that correspond to physical frequencies and that can be directly measured. The link between the behavior of the system transfer function and the requirements of stability can be derived using standard complex analysis methods [102, 103].

The starting point is the well known *argument principle* [56]: the variation over a closed contour Γ of the phase of a function, analytic in the domain bounded by Γ except for a finite number of poles, is given by the following equation:

$$\frac{1}{2\pi i}\Delta \mathrm{Arg}\, F(s) = \oint_\Gamma \frac{F'(s)}{F(s)}\, ds = n_z(\Gamma) - n_p(\Gamma) \tag{E.3}$$

where the contour is covered in counter clock-wise sense, n_p and n_z denote the number of poles and zeros encircled by Γ. The integrand is called the *logarithmic*

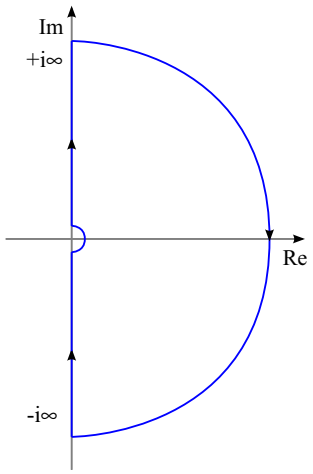

Figure E.2: Contour in the complex plane used for the derivation of the Nyquist stability criterion.

derivative of the function F.

The *Nyquist criterion* for the stability of a closed-loop feedback system can be derived starting from the open loop transfer function $G_{OLTF}(s)$ and considering the contour in the Laplace s-plane shown in figure E.2: it consists of the entire imaginary axis, with a small half-circle around the origin if $G_{OLTF}(s)$ has poles there, covered in clock-wise direction from $-i\infty$ to $+i\infty$ and closed by a half-circle at infinity. The case of poles on the imaginary axis is not taken into account here. If the system is stable in the open-loop configuration, then the function $1 + G_{OLTF}(s)$ has no pole in the right half-plane. The closed-loop system is stable if and only if this function has also no zeros in the right half-plane. Using the argument principle, this is equivalent to the following integral being zero:

$$0 = \oint_{\Gamma} \frac{G'_{OLTF}(s)}{1 + G_{OLTF}(s)}\, ds = \Delta \mathrm{Arg}\left(1 + G_{OLTF}(s)\right) \tag{E.4}$$

The *Nyquist plot* of the open loop transfer function is the image of the Γ contour, which is the curve obtained plotting the complex value of the transfer function while varying the frequency from $-\infty$ to $+\infty$. Since the time-domain response of the system must be real, the transfer function obeys the relation $G(-i\omega) = G^*(i\omega)$ and therefore it is enough to plot the transfer function for the positive physical frequencies and to complete it with its mirror image with respect to the real axis. The Nyquist plot must be covered in the direction corresponding to frequency going from 0 to $+\infty$ and then from $-\infty$ to 0.

Since the contour Γ is covered in clock-wise direction, the right hand term of eq. E.4 is given by the number of times the point -1 is encircled in clock-wise

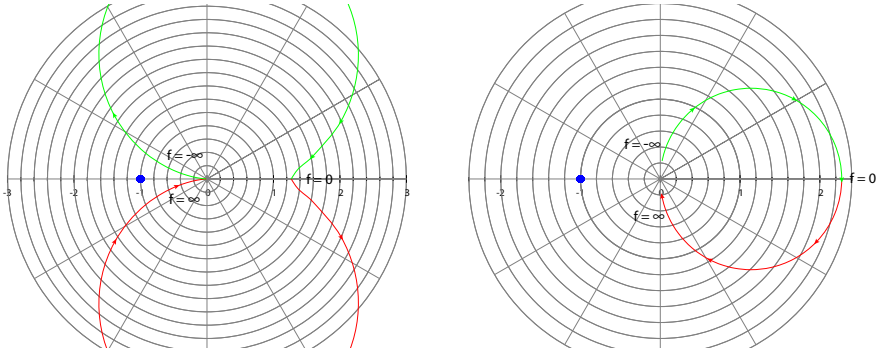

Figure E.3: Examples of Nyquist plot for a system of the first order (right) and of the second order (left).

sense by the *Nyquist plot* of the open-loop transfer function.

In conclusion the following criterion for the stability of closed-loop feed-back system is established:

Nyquist stability criterion. Given a system with stable open-loop transfer function, it is also stable in the closed-loop configuration if and only if its Nyquist plot does not encircle the *critical point* -1 in clock-wise sense.

It is worth to better explain this result by means of some examples. If the system has no pole at zero frequency, the Nyquist plot has no point at infinity and the application of the criterion is straightforward. In fig. E.3 the Nyquist plots for very simple first and second order system are shown:

$$\begin{aligned} F_1(s) &= \frac{1}{s-\omega_0} \\ F_2(s) &= \frac{1}{s^2 - \frac{\omega_0}{Q}s - \omega_0^2} \end{aligned}$$

Both system are stable since the -1 point is never encircled. Both transfer functions go to zero when the frequency goes to $\pm\infty$ and therefore there is no need to complete the Nyquist plot with the image of a circle at infinite frequency. In both cases if the sign of the transfer function is changed, which corresponds to changing the sign of the control filter, the system becomes unstable, since both Nyquist plots encircle the critical point.

As explained in the previous section, the corrector filters often includes one or more pure integrators. In this cases the application of the Nyquist criterion is made a bit more complex by the presence of the singularity in the origin. The Nyquist contour Γ must include a semicircle around the origin, in the right half plane. To understand the Nyquist plot at infinity, it is sufficient to consider the asymptotical behavior of the open loop transfer function, which is characterized

only by the number of real poles at zero frequency. For a first order system

$$G(s) \sim \frac{1}{s}$$

The small circle around the origin in the s-plane can be parametrized as

$$s = \varepsilon e^{i\phi}$$

with ϕ varying from $-\frac{\pi}{2}$ to $+\frac{\pi}{2}$. The corresponding section of the Nyquist plot describes a half circle with very large radius in clock-wise sense:

$$G(s) \sim \frac{1}{\varepsilon} e^{-i\phi}$$

starting from the point at $i\frac{1}{\varepsilon}$ and ending at $-i\frac{1}{\varepsilon}$. This circle moves to infinity when ε goes to zero. In any case it never encircles the critical point. If instead the sign of the open loop transfer function is changed, the portion at infinity of the Nyquist plot encircles the critical point and the system becomes unstable. This allows to state as a general rule that for a system including a pure integrator the phase of the open loop transfer function for frequencies going to zero must be -90 degrees.

A similar result can be obtained for a double pole at the origin. It must be noted that a system whose open loop transfer function is described by only a double real pole at zero frequency can not be stable, since whatever is the sign chosen, the Nyquist plot always pass through the critical point. Therefore some more poles and zeros must be added to the corrector filter to stabilize the system. However, for what concerns the behavior at infinity of the Nyquist plot, the same trick as before can be used. If the open loop transfer function for small frequencies can be approximated by

$$G(s) \sim \frac{1}{s^2}$$

then the part of the Nyquist plot at infinity is a circle starting from a phase close to -180 degrees from above and ending again close to -180 from below. This circle is covered in clock-wise direction. As before, the system is stable with the chosen sign, while it is unstable with the opposite one. In other words, in presence of a double pure integrator, the phase of the open loop transfer function in the limit of zero frequency must be -180 degrees.

In general, in presence of poles in the origin, the Nyquist plot must be completed with a contour at infinity consisting in one half clock-wise circle for each pole, starting from the point at positive infinite frequency and ending in the one at negative infinite frequency.

E.4 Bode and Nichols plots

Together with the Nyquist plot, there are two other common ways to represent the open loop transfer function of a system.

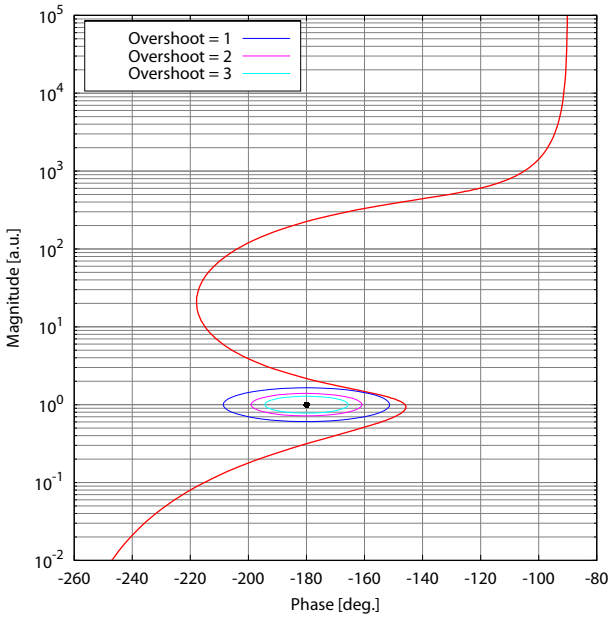

Figure E.4: Example of Nichols plot of the open loop transfer function of a stable system. The ellipses around the critical point show the minimum margin allowed for a given overshoot near the unity gain frequency.

The first one is the *Bode plot*: it simply represents in two different panels the absolute value of the transfer function and its phase as a function of frequency. This plot is useful to get an idea of where the unity gain frequency sits and of the gain of the transfer function at different frequencies. However it is not straightforward to infer the stability of the closed-loop system from this kind of plot.

The *Nichols plot* of the system is obtained plotting the logarithm of the absolute value against the phase of the open loop transfer function (see fig. E.4) when the frequency varies from 0 to $+\infty$. The Nyquist stability criterion can be translated in terms of the Nichols plot. If the transfer function includes pure integrators, the plot must start for large amplitudes from the correct phase: -90 degrees for one pure integrator, -180 for a double integrator and so on. The request that the critical point -1 is not encircled corresponds to the request that the Nichols plot crosses the unity gain axis between the two points corresponding to -180 and 0 phases. If the unity gain line is crossed on the left of this segment, the plot must return again to gains greater than one remaining on the left of the critical point.

The Nichols plot is particularly useful to easily obtain information on the behavior of the closed loop transfer function near the unity gain frequency.

Indeed, if the open loop transfer function passes close to the critical point, the motion of the system can be enhanced instead of reduced at that frequency, since the closed loop transfer function:

$$G_{CLFT}(s) = \frac{1}{1 + G_{OLTF}(s)} \tag{E.5}$$

can become even much larger than one. A limit on this *overshoot* ε can be imposed:

$$\left| \frac{1}{1 + G_{OLTF}(s)} \right| \leq 1 + \varepsilon$$

Usually the system transfer function is much greater than one at low frequency and the closed loop transfer function is smaller than one. It also decreases at high frequency and the closed loop transfer function is then very close to unity. Therefore to characterize the overshoot only the behavior around the unity gain frequency is needed. If the open loop transfer function is close to one, it can be approximated as

$$G_{OLTF}(s) \approx e^{M} e^{i\pi + i\phi} \approx -1 - M + i\phi$$

The request of eq. E.5 translates to

$$M^2 + \phi^2 \geq \frac{1}{(1+\varepsilon)^2}$$

which is the equation of a circle in the Nichols plot, with radius given by $\frac{1}{1+\varepsilon}$. The circles corresponding to overshoots of 1, 2 and 3 are shown in fig. E.4.

Moreover, in the Nichols plot a change in the overall gain of the open loop transfer function corresponds to a vertical translation of the curve. If the translation is large enough to make the plot cross the critical point, the system becomes unstable. The distances along the vertical direction of the critical point from the Nichols plot are called *gain margins* since they give the maximum possible changes in the overall gain that leave the system stable. The two points of the Nichols plot that intersect the -180 degrees vertical line give also the typical frequencies of the instability oscillations that arise if the gain of the control loop changes too much.

Finally, the distance along the horizontal direction from the critical point to the Nichols plot gives the *phase margin* which is an indication of the robustness of the control against changes in the system transfer function.

E.5 An example: locking of a Fabry-Perot cavity

The simplest example of the kind of control system used in Virgo is the locking of a single Fabry-Perot resonant cavity.

E.5.1 Pound-Drever-Hall signal

The optical behavior of the cavity is described in detail in appendix A. If the length is not controlled, the resonance condition changes and the reflected and transmitted powers are not stable.

To keep the cavity on resonance it is necessary to find a good optical signal that can measure the length variation with respect to the resonant one. The first idea could be to use for example the power in the beam transmitted through the cavity. Even if this signal would be maximum at resonance, it decreases both if the cavity gets longer or shorter. Therefore it does not contain enough information for control purposes. One possible solution is the *detuned locking*: the cavity is kept slightly away from resonance and therefore the transmitted power signal has a non-zero slope against length changes. A method very similar to this one is used during the lock acquisition procedure for the full Virgo interferometer (see chapter 3).

The most common method used to lock a Fabry-Perot cavity at resonance is the *Pound-Drever-Hall technique* [104, 105]. As in the frontal modulation scheme for a Michelson interferometer (already explained in Chapter 1), the beam sent into the cavity is first modulated in phase at a given frequency $\Omega/2\pi$. The beam entering the cavity can be described in term of one carrier field and two (upper and lower) radio-frequency (RF) sidebands (see app. A):

$$E_{in}(t) = E_0\, e^{i\omega t}\left[J_0(m) + J_1(m)\, e^{i\Omega t} + J_{-1}(m)\, e^{-i\Omega t}\right] \tag{E.6}$$

where the Bessel functions $J_k(m)$ are used. Being the system linear, the fields transmitted or reflected by the cavity are still given by the superposition of a carrier and two sidebands, with different amplitudes and phases:

$$E_T(t) = e^{i\omega t}\left(A_0 + A_+\, e^{i\Omega t} + A_-\, e^{-i\Omega t}\right) \tag{E.7}$$

The power measured by a photo-diode placed in transmission or reflection is

$$\begin{aligned} P_T(t) \;=\; & |A_0|^2 + |A_+|^2 + |A_0-|^2 \\ & + \cos\Omega t\; \mathcal{R}e\left(A_0^* A_- + A_0 A_+^*\right) \\ & + \sin\Omega t\; \mathcal{I}m\left(A_0^* A_- + A_0 A_+^*\right) \\ & + 2\mathcal{R}e\left(A_+^* A_- e^{-2i\Omega t}\right) \end{aligned} \tag{E.8}$$

The *in-phase* (ACp) and *in-quadrature* (ACq) demodulated signals are obtained by multiplying the output of the photo-diode by two sine-waves at frequency $\Omega/2\pi$, time-shifted by one quarter of period, and afterward by low-pass filtering with a cut-off below the modulation frequency. Therefore the two demodulated signals are given by

$$ACp \;=\; \mathcal{I}m\left(A_0^* A_- + A_0 A_+^*\right) \tag{E.9}$$

$$ACq \;=\; \mathcal{R}e\left(A_0^* A_- + A_0 A_+^*\right) \tag{E.10}$$

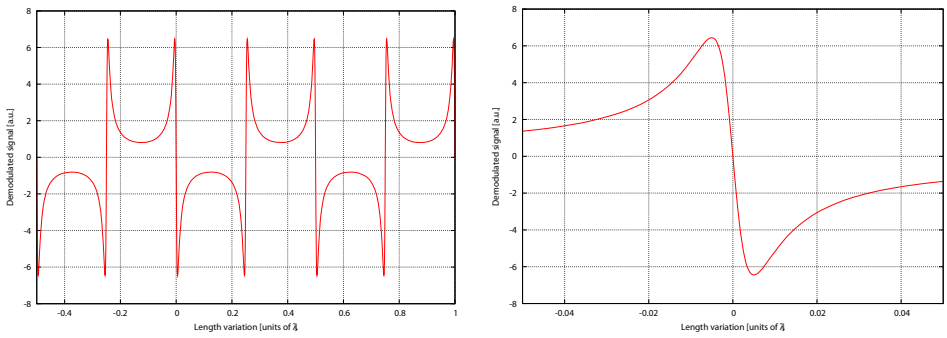

Figure E.5: Left: shape of the Pound-Drever-Hall signal for a Fabry-Perot cavity similar to Virgo arm cavities. Right: zoom around the resonance.

The amplitude of the fields transmitted by the cavity are computed in appendix A and the demodulated signals are given by

$$ACp = -2J_1(m)J_0(m)\left(t_I t_E\right)^2 r_I r_E \frac{\sin(2kx)}{1+\left(r_I r_E\right)^4 - 2\left(r_I r_E\right)^2\cos(4kx)}$$

$$ACq = 0$$

This is the general expression for the Pound-Drever-Hall signal, plotted in fig. E.5. In a narrow region around the resonance the response of the signal to length variation is linear:

$$ACp \approx -\frac{8m\mathcal{F}}{\pi\lambda}\,x \tag{E.11}$$

therefore allowing to reconstruct the displacement from resonance of the two mirrors and to act in order to correct it. In terms of control theory this is a good error signal for stabilizing the length of the Fabry-Perot cavity.

E.5.2 Frequency response of the cavity

To completely determine the behavior of the optical system, which is the plant to be controlled, it is necessary to compute the frequency dependence of the cavity response, which is the transfer function between one of the mirrors motion (the end one for example) and the transmitted signal [12]. In appendix A this transfer function is computed:

$$H(\omega_x) = -2i\frac{\left(t_I t_E\right)^2}{1-\left(r_I r_E\right)^2}\frac{\mathcal{F}}{\pi}\,\frac{1}{1-i\frac{\omega_x}{2\pi f_p}} \tag{E.12}$$

where $f_p = \frac{c}{4L\mathcal{F}}$ is the *pole* of the Fabry-Perot cavity. This transfer function (see fig. E.6) is a low pass filter with a simple pole which for the Virgo arm cavities is $f_p \approx 500$ Hz.

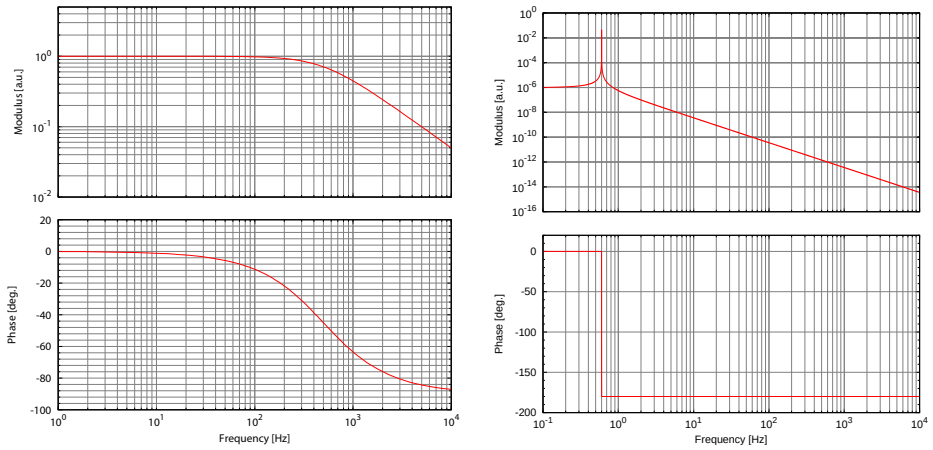

Figure E.6: **Left**: absolute value (top) and phase (bottom) of the frequency response of a Fabry-Perot cavity demodulated transmission to longitudinal motion, for a finesse of $\mathcal{F} = 50$ and a length of $L = 3000$ m, corresponding to a cavity pole at 500 Hz. The absolute value is rescaled in order to be equal to 1 at low frequencies. **Right**: transfer function of the actuators, namely a simple pendulum with resonant frequency at 600 mHz and very high quality factor.

E.5.3 Actuators and corrector

The last missing point is the frequency response of the actuators: for the locking of a single cavity, acting only on the end mirror, this can be modeled by a simple pendulum (see chap. 2), with resonant frequency at about 600 mHz and very high quality factor (see fig. E.6).

The corrector filter designed to control the length of the cavity is a very simple one, see fig. E.7, consisting in a double integrator, compensated at 10 Hz by a complex zero and again at 800 Hz with a complex pole, to have a unity gain frequency around 50 Hz. In this way below the resonant frequency of the actuators the system is a double integrator, capable of maintaining fixed the length of the cavity even in presence of big motions of the input mirror. The pole and zero pair is a common method used to stabilize the system.

The Nichols plot of this system is shown in fig. E.8. The loop margins can be easily read from this plot: the overall gain can be increased or decreased by a factor 5. The phase margin is 50 degrees. This is a really robust feedback system, capable of maintain the control of the cavity even with large changes in the optical transfer function. This robustness is indeed needed in the first moments of the lock acquisition, when the system response is highly non-linear.

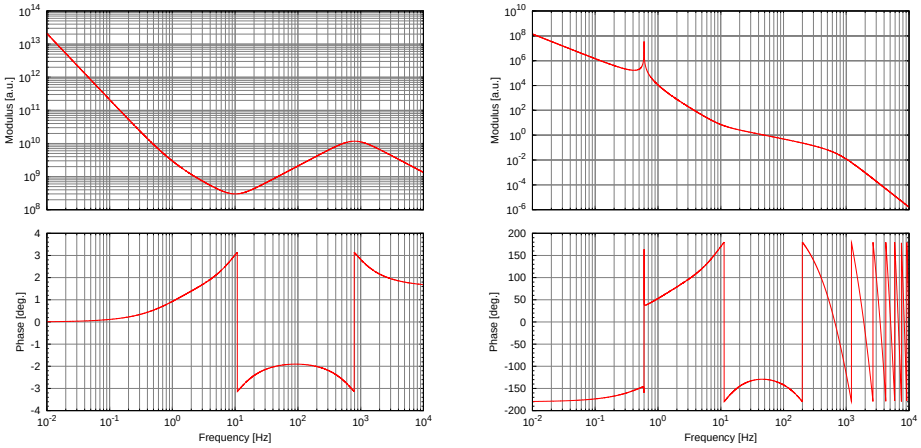

Figure E.7: **Left**: Bode plot of the corrector filter implemented for the control of a single arm cavity. **Right**: open loop transfer function for the control of a single cavity. The unity gain frequency is set at 50 Hz.

E.6 Multi-dimensional control systems

So far only systems with one single degree of freedom has been described. In practice, the most common case is to have multiple degrees of freedom to control at the same time: for example the Virgo longitudinal control system deals with 4 d.o.f. (see chapter 3 for an extended discussion) and the angular control system with 14 d.o.f. (see chapter 4). The main difficulty that can arise in this system is the presence of *cross-couplings* between the various d.o.f.: this can happen at the level of the error signals, meaning that one signal is sensitive to more than one d.o.f. at the same time, or in the actuation part, meaning that the corrections can not be applied directly to single d.o.f., but only to combinations of them. Such kind of systems is usually called MIMO (multiple-input multiple-output) in control system literature.

This situation can be described in a way similar to the single d.o.f. case (see fig. E.9). Let $\mathbf{z}$ denote the vector of free motions of the n system degrees of freedom:

$$\mathbf{z} = \begin{pmatrix} z_1 \\ z_2 \\ \vdots \\ z_n \end{pmatrix} \tag{E.13}$$

and let $\mathbf{e}$ and $\mathbf{c}$ denote respectively the vectors of error and correction signals. The plant can be described in the most general case with a matrix $\mathbf{G}(s)$ of transfer functions, which converts the n motions of the d.o.f. to a given number m of error signals. Of course for the system to be controllable it is necessary that

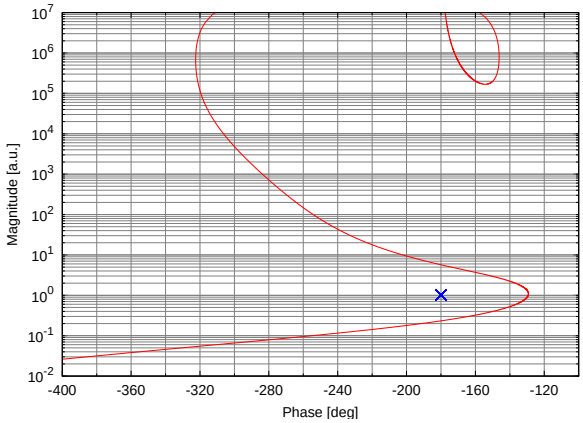

Figure E.8: Nichols plot of the control system for a single arm cavity.

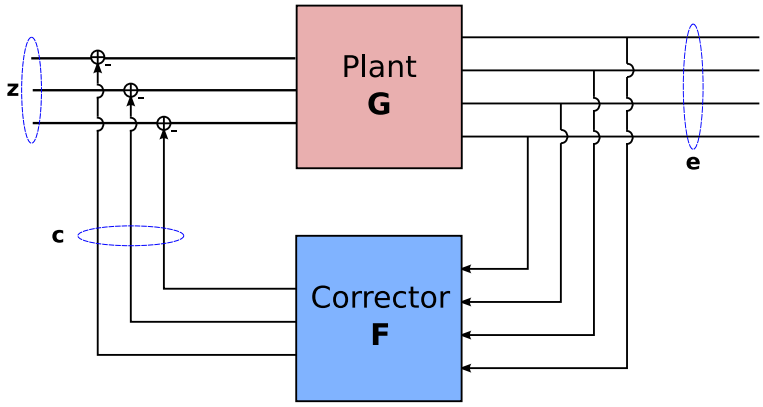

Figure E.9: Scheme of multiple-input multiple-output (MIMO) system. **z** contains the free motions of the system, **e** the error signals and **c** the corrections.

$m \geq n$. In the same way the corrector can be described with another matrix of transfer functions $\mathbf{F}(s)$. The most common way to construct this matrix is to write it as a product of a *sensing* one, which from the various signals reconstruct as well as possible n independent error signals for the n system d.o.f.; a diagonal matrix of correction filters, one for each d.o.f.; finally a *driving* matrix which combines the corrections to obtain suitable signals to be sent to the actuators.

The computation of the effect of closing the feedback can be carried out in a similar way to the SISO case, taking care that all objects are vectors and matrices, therefore the order of operators matters:

$$\mathbf{e} = [\mathbf{1} + \mathbf{G}(s)\mathbf{F}(s)]^{-1}\,\mathbf{G}(s)\,\mathbf{z}$$

and in particular the open loop and closed loop transfer functions are given by:

$$\begin{aligned} \mathbf{G}_{OLTF}(s) &= \mathbf{G}(s)\mathbf{F}(s) \\ \mathbf{G}_{CLTF}(s) &= [\mathbf{1} + \mathbf{G}(s)\mathbf{F}(s)]^{-1} \end{aligned}$$

For the system to be controllable, the open loop transfer function (which is always a $n \times n$ matrix) must be invertible, otherwise there would be at least one linear combination of the system degrees of freedom which has a correction identically equal to zero: in other words the corresponding motion of the system is not controlled. One necessary requirements is that the rank of all matrices must be maximum, i.e. equal to the number n of degrees of freedom to be controlled.

The behavior of multidimensional coupled systems can be quite complex to understand and model. As already stated, an example of such a system is the length sensing and control of the Virgo interferometer, which is described in chapter 3.

Appendix F

Non-stationary noise couplings

It is quite common to permanently add some external perturbation to various control loops, mainly in the form of single lines, in order to measure loop parameters and also for calibration purposes. It turned out to be quite useful to track their evolution in time and also the variations of the ratio of lines as seen in different signals, since this can provide information on the time variations of control noise couplings.

In general, one calibration line at a given frequency f is added into one of the control loops, usually to the error point. The typical situation is to track the coupling of the noise from the error point to the dark fringe. One possible way is to measure the power in the line in both signals, using band-limited RMS computations or line identification algorithms, and to estimate the coupling by the ratio of the amplitudes in the two signals. In this way however no information on the phase of the coupling coefficient can be recovered. To overcome this limitation, the transfer function between the two signals can be computed, using standard methods described in appendix D. The coherence gives a quality check for the measurement

This method is however not the more convenient way to track a single lines, since it implies estimation of full Fourier transforms to look at a single bin. Even if it is possible to compute the Fourier transform at the line frequency only, a more convenient method to compute the amplitude of a line is to implement a *demodulation algorithm* similar to what it is done in the frontal modulation scheme for extracting control signals from an interferometer.

A first kind of demodulation can be used to extract the amplitude and phase of the line at frequency f in a given signal with respect to a reference pure sine wave. Referring to fig. F.1, the input signal x is first passed through a resonant filter (made of a zero at 0 Hz and a pole with high Q at the demodulation

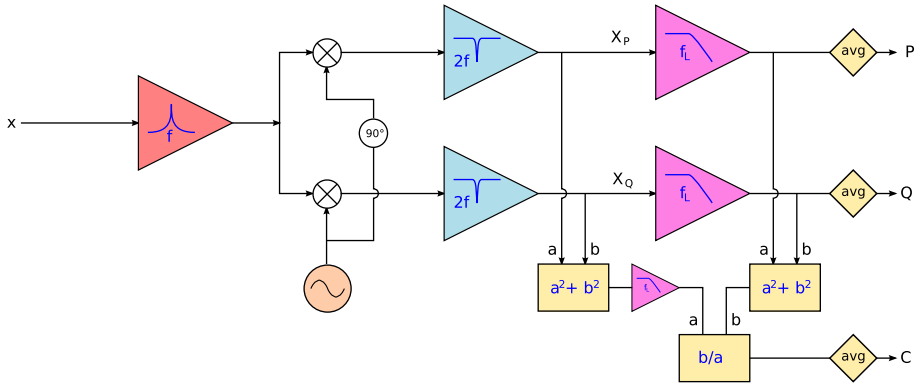

Figure F.1: Scheme of the algorithm used for the demodulation of a signal at a given frequency f using a internally generated reference sine wave.

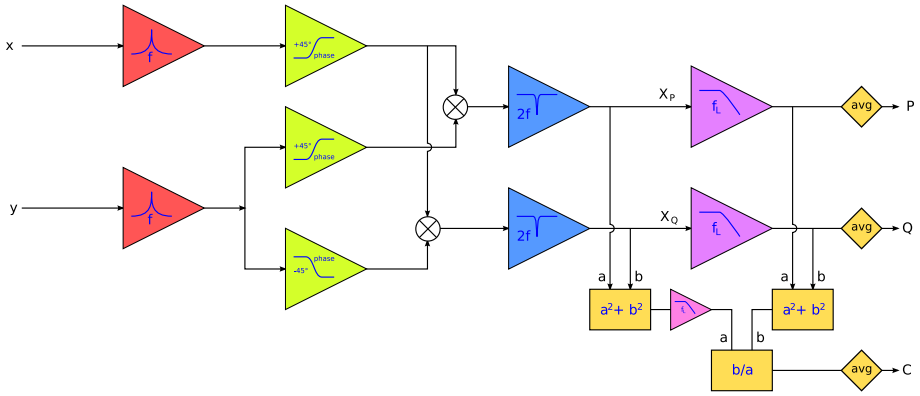

Figure F.2: Scheme of the algorithm used for the demodulation of a signal at a given frequency f with respect to another reference signal.

frequency f), in order to strongly suppress all components of the signals far from the interesting frequency. If the original signal contains a modulated line at the f frequency, the result of this resonant filtering can be modeled as

$$r(t) = A(t)\,\sin\left(2\pi f t + \phi(t)\right) = A_s(t)\,\sin(2\pi f t) + A_c(t)\,\cos(2\pi f t)$$

where both amplitude and phase modulations are considered. Here $A(t)$, $\phi(t)$, $A_s(t)$ and $A_c(t)$ are changing slowly in time, meaning that their spectra are mainly confined to frequencies much smaller than f.

The resulting $r(t)$ is mixed with a reference sine wave and with the corresponding cosine wave:

$$\begin{aligned} s(t) &= \sin(2\pi f + \phi_0) \\ c(t) &= \cos(2\pi f + \phi_0) \end{aligned}$$

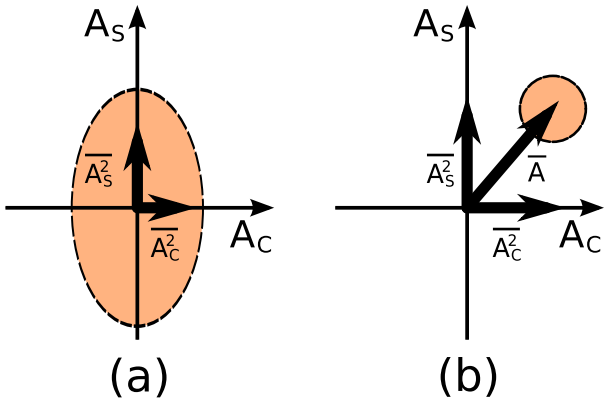

Figure F.3: Scheme of the behavior of P and Q values if there is (b) or not (a) a signal at the demodulation frequency. Refer to the text for an explanation of how this difference can be used to compute a quality check.

so that the two resulting signals contain both a component at low frequency and one at $2f$:

$$\begin{aligned} r(t) \cdot s(t) &= A_s(t)\,\frac{1-\cos(4\pi f t)}{2} + A_c(t)\,\frac{\sin(4\pi f t)}{2} \\ r(t) \cdot c(t) &= A_s(t)\,\frac{\sin(4\pi f t)}{2} + A_c(t)\,\frac{1+\cos(4\pi f t)}{2} \end{aligned}$$

The amplitude of the line, divided into the in-phase and in-quadrature components, can be recovered by considering only the component at low frequency. For this reason the two signals resulting from the mixing are passed through a notch filter at two times the demodulation frequency (a filter equal to one everywhere except for a narrow dip at $2f$) and then low-passed with a second-order filter with corner frequency well below the demodulation one. Finally the output signals are computed by down-sampling the results with simple averages. In this way the two amplitudes $A_s(t)$ and $A_c(t)$ are recovered and if needed these can be used to reconstruct the line amplitude and phase.

This procedure gives clearly an output even if there is no line at the demodulation frequency and therefore it is important to build a quality check, similar to coherence. Suppose first that there is no signal at the demodulation frequency. In this case both $A_s(t)$ and $A_c(t)$ are varying randomly with zero mean on a fast time scale. The signals obtained immediately after the $2f$ notch and before the low-pass filter (called X_P and X_Q in fig. F.1) have zero mean and non zero RMS (see fig. F.3a). The sum of the two squared signals is then computed and passed through a low-pass filter, equivalent to averaging. On the contrary, the two signals after passing through the low-pass filter, are small compared to the

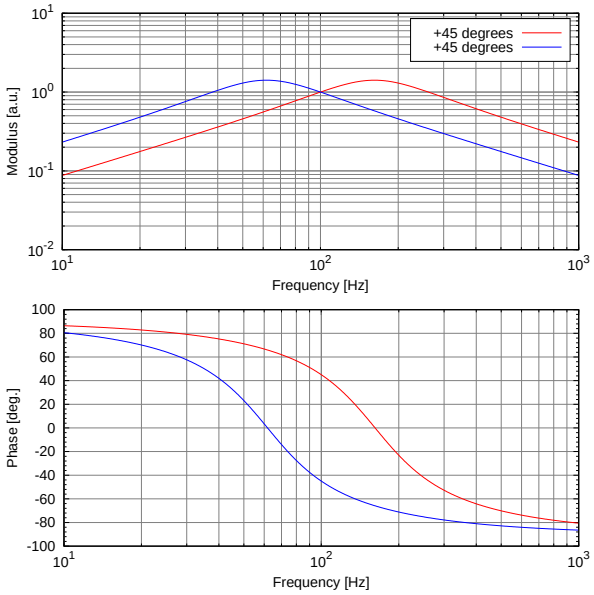

Figure F.4: Bode plots of the phase lag filters used in the demodulation algorithm to add a dephasing to the input signals. The plotted filters are tuned for a frequency $f = 100$ Hz.

previously computed total RMS. Therefore the following quantity

$$C = \frac{\overline{X_P}^2 + \overline{X_Q}^2}{\overline{X_P^2 + X_Q^2}} \tag{F.1}$$

is small when there is no signal at the demodulation frequency. Suppose now that some signal is present (see fig. F.3b). In this case both X_P and X_Q have non-zero mean, greater than their standard deviation. Therefore the sum of their RMS is close to (and always greater of) the sum of their squared mean values. From this follows that the quantity computed in eq. F.1 is close to 1: in conclusion this is a good estimate of the coherence between the signal and the reference sine and cosine waves, at the demodulation frequency.

A similar procedure can be used to demodulate a signal using another one as reference. A typical example is the injection of a calibration line and the demodulation of the dark fringe signal with respect to the injected line itself. In this kind of demodulation (see fig. F.2) the two input signals are first passed through the resonant filter. The in-phase component of the demodulation can be recovered simply mixing the two resulting signals. To obtain the in-quadrature components it would be necessary to add a delay of one quarter of period to the reference signal: this can be done easily by shifting the samples only if the required delay is a precise multiple of the sampling time. Since this is not often

the case, an alternative technique must be used. Two filters are developed in order to produce a phase shift of ± 45 degrees at the frequency f. This is done by using a filter with a broad resonance around a frequency tuned to have the correct phase at f and unitary gain at the same frequency (see fig. F.4). The two resonant frequencies are given by

$$f_{\pm} = \frac{2f}{\sqrt{5} \mp 1}$$

One signal is passed through the $+45$ degrees filter only, while the other one is passed through both $+45$ degrees and -45 degrees filters. Then mixing the first signals with the other two gives both in-phase and in-quadrature components. The rest of the demodulation process is equal to that already described.

Bibliography

[1] K. S. Thorne, C. W. Misner and J. A. Wheeler, *"Gravitation"*, W. H. Freeman publisher (1973)

[2] R. M. Wald, *"General Relativity"*, University Of Chicago Press (1974)

[3] R. A. Hulse and J. H. Taylor, *"Discovery of a pulsar in a binary system"*, Astrophys. J. **195** (1975) L51.

[4] J. M. Weisberg and J. H. Taylor, *"Relativistic Binary Pulsar B1913+16: Thirty Years of Observations and Analysis"*, arXiv:astro-ph/0407149

[5] L. Blanchet, T. Damour, G. Esposito-Farese and B. R. Iyer, *"Gravitational radiation from inspiralling compact binaries completed at the third post-Newtonian order"*, Phys. Rev. Lett. **93** (2004) 091101 [arXiv:gr-qc/0406012].

[6] P. S. Saulson, *"Fundamentals of Interferometric Gravitational Wave Detectors"*, World Scientific Publishing (1994)

[7] D. Sigg for the LIGO Science Collaboration, *"Status of the LIGO detectors"* in "Selected papers from the 6th Edoardo Amaldi Conference on Gravitational Waves", Class. Quant. Grav. **23** (2006) S51

[8] H. Lück and al., *"Status of the GEO600 detector"* in "Selected papers from the 6th Edoardo Amaldi Conference on Gravitational Waves", Class. Quant. Grav. **23** (2006) S71

[9] K. Arai for the TAMA collaboration, *"Current efforts on the TAMA300 detector"*, Proceeding of the 6th Edoardo Amaldi Conference on Gravitational Waves

[10] F. Acernese et al., *"Status of Virgo detector"*, Class. Quant. Grav. **24** (2007) S81

[11] See for example the web site `http://www.anu.edu.au/Physics/ACIGA`

[12] J.-Y. Vinet et al., *"The Virgo Physics Book, Vol II"* (2004) [http://wwwcascina.virgo.infn.it/vpb/]

[13] B. F. Schutz, *"Gravitational wave astronomy"*, Class. Quant. Grav. **16** (1999) A131 [arXiv:gr-qc/9911034].

[14] E. E. Flanagan, *"Astrophysical sources of gravitational radiation and prospects for their detection"*, arXiv:gr-qc/9804024

[15] V. Kalogera, R. Narayan, D. N. Spergel and J. H. Taylor, *"The Coalescence Rate of Double Neutron Star Systems"*, Astrophys. J. **556** (2001) 340 [arXiv:astro-ph/0012038]

[16] K. Belczynski, V. Kalogera and T. Bulik, *"A comprehensive study of binary compact objects as gravitational wave sources: Evolutionary channels, rates, and physical properties"*, Astrophys. J. **572** (2001) 407 [arXiv:astro-ph/0111452].

[17] E. Mueller, *"Gravitational radiation from core-collapse supernovae"* Class. Quant. Grav. **14** (1997) 1455

[18] C. Palomba, *"Detectability of Gravitational Radiation from Prompt and Delayed Star Collapse to a Black Hole"*, astro-ph/0003321 (2000)

[19] A. Giazotto, S. Bonazzola and E. Gourgoulhon, *"Gravitational waves emitted by an ensemble of rotating neutron stars"*, Phys. Rev. D **55** (1997) 2014

[20] L. P. Grishchuk, V. M. Lipunov, K. A. Postnov, M. E. Prokhorov and B. S. Sathyaprakash, *"Gravitational wave astronomy: In anticipation of first sources to be detected"*, Phys. Usp. **44** (2001) 1 [Usp. Fiz. Nauk **171** (2001) 3] [arXiv:astro-ph/0008481].

[21] B. Allen and J. D. Romano, *"Detecting a stochastic background of gravitational radiation: Signal processing strategies and sensitivities"*, Phys. Rev. D **59** (1999) 102001 [arXiv:gr-qc/9710117]

[22] T. Damour and A. Vilenkin, *"Gravitational radiation from cosmic (super)strings: Bursts, stochastic background, and observational windows"* Phys. Rev. D **71** (2005) 063510 [arXiv:hep-th/0410222].

[23] C. M. Caves, *"Quantum-mechanical noise in a interferometer"*, Phys. Rev. D **23** (1981)1693

[24] B. J. Meers and K. A. Strain, *"Modulation, signal and quantum noise in interferometers"*, Phys. Rev. A **44** (1991) 4693

[25] A. Vicere, *"Introduction to the data analysis in interferometric gravitational wave experiments"*, SPIRES entry *Prepared for International Summer School on Experimental Physics of Gravitational Waves, Urbino, Italy, 6-18 Sep 1999*

[26] P. Hello, *"Detection rates of inspiralling neutron star-neutron star binaries"*, in Proceedings of GWDAW2 (1998)

[27] M. Zimmermann, *"Gravitational Waves From Rotating And Precessing Rigid Bodies. 1. General Solutions And Computationally Useful Formulas"*, Phys. Rev. D **21** (1980) 891

[28] J. D. Scargle, *"Studies in astronomical time series analysis. 2. Statistical aspects of spectral analysis of unevenly spaced data"*, Astrophys. J. **263** (1982) 835

[29] D. Passuello and S. Braccini, *"Correction of Doppler effect by discrete signal resampling"*, Virgo Internal Note VIR-046A-07 (2007)

[30] M. Camarda and A. Ortolan, *"Search for gravitational wave bursts by wavelet packet decomposition: the detection algorithm"*, Phys. Rev. D **74** (2006) 062001

[31] P. Ruggi, *"L'attenuazione del rumore sismico nel rivelatore di onde gravitazionali VIRGO"*, Tesi di laurea, University of Pisa (2003)

[32] S. Braccini et al., *"Measurement of the seismic attenuation performance of the VIRGO superattenuator"*, Astropart. Phys. **23** (2005) 557.

[33] M. Beccaria *et al.*, *"Extending the VIRGO gravitational wave detection band down to a few Hz: Metal blade springs and magnetic antisprings"*, Nucl. Instrum. Meth. A **394** (1997) 397.

[34] G. Losurdo, *"Ultra-low frequency inverted pendulum for the VIRGO test-mass suspension"*, Ph. D. thesis, Scuola Normale Superiore, Pisa (1998)

[35] G. Losurdo for the Virgo Coll., *"The inertial damping of the Virgo SA and the residual motion of the mirror"*, Class. Quantum Grav., **19** (2002) 1631

[36] F.Acernese et al. (Virgo Coll.), *"A local control system for the test masses of the Virgo GW detector"*, Astrop. Phys., **20** (2004) 617

[37] E. Genin and P. La Penna, *"Scanning Fabry-Perot : Principle and characterization"*, Virgo internal note VIR-014B-07 (2007)

[38] K. Blackburn, A. Lazzarini and B. Mours, *"Specification of a Common Data Frame Format for Interferometric Gravitational Wave Detectors"*, Virgo internal document VIR-SPE-LAP-5400-102 and LIGO internal document LIGO-T970130-01-E

[39] C. Cagnoli, L. Gammaitoni, J. Kovalik, F. Marchesoni, M. Punturo, *"The Virgo sensitivity curve"*, Virgo Internal Note VIR-NOT-PER-1390-51 (2004) and references therein

[40] G. Cella, E. Cuoco et al. *"Relevance of Newtonian seismic noise for the VIRGO interferometer sensitivity"*, Class. Quantum Grav **15** (1998) 3339

[41] P. R. Saulson, *"Terrestrial gravitational noise on a gravitational wave antenna"*, Phys. Rev. D **30** (1984) 732.

[42] P. R. Saulson, *"Thermal Noise In Mechanical Experiments"*, Phys. Rev. D **42** (1990) 2437

[43] G. Cagnoli, L. Gammaitoni, J. Kovalik, F. Marchesoni and M. Punturo, *"Low-frequency internal friction in clamped-free thin wires"*, Phys. Lett. A **225** (1999), 230

[44] B. J. Meers, *"Recycling In Laser Interferometric Gravitational Wave Detectors"*, Phys. Rev. D **38** (1988) 2317

[45] F. Bondu et al., *"Dark Fringe Shot Noise Sensitivity"*, Virgo internal note VIR-NOT-OCA-1390-243 (1998)

[46] L. Barsotti, *"The control of the Virgo interferometer for gravitational wave detection"*, Ph.D. thesis, Universitá di Pisa (2006)

[47] F. Bondu, *"Étude bu bruit thermique et stabilization en fréquence du laser du détecteur interférométrique d'ondes gravitationnelles Virgo"*, Ph.D. thesis, Université de Paris-Sud (1996)

[48] M. Barsuglia, *"Stabilisation en fréquence du laser et contrôle des cavités optiques à miroirs suspendus pour le détecteur interférométrique d'ondes gravitationnelles Virgo"*, Ph.D. thesis, Université de Paris-Sud (1999)

[49] M. Evans, *"Lock acquisition in resonant optical interferometers"*, Ph.D. thesis, California Institute of Technology (2001)

[50] K. Arai and TAMA collaboration, *"Sensing and controls for power-recycling of TAMA300"*, Class.Quant.Grav. **19(7)** (2002) 1843

[51] B. Willke *et al.*, *"The GEO600 stabilized laser system and the current-lock technique"* Prepared for 3rd Edoardo Amaldi Conference on Gravitational Waves (Amaldi 99), Pasadena, California, 12-16 Jul 1999

[52] S. Kreckelbergh, *"Contrôle longitudinal et caractérisation optique du détecteur Virgo"*, Ph.D. thesis, Université de Paris-Sud Orsay (2005)

[53] *Virgo Optics Description Web-page*, [http://wwwcascina.virgo.infn.it/optics]

[54] M. Mantovani, *"The automatic alignment system of the Virgo interferometer"*, Ph.D. thesis, University of Siena (2008)

[55] A. E. Siegman, *"Lasers"*, University Science Books (1986)

[56] R. Courant and D. Hilbert, *"Methods of Mathematical Physics"*, Wiley-Interscience (1989)

[57] E. Morrison, B. J. Meers, D. I. Robertson and H. Ward, *"Experimental demonstration of an automatic alignment system for optical interferometers"*, Appl. Opt. **33** (1994), 5037

[58] E. Morrison, B. J. Meers, D. I. Robertson and H. Ward, *"Automatic alignment of optical interferometers"*, Appl. Opt. **33** (1994), 5041

[59] D. Z. Anderson, *"Alignment of resonant optical cavities"*, Appl. Opt. **23** (1984), 2944

[60] N. Mavalvala, *"Alignment Issues in Laser Interferometric Gravitational-Wave Detectors"*, Ph.D. thesis, MIT (1997)

[61] A. Freise, G. Heinzel, H. Luck, R. Schilling, B. Willke and K. Danzmann, *"Frequency domain interferometer simulation with higher-order spatial modes"*, Class. Quant. Grav. **21** (2004) S1067 [arXiv:gr-qc/0309012]

[62] B. Swinkels, E. Campagna, G. Vajente, *"Noise subtraction techniques"*, Virgo Internal note VIR-XXX (2008)

[63] M. Punturo, *"Overview of the resonant mode method to extract the mirror absorption"*, talk at May 2007 LSC-Virgo Collaboration meeting

[64] M. Punturo, *"Etalon Effect and Virgo+"*, talk at July 2007 Virgo Collaboration Meeting

[65] G. Vajente, E. Campagna and B. Swinkels, *"Locking characterization"*, Virgo Internal note VIR-005A-08 (2008)

[66] L. Rolland, talk at the May 2007 Virgo-LSC Collaboration Meeting

[67] L. Rolland, F. Marion and B. Mours, *"Mirror and marionette actuation calibration for VSR1"*, Virgo Internal Note VIR-015A-08 (2008)

[68] J. R. Smith, *"Formulation of instrument noise analysis techniques and their use in the commissioning of the gravitational wave observatory GEO600"*, Ph.D. thesis, Hannover University (2006)

[69] F. Acernese *et al.*, *"NAP: A tool for noise data analysis. Application to Virgo engineering runs"*, Class. Quant. Grav. **22** (2005) S1041.

[70] See the Calibration and Reconstruction web page at `http://wwwcascina.virgo.infn.it/DataAnalysis/Calibration` and F. Beauville, *"Prélude à l'analyse des donneés du détecteur Virgo: de l'étalonnage à la recherche de coalescences binaires"*, Ph.D. thesis, Université de Savoie (2005)

[71] J. R. Smith, P. Ajith, H. Grote, M. Hewitson, S. Hild, H. Lück, K. A. Strain, B. Willke, J. Hough and K. Danzmann, *"Linear projection of technical noise for interferometric gravitational-wave detectors"*, Class. Quant. Grav. **23** (2006) 527

[72] G. Vajente, *"Measurement of control noise budget"*, Virgo Internal note VIR-003A-08 (2008)

[73] R. Gouaty, *"Analyse de la sensibilité du détecteur d'ondes gravitationnelles Virgo"*, Ph.D. thesis, Université de Savoie (2006)

[74] V. Granata, *"Noise budget August-September 2006"*, talk at the September 2006 Virgo Collaboration Meeting

[75] G. Cagnoli, L. Gammaitoni, J. Kovalik, F. Marchesoni, and M. Punturo, *"Eddy current damping of high Q pendulums in gravitational wave detection experiments"*, Rev. of Sci. Instr. **69** (1999) 2777

[76] F. Barone, E. Calloni, L. Di Fiore, A. Grado, L. Milano, P. Hello and G. Russo, *"Effects of misalignments and beam jitters in interferometric gravitational wave detectors"*, Phys. Lett. A **217** (1996) 90

[77] T. M. Niebauer, R. Schilling, K. Danzmann, A. Rüdiger and W. Winkler, *"Nonstationary shot noise and its effect on the sensitivity of interferometers"*, Phys. Rev. A **43** (1991) 5022

[78] I. Fiori, N. Christensen, E. Cuoco, F. Paoletti, G. Vajente, *"Analysis of frequency lines in C7 run"*, Virgo Internal note VIR-031B-07 (2007)

[79] F. Acernese *et al.*, *"A simple line detection algorithm applied to Virgo data"*, Class. Quant. Grav. **22** (2005) S1189.

[80] G. Vajente, *"NonStatMoni technical description"*, Virgo Internal note VIR-004A-08 (2008)

[81] http://wwwcascina.virgo.infn.it/MonitoringWeb/NonStatMoni

[82] G. Vajente, *"Study of dark-fringe noise slow non-stationarities during VSR1"*, Virgo Internal note VIR-009A-08 (2008)

[83] N. R. Draper and H. Smith, *"Applied Regression Analysis"*, Wiley Series in Probability and Statistics, Wiley-Interscience (1998)

[84] I. S. Heng, R. Balasubramanian, B. S. Sathyaprakash and B. F. Schutz, *"First steps towards characterizing the hierarchical algorithm for curves and ridges pipeline"*, Class. Quant. Grav. **21** (2004) S821

[85] P. Ajith, M. Hewitson, J. R. Smith and K. A. Strain, *"Robust vetoes for gravitational-wave burst triggers using known instrumental couplings"*, Class. Quant. Grav. **23** (2006) 5825

[86] G. Vajente, *"The HACR algorithm for short transient detection"*, Virgo Internal note VIR-002A-08 (2008)

[87] http://wwwcascina.virgo.infn.it/MonitoringWeb/HACR

[88] Virgo collaboration, *"Detector report: Virgo+ evolution preparation"*, Virgo Internal Document

[89] R. Flaminio, *"Virgo+ sensitivity versus Fabry-Perot cavities finesse"*, Virgo internal note

[90] M. Rakhmanov, *"Dynamics of Laser Interferometric Gravitational Wave Detectors"*, Ph.D. Thesis, California Institute of Technology (2000)

[91] Virgo Collaboration, *"Virgo Progress Report for the STAC and EGO Council"*, Virgo Internal Document (2007)

[92] L. Barsotti and M. Evans, *"Lock acquisition of Virgo: technical description"*, Virgo internal note (2007)

[93] L. Barsotti and M. Evans, *"Virgo automation: thermal transient and transition to low noise"*, Virgo internal note (2007)

[94] J. Marque, *"Input mirrors thermal lensing effect in Virgo"*, talk at the 12th ILIAS N5-WP1 Meeting (2007)

[95] M. Punturo, *"Thermal lensing analysis and simulation"*, talk at the September 2006 Virgo Collaboration meeting

[96] A. Papoulis and S. U. Pillai, *"Probability, Random Variables and Stochastic Processes"*, McGraw-Hill Publishing Co. (2001)

[97] S. M. Kay, *"Modern Spectral Estimation: Theory and Application"*, Prentice Hall (1988)

[98] S. M. Kay, *"Fundamentals of Statistical Signal Processing, Volume I: Estimation Theory"*, Prentice Hall PTR (1993)

[99] P. D. Welch, *"The use of fast Fourier transforms for the estimation of power spectra: A method based on time averaging over short modified periodograms"*, IEEE Transactions on Audio and Electroacoustics, **15** (1967) 70

[100] W. H. Press, S. A. Teukolsky, W. T. Vetterling and B. P. Flannery, *"Numerical Recipes in C++: The Art of Scientific Computing"*, Cambridge University Press (2002)

[101] S. W. Smith, *"The Scientist and Engineer's Guide to Digital Signal Processing"*, California Technical Publishing (1999)

[102] J. Doyle, B. Francis and A. Tannenbaum, *"Feedback control theory"*, Macmillan Publishing Co. (1990)

[103] G. Marro, *"Controlli automatici"*, Zanichelli (1992)

[104] R. V. Pound, *"Electronic frequency stabilization of microwave oscillators"*, Rev. Sci. Inst., **17** (1946) 490

[105] R. W. Drever, J. L. Hall, F. V. Kowalski, J. Hough, G. M. Ford, A. J. Munley and H. Ward, *"Laser phase and frequency stabilization using an optical resonator"*,